AN ABSTRACT OF THE THESIS OF

Mary L. Batteen for the degree of Doctor of Philosophy in Atmospheric Sciences presented on April 30, 1984.

Title: Numerical Studies of Mesoscale Eddies Using Quasigeostrophic and Primitive Equation Ocean Models

Abstract approved: Redacted for privacy

Dr. William R. Holland

Redacted for privacy

Dr. Young-June Han

The dynamical role of mesoscale eddies in the ocean general circulation is investigated using eddy-resolving quasigeostrophic (QG) and primitive equation (PE) models which are parametrically identical. The results of both QG and PE numerical experiments in mid-latitude, rectangular ocean basins are systematically intercompared and extensively analyzed in terms of basic quantities: energetics, relative and potential vorticity, and eddy momentum and heat transports.

Although overall the analyses show that the results are fairly similar between the two models, a closer examination reveals some significant differences. Most of these differences are due to the presence of Kelvin waves along the lateral boundaries of the PE model. These waves are the main source for mean and eddy divergent kinetic energy. Further model parameter

studies are needed to determine whether the presence of these Kelvin waves is due to numerics, physics, or a combination of the two, and if the two-day sampling rate commonly used for obtaining eddy statistics significantly aliases these high frequency waves.

Numerical Studies of Mesoscale Eddies Using Quasigeostrophic and Primitive Equation Ocean Models

by

Mary L. Batteen

A THESIS

submitted to

Oregon State University

in partial fulfillment of
the requirements for the
degree of

Doctor of Philosophy

Completed April 30, 1984

Commencement June 1984

APPROVED:

Redacted for privacy

Co-major Professor of Atmospheric Sciences in charge of major

Redacted for privacy

Co-major Professor of Atmospheric Sciences in charge of major

Redacted for privacy

Chairman of the Department of Atmospheric Sciences

Redacted for privacy

Dean of Graduate School

Date thesis is presented April 30, 1984

Typed by Sally Hawkins for Mary L. Batteen

ACKNOWLEDGEMENTS

This thesis is the result of a cooperative effort between the National Center for Atmospheric Research (NCAR) and Oregon State University (OSU). Funding was provided by a National Science Foundation fellowship from the Oceanography Section in the Atmospheric Analysis and Prediction Division at NCAR. Extensive computing support was provided by the Scientific Computing Division at NCAR through University Requests. Additional computing resources, especially in the earlier stages, were provided by the Oceanography Section.

I wish to thank all of those involved in this cooperative effort both at OSU and at NCAR. In particular, I wish to thank my advisors, Dr. William R. Holland and Dr. Y.-J. Han, and the members of my thesis committee, Dr. W. L. Gates and Dr. Steven Esbensen.

Before I arrived at NCAR, Dr. Han provided a large part of the incentive and background for this study. Without the unselfish devotion of his time, the project would never have been initiated.

This study was carried out at NCAR under the expert guidance of Dr. Holland. His insight and knowledge of ocean modeling and ocean general circulation were invaluable, and contributed much to the content of this work. He graciously provided the code for both his QG and PE models.

Many other people contributed to the final output. Rick Wolski, in particular, devoted much of his time to the programming, drafting, and final preparation of the thesis. The secretarial assistance of Sally Hawkins who typed the manuscript is appreciated. Stephanie Honaski drafted some of the figures. Julianna Chow provided valuable assistance with the model codes. Barb Hill was always available for administrative assistance and Mary Niemczewksi for general assistance.

In addition the thesis benefited from my discussions with many people at NCAR, in particular, Chuck Leith, Akira Kasahara, Ron Errico, Bach-Lien Hua, Warren Washington, Francis Bretherton, Roger Daley, Bert Semtner and Dale Haidvogel.

TABLE OF CONTENTS

LIST OF FIGURES

LIST OF TABLES

NUMERICAL STUDIES OF MESOSCALE EDDIES USING QUASIGEOSTROPHIC AND PRIMITIVE EQUATION OCEAN MODELS

CHAPTER 1. INTRODUCTION

The role of the ocean in climatic change is becoming an increasingly important element of climate research. The large heat capacity, coupled with the large transport of heat by currents, give the oceans the potential for exerting a strong influence upon climate and its variation (Manabe, 1983). Observational studies have shown that the kinetic energy of mesoscale eddies can be one or two orders of magnitude greater than that of the time-averaged motions, at least in certain parts of the world ocean (see Wyrtki et al., 1976, for example). These observations suggest that the ocean general circulation may be significantly influenced by the mesoscale eddy field, especially in areas of intense currents, such as the Gulf Stream, where active air-sea interaction occurs. Since eddies have been shown to be important mechanisms for transporting momentum and potential vorticity (Holland, 1983), it seems likely that they could also be important mechanisms for transporting heat.

In order to properly assess the role of mesoscale eddies in climate, we need an appropriate tool that will allow us to systematically investigate not only the eddies' contribution to the ocean heat transport, but also their effect on the ocean

general circulation. Observations, analytical investigations, and numerical models are all possible tools.

In the following chapter, we will briefly review how the use of each of these tools has contributed to our present understanding of eddies and the ocean general circulation, and then consider the use of these tools for studying the role of mesoscale eddies in both the ocean general circulation and in climate. Currently, eddy-resolving general circulation models (EGCMs) appear to be the most appropriate tool for an in-depth, quantitative analysis, and so they will form the basis for this study.

We next survey the types of EGCMs available, and review intercomparisons between the models to help decide what type of EGCM to use. From this survey we see that there is at the present time no "ideal" model to study the role of mesoscale eddies in climate. An "ideal" model for our purposes would be one that incorporates complete thermodynamic processes yet uses reasonable amounts of computer time.

A good candidate for this EGCM might be a model intermediate between quasigeostrophic (QG) and primitive equation (PE) models. This type of model could possibly incorporate thermal effects not found in a QG model, yet use less computer time than a PE model. It soon becomes apparent that the proper development and evaluation of such a model requires a deeper understanding of QG and PE physics.

This has led to the present study: a quantitative intercomparison of QG and PE models which have both been modified in order to emphasize differences and similarities. The main purpose of this model intercomparison is to explore the following questions:

a) Can the two models be configured to give nearly similar results?

b) Are the differences due to numerics or to physics?

c) What is the best choice of model configuration for the basic problem, i.e., the role of mesoscale eddies in climate?

d) What is the best configuration for an intermediate model?

e) How well does QG physics represent more complete physics?

We begin this study in Chapter 3 by describing the PE and QG model equations, and discussing their similarities and differences. Next, in order to overcome differences in model equations and prognostic variables, we start with the PE system of equations and derive a set of equations which has the same form and prognostic variables as the QG system, as well as some variables not found in QG. We then make the following approximations to this set: 1) full balance, 2) linear balance, and 3) QG. Either the full or linear balance set of equations could be the basis of the "ideal" model described previously. As a

result we obtain a hierarchy of systems of equations from PE to QG, which allows us to evaluate the importance of each of the terms involved in this sequence of approximations.

Using these and other methods of analysis presented in Chapter 4, the results of two QG and PE numerical experiments are systematically intercompared (Chapters 5 and 6). In Chapter 7, the results of these comparisons are discussed. Finally, in Chapter 8 we summarize the results.

CHAPTER 2. BACKGROUND

2.1 Current state of knowledge

Observational studies of currents in many parts of the world ocean have revealed the presence of mesoscale eddies (Swallow and Hamon, 1960; Crease, 1962; Koshlyakov and Grachev, 1973; Kitano, 1974, 1975; Bernstein and White, 1974; Dantzler, 1976; Wyrtki et al., 1976; Richman et al., 1977; Schmitz, 1977; Baker et al., 1977). Field programs (POLYGON, MODE, POLYMODE, ISOS, NORPAX) have been conducted to determine the basic characteristics of these eddy systems.

What is known about eddies from observations on a global basis has recently been summarized by: 1) Dickson (1983), using flow statistics from long-term current meter moorings; and 2) Emery (1983), using temperature measurements. Regional summaries have been presented by: 1) Schmitz (1978), Richardson (1983), Wunsch (1983), Rossby et al. (1983) and McWilliams et al. (1983) for the Western North Atlantic Ocean; 2) Gould (1983) for the Northeast Atlantic Ocean; 3) Bernstein (1983) for the North Pacific Ocean; 4) Needler (1983) for the subpolar gyre and Arctic Ocean; 5) Siedler (1983) for tropical equatorial regions; 6) Swallow (1983) for the Indian Ocean; 7) Bennett (1983) for the South Pacific Ocean and East Australian Current; 8) Gründlingh (1983) for the Southern Indian Ocean and Agulhaus

Current; and 9) Bryden (1983) for the Southern Ocean.

The results of these observational studies have shown that the mesoscale eddy field has wavelengths of tens to hundreds of kilometers and periods on the order of weeks to months. The kinetic energy of such eddies can be one or two orders of magnitude greater than that of the time-averaged motions (Dickson, 1983). The intensity of these eddies varies geographically, being weakest in mid-ocean regions such as the center of the subtropical gyres, and strongest in the vicinity of strong flows such as the Gulf Stream, Kuroshio and North Equatorial Currents (Dantzler, 1977; Wyrtki et al., 1976; Leetma et al., 1977; Dickson, 1983; Schmitz et al., 1983).

Despite a steadily growing data base on oceanic mean flows and statistics, there are still many data-sparse regions of the ocean, and no synoptic coverage of the ocean presently exists. As technology advances, especially in the area of remote sensing (Heinmiller, 1983), synoptic coverage of mesoscale eddies could be obtained on a regular basis. Until this advancement is made, however, we are left with sparse oceanographic data sets, which are a far cry from the "ideal" description of the mesoscale eddy field which would consist of an "adequately resolved continuous time series of the three-dimensional physical (and chemical) fields throughout the global ocean" (Robinson, 1983).

In addition to the observational studies, analytical investigations have been undertaken to understand the dynamics

of mesoscale eddies and their role in the ocean general circulation. (See Bretherton, 1975; MacLeish, 1976; Rhines, 1977; McWilliams, 1979; Schmitz et al., 1983; Holland et al., 1983; and Robinson, 1983, for reviews on both observational and theoretical studies.) One of the earliest mechanisms proposed for eddy production was baroclinic instability (Schulman, 1967; Gill et al., 1974; Robinson and McWilliams, 1974; Holland and Lin, 1975a,b; Tang, 1975; Haidvogel and Holland, 1978; Holland and Haidvogel, 1980). Direct atmospheric forcing (Frankignoul and Müller, 1979) has also been suggested.

Schmitz et al., (1983), after surveying twenty years of mesoscale eddy research, concluded that: 1) eddies seem to be generated via baroclinic, barotropic or mixed instabilities of the strong mean flows; and 2) transient wind forcing seems to be less important in generating the eddies. It should be pointed out, however, that because of the lack of both atmospheric and oceanographic data sets, the significance of direct transient atmospheric forcing in most parts of the ocean is difficult to determine. It may well turn out that a significant part of the variability may be due to such time-dependent direct forcing, either wind or thermohaline, particularly in the eastern basins of the world ocean.

In addition to observational and analytical studies, mesoscale eddies have been simulated using numerical models. This approach has provided great insight into the eddy dynamics and generation mechanisms, and permits a systematic exploration of

the dynamical role of eddies in the ocean general circulation.

Simulations of mesoscale eddies in regional open ocean domains by Bretherton (1975), Bretherton and Karweit (1975), Owens and Bretherton (1978), Rhines (1975, 1977), Bretherton and Haidvogel (1976), and Haidvogel (1983), have shown that the statistical structure of the mesoscale eddies agrees well with the available observations. In particular, Bretherton (1975) has claimed that QG dynamics essentially determine the structure of mid-ocean eddies.

Simulations of mesoscale eddies in enclosed midlatitude ocean basins have been explored by Holland and Lin (1975a,b), Han (1975), Robinson et al., (1977), Semtner and Mintz (1977), Holland (1978), Mintz (1979), and Semtner and Holland (1980). These studies have shown that eddies can originate when fine-scale horizontal resolution (< 50 km) and low viscosity are used even when the forcing is entirely steady. The eddies and mean flow can then interact through exchanges of momentum and energy. Through these interactions, a statistically steady state is reached in which the characteristics of the large-scale ocean circulation are established. Holland (1978), in particular, has suggested that the eddies determine the character of the large-scale ocean circulation by limiting the amplitude of the mean flow in the upper ocean and by causing a downward momentum flux to the deeper water. Semtner and Mintz (1977) and Mintz (1979) have shown that the poleward heat transfer across

the mean position of the Gulf Stream front is primarily due to the mesoscale eddies.

In order to investigate the role of eddies in particular regions of the oceans (since eddies are not spatially homogeneous), regional budgets have been analyzed by: 1) Han (1975), Harrison and Robinson (1978), and Harrison (1979) for energy; and 2) Rhines and Holland (1979), Holland and Rhines (1980), and Harrison and Holland (1981) for vorticity. The energy budget studies have shown that 1) eddies in the Gulf Stream region are produced by baroclinic, barotropic, or "mixed" instabilities, and 2) in the interior region eddies are maintained against frictional dissipation by secondary baroclinic instabilities in the southwestward and westward flow of the Sverdrup gyre. The vorticity budget studies have shown that eddies can play a major role in the mean circulation, because they transport most of the vorticity put into each gyre by the wind stress curl across the boundary between the gyres, thereby allowing equilibration to take place without much need for a frictional vorticity sink (Holland et al., 1983).

Comparisons of model and ocean data have been made by Holland and Lin (1975a,b), Robinson et al. (1977), Holland (1978), and by Schmitz and Holland (1982). Since only a few long-term time series of ocean data exist, and due to the idealized framework of the models, such comparisons are difficult. As pointed out by Holland et al. (1983), it is not clear just how such comparisons should be carried out.

Although these comparisons have so far been primarily qualitative, as the ocean data base grows and models become more realistic, quantitative comparisons will be possible. These comparisons, together with theoretical investigations, will certainly help us to advance from the "zero-order" description of the eddy field that presently exists (see Schmitz et al., 1983) to a first-order, more quantitative understanding of the dynamics of the ocean general circulation.

2.2 Survey of eddy-resolving ocean general circulation models (EGCMs)

2.2.1 Types of EGCMs available

The requirements for an EGCM, according to Holland (1978), are: 1) fine horizontal resolution (~10 or 20 km) in a baroclinic ocean, and 2) the ability to perform extended calculations in time in order to reach a "statistically steady state", in which eddies and the mean flow are in mutual balance. Three types of EGCMs presently exist: 1) adiabatic PE models, 2) QG models, and 3) non-adiabatic PE models. To help decide what type of EGCM to use for the present study, we examine the capabilities of each type of model.

Adiabatic PE EGCMs

Adiabatic PE EGCMs have been used by Holland and Lin (1975a,b) for enclosed ocean basins. Because the PE system of equations is used, all of the experiments require relatively large amounts of computer time to reach a statistically steady state. Because of the expense involved, extensive parameter studies cannot be made with this type of model and realistic basins (in size and shape) are extremely expensive. In addition such adiabatic models do not allow for possibly important water mass conversion processes such as convective overturning and thermohaline mixing. As a result, these models may be appropriate for ocean general circulation studies, but cannot be considered "complete" models for climate studies. However, it should be kept in mind that models with simpler physics are also much easier to understand, so there is a trade-off here, even for understanding "climate".

QG EGCMs

The models used by Holland (1978) for an enclosed ocean basin and by McWilliams et al. (1978) for a zonally open basin (analogous to the Antarctic Circumpolar Ocean) are both based on the Phillips (1956) system of QG equations. This system may be solved much more economically than the PE equations. As a

result parameter studies needed at the present stage of eddy modeling are feasible and basins of realistic size (~5000 km) can be used. According to Holland (1978), Haidvogel (1979), and Robinson et al. (1979), the choice of model parameters can significantly influence the results so that a large number of case studies is needed.

In these adaptations of Phillips' system of equations, wind stress is the only energy source. Although these models can be modified to include thermal forcing, it has not yet been done.

In addition, the static stability of these models is not allowed to change either temporally or spatially in the QG thermodynamic energy equation. The importance of static stability variations has been discussed by Lorenz (1960, 1962). In short, Lorenz argued that static stability is a factor in determining the dynamic stability of a baroclinic flow. Because the baroclinically unstable waves are accompanied by a sinking of colder fluid and simultaneous rising of warmer fluid across the same level, the static stability should increase in an overall sense. It is also well known that the static stability partially controls the preferred scale and growth rate of baroclinically unstable waves (Charney, 1947; Eady, 1949; Robinson and McWilliams, 1974; Gill et al., 1974). According to Lorenz (1960), the release of kinetic energy without static stabilization could overpredict the growth of disturbances. Because of these and other approximations to the thermodynamic energy equations, the QG EGCMs, by themselves, will not be adequate for

climate studies.

In addition, even for dynamic studies, the models are limited to areas of the ocean where the QG approximation is valid. Examples of where the QG approximation may be invalid are: 1) near steep topography, seamounts, islands, and continental boundaries, and 2) where "contorted meandering and eddying of intense currents, rings, and smaller long-lived isolated lenses...have strong centripetal acceleration (cyclostrophic effects)" (Robinson, 1983).

Non-adiabatic PE EGCMs

Non-adiabatic PE EGCMs have been used by Han (1975), Robinson et al. (1977), Semtner and Mintz (1977), and Mintz (1979). Like the adiabatic PE EGCMs, large amounts of computer time are required to reach a statistically steady state. Because of the expense involved, extensive parameter studies cannot be made even though there are more parameters involved (those having to do with subgrid scale heat diffusion parameterization). Although the models can incorporate most physics, they cannot presently be run to a complete thermodynamic equilibrium state because of the expense. As a result, these models may be appropriate for ocean general circulation studies, but are limited in their application to climate studies.

2.2.2 EGCM intercomparison studies

Two intercomparison studies between EGCMs have been made: 1) QG and adiabatic PE studies, and 2) QG and non-adiabatic PE studies. The first intercomparison was done by Holland (1978), and the second by Semtner and Holland (1978).

In the first study, qualitative agreement was obtained for a number of cases. However, because the product of height and horizontal velocity, rather than velocity itself, is the basic prognostic variable in the PE momentum equation used in the study, the PE and QG models could not be readily compared. Quantitative intercomparisons have yet to be made.

In the second study, qualitative agreement was also obtained. There were several significant differences between these models however, most notably: 1) model physics; 2) vertical resolution (two-layer QG model compared to five-layer PE model); and 3) effective horizontal resolution (B-grid PE model compared to C-grid QG model). As a result, observed differences between the models cannot be ascribed to any one factor, and comparisons of any similarities can be made on a qualitative basis only.

In fact, as Semtner and Holland (1978) have discussed, no two EGCM experiments have ever been parametrically identical. As a result, differences between model results could be due to any number of factors.

2.3 The "ideal" EGCM for climate studies

From our survey of the types of EGCMs available, we see that there is at the present time no single "ideal" model to study the role of mesoscale eddies in climate. At the present time some mix of all these models is needed to get at the array of problems involved.

A useful candidate might be a model intermediate between QG and non-adiabatic PE models. This type of model could possibly incorporate thermal effects not found in a QG model, yet use less computer time than a PE model. As stated in Chapter 1, the proper development and evaluation of such a model requires a deeper understanding of QG and PE physics, which is the aim of this thesis.

In the following chapters, we will provide a foundation for the first quantitative intercomparison of QG and PE models. In particular, a hierarchy of systems of equations from PE to QG will be obtained. This will allow us to evaluate the importance of each of the terms involved in the sequence of approximations, and eventually help us to design the "ideal" EGCM for climate studies.

CHAPTER 3. MODEL FORMULATIONS

One of the primary goals of this study is to try to obtain a deeper understanding of PE and QG physics. In this chapter we demonstrate how, without rebuilding or reformulating PE and QG models, we can derive a set of consistent quantities that can be intercompared. Before presenting this set, the PE and QG model equations will be briefly described.

3.1 The basic models

The PE model used in this study is a new one (see Appendix A for the numerical details), and makes use of the following assumptions and approximations:

1) the hydrostatic and traditional approximations characteristic of PE models in general (Phillips, 1966);
2) the Boussinesq approximation which assumes that density variations are important only in calculations involving the buoyancy force (Phillips, 1969); and
3) the assumption that density is a function only of temperature.

The fluid motion is represented in Cartesian coordinates x,y and z, where x is the east-west direction, y the north-south direction and z the vertical direction. The velocity components are u,v and w in the zonal, meridional and vertical directions,

respectively. The equations of motion can be written as

$$u_t + L(u) + (wu)_z = fv - \frac{1}{\rho o} p_x + \kappa_m u_{zz} \begin{cases} + A_m \nabla^2 u \\ \text{or} \\ -B_m \nabla^4 u \end{cases} \qquad (3\text{-}1)$$

and

$$v_t + L(v) + (wv)_z = -fu - \frac{1}{\rho o} p_y + \kappa_m v_{zz} \begin{cases} + A_m \nabla^2 v \\ \text{or} \\ -B_m \nabla^4 v \end{cases}, \qquad (3\text{-}2)$$

where t is time, p is pressure, ρ_o is a reference density, ∇^2 is the horizontal Laplacian operator, ∇^4 is the horizontal biharmonic operator, κ_m is the eddy viscosity coefficient in the vertical direction, and A_m and B_m are eddy viscosity coefficients in the horizontal direction for Laplacian and biharmonic momentum diffusion, respectively. The subscripts t, x, y and z in the equations are used to denote differentiation with respect to these variables. The Coriolis parameter f is a linear function of latitude so that $f = f_o + \beta y$. The advection operator L is defined as

$$L(\ ) \equiv [u(\ )]_x + [v(\ )]_y \ .$$

The hydrostatic equation is

$$p_z = -\rho g \ , \qquad (3\text{-}3)$$

where ρ is the density and g is the acceleration of gravity. The continuity equation, which assumes the fluid to be incompressible, is

$$u_x + v_y + w_z = 0 \ . \tag{3-4}$$

The first law of thermodynamics is

$$T_t + L(T) + (wT)_z = \kappa_H T_{zz} \begin{cases} +A_H \nabla^2 T \\ \text{or} \\ -B_H \nabla^4 T \end{cases} , \tag{3-5}$$

where T is temperature, κ_H is the eddy diffusivity coefficient in the vertical direction, and A_H and B_H are eddy diffusivity coefficients in the horizontal direction for Laplacian and biharmonic heat diffusion, respectively. The equation of state is

$$\rho = \rho_o(1-\alpha(T-T_o)), \tag{3-6}$$

where T_o is a reference temperature and α is the thermal expansion coefficient. The prognostic variables for this system are the zonal velocity u, the meridional velocity v and the temperature T.

The QG model used in this study is essentially that of Holland (1978). The governing equations consist of relative vorticity and thermal wind equations:

$$(\nabla^2\psi)_t = -J(\psi,\nabla^2\psi + f) - f_o w_z + \kappa_m \zeta_{zz} \begin{cases} +A_m \nabla^2 \zeta \\ \text{or} \\ -B_m \nabla^2 \zeta \end{cases} \tag{3-7}$$

$$(\psi_z)_t = -J(\psi,\psi_z) + (g'/f_o)w \ . \qquad (3\text{-}8)$$

Here ψ is the QG streamfunction, $\zeta = \nabla^2\psi$ is the relative vorticity, $g' = g\Delta\rho/\rho_o$ is "reduced gravity", and all other variables are defined as before. The prognostic variables for this system are the relative vorticity $\nabla^2\psi$ and the thermal wind ψ_z.

A comparison of the PE and QG model equations shows that the models have different equations and prognostic variables. In order to quantitatively intercompare the models, some modifications are necessary. Without rebuilding or reformulating the models themselves, we would like to derive a set of consistent quantities that can be intercompared. Then we can use this set to address some of the questions posed in Chapter 1. In particular, we could address the questions: Can the two models be configured to give nearly similar results?; and, Are the differences due to numerics or to physics? In the next section, we show how a particular set of consistent quantities can be obtained.

3.2 Continuous form of the comparison equations

Starting with the PE system of equations, we derive a set of equations which has the same form and prognostic variables as the QG system. In particular, we form vorticity and divergence

equations from the momentum equations. From the divergence equation, we obtain the thermal wind relationship (which we will later substitute into the thermodynamic energy equation). We next decompose the horizontal velocity field into rotational and divergent components, and substitute this decomposition into all of the equations.

3.2.1 The PE comparison equations

The Cartesian form of the horizontal equations of motion, Eqs. (3-1) and (3-2), can be written in vector form as

$$\vec{v}_t + \vec{v}\cdot\nabla\vec{v} + w\vec{v}_z + f\hat{k} \times \vec{v} = -\frac{1}{\rho_o}\nabla p + \kappa_m \vec{v}_{zz} \begin{cases} +A_m\nabla^2\vec{v} \\ \text{or,} \\ -B_m\nabla^4\vec{v} \end{cases} \quad (3\text{-}9)$$

where $\vec{v}$ is the horizontal velocity vector. Using the vector identity

$$\vec{v}\cdot\nabla\vec{v} = \nabla\left(\frac{\vec{v}\cdot\vec{v}}{2}\right) + \hat{k} \times \vec{v}\zeta,$$

where $\zeta = \hat{k}\cdot\nabla \times \vec{v}$ is the vertical component of vorticity, we can rewrite Eq. (3-9) as

$$\vec{v}_t = -\nabla\left(\frac{p}{\rho_o} + \frac{\vec{v}\cdot\vec{v}}{2}\right) - \hat{k} \times \vec{v}(\zeta+f) - wv_z + \kappa_m \vec{v}_{zz} \begin{cases} +A_m\nabla^2\vec{v} \\ \text{or} \\ -B_m\nabla^4\vec{v} \end{cases} \quad (3\text{-}10)$$

Operating on Eq. (3-10) with the vector operator $\hat{k}\cdot\nabla\times(\ )$, we obtain the vorticity equation

$$\zeta_t = -\vec{v}\cdot\nabla(\zeta+f) - w\zeta_z - (\zeta+f)\nabla\cdot\vec{v} + \hat{k}\cdot(\vec{v}_z \times \nabla w) + \kappa_m\zeta_{zz} \begin{cases} +A_m\nabla^2\zeta \\ \text{or} \\ -B_m\nabla^4\zeta \end{cases} \quad (3\text{-}11)$$

Operating on Eq. (3-10) with the vector operator $\nabla\cdot(\ )$, we obtain the divergence equation

$$\delta_t = -\nabla^2\left(\frac{p}{\rho_o} + \frac{\vec{v}\cdot\vec{v}}{2}\right) - \nabla\cdot[\hat{k}\times\vec{v}(\zeta+f)] - w\delta_z - \vec{v}_z\cdot\nabla w + \kappa_m\delta_{zz} \begin{cases} +A_m\nabla^2\delta \\ \text{or} \\ -B_m\nabla^4\delta \end{cases}, \quad (3\text{-}12)$$

where the horizontal divergence $\delta \equiv \nabla\cdot\vec{v}$. From Eq. (3-12), we can obtain the thermal wind relationship. Taking the vertical derivative of Eq. (3-12), solving for the pressure term and substituting the relationship

$$\nabla^2 p_z = -g\nabla^2\rho = \alpha g\nabla^2 T$$

(where Eq. (3-3) and (3-6) have been used) into the pressure term, we can obtain

$$\alpha g\nabla^2 T = -\delta_{zt} - \nabla^2\left(\frac{\vec{v}\cdot\vec{v}}{2}\right)_z - \nabla\cdot[\hat{k}\times\vec{v}(\zeta+f)]_z - (w\delta_z)_z - (v_z\cdot\nabla w)_z + (\kappa_m\delta_{zz})_z$$

$$\begin{cases} +A_m\nabla^2\delta_z \\ \text{or} \\ -B_m\nabla^4\delta_z \end{cases}, \quad (3\text{-}13)$$

which is analogous to the the thermal wind relationship, but without any balance conditions assumed.

Using a theorem of Helmholtz (see Bourne and Kendall, 1968), which states that any velocity field can be decomposed into non-divergent and irrotational components, we can let $\vec{v}$ be expressed as

$$\vec{v} = \hat{k} \times \nabla\psi + \nabla\chi, \tag{3-14}$$

where ψ is a streamfunction for the non-divergent part of $\vec{v}$ and χ is the velocity potential for the irrotational part. Hence, the vorticity $\zeta = \nabla^2\psi$ and the horizontal divergence $\delta = \nabla^2\chi$. In order to make this decomposition unique, we need to consider the kinematic condition on the side walls, $\vec{v}\cdot\vec{n} = 0$, which means $\vec{n}\cdot\hat{k} \times \nabla\psi + \vec{n}\cdot\nabla\chi = 0$. We shall choose to completely specify ψ and χ by choosing $\vec{n}\cdot\nabla\chi = 0$ and $\vec{n}\cdot\vec{k} \times \nabla\psi = 0$ independently. This means the normal derivative of the divergent velocity is zero at the boundary and the streamfunction ψ is a constant there. This is consistent with the boundary condition choice in the Holland (1978) QG model, i.e., ψ = constant on the boundary, and with integral continuity constraints.

Substituting Eq. (3-14) into Eq. (3-11), the vorticity equation becomes

$$\zeta_t = -J(\psi,\zeta+f) - \nabla\cdot f\nabla\chi - \nabla\chi\cdot\nabla\zeta - \zeta\nabla^2\chi - w\zeta_z - \nabla w\cdot\nabla\psi_z - J(w,\chi_z) + \kappa_m\zeta_{zz} \begin{cases} +A_m\nabla^2\zeta \\ \text{or} \\ -B_m\nabla^4\zeta \end{cases}, \tag{3-15}$$

where J is the Jacobian operator. Substituting Eq. (3-14) into

Eq. (3-12), the divergence equation becomes

$$\delta_t = -\nabla^2\left(\frac{p}{\rho_o}\right) + \nabla\cdot(f\nabla\psi) - J(f,\chi)$$
$$-\nabla\cdot((\hat{k}\times\nabla\psi)\cdot\nabla(\hat{k}\times\nabla\psi)) - \nabla\cdot((\hat{k}\times\nabla\psi)\cdot\nabla^2\chi)$$
$$-\nabla\cdot(\nabla\chi\cdot\nabla(\hat{k}\times\nabla\psi)) - \nabla w\cdot(\hat{k}\times\nabla\psi)_z$$
$$-\nabla\cdot(\nabla\chi\cdot\nabla^2\chi) - \nabla w\cdot\nabla\chi_z + \kappa_m\delta_{zz}\begin{cases} +A_m\nabla^2\delta \\ \text{or} \\ -B_m\nabla^4\delta \end{cases}. \qquad (3\text{-}16)$$

Using Eq. (3-14), the thermal wind relationship becomes

$$\alpha g\nabla^2 T = -(\nabla^2\chi)_{zt} + \nabla\cdot(f\nabla\psi)_z - (J(f,\chi))_z$$
$$-\nabla\cdot((\hat{k}\times\nabla\psi)\cdot\nabla(\hat{k}\times\nabla\psi))_z$$
$$-\nabla\cdot(\hat{k}\times\nabla\psi)\cdot\nabla^2\chi)_z - \nabla\cdot(\nabla\chi\cdot\nabla(\hat{k}\times\nabla\psi))_z$$
$$-(\nabla w\cdot(\hat{k}\times\nabla\psi))_z - \nabla\cdot((\nabla\chi\cdot\nabla^2\chi))_z$$
$$-(\nabla w\cdot\nabla\chi_z)_z + \kappa_m\delta_{zz}\begin{cases} +A_m\nabla^2\delta_z \\ \text{or} \\ -B_m\nabla^4\delta_z \end{cases}. \qquad (3\text{-}17)$$

Again using Eq. (3-14), the continuity equation (3-4) can be rewritten as

$$\nabla^2\chi + w_z = 0. \qquad (3\text{-}18)$$

The thermodynamic energy equation (3-5) can be rewritten in vector and advective form as

$$T_t + \vec{v}\cdot\nabla T + wT_z = \kappa_H T_{zz}\begin{cases} +A_H\nabla^2 T \\ \text{or} \\ -B_H\nabla^4 T \end{cases}. \qquad (3\text{-}19)$$

If we substitute Eq. (3-14) into Eq. (3-19) we can obtain

$$T_t + J(\psi,T) + \nabla\chi\cdot\nabla T + wT_z = \kappa_H T_{zz} \begin{cases} +A_H\nabla^2 T \\ \text{or} \\ -B_H\nabla^4 T \end{cases} . \qquad (3\text{-}20)$$

The vorticity equation (3-15), the divergence equation (3-16), the derived thermal wind relationship (3-17), the continuity equation (3-18) and the thermodynamic energy equation (3-20) form the basic PE comparison set of equations. In the next section we will make the following approximations to this set: 1) full balance, 2) linear balance, and 3) QG. As a result we can obtain a hierarchy of systems of equations from PE to QG, and can then make systematic comparisons among these systems. This also allows us to evaluate the importance of each of the terms involved in this sequence of approximations.

3.2.2 Approximations to the PE comparison equations

Following Lorenz (1960), systematic approximations to the intercomparison set of PE equations, which were obtained in the last section, will be made in order to obtain energetically consistent sets of full balance, linear balance and QG equations. We first replace the divergence equation with the full balance equation, which is obtained by neglecting all terms containing divergence in the divergence equation. In an

analogous fashion we neglect certain terms containing divergence in other equations. We next neglect certain nonlinear terms in the above equations to obtain linear balance equations. Lastly we omit certain additional terms from the linear balance equations to obtain the QG system of equations, which is the basic set of equations we will use in intercomparisons with the PE model.

The full balance approximation and equations

In order to obtain the full balance equations, we assume that the horizontal velocity is quasi-non-divergent, i.e.,

$$\left|\nabla\chi\right| << \left|\hat{k} \times \nabla\psi\right| , \tag{3-21}$$

where the notation introduced in Eq. (3-14) has been used. We then find that terms involving w and $\nabla\chi$ in the divergence equation (3-16) may all be neglected. Eq. (3-16) then reduces to

$$0 = -\nabla^2\left(\frac{p}{\rho_o}\right) + \nabla\cdot(f\nabla\psi) - \nabla\cdot((\hat{k} \times \nabla\psi)\cdot\nabla(\hat{k} \times \nabla\psi)) ,$$

which can be rewritten as

$$\nabla^2\left[\frac{p}{\rho_o} + \frac{1}{2}(\nabla\psi)^2\right] = \nabla\cdot[(f + \nabla^2\psi)\nabla\psi] \quad . \tag{3-22}$$

This equation, called the full balance equation, expresses a rather complicated nonlinear relationship between ψ and p,

similar to a gradient wind balance. It is important to note that dropping the divergence tendency omits gravity waves from the system.

Using the assumption (3-21), the thermal wind relationship (3-17) reduces to

$$\alpha g \nabla^2 T = -\nabla^2 [\frac{1}{2}(\nabla\psi)^2]_z + \nabla\cdot[(f + \nabla^2\psi)\nabla\psi]_z \qquad (3\text{-}23)$$

and the vorticity equation (3-15) to

$$\zeta_t = -J(\psi,\zeta + f) - \nabla\cdot f\nabla\chi - \nabla\chi\cdot\nabla\zeta - \zeta\nabla^2\chi$$

$$-w\zeta_z - \nabla w\cdot\nabla\psi_z + \kappa_m\zeta_{zz} \begin{cases} +A_m\nabla^2\zeta \\ \text{or} \\ -B_m\nabla^4\zeta \end{cases} . \qquad (3\text{-}24)$$

We note in Eq. (3-24) that all terms involving both the rotational and divergent part of the horizontal velocity field are still retained. As shown by Lorenz (1960), this retention is necessary in order for the full balance system of equations to possess suitable energy invariants.

The thermodynamic energy equation (3-20) along with the continuity equation (3-18) are left intact. In particular, the term $\nabla\chi\cdot\nabla T$ in Eq. (3-20), which might otherwise be neglected, is retained for energetic consistency.

Eqs. (3-23), (3-24), (3-20) and (3-18) make up the full balance system of equations.

The linear balance approximation and equations

In order to obtain the linear balance equations, we assume that nonlinear terms are negligible compared to linear terms in the divergence equation. The divergence equation (3-22) then reduces to

$$\nabla^2\left(\frac{p}{\rho_o}\right) = \nabla\cdot(f\nabla\psi) \quad , \tag{3-25}$$

which is the linear balance equation. This equation expresses a simple linear relationship between ψ and p.

Neglecting nonlinear terms in the thermal wind relationship Eq. (3-23) and small terms in the vorticity equation (3-24), we obtain

$$\alpha g\nabla^2 T = \nabla\cdot(f\nabla\psi)_z \tag{3-26}$$

and

$$\zeta_t = -J(\psi,\zeta+f) - \nabla\chi\cdot\nabla f + f\nabla^2\chi + \kappa_m\zeta_{zz} \begin{cases} +A_m\nabla^2\zeta \\ \text{or} \\ -B_m\nabla^4\zeta \end{cases} . \tag{3-27}$$

The term $-\nabla\chi\cdot\nabla f$, which is the advection of the planetary vorticity by the divergent component of the horizontal velocity field, although small compared to other terms in Eq. (3-27), must be retained for energetic consistency (Lorenz, 1960).

Eqs. (3-20) and (3-18) remain intact and together with Eqs. (3-26) and (3-27) make up the linear balance system of equations.

The QG approximation and equations

In order to obtain the QG equations, we assume that the advection of the planetary vorticity by the divergent component of the horizontal velocity field, i.e., $-\nabla\chi\cdot\nabla f$, is negligible compared to other terms in Eq. (3-27). For energetic consistency (Lorenz, 1960), it is necessary to simultaneously replace f by a constant mean value f_o in the term $f\nabla^2\chi$ in Eq. (3-27) and in the term $\nabla\cdot(f\nabla\psi)$ in Eq. (3-25). The vorticity equation (3-27) then reduces to

$$\zeta_t = -J(\psi,\zeta+f) + f_o\nabla^2\chi + \kappa_m\zeta_{zz} \begin{cases} +A_m\nabla^2\zeta \\ \text{or} \\ -B_m\nabla^4\zeta \end{cases} , \tag{3-28}$$

and the divergence equation (3-5) to

$$\nabla^2\left(\frac{p}{\rho_o}\right) = f_o\nabla^2\psi \ . \tag{3-29}$$

The latter equation states that the streamfunction ψ can be given approximately by $p/(f_o\rho_o)$ and that the pressure field is approximately proportional to the streamfunction field.

If we replace f by f_o in Eq. (3-26), we obtain the thermal wind relationship

$$\alpha g\nabla^2 T = f_o\nabla^2\psi_z \ . \tag{3-30}$$

This equation states that ψ_z can be given approximately by

$\alpha gT/f_o$.

According to Lorenz (1960), no approximations need be made to either Eqs. (3-20) or (3-18), so that the equations (3-28), (3-30), (3-20) and (3-18) form a suitable energetically consistent system of equations. In our study, however, in order to use the Holland (1978) model, we wish to simplify the thermodynamic energy equation by replacing variable static stability by a constant value. For energetic consistency, following Lorenz (1960), it is necessary to simultaneously neglect in the thermodynamic energy equation (3-20) the advection of temperature by the divergent component of the horizontal velocity field. With these simplifications the thermodynamic energy equation (3-20) reduces to

$$T_t + J(\psi,T) + \sigma_o w = \begin{cases} +A_H\nabla^2 T \\ \text{or} \\ -B_H\nabla^4 T \end{cases} , \qquad (3\text{-}31)$$

where σ_o is the static stability, which is constant in time and in the horizontal domain. Using the thermal wind relationship (3-30), Eq. (3-31) can be rewritten as

$$\psi_{zt} + J(\psi,\psi_z) - \frac{\alpha g}{f_o}\sigma_o w = \begin{cases} +A_H\nabla^2\psi_z \\ \text{or} \\ -B_H\nabla^4\psi_z \end{cases} . \qquad (3\text{-}32)$$

The set of equations (3-28), (3-30), (3-18) and either (3-31) or (3-32) make up the QG system of equations.

3.3 Choice of model parameters

Besides a consistent set of equations and prognostic variables to intercompare the results of PE and QG numerical experiments, we need to obtain a consistent model set-up. In particular the models should have not only the same model parameters, but also the same vertical and horizontal distribution of variables.

3.3.1 Basic experimental design

Before any experiments are conducted, the numerical aspects of each model must be tested, i.e., grid resolution, choice of layer depths, choice of friction formulations, forcing function structure and amplitude, and boundary conditions. The results of these tests determine the choice of model parameters to be used in the experiments.

Since the QG model has already had the numerical aspects tested and has been successful in generating mesoscale eddies (see Holland, 1978), we initially base our choice of model parameters for both models on what Holland (1978) used. Because of the great expense involved in running the PE model, we are limited to running only two experiments for our intercomparison study. We choose to run single-gyre and double-gyre experiments using many of the model parameters used in Holland's Case 1.

3.3.2 Domain of the ocean and grid system

For both experiments a rectangular ocean basin centered at midlatitudes is used. For single-gyre runs a 1000 x 1000 km basin, centered at 35°N, is used; for double-gyre runs, a 2000 (north-south extent) x 1000 km basin, centered at 40°N, is used.

The horizontal grid size to be used in all experiments is 20 km. This size meets a basic requirement cited by Holland (1978) for an eddy-resolving model, namely that fine horizontal resolution (~10 or 20 km) is needed, and is the size that Holland consistently uses. It should be pointed out that this choice of horizontal grid size is twice as fine as that used in all previous non-adiabatic "eddy-resolving" PE ocean models (e.g., Han, 1975; Robinson et al., 1977; Semtner and Mintz, 1977). The use of these coarser resolutions (i.e., greater than or equal to 40 km), according to Han (1975), may not be adequate to resolve baroclinic and barotropic eddy processes, particularly in the western boundary and subarctic regions.

Although it is known that continental margins and bottom topography influence both large-scale currents and eddy dynamics (Warren, 1963; Holland, 1967; Orlanski and Cox, 1973; Bretherton, 1975; Bretherton and Haidvogel, 1976; Rhines, 1977; Semtner and Mintz, 1977), flat-bottomed models are used, following the philosophy of Holland (1978), who recommends proceeding from simple to more complex models. The use of flat-bottomed

models should result in fewer computational requirements and more straightforward intercomparisons between the QG and PE models.

For the same reasons, we use two-layer instead of multi-layer versions of the models in both experiments. The upper layer represents the warm water above the thermocline while the lower layer represents the deep ocean.

The vertical structure of the PE and QG models is shown in Figs. 3.1 and 3.2, respectively. The fundamental variables of the PE model (u,v,T, and w) plus the derived variables (ψ and χ) are shown in Fig. 3.1. The fundamental variables of the QG model (ψ and w) are shown in Fig. 3.2. For both models, the layers are numbered from top to bottom with the layer thickness (constant for each layer) given by h_k. The vertical coordinate is the height z, which is positive upwards with z = 0 at the surface. In both experiments, the same two-layer versions of the models are used with h_1 = 1000 m and $H = h_1 + h_2$ = 5000 m.

The horizontal arrangement of variables for the PE model is shown in Fig. 3.3. The zonal velocity u and Coriolis parameter f are carried at a distance $\Delta/2$ (Δ being the uniform grid interval in both the x and y directions) to the east and west of the point of a rectangular grid where the temperature T is carried. The meridional velocity v is carried at the same distance to the north and south of the temperature point. The pressure p is located at the same point as temperature. The vertical velocity

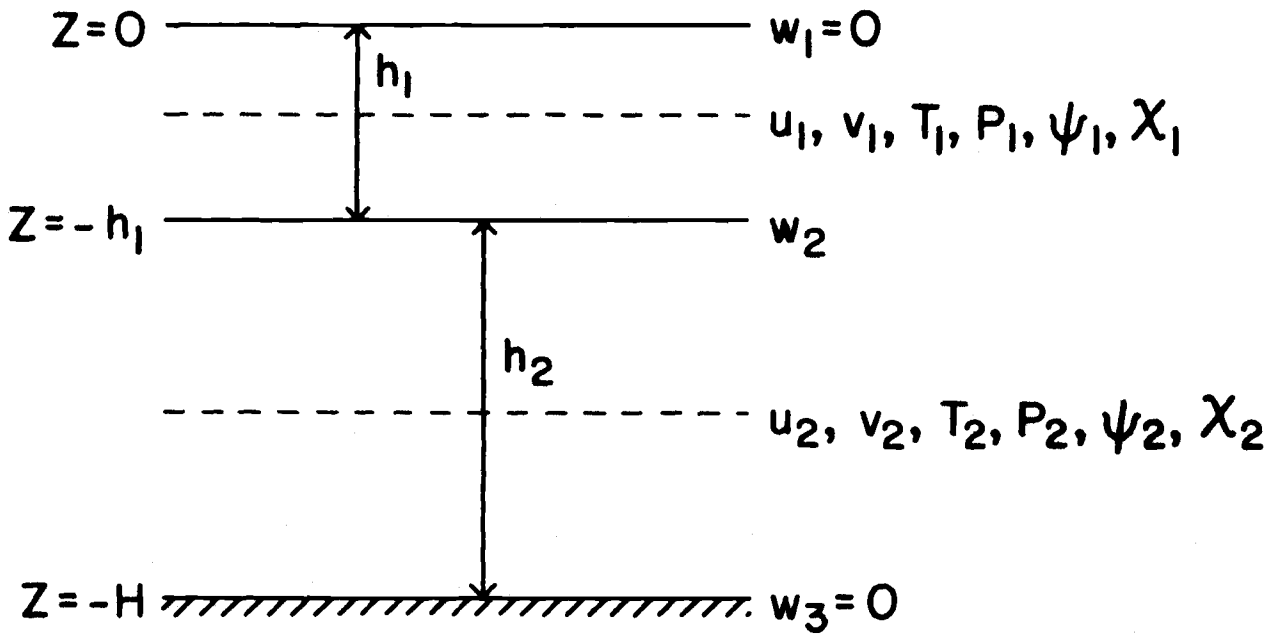

Fig. 3.1 The vertical structure of the two-layer PE model.

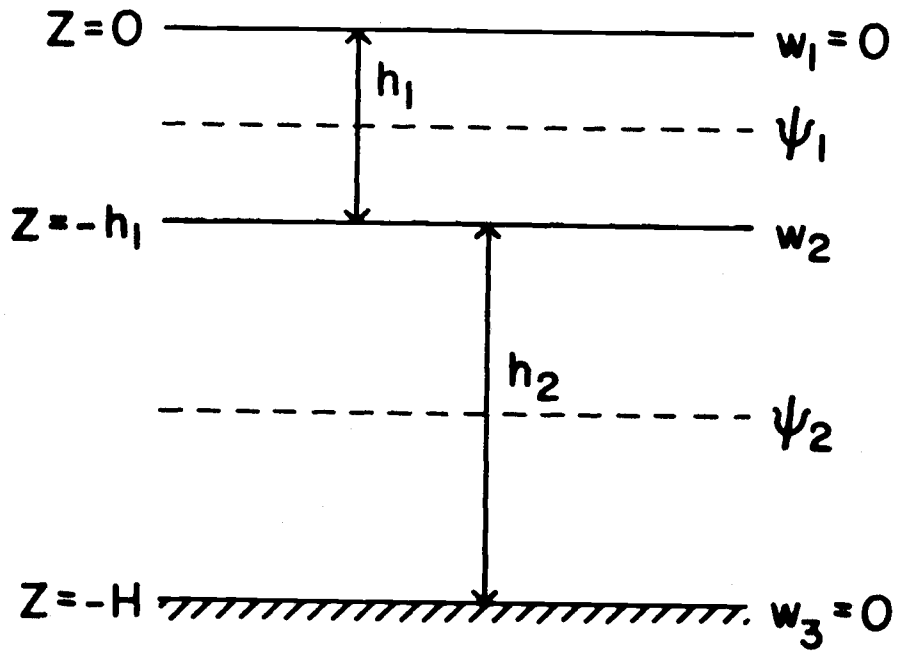

Fig. 3.2 The vertical structure of the two-layer QG model.

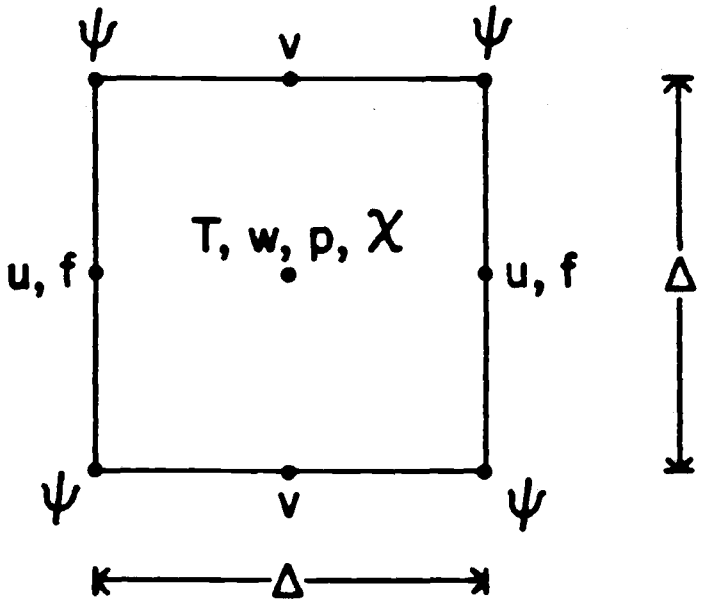

Fig. 3.3 Arrangement of variables in the PE finite-difference grid system.

w is located at a distance $\Delta/2$ to the east of u and to the north of v (i.e., also at T points) in order to facilitate differentiation of the continuity equation.

This space-staggered grid, called the C-scheme by Arakawa and Lamb (1977), has been shown by Batteen and Han (1981) to be free of noise for the gravest mode when fine-scale resolution (<40 km for the ocean), as in mesoscale ocean eddy models, is used. It has been used extensively in both ocean and atmospheric general circulation modeling (Holland and Lin, 1975a,b; Arakawa, 1966, 1972). When the grid size is smaller than the Rossby radius of deformation (~50 km in the ocean, ~1000 km in the atmosphere), this scheme will simulate geostrophic adjustment more adequately than other schemes (Winninghoff, 1968; Arakawa and Lamb, 1977; Schoenstadt, 1978).

Also shown in Fig. 3.3 are the derived variables ψ, defined at the corner points of the grid, and χ, defined at the center point of the grid. This grid arrangement facilitates the decomposition of the horizontal velocity field into its rotational and divergent components, i.e.,:

$$u = \chi_x - \psi_y \ , \qquad (3\text{-}33a)$$

and

$$v = \chi_y + \psi_x \ . \qquad (3\text{-}33b)$$

Two different horizontal arrangements of variables are shown for the QG model in Fig. 3.4. Fig. 3.4a shows the horizontal arrangement of variables for actual QG runs, while Fig.

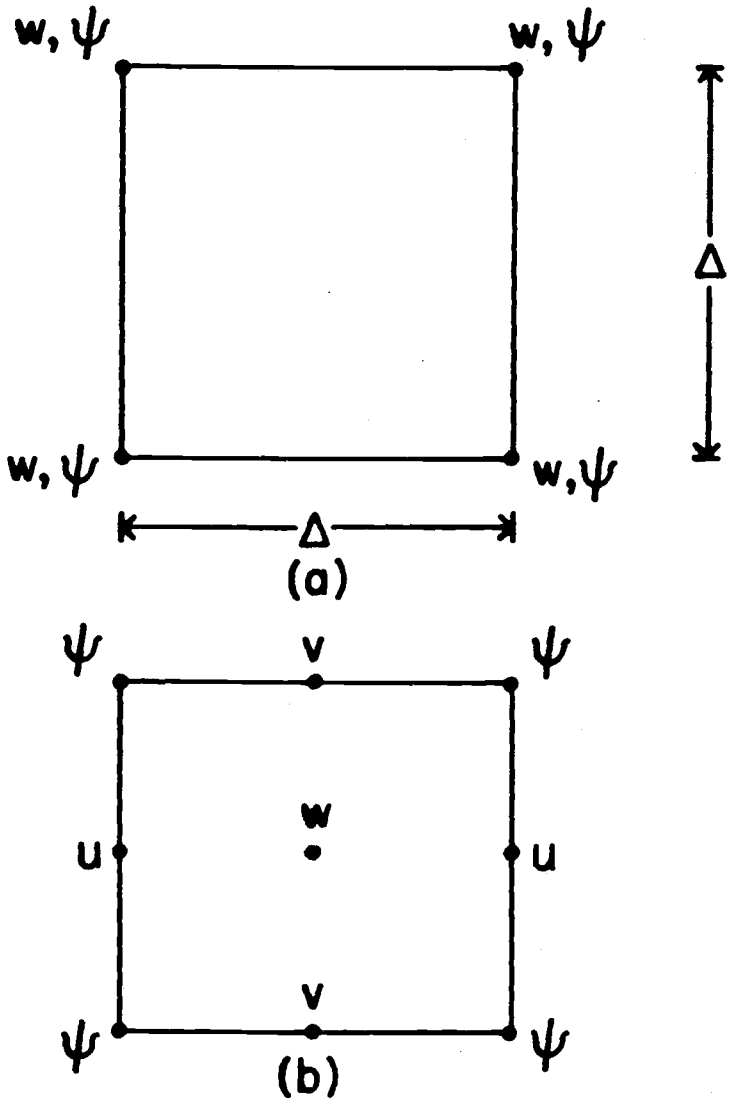

Fig. 3.4 Arrangement of variables in the QG finite-difference grid system for (a) actual runs and (b) intercomparisons with the PE model.

3.4b shows the arrangement of the additional derived variables when intercomparisons with the PE model are to be made.

Both ψ and w are carried at the corner points of the grid in Fig. 3.4a; in Fig. 3.4b, however, the variables are arranged to be consistent with the PE arrangement of variables (see Fig. 3.3). An averaging of w at the corner points of the grid in Fig. 3.4a is made to determine w in the center of the grid in Fig. 3.4b. The horizontal velocities u and v in Fig. 3.4b are arranged, as in the PE model, to facilitate the decomposition of the horizontal velocity field into its components, which, in the quasigeostrophic system, is just the rotational component, i.e.,

$$u = -\psi_y \tag{3-34a}$$

and

$$v = \psi_x. \tag{3-34b}$$

3.3.3 Wind forcing

Following Holland (1978), the upper layer of the ocean is driven by a zonal wind stress which is steady in time and varies with latitude in a simple sinusoidal manner. For single-gyre runs,

$$\tau(y) = -\tau_o \cos(\pi y/D). \tag{3-35}$$

where τ is the wind stress acting on the surface, τ_o is the

constant wind stress amplitude, and D is the north-south extent of the rectangular basin. For double-gyre runs

$$\tau(y) = -\tau_o \cos (2\pi y/D). \qquad (3\text{-}36)$$

The use of a wind forcing steady in time rather than transient does not significantly suppress eddy generation. As stated earlier, eddies are primarily generated by instabilities of strong mean flows, and the eddy response to transient wind forcing may be a second-order effect in midlatitude gyres (Schmitz et al., 1983).

3.3.4 Friction formulations

Lateral momentum diffusion and bottom friction

Holland (1978) used two forms for lateral momentum diffusion, which he called "Laplacian" and "biharmonic" friction. In several of his experiments, Laplacian friction was incorporated:

$$F = A_m \nabla^4 \psi, \qquad (3\text{-}37)$$

where F represents lateral momentum diffusion. In other experiments, biharmonic friction was used:

$$F = -B_m \nabla^6 \psi. \qquad (3\text{-}38)$$

When Laplacian friction was incorporated, no bottom friction was included; when biharmonic friction was used, bottom friction was included in a simple linear form:

$$B = -C_B \nabla^2 \psi, \qquad (3\text{-}39)$$

where B represents bottom friction, and C_B is the bottom friction coefficient.

For single-gyre experiments, Holland (1978) investigated two cases (see Table 2 in Holland (1978) for a complete list of cases and choices of model parameters): Case 1) Laplacian friction ($A_M = 330\ m^2 s^{-1}$) with no bottom friction included, and Case 2) biharmonic friction ($B_M = 8 \times 10^9\ m^4 s^{-1}$) with bottom friction ($C_B = 1 \times 10^{-7}\ s^{-1}$) incorporated. Case 2 was only briefly discussed in Holland (1978), but Case 1 was extensively explored. We therefore use Case 1 as guidance for the single-gyre experiment and so choose Laplacian friction ($A_M = 330\ m^2 s^{-1}$) with no bottom friction included.

For double-gyre experiments, we also use Laplacian friction ($A_M = 330\ m^2 s^{-1}$) but include bottom friction ($C_B = 1 \times 10^{-7}\ s^{-1}$). The choice of the same lateral momentum diffusion coefficient as in our single-gyre case allows some comparisons to be made between the single-gyre and double-gyre results. The additional incorporation of bottom friction also allows the role of bottom friction in the ocean general circulation to be examined in a limited way.

Lateral heat diffusion

Lateral heat diffusion is incorporated in non-adiabatic PE

models in order to suppress computational noise that would otherwise develop. In QG models, no computational noise will develop if this term is neglected. As a result, Holland (1978) does not include heat diffusion in his QG model, and we cannot use his case studies as a guide for the choices of heat diffusion formulation and coefficient in our PE model.

Since we had already decided to use a Laplacian momentum diffusion formulation, we initially decided to use a Laplacian heat diffusion formulation:

$$G = A_H \nabla^2 T, \tag{3-40}$$

where G represents lateral heat diffusion. We used the same value for the heat diffusion coefficient as the momentum diffusion coefficient, i.e., 330 $m^2 s^{-1}$. We found that this value was large enough to successfully suppress computational noise. We also found, however, that no mesoscale eddies were generated. Instead of reaching a statistically steady state in which eddies and the mean flow are in mutual balance, a steady state without eddies was obtained.

The cause of this mesoscale eddy suppression was not clear. A combination of model parameter choices could be responsible. Given these model parameters, the heat diffusion could be more effective at suppressing the eddies than the momentum diffusion.

Since the PE model is too expensive to carry out a parameter study, we conducted the following investigation. We

knew that the choices Holland (1978) had used in his Case 1 were not responsible for mesoscale eddy suppression, since eddies had been successfully generated with these choices. He effectively had no heat diffusion. But heat diffusion has not been neglected in Eqs. (3-31) and (3-32) when the QG approximation was made, and it was decided to incorporate this term, which we call "thermal wind" diffusion, in the QG model. This allowed us to conduct an inexpensive parameter study with the QG model in which: 1) different types of thermal wind diffusion, i.e., Laplacian and biharmonic formulations, could be incorporated, and 2) different diffusion coefficients could be used, ranging from zero (the Holland case) to typical choices used in PE models. From such a study, we could examine the extent to which the use of each diffusive parameterization would result in any suppression of instability processes. The results could be used as a guide for determining the heat diffusion formulation and coefficient for the PE model which would suppress computational noise, yet still allow the active generation of mesoscale eddies.

The results of this study showed that, if Laplacian thermal wind diffusion is used, values consistent with those used in PE models can result in the suppression of mesoscale eddies altogether. When a biharmonic formulation is used, however, typical PE choices of biharmonic diffusion coefficients do <u>not</u> lead to any suppression of mesoscale eddies. Because of this

finding, we use a biharmonic rather than a Laplacian heat diffusion formulation in the PE model, i.e.,

$$G = -B_H \nabla^4 T \quad . \tag{3-41}$$

With this choice, we find that we can use the same coefficient for heat diffusion that Holland (1978) used for the biharmonic momentum diffusion i.e., $\sim 10^{10}$ $m^4 s^{-1}$, without any noticeable generation of computational noise in the PE model.

3.3.5 Boundary conditions

The lateral boundary condition on the velocity can be either free-slip or no-slip. In the present models, following Holland (1978), free-slip conditions are used. The use of this condition not only reduces dissipation by lateral friction (Blandford, 1971), but also allows a strong inertial boundary current to develop (Holland and Lin, 1975a,b). The free-slip boundary condition for the PE model is:

$$v_x = 0 \qquad \text{on } x = 0,L \tag{3-42}$$

and

$$u_y = 0 \qquad \text{on } y = 0,D, \tag{3-43}$$

where L is the east-west length of the basin.

The use of biharmonic temperature diffusion requires two boundary conditions. As in Semtner and Mintz (1977), in order to conserve heat in exchanges between gridpoints and to prevent

heat transfer across all of the boundaries, the values of T and $\nabla^2 T$ are reflected across the boundary.

The rigid-lid assumption, $w = 0$ at the surface of the ocean, is made to exclude external gravity waves for economy in computation. The constraint this assumption makes on the method of solution for the PE model is discussed in Appendix A.

The boundary conditions on the ocean bottom are those of no vertical velocity and no vertical heat flux. As in Holland (1978), there is no incorporation of interfacial friction that would couple the layers together.

Physical boundaries

In the PE model, following Holland and Lin (1975a), the physical boundaries of the basin are set up to coincide with lines of u points at the north-south boundaries and with lines of v points at the east-west boundaries. This choice of the boundaries readily accommodates the kinematic boundary condition of having no normal flow across the lateral walls, i.e.,

$$u = 0 \qquad \text{on } x = 0, L \qquad (3\text{-}44a)$$

and

$$v = 0 \qquad \text{on } y = 0, D. \qquad (3\text{-}44b)$$

At a distance $\Delta/2$ outside each boundary, an extra array of grid points is introduced both to allow the same computing algorithm to be utilized for points next to the boundary as for points in the interior, and to provide a way for specifying the free-slip boundary condition. In particular, the tangential velocity outside is set equal to that of its mirror-reflection counterpart inside the boundary.

In the QG model, the physical boundaries of the basin are set up to coincide with lines of ψ points on the boundaries. This choice of the boundaries, like the PE model, also accommodates the kinematic boundary condition. At a distance Δ outside each boundary, an extra array of grid points is introduced to accommodate the free-slip boundary conditions.

3.4 Semi-discrete form of the comparison equations

In previous sections we have obtained: 1) a consistent set of comparison equations and prognostic variables in continuous form, and 2) a consistent model set-up. In this section we present the semi-discrete form of the comparison equations as a hierarchy from PE to QG. This will allow us to evaluate the importance of each of the terms involved in the sequence of approximations from PE to QG.

3.4.1 The vorticity equations

In order to facilitate the vertical differencing of the vorticity equation, Eq. (3-15) is first rewritten as

$$(\nabla^2\psi)_t = -J(\psi,\nabla^2\psi+f) + f_o w_z + (f-f_o)w_z - \nabla\chi\cdot\nabla f$$
$$- \nabla\chi\cdot\nabla\zeta + \zeta w_z - (w\nabla^2\psi)_z$$
$$+ \zeta w_z + (\nabla w\cdot\nabla\psi)_z + \nabla\psi\cdot w_z$$
$$-(J(w,\chi))_z + J(\chi,w_z) + \kappa_m\zeta_{zz} + A_m\nabla^2\zeta \quad ,$$

where, as explained earlier, the alternative choice of biharmonic momentum diffusion term is no longer retained. Dividing the ocean into two layers, with h_1 representing the thickness of the upper layer, h_2 the thickness of the lower layer (see Fig. 3.1), and defining ψ at layer mid-points, we find the semi-discrete analogue of the above equation:

$$(\nabla^2\psi_1)_t = A_{1QG} + A_{1LB} + A_{1FB} + A_{1PE} \tag{3-45}$$

and

$$(\nabla^2\psi_2)_t = A_{2QG} + A_{2LB} + A_{2FB} + A_{2PE}, \tag{3-46}$$

where

$$A_{1QG} \equiv -J(\psi_1,\nabla^2\psi_1 + f) - (f_o/h_1)w_2$$
$$+h_1^{-1}\mathrm{curl}_z\tau(y) + A_m\nabla^4\psi_1, \tag{3-47}$$

$$A_{1LB} \equiv -(f - f_o)/h_1)w_2 - \nabla\chi_1\cdot\nabla f, \tag{3-48}$$

$$A_{1FB} \equiv -\nabla\chi_1\cdot\nabla\zeta_1 - (2/h_1)\zeta_1 w_2 + h_1^{-1} w_2 \zeta^* - h_1^{-1}(\nabla w_2\cdot\nabla\psi^*) - h_1^{-1}(\nabla\psi_1) w_2 \quad , \tag{3-49}$$

$$A_{1PE} \equiv -h_1^{-1} J(\chi_1, w_2) + h_1^{-1} J(w_2, \chi^*) \quad , \tag{3-50}$$

$$A_{2QG} \equiv -J(\psi_2, \nabla^2\psi_2 + f) + (f_o/h_2) w_2 + A_m \nabla^4 \psi_2 - C_B \nabla^2 \psi_2 , \tag{3-51}$$

$$A_{2LB} \equiv ((f - f_o)/h_2) w_2 - \nabla\chi_2\cdot\nabla f , \tag{3-52}$$

$$A_{1PE} \equiv -h_1^{-1} J(\chi_1, w_2) + h_1^{-1} J(w_2, \chi^*) \quad , \tag{3-50}$$

$$A_{2QG} \equiv -J(\psi_2, \nabla^2\psi_2 + f) + (f_o/h_2) w_2 + A_m \nabla^4 \psi_2 - C_B \nabla^2 \psi_2 , \tag{3-51}$$

$$A_{2LB} \equiv ((f - f_o)/h_2) w_2 - \nabla\chi_2\cdot\nabla f , \tag{3-52}$$

$$A_{2FB} \equiv -\nabla\chi_2\cdot\nabla\zeta_2 + (2/h_2)\zeta_2 w_2 - h_2^{-1} w_2 \zeta^* + h_2^{-1}(\nabla w_2 \nabla\psi^*) + h_2^{-1}(\nabla\psi_2) w_2 \quad , \tag{3-53}$$

$$A_{2PE} \equiv h_2^{-1} J(\chi_2, w_2), \; -h_2^{-1} J(w_2, \chi^*) \quad ,$$

$$\zeta^* \equiv (\zeta_1 + \zeta_2)/2 \quad , \tag{3-54}$$

$$\psi^* \equiv (\psi_1 + \psi_2)/2 , \tag{3-55}$$

$$\chi^* \equiv (\chi_1 + \chi_2)/2 , \tag{3-56}$$

and $\mathrm{curl}_z\tau(y)$ is the vertical component of the wind stress curl.

Here and in the following equations, the subscripts PE, FB, LB and QG are introduced to symbolize the terms retained in the hierarchy of equations from PE to QG. The notations FB and LB stand for full balance and linear balance, respectively.

3.4.2 The divergence equations

In order to facilitate the vertical differencing of the divergence equation, Eq. (3-16) is first rewritten as

$$
\begin{aligned}
(\nabla^2\chi)_t = & -\rho_o^{-1}\nabla^2 p + f_o\nabla^2\psi + (f-f_o)\nabla^2\psi + \nabla\psi\cdot(f-f_o) \\
& -J(f,\chi) - \nabla\cdot((\hat{k}\times\nabla\psi)\cdot(\nabla(\hat{k}\times\nabla\psi)) \\
& +\nabla\cdot((\hat{k}\times\nabla\psi)w_z) - \nabla\cdot(\nabla\chi\cdot\nabla(\hat{k}\times\nabla\psi)) \\
& -((\hat{k}\times\nabla\psi)\cdot\nabla w)_z + ((\hat{k}\times\nabla\psi)\cdot\nabla w_z) \\
& +\nabla\cdot(\nabla\chi\cdot w_z) - (\nabla w\cdot\nabla\chi)_z + (\nabla\chi\cdot\nabla w_z) \\
& +\kappa_m\delta_{zz} + A_m\nabla^2\delta \quad .
\end{aligned}
$$

Defining χ at layer mid-points in Fig. 3.1, the semi-discrete analogue of the above equation is

$$0 = B_{1QG} + B_{1LB} + B_{1FB} + B_{1PE} \tag{3-57}$$

and

$$0 = B_{2QG} + B_{2LB} + B_{2FB} + B_{2PE}, \tag{3-58}$$

where

$$B_{1QG} \equiv -\rho_o^{-1}\nabla^2 p_1 + f_o\nabla^2\psi_1, \tag{3-59}$$

$$B_{1LB} \equiv (f - f_o)\nabla^2\psi_1 + \nabla\psi_1\cdot\nabla f, \tag{3-60}$$

$$B_{1FB} \equiv -\nabla\cdot((\hat{k} \times \nabla\psi_1)\cdot\nabla(\hat{k} \times \nabla\psi_1)), \tag{3-61}$$

$$B_{1PE} \equiv -(\nabla^2\chi_1)_t - J(f,\chi_1)$$

$$-h_1^{-1}\nabla\cdot((\hat{k} \times \nabla\psi_1)w_2) - \nabla\cdot(\nabla\chi_1\cdot\nabla(\hat{k} \times \nabla\psi_1))$$

$$+h_1^{-1}(\hat{k} \times \nabla\psi^*)\cdot\nabla w_2 + h_1^{-1}(\hat{k} \times \nabla\psi_1)\cdot\nabla w_2 - h_1^{-1}\nabla\cdot(\nabla\chi_1\cdot w_2)$$

$$+ h_1^{-1}(\nabla w_2\cdot\nabla\chi^*) - h_1^{-1}(\nabla\chi_1\cdot\nabla w_2)$$

$$+ \nabla\cdot\tau(y) + A_m\nabla^4\chi_1 , \tag{3-63}$$

$$B_{2QG} \equiv -\rho o^{-1}\nabla^2 P_2$$

$$= -\rho o^{-1}\nabla^2 P_1 - (g\alpha H/2)\nabla^2 T^* + f_o\nabla^2\psi_2, \tag{3-64}$$

$$B_{2LB} \equiv (f - f_o)\nabla^2\psi_2 + \nabla\psi_2 \cdot \nabla f , \tag{3-65}$$

$$B_{2FB} \equiv -\nabla\cdot((\hat{k} \times \nabla\psi_2)\cdot\nabla(\hat{k} \times \nabla\psi_2)) , \tag{3-66}$$

$$B_{2PE} \equiv -(\nabla^2\chi_2)_t - J(f,\chi)$$

$$+h_2^{-1}((\hat{k} \times \nabla\psi_2)w_2) - \nabla\cdot(\nabla\chi_2\cdot\nabla(\hat{k} \times \nabla\psi_2))$$

$$-h_2^{-1}(\hat{k} \times \nabla\psi^*)\cdot\nabla w_2 + h_2^{-1}(\hat{k} \times \nabla\psi_2)\cdot\nabla w_2$$

$$+h_2^{-1}\nabla\cdot(\nabla\chi_2\cdot w_2) - h_2^{-1}(\nabla w_2\cdot\nabla\chi^*)$$

$$+h_2^{-1}(\nabla\chi_2\cdot\nabla w_2) \quad +A_m\nabla^4\chi_2 \; -C_B\nabla^2\chi_2 , \tag{3-67}$$

$$T^* \equiv (T_1 + T_2)/2 , \tag{3-68}$$

and Eq. (A-4) has been used. (See Appendix A for the derivation of Eq. (A-4).) The definition of T* in Eq. (3-68) is chosen in order to guarantee total energy conservation in the PE system of equations, and to satisfy conservation of the first and second moments of temperature as far as vertical advection is concerned (Lorenz, 1960). (Demonstrations of these conservation principles are given in Appendix A.)

3.4.3 The thermal wind relationship

In order to facilitate the vertical differencing of the thermal wind relationship, we first rewrite Eq. (3-17) as

$$\begin{aligned}\alpha g\nabla^2 T = {} & f_o\nabla^2\psi_z + (f-f_o)\nabla^2\psi_z + \nabla\psi_z\cdot(f-f_o) - (\nabla^2\chi)_{zt} \\ & -(J(f,\chi))_z - \nabla\cdot((\hat{k}\times\nabla\psi)\cdot\nabla(\hat{k}\times\nabla\psi))_z \\ & +\nabla\cdot((k\times\nabla\psi)w_z)_z - \nabla\cdot(\nabla\chi\cdot\nabla(\hat{k}\times\nabla\psi)_z \\ & -((\hat{k}\times\nabla\psi)\cdot\nabla w)_{zz} + ((\hat{k}\times\nabla\psi)\cdot\nabla w_z)_z \\ & +\nabla\cdot(\nabla\chi\cdot w_z)_z - (\nabla w\cdot\nabla\chi)_{zz} + (\nabla\chi\cdot\nabla w_z) \\ & +\kappa_m\delta_{zzz} + A_m\nabla^2\delta \quad .\end{aligned}$$

The semi-discrete analogue of the above equation is

$$\alpha g\nabla^2 T^* = C_{QG} + C_{LB} + C_{FB} + C_{PE} \ , \qquad (3\text{-}69)$$

where

$$C_{QG} \equiv (2f_o/H)\nabla^2(\psi_1 - \psi_2) \ , \tag{3-70}$$

$$C_{LB} \equiv (2/H)(f - f_o)\nabla^2(\psi_1 - \psi_2) + (2/H)\nabla(\psi_1 - \psi_2)\cdot(f - f_o) \ , \tag{3-71}$$

$$C_{FB} \equiv -H^{-1}\nabla\cdot[(\nabla^2\psi_1\cdot\nabla\psi_1 - \nabla^2\psi_2\cdot\nabla\psi_2) - H^{-1}\nabla(\nabla\psi_1\cdot\nabla\psi_1 - \nabla\psi_2\cdot\nabla\psi_2)] \ , \tag{3-72}$$

and

$$\begin{aligned} C_{PE} \equiv & -(2/H)\nabla^2(\chi_1-\chi_2)_t - (2/H)J(f,\chi_1-\chi_2) \\ & -(2/H)\nabla^2(\nabla\psi_1\nabla\chi_1 - \nabla\psi_2\nabla\chi_2) \\ & -H^{-1}(\nabla\chi_1\nabla\chi_1 - \nabla\chi_2\nabla\chi_2) \\ & +(2/H)(h_1^{-1}w_2\nabla^2\chi^* + h_2^{-1}w_2\nabla^2\chi^*) \\ & +(2/H)(h_1^{-1}\nabla w_2\cdot\nabla\chi^* + h_2^{-1}\nabla w_2\nabla\chi^*) \\ & +(2A_m/H)\nabla^4(\chi_1-\chi_2) - (2C_B/H)\nabla^2(\chi_1-\chi_2) \ . \end{aligned} \tag{3-73}$$

3.4.4 The continuity equation

The semi-discrete analogue of the continuity equation (3-18) is

$$\nabla^2\chi_1 - w_2/h_1 = 0 \tag{3-74a}$$

and

$$\nabla^2\chi_2 + w_2/h_2 = 0. \tag{3-74b}$$

3.4.5 The thermodynamic energy equation

To facilitate vertical differencing of the thermodynamic energy equation for the PE model, we first rewrite Eq. (3-20) as

$$T_t + J(\psi,T) + \nabla\chi\cdot\nabla T + (wT)_z - Tw_z$$
$$= \kappa_H T_{zz} - B_H\nabla^4 T \ ,$$

where, as explained previously, the Laplacian heat diffusion term is no longer retained.

The semi-discrete analogue of the above equation, is

$$T_{1t} + J(\psi_1,T_1) + \nabla\chi_1\cdot\nabla T_1 - h_1^{-1}T^*w_2$$
$$+ h_1^{-1}T_1w_2 = 1(2\kappa_H/h_1H)(T_1 - T_2) - B_H\nabla^4 T_1 \qquad (3\text{-}75)$$

and

$$T_{2t} + J(\psi_2,T_2) + \nabla\chi_2\cdot\nabla T_2 + h_2^{-1}T^*w_2$$
$$- h_2^{-1}T_2w_2 = (2\kappa_H/(h_2H)(T_1 - T_2) - B_H\nabla^4 T_2, \qquad (3\text{-}76)$$

where Eq. (3-68) has been used.

Since the QG model does not have mid-layer temperatures (see Fig. 3.2), but only the interfacial temperature T* defined by the thermal wind relationship Eq. (3-70), the QG semi-discrete analogue of the thermodynamic energy equation cannot be readily obtained from Eqs. (3-75) and (3-76). In the following we derive a set of equations from Eqs. (3-75) and (3-76), which we will hereafter use for comparisons between the QG and PE models, since this new set will allow QG temperature equations to be readily obtained.

Decomposition of the temperature equations

Defining static stability as

$$\sigma \equiv (T_1 - T_2)/(H/2) \tag{3-77}$$

and recalling Eq. (3-68), we note that we can decompose the temperature fields T_1 and T_2 into T* and σ components as follows:

$$T_1 = T^* + (H/4)\sigma \tag{3-78}$$

and

$$T_2 = T^* - (H/4)\sigma \quad . \tag{3-79}$$

We can use these relationships to obtain both T* and σ prediction equations from Eqs. (3-75) and (3-76). If we divide Eqs. (3-75) and (3-76) by 2, substitute the relationships (3-78) and (3-79) into the resulting equation and add, we can obtain

$$T^*_t = D_{QG} + D_{PE} \ , \tag{3-80}$$

where

$$D_{QG} \equiv J(\psi^*,T^*) + (H^2/(8h_1h_2))w_2\sigma_o - B_H\nabla^4T^* \ , \tag{3-81}$$

$$\begin{aligned} D_{PE} \equiv\ & (H^2/(8h_1h_2))w_2\sigma' + J(\tau,\sigma') + (1/2)\nabla\chi\cdot\nabla T^* \\ & + (1/2)\nabla\chi_2\cdot\nabla T^* + (H/8)\nabla\chi_1\cdot\nabla\sigma' \\ & + (H/8)\nabla\chi_2\cdot\nabla\sigma' - (h_2-h_1)/(2h_1h_2)\kappa\sigma', \end{aligned} \tag{3-82}$$

$$\sigma \equiv \sigma_o + \sigma'(x,y,z,t), \tag{3-83}$$

and

$$\tau \equiv (H/8)(\psi_1-\psi_2) \quad .$$

Here σ_o represents constant static stability. No subscripts for the full and linear balance approximations are used since the thermodynamic energy equation does not involve these approximations. If we multiply Eqs. (3-75) and (3-76) by (2/H), substitute the relationships (3-78) and (3-79) into the resulting equations, subtract Eq. (3-79) from Eq. (3-78), and use the relationship (3-83), we can obtain

$$\sigma_t = E_{QG} + E_{PE}, \tag{3-84}$$

where

$$E_{QG} = \sigma_{ot} = 0 \tag{3-85}$$

and

$$E_{PE} = \sigma_t' = J(\psi^*,\sigma') - J(\tau,T^*) - (2/H)\nabla\chi_1\cdot\nabla T_1 + (2/H)\nabla\chi_2\cdot\nabla T_2 - ((h_2-h_1)/(2h_1h_2)w_2\sigma - (2H/h_1h_2)\sigma - B_H\nabla^4\sigma'. \tag{3-86}$$

Using the relationship (3-83) and Eq. (3-85), we can also obtain the QG counterparts to Eqs. (3-77) - (3-79):

$$\sigma_{oQG} \equiv (T_1 - T_2)_o/(H/2), \tag{3-87}$$

$$T_{1QG} \equiv T^* + (H/4)\sigma_o , \tag{3-88}$$

and

$$T_{2QG} \equiv T^* = (H/4)\sigma_o . \tag{3-89}$$

In Eq. (3-87) a subscript has been attached to $(T_1 - T_2)$ to denote that $(T_1 - T_2)$ is constant in our QG system.

Eqs. (3-80) and (3-84) form the temperature set of equations. This set completes the semi-discrete form of comparison equations that we will use in the following chapters.

CHAPTER 4. METHODS OF COMPARISON

The analyses of energy, relative vorticity, and potential vorticity each emphasize different aspects of the dynamics of the ocean general circulation. The analysis of energy sources, sinks and transformations associated with the motions can be used to explore generation processes for eddy kinetic energy. Relative vorticity equations can be used to investigate the degree of quasigeostrophy. According to Holland and Rhines (1980), potential enstrophy (i.e., the square of the potential vorticity) can be used as the principal measure of mesoscale eddy activity, since the "time-mean potential vorticity Q is the fundamental reference field for the mean circulation."

In this chapter we use the set of equations just derived to develop analysis procedures in the following areas: 1) energy, 2) relative vorticity, and 3) potential vorticity. The results of the single-gyre and double-gyre QG and PE numerical experiments (Chapters 5 and 6) will be analyzed in each of these areas.

4.1 Energetics

In the present experiments, two sets of energy equations are used. The first set is composed of time-dependent energy quantities, and the second describes time-averaged and eddy

motions. We first show how the kinetic energy can be decomposed into rotational and divergent components.

Using the identity (3-14), the kinetic energy per unit mass can be written as

$$\frac{1}{2}\vec{v}\cdot\vec{v} = \frac{1}{2}\nabla\psi\cdot\nabla\psi + J(\psi,\chi) + \frac{1}{2}\nabla\chi\cdot\nabla\chi \ .$$

If the above relationship is horizontally averaged, the Jacobian term will vanish, and the kinetic energy becomes

$$\frac{1}{2}\langle\vec{v}\cdot\vec{v}\rangle = \frac{1}{2}\langle\nabla\psi\cdot\nabla\psi\rangle + \frac{1}{2}\langle\nabla\chi\cdot\nabla\chi\rangle \ , \qquad (4\text{-}1)$$

where the angle brackets denote a horizontal average over the entire basin. If we differentiate Eq. (4-1) with respect to time, we can obtain

$$\frac{1}{2}\langle\vec{v}\cdot\vec{v}\rangle_t = \frac{1}{2}\langle(\nabla\psi)^2\rangle_t + \frac{1}{2}\langle(\nabla\chi)^2\rangle_t \ ,$$

which can also be written as

$$= -\langle(\psi-\psi_B)\nabla^2\psi_t\rangle - \langle\chi\nabla^2\chi_t\rangle \ . \qquad (4\text{-}2)$$

where ψ_B represents ψ on the lateral boundary points. We note that we can use the above relationships to obtain time-dependent kinetic energy equations from the vorticity and divergence equations.

4.1.1 Time-dependent energy equations

Rotational and divergent kinetic energy

The rotational component of kinetic energy for each layer is obtained by multiplying the relative vorticity equations (3-45) and (3-46) by $-h_1(\psi_1-\psi_{1B})$ and $-h_2(\psi_2-\psi_{2B})$, respectively, and horizontally averaging:

$$(K_{1R})_t \equiv (h_1/2)\langle(\nabla\psi_1)^2\rangle_t = G_{1QG} + G_{1LB} + G_{1FB} + G_{1PE} \quad (4\text{-}3)$$

and

$$(K_{2R})_t \equiv (h_2/2)\langle(\nabla\psi_2)^2\rangle_t = G_{2QG} + G_{2LB} + G_{2FB} + G_{2PE}, \quad (4\text{-}4)$$

where

$$G_{1QG} \equiv f_o\langle(\psi_1-\psi_{1B})w_2\rangle$$

$$-\langle(\psi_1-\psi_{1B})\,\mathrm{curl}_z\,\tau(y)\rangle - A_m h_1\langle(\psi_1-\psi_{1B})\nabla^4\psi_1\rangle \quad (4\text{-}5a)$$

$$= f_o\langle(\psi^*-\psi^*_B)w_2\rangle + (f_o/2)\langle w_2((\psi_1-\psi_{1B})-(\psi_2-\psi_{2B}))\rangle$$

$$-\langle(\psi_1-\psi_{1B})\,\mathrm{curl}_z\,\tau(y)\rangle - A_m h_1\langle(\psi_1-\psi_{1B})\nabla^4\psi_1\rangle, \quad (4\text{-}5b)$$

$$G_{1LB} \equiv (f-f_o)\langle(\psi_1-\psi_{1B})w_2\rangle \quad (4\text{-}6a)$$

$$= (f-f_o)\langle(\psi^*-\psi^*_B)w_2\rangle$$

$$+((f-f_o)/2)\langle w_2((\psi_1-\psi_{1B})-(\psi_2-\psi_{2B}))\rangle, \quad (4\text{-}6b)$$

$$G_{1FB} \equiv -h_1\langle(\psi_1-\psi_{1B})\cdot A_{1FB}\rangle, \quad (4\text{-}7)$$

$$G_{1PE} \equiv 0,$$

$$G_{2QG} \equiv -f_o\langle w_2(\psi_2-\psi_{2B})\rangle$$

$$-A_m h_2\langle(\psi_2-\psi_{2B})(\nabla^4\psi_2)\rangle + C_B h_2\langle(\psi_2-\psi_{2B})\nabla^2\psi_2\rangle \quad (4\text{-}8a)$$

$$= -f_o\langle w_2(\psi^*-\psi^*_B)\rangle + (f_o/2)\langle w_2((\psi_1-\psi_{1B})-(\psi_2-\psi_{2B}))\rangle$$

$$-A_m h_2\langle(\psi_2-\psi_{2B})(\nabla^4\psi_2)\rangle + C_B h_2\langle(\psi_2-\psi_{2B})\nabla^2\psi_2\rangle, \quad (4\text{-}8b)$$

$$G_{2LB} \equiv -(f - f_o)\langle w_2(\psi_2-\psi_{2B})\rangle \quad (4\text{-}9a)$$

$$= -(f-f_o)\langle w_2(\psi^*-\psi^*_B)\rangle$$

$$+((f-f_o)/2)\langle w_2((\psi_1-\psi_{1B})-(\psi_2-\psi_{2B}))\rangle, \quad (4\text{-}9b)$$

$$G_{2FB} \equiv -h_2\langle(\psi_2-\psi_{2B})\cdot A_{2FB}\rangle , \quad (4\text{-}10)$$

$$G_{2PE} \equiv 0,$$

and K_{1R} and K_{2R} are the rotational components of kinetic energy for the upper and lower layers, respectively. We note that in Eqs. (4-5b), (4-6b), (4-8b), and (4-9b), the relationship (3-55) has been used.

The divergent component of the kinetic energy for each layer is obtained by multiplying the divergence equations (3-57) and (3-58) by $-h_1\chi_1$ and $-h_2\chi_2$, respectively, and horizontally averaging:

$$(K_{1D})_t \equiv (h_1/2)\langle(\nabla\chi_1)^2\rangle_t = M_{1QG} + M_{1LB} + M_{1FB} + M_{1PE} \quad (4\text{-}11)$$

and

$$(K_{2D})_t \equiv (h_2/2)\langle(\nabla\chi_2)^2\rangle_t = M_{2QG} + M_{2LB} + M_{2FB} + M_{2PE} \quad (4\text{-}12)$$

where

$$M_{1QG} \equiv h_1\rho_o^{-1}\langle\chi_1\nabla^2 p_1\rangle - f_o h_1\langle\chi_1\nabla^2\psi_1\rangle , \quad (4\text{-}13)$$

$$M_{1LB} \equiv -(f - f_o)h_1\langle\chi_1\nabla^2\chi_1\rangle - h_1\langle\chi_1(\nabla\psi_1\cdot\nabla f)\rangle, \quad (4\text{-}14)$$

$$M_{1FB} \equiv -h_1\langle\chi_1 \cdot B_{1FB}\rangle \ , \tag{4-15}$$

$$M_{1PE} \equiv -h_1\langle\chi_1 \cdot B_{1PE}\rangle \ , \tag{4-16}$$

$$M_{2QG} \equiv h_2\rho_o^{-1}\langle\chi_2 \cdot \nabla^2 p_2\rangle - f_o h_2\langle\chi_2 \cdot \nabla^2\psi_2\rangle, \tag{4-17}$$

$$M_{2LB} \equiv -(f - f_o)h_2\langle\chi_2 \cdot \nabla^2\psi_2\rangle - h_2\langle\chi_2(\nabla\psi_2 \cdot \nabla f)\rangle, \tag{4-18}$$

$$M_{2FB} \equiv -h_2\langle\chi_1 \cdot B_{2FB}\rangle, \tag{4-19}$$

$$M_{2PE} \equiv -h_2\langle\chi_2 \cdot B_{2PE}\rangle, \tag{4-20}$$

and K_{1D} and K_{2D} are the divergent components of kinetic energy for the upper and lower layers, respectively.

PE kinetic and available potential energy

The total kinetic energy for each layer is obtained as follows. First, the semi-discrete analogues of the PE momentum equations (3-1) and (3-2) are obtained:

$$u_{1t} + (u_1u_1)_x + (v_1u_1)_y - h_1^{-1}(w_2u^*)$$
$$= fv_1 - \rho_o^{-1} p_{1x} + A_m\nabla^2 u_1 + h_1^{-1}\tau(y), \tag{4-21}$$

$$u_{2t} + (u_2u_2)_x + (v_2u_2)_y + h_2^{-1}(w_2u^*)$$
$$= fv_2 - \rho_o^{-1} p_{2x} + A_m\nabla^2 u_2 - C_B u_2, \tag{4-22}$$

$$v_{1t} + (u_1v_1)_x + (v_1v_1)_y - h_1^{-1}(w_2v^*)$$
$$= -fu_1 - \rho_o^{-1} p_{1y} + A_m\nabla^2 v_1 \ , \tag{4-23}$$

$$v_{2t} + (u_2v_2)_x + (v_2v_2)_y + h_2^{-1}(w_2v^*)$$

$$= -fu_2 - \rho_o^{-1} p_{2y} + A_m \nabla^2 v_2 , \tag{4-24}$$

$$u^* \equiv (u_1 + u_2)/2 , \tag{4-25}$$

$$v^* \equiv (v_1 + v_2)/2 , \tag{4-26}$$

where, as explained earlier, the biharmonic momentum diffusion term is no longer retained. Next, the kinetic energy for each layer is obtained by: 1) multiplying Eq. (4-21) by $(h_1 u_1)$, (4-22) by $(h_2 u_2)$, and adding them together; 2) multiplying Eq. (4-23) by $(h_1 v_1)$, and (4-24) by $(h_2 v_2)$ and adding them; and 3) horizontally averaging the resulting equations:

$$\begin{aligned} h_1 \langle \tfrac{1}{2} u_{1t}^2 + \tfrac{1}{2} v_{1t}^2 \rangle &\equiv (K_1)_t \\ &= A_m h_1 \langle u_1 \nabla^2 u_1 + v_1 \nabla^2 v_1 \rangle - \rho_o^{-1} \langle u_1 p_{1x} + v_1 p_{1y} \rangle \\ &\quad + \langle u_1 \tau(y) \rangle \end{aligned} \tag{4-27}$$

$$\begin{aligned} h_2 \langle \tfrac{1}{2} u_{2t}^2 + \tfrac{1}{2} v_{2t}^2 \rangle &\equiv (K_2)_t \\ &= A_m h_2 \langle u_2 \nabla^2 u_2 + v_2 \nabla^2 v_2 \rangle - \rho_o^{-1} \langle u_2 p_{2x} + v_2 p_{2y} \rangle \\ &\quad - C_B h_2 \langle u_2^2 + v_2^2 \rangle \end{aligned} \tag{4-28}$$

$$p^* \equiv (p_1 + p_2)/2 .$$

The available potential energy of the system is chosen to be consistent with the definition of Lorenz (1955); it is proportional to the horizontal temperature variance, i.e., the

square of the deviation of the temperature from its horizontal average. First, the semi-discrete analogue of the PE temperature equation (3-5) is obtained:

$$T_{1t} + (u_1T_1)_x + (v_1T_1)_y - h_1^{-1}(w_2T^*)$$
$$= -((2\kappa_H)/(h_1H))(T_1 - T_2) - B_H\nabla^4T_1 \qquad (4\text{-}29a)$$

$$T_{2t} + (u_2T_2)_x + (v_2T_2)_y + h_2^{-1}(w_2T^*)$$
$$= ((2\kappa_H)/(h_2H))(T_1 - T_2) - B_H\nabla^4T_2 \ , \qquad (4\text{-}29b)$$

where, as explained earlier, the Laplacian heat diffusion term is no longer retained. Next, using angle brackets as before to denote the horizontal average, and the symbol tilde (~) to denote the deviation from the horizontal average, we can derive the following equations:

$$\frac{1}{2}\langle\tilde{T}_{1t}^2\rangle + \frac{1}{2}\langle\tilde{T}_1\tilde{w}_2\rangle\langle\sigma\rangle - (1/(2h_1))\langle\tilde{T^*}^2\tilde{w}_2\rangle$$
$$= -((2\kappa_H)/(h_1H))\langle\tilde{T}_1(\tilde{T}_1 - \tilde{T}_2)\rangle - \frac{1}{2}B_H\langle\nabla^4\tilde{T}_1^2\rangle \qquad (4\text{-}30a)$$

and

$$\frac{1}{2}\langle\tilde{T}_{2t}^2\rangle + \frac{1}{2}\langle\tilde{T}_2\tilde{w}_2\rangle\langle\sigma\rangle + (1/(2h_2))\langle\tilde{T^*}^2\tilde{w}_2\rangle$$
$$= ((2\kappa_H)/(h_2H)\langle\tilde{T}_2(\tilde{T}_1 - \tilde{T}_2)\rangle - \frac{1}{2}B_H\langle\nabla^4\tilde{T}_2^2\rangle \ . \qquad (4\text{-}30b)$$

If we multiply Eq. (4-30a) by $(h_1\alpha g/\langle\sigma\rangle)$ and Eq. (4-30b) by $(h_2\alpha g/\langle\sigma\rangle)$ we can obtain

$$((h_1\alpha g)/2)\langle\sigma^{-1}\rangle\langle\tilde{T}_{1t}^2\rangle \equiv \langle P_{1t}\rangle$$

$$= ((h_1\alpha g)/2)\ \langle\tilde{T}_1\tilde{w}_2\rangle - (\alpha g/2)\langle\sigma^{-1}\rangle\langle\tilde{T}^{*2}\tilde{w}_2\rangle$$

$$=-(2\kappa_H\alpha g/H)\langle\sigma^{-1}\rangle\langle\tilde{T}_1(\tilde{T}_1-\tilde{T}_2)\rangle-B_H(h_1\alpha g/2)\langle\sigma^{-1}\rangle\langle\nabla^4\tilde{T}_1^2\rangle \quad (4\text{-}31)$$

and

$$((h_2\alpha g)/2)\langle\sigma^{-1}\rangle\langle\tilde{T}_{2t}^2\rangle = \langle P_{2t}\rangle$$

$$= ((h_2\alpha g)/2)\langle\tilde{T}_2\tilde{w}_2\rangle + (\alpha g/2)\langle\sigma^{-1}\rangle\langle\tilde{T}^{*2}\tilde{w}_2\rangle$$

$$= (2\kappa_H\alpha g/H)\langle\sigma^{-1}\rangle\langle\tilde{T}_2(\tilde{T}_1-\tilde{T}_2)\rangle-B_H(h_2\alpha g/2)\langle\sigma^{-1}\rangle\langle\nabla^4\tilde{T}_2^2\rangle \quad (4\text{-}32)$$

where P_1 and P_2 are the available potential energies for the upper and lower layers, respectively.

We note that in order to have consistent conversions of available potential energy into kinetic energy, some manipulation of Eqs. (4-27) and (4-28) is necessary. Using the semi-discrete forms of Eqs. (3-3) and (3-6), the terms $-\rho_o^{-1}\langle u_1 p_{1x} + v_1 p_{1y}\rangle$ and $-\rho_o^{-1}\langle u_2 p_{2x} + v_2 p_{2y}\rangle$ can be rewritten as

$$-\rho_o^{-1}\langle u_1 p_{1x} + v_1 p_{1y}\rangle = \langle\tilde{w}_2\tilde{p}^*\rangle - (h_1\alpha g/2)\langle\tilde{T}_1\tilde{w}_2\rangle \quad (4\text{-}33a)$$

and

$$\rho_o^{-1}\langle u_2 p_{2x} + v_2 p_{2y}\rangle = -\langle\tilde{w}_2\tilde{p}^*\rangle - (h_2\alpha g/2)\langle\tilde{T}_2\tilde{w}_2\rangle, \quad (4\text{-}33b)$$

where the continuity equations (3-74a,b) and the substitution

$w_2 = \tilde{w}_2$ have been used. If the relationships, (4-33a) and (4-33b) are substituted into Eqs. (4-27) and (4-28), respectively, we can obtain

$$h_1\langle\frac{1}{2}\,u_{1t}^2 + \frac{1}{2}\,v_{1t}^2\rangle \equiv (K_1)_t$$

$$= A_m h_1\langle u_1\nabla^2 u_1 + v_1\nabla^2 v_1\rangle + \langle\tilde{w}_2\tilde{p}^*\rangle$$

$$-(h_1\alpha g/2)\ \langle\tilde{T}_1\tilde{w}_2\rangle + \langle u_1\tau(y)\rangle \qquad (4\text{-}34a)$$

and

$$h_2\langle\frac{1}{2}\,u_{2t}^2 + \frac{1}{2}\,v_{2t}^2\rangle \equiv (K_2)_t$$

$$= A_m h_2\langle u_2\nabla^2 u_2 + v_2\nabla^2 v_2\rangle - \langle\tilde{w}_2\tilde{p}^*\rangle$$

$$-(h_2\alpha g/2)\ \langle\tilde{T}_2\tilde{w}_2\rangle - C_B h_2\langle u_2^2 + v_2^2\rangle\ , \qquad (4\text{-}34b)$$

where

$$\tilde{p}^* \equiv (\tilde{p}_1 + \tilde{p}_2)/2\ .$$

The instantaneous energy conversions then become apparent. They are

$$\langle\tau \rightarrow K_1\rangle \equiv \langle u_1\tau(y)\rangle \qquad (4\text{-}35a)$$

$$\langle K_1 \rightarrow P_1\rangle \equiv (h_1\alpha g/2)\langle\tilde{T}_1\tilde{w}_2\rangle \qquad (4\text{-}35b)$$

$$\langle K_2 \rightarrow P_2\rangle \equiv (h_2\alpha g/2)\langle\tilde{T}_2\tilde{w}_2\rangle \qquad (4\text{-}35c)$$

$$\langle K_1 \rightarrow K_2\rangle \equiv -\langle\tilde{w}_2\tilde{p}^*\rangle \qquad (4\text{-}35d)$$

$$\langle K_1 \rightarrow D_{H1}\rangle \equiv -A_m h_1\langle(u_1\nabla^2 u_1 + v_1\nabla^2 v_1)\rangle \qquad (4\text{-}35e)$$

$$\langle K_2 \rightarrow D_{H2}\rangle \equiv -A_m h_2\langle(u_2\nabla^2 u_2 + v_2\nabla^2 v_2)\rangle \qquad (4\text{-}35f)$$

$$\langle K_2 \rightarrow D_B \rangle \equiv C_B h_2 \langle (u_2^2+v_2^2) \rangle \tag{4-35g}$$

$$\langle P_2 \rightarrow P_1 \rangle \equiv -(\alpha g/2)\langle \sigma^{-1} \rangle \langle \tilde{T}^{*2} \tilde{w}_2 \rangle \tag{4-35h}$$

$$\langle P_1 \rightarrow B_1 \rangle \equiv (B_H h_1 \alpha g/2)\langle \sigma^{-1} \rangle \langle \nabla^4 \tilde{T}_1^2 \rangle + (2\kappa_H \alpha g/H)\langle \sigma^{-1} \rangle \langle \tilde{T}_1 (\tilde{T}_1 - \tilde{T}_2) \rangle \tag{4-35i}$$

$$\langle P_2 \rightarrow B_2 \rangle \equiv (B_H h_2 \alpha g/2)\langle \sigma^{-1} \rangle \langle \nabla^4 \tilde{T}_2^2 \rangle + (2\kappa_H \alpha g/H)\langle \sigma^{-1} \rangle \langle \tilde{T}_2 (\tilde{T}_1 - \tilde{T}_2) \rangle \; . \tag{4-35j}$$

Here (4-35a) represents the energy transfer rate from the surface wind to the upper layer of the ocean. Eqs. (4-35b) and (4-35c) represent the work done by buoyancy forces in the upper and lower layers, respectively. Eq. (4-35d) represents the work done by pressure forces at the interface in transferring energy downward. The terms (4-35e) and (4-35f) are the rates of energy dissipation by Laplacian momentum diffusion in the upper and lower layers, respectively. The term (4-35g) is the rate of energy dissipation by bottom friction in the lower layer. The term (4-35h) represents the work done by buoyancy forces at the interface in transferring energy downward. The terms (4-35i) and (4-35j) are the rates of energy dissipation by biharmonic heat diffusion and vertical heat diffusion for the upper and lower layers, respectively. The energy transfer rates and energy levels are summarized by means of the energy box diagram shown in Fig. 4.1.

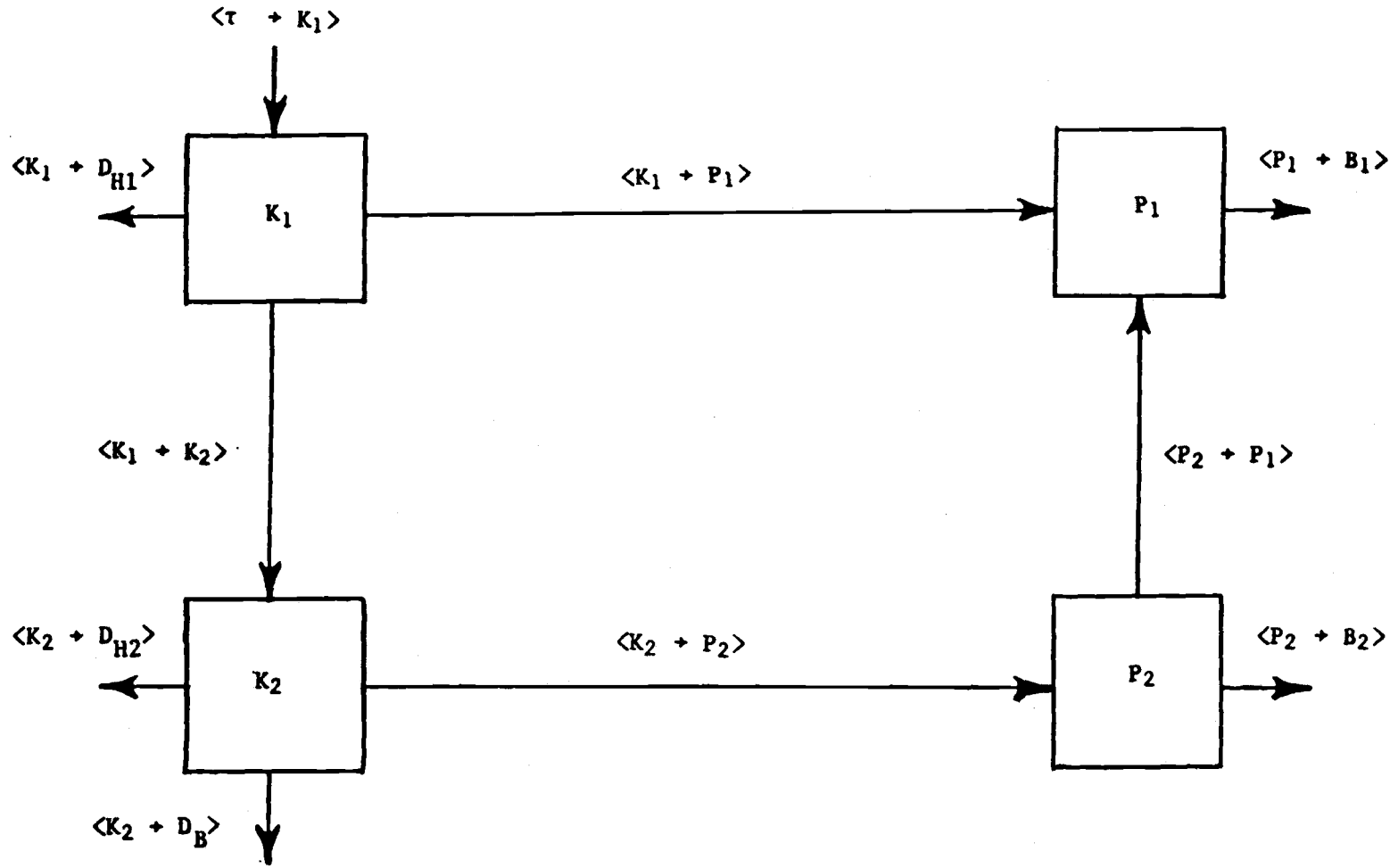

Fig. 4.1 The global energetics diagram for the PE model showing the energy levels and energy transfer rates defined by Eq. (4-35).

Energy comparisons

There are several forms of energy equations which can be used in the PE-QG comparison. From Eq. (4-2), we see that the total kinetic energy is the sum of the rotational and divergent components, i.e.,

$$(K_1)_t \equiv (K_{1R})_t + (K_{1D})_t \tag{4-36}$$

and

$$(K_2)_t \equiv (K_{2R})_t + (K_{2D})_t \ . \tag{4-37}$$

We note that for the QG, LB and FB systems of equations, Eqs. (4-36) and (4-37) reduce to

$$(K_1)_t = (K_{1R})_t \tag{4-38}$$

and

$$(K_2)_t = (K_{2R})_t \ . \tag{4-39}$$

As a result, the divergent kinetic energy equations (4-11) and (4-12) will not be used in the comparisons. Instead, the total and rotational kinetic energy equations will be used, with the divergent component computed as the difference between total and rotational kinetic energy.

The form of the available potential energy to be used in conjunction with the rotational component of the kinetic energy is chosen to be consistent with the definition of Lorenz (1955). From Eq. (3-80), we can derive the following equation:

$$\frac{1}{2}\langle\tilde{T}^{*2}\rangle_t = (H^2/(8h_1h_2))\sigma_o\langle\tilde{T}^*\tilde{w}_2\rangle$$

$$- \frac{1}{2} B_H\langle\nabla^4\tilde{T}^{*2}\rangle + \langle\tilde{T}^*\tilde{D}_{PE}\rangle \ . \qquad (4\text{-}40)$$

We note that in order to have consistent conversions of available potential energy into kinetic energy, some manipulation of the rotational kinetic energy equations (4-3)-(4-10) is necessary. Using the thermal wind relationship (3-69) we can obtain

$$f_o\langle\tilde{w}_2(\tilde{\psi}_1 - \tilde{\psi}_2)\rangle = (\alpha gH/2)\langle\tilde{w}_2\tilde{T}^*\rangle \qquad (4\text{-}41a)$$

and

$$(f - f_o)\langle\tilde{w}_2(\tilde{\psi}_1 - \tilde{\psi}_2)\rangle = (\alpha gH/2)\langle\tilde{w}_2\tilde{T}^*\rangle \qquad (4\text{-}41b)$$

for the QG and LB approximations, respectively. Similarly, using the divergence equations (3-57) and (3-58) we can obtain

$$f_o\langle\tilde{w}_2\tilde{\psi}^*\rangle = \rho_o^{-1}\langle\tilde{w}_2\tilde{p}^*\rangle \qquad (4\text{-}42a)$$

and

$$(f - f_o)\langle\tilde{w}_2\tilde{\psi}^*\rangle = \rho_o^{-1}\langle\tilde{w}_2\tilde{p}^*\rangle \qquad (4\text{-}42b)$$

for the QG and LB approximations, respectively. If we now substitute the thermal wind relationship (3-69) into Eq. (4-40), and multiply the resulting equation by (f^2/g') we can obtain

$$(P_R)_t = (P_{RQG})_t + (P_{RLB})_t \ , \qquad (4\text{-}43)$$

where

$$(P_{RQG})_t = (f_o^2/2g')\langle(\psi_1 - \psi_2)_t^2\rangle$$

$$= -f_o \langle w_2(\psi_1 - \psi_2)\rangle$$

$$-B_H\langle\nabla^4 P_{RQG}\rangle \ , \qquad (4\text{-}43a)$$

$$(P_{RLB})_t = ((f^2 - f_o^2)/2g')\langle\psi_1 - \psi_2)^2_t\rangle$$

$$= -(f^2 - f_o^2)\ \langle w_2(\psi_1 - \psi_2)\rangle$$

$$-B_H\langle\nabla^4 P_{RLB}\rangle$$

$$+((f^2 - f_o^2)g\alpha H/2g')\langle(\psi_1 - \psi_2)D_{RPE}\rangle \ , \qquad (4\text{-}43b)$$

and

$$g' \equiv -(\alpha g H^3)/(16 h_1 h_2)\sigma_o \ , \qquad (4\text{-}44)$$

where, for the sake of simplifying notation, we drop the tilde symbol.

The system of equations (4-43a) and (4-43b), and the relationships (4-41) and (4-42), will be used in conjunction with the QG and LB rotational kinetic energy equations (4-5), (4-6), (4-8) and (4-9). Terms of higher order than LB will be treated as a residual. As in the PE system, we can make use of energy box diagrams to examine the global energy transfers for the rotational components of energy. In the next section, we will present such a diagram for the statistically steady state.

4.1.2 Time-mean and eddy energy equations

When the flow is examined over a period of time in the statistically steady state, the time-dependent variables can be divided into a time-mean part (denoted by an overbar) and an eddy part (denoted by a prime), which is the deviation from the time-mean. Thus, for the rotational component of kinetic energy

$$\overline{K}_{1R} \equiv (h_1/2)\ \langle(\nabla\overline{\psi}_1)^2\rangle$$

$$\overline{K}_{2R} \equiv (h_2/2)\ \langle(\nabla\overline{\psi}_2)^2\rangle$$

$$\overline{P}_R \equiv (f^2/2g')\langle(\overline{\psi}_1 - \overline{\psi}_2)^2\rangle$$

$$K'_{1R} \equiv (h_1/2)\ \langle\overline{(\nabla\psi'_1)^2}\rangle$$

$$K'_{2R} \equiv (h_2/2)\ \langle\overline{(\nabla\psi'_2)^2}\rangle$$

$$P'_R \equiv (f^2/2g')\langle\overline{(\psi_1' - \psi_2')^2}\rangle$$

are the kinetic energies and available potential energy of the mean flow and the eddies, respectively. The energy relations between the mean and the eddies over the period of time averaging can then be summarized by means of the energy diagram shown in Fig. 4.2, where the energy transfer terms are

$$\{\tau \rightarrow \overline{K}_{1QG}\}_R = -\langle\overline{\psi}_1\ \mathrm{curl}_z\ \tau(y)\rangle, \qquad (4\text{-}45a)$$

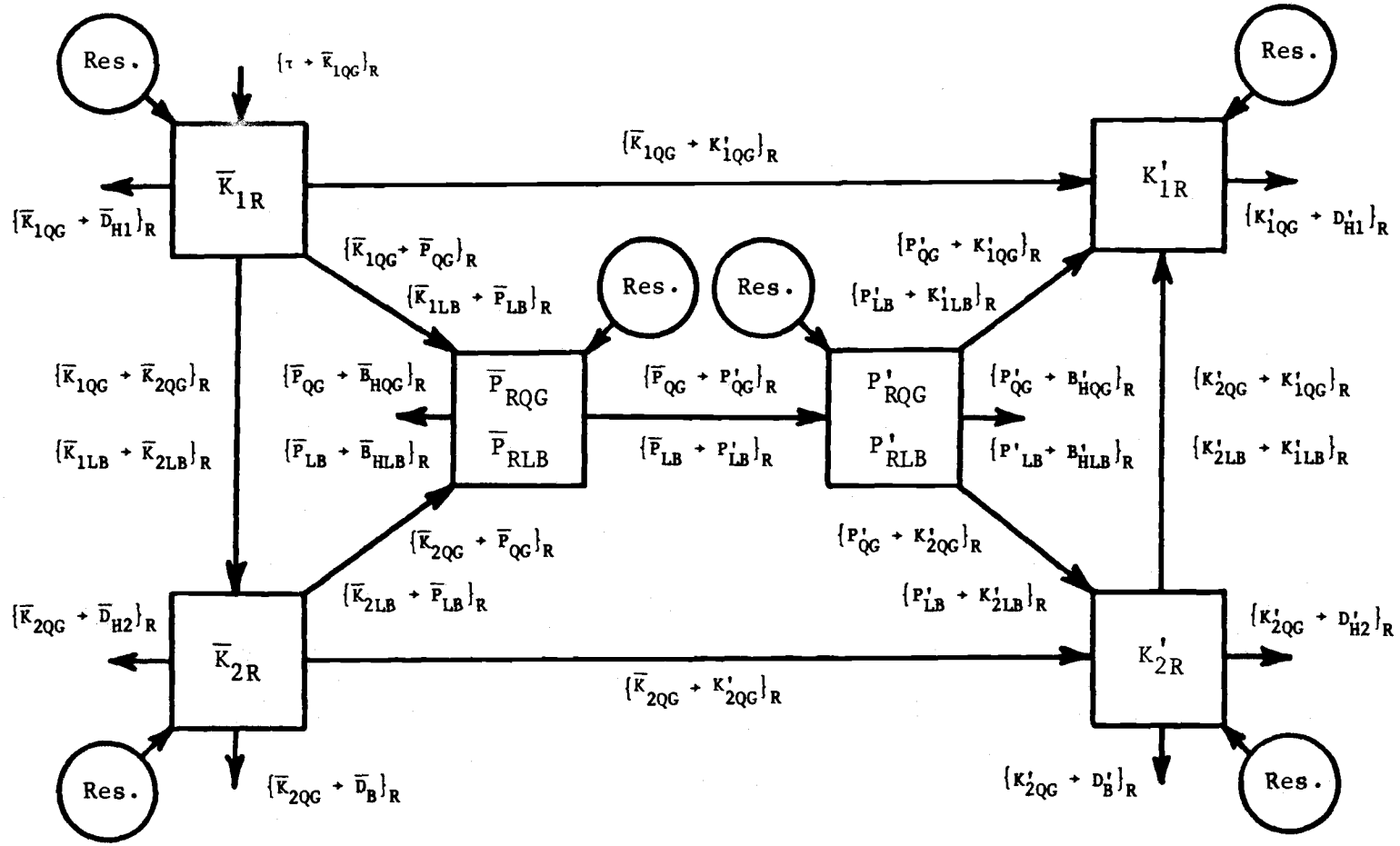

Fig. 4.2 The global energetics diagram for the final statistically steady state showing the energy levels and energy transfer rates defined by Eq. (4-45).

$$\{\overline{K}_{1QG} \rightarrow \overline{P}_{QG}\}_R = -(f_o/2)\langle\overline{w}_2(\overline{\psi}_1 - \overline{\psi}_2)\rangle, \tag{4-45b}$$

$$\{\overline{K}_{2QG} \rightarrow \overline{P}_{QG}\}_R = -(f_o/2)\langle\overline{w}_2(\overline{\psi}_1 - \overline{\psi}_2)\rangle, \tag{4-45c}$$

$$\{\overline{K}_{1QG} \rightarrow \overline{K}_{2QG}\}_R = -f_o\langle\overline{w}_2\overline{\psi}^*\rangle , \tag{4-45d}$$

$$\{\overline{K}_{1QG} \rightarrow \overline{D}_{H1}\}_R = A_m h_1\langle\overline{\psi}_1\nabla^4\overline{\psi}_1\rangle, \tag{4-45e}$$

$$\{\overline{K}_{2QG} \rightarrow \overline{D}_{H2}\}_R = A_m h_2\langle\overline{\psi}_2\nabla^4\overline{\psi}_2\rangle, \tag{4-45f}$$

$$\{\overline{K}_{2QG} \rightarrow \overline{D}_B\}_R = -C_B h_2\langle\overline{\psi}_2\nabla^2\overline{\psi}_2\rangle, \tag{4-45g}$$

$$\{\overline{K}_{1LB} \rightarrow \overline{P}_{LB}\}_R = -((f - f_o)/2)\langle\overline{w}_2(\overline{\psi}_1 - \overline{\psi}_2)\rangle , \tag{4-45h}$$

$$\{\overline{K}_{2LB} \rightarrow \overline{P}_{LB}\}_R = -((f - f_o)/2)\langle\overline{w}_2(\overline{\psi}_1 - \overline{\psi}_2)\rangle, \tag{4-45i}$$

$$\{\overline{K}_{1LB} \rightarrow \overline{K}_{2LB}\}_R = -(f - f_o)\langle\overline{w}_2\overline{\psi}^*\rangle, \tag{4-45j}$$

$$\{\overline{P}_{QG} \rightarrow \overline{B}_{HQG}\}_R = -B_H(f_o^2/2g')\langle\nabla^4(\overline{\psi}_1 - \overline{\psi}_2)^2\rangle, \tag{4-45k}$$

$$\{\overline{P}_{LB} \rightarrow \overline{B}_{HLB}\}_R = -B_H((f^2-f_o^2)/2g')\langle\nabla^4(\overline{\psi}_1 - \overline{\psi}_2)^2\rangle, \tag{4-45l}$$

$$\{\overline{K}_{1QG} \rightarrow K'_{1QG}\}_R = h_1\langle\overline{\psi}_1\overline{J(\nabla^2\psi'_1,\psi'_1)}\rangle, \tag{4-45m}$$

$$\{\overline{K}_{2QG} \rightarrow K'_{2QG}\}_R = h_2\langle\overline{\psi}_2\overline{J(\nabla^2\psi'_2,\psi'_2)}\rangle, \tag{4-45n}$$

$$\{P'_{QG} \rightarrow K'_{1QG}\}_R = (f_o/2)\langle\overline{w'_2(\psi'_1 - \psi'_2)}\rangle, \tag{4-45o}$$

$$\{P'_{QG} \rightarrow K'_{2QG}\}_R = (f_o/2)\langle\overline{w'_2(\psi'_1 - \psi'_2)}\rangle, \tag{4-45p}$$

$$\{P'_{LB} \rightarrow K'_{1LB}\}_R = ((f - f_o)/2)\langle\overline{w'_2(\psi'_1 - \psi'_2)}\rangle, \tag{4-45q}$$

$$\{P'_{LB} \rightarrow K'_{2LB}\}_R = ((f - f_o)/2)\langle\overline{w'_2(\psi'_1 - \psi'_2)}\rangle, \tag{4-45r}$$

$$\{K'_{1QG} \rightarrow D'_{H1}\}_R = A_m h_1 \langle\overline{\psi'_1 \nabla^4 \psi'_1}\rangle \ , \tag{4-45s}$$

$$\{K'_{2QG} \rightarrow D'_{H2}\}_R = A_m h_2 \langle\overline{\psi'_2 \nabla^4 \psi'_2}\rangle, \tag{4-45t}$$

$$\{K'_{2QG} \rightarrow D'_{B}\}_R = -C_B h_2 \langle\overline{\psi'_2 \nabla^2 \psi'_2}\rangle \ , \tag{4-45u}$$

$$\{\overline{P}_{QG} \rightarrow P'_{QG}\}_R = -(f_o^2/g')\langle(\overline{\psi}_1 - \overline{\psi}_2)\overline{J(\psi'_1, \psi'_2)}\rangle, \tag{4-45v}$$

$$\{\overline{P}_{LB} \rightarrow P'_{LB}\}_R = -((f^2 - f_o^2)/g')\langle(\overline{\psi}_1 - \overline{\psi}_2)\overline{J(\psi'_1, \psi'_2)}\rangle, \tag{4-45w}$$

$$\{K'_{2QG} \rightarrow K'_{1QG}\}_R = f_o \langle\overline{w'_2 \psi^{*\prime}}\rangle \ , \tag{4-45x}$$

$$\{K'_{2LB} \rightarrow K'_{1LB}\}_R = (f - f_o)\langle\overline{w'_2 \psi^{*\prime}}\rangle, \tag{4-45y}$$

$$\{P'_{QG} \rightarrow B'_{HQG}\}_R = -B_H(f_o^2/2g')\langle\overline{\nabla^4(\psi'_1 - \psi'_2)^2}\rangle, \tag{4-45z}$$

$$\{P'_{LB} \rightarrow B'_{HLB}\}_R = -B_H((f^2 - f_o^2)/2g')\langle\overline{\nabla^4(\psi'_1 - \psi'_2)^2}\rangle \ . \tag{4-45aa}$$

Terms of higher order than LB will be treated as a residual, indicated by the symbol "Res." in Fig. 4.2. Note that "Res." should be identically zero for the QG model, except for time averaging (i.e., our time series for the eddy/mean breakdown may not be quite long enough). However, "Res." for PE may also represent real energy fluxes from the divergent component of flow to the rotational part (or vice versa). We will make use of this energy box diagram to examine the global energy transfers. In addition, in order to examine the local energy transfers, we will obtain plots of the spatial distributions of some of the integrands on the right hand side of Eq. (4-45).

4.2 Time-mean relative vorticity equations

Averaging the vorticity equations (3-45) and (3-46) in time, we can obtain

$$(\nabla^2\overline{\psi}_1)_t = \overline{A}_{1QG} + \overline{A}_{1LB} + \overline{A}_{1FB} + \overline{A}_{1PE} \tag{4-46}$$

and

$$(\nabla^2\overline{\psi}_2)_t = \overline{A}_{2QG} + \overline{A}_{2LB} + \overline{A}_{2FB} + \overline{A}_{2PE} \ , \tag{4-47}$$

where

$$\overline{A}_{1QG} = -J(\overline{\psi}_1, \overline{\zeta}_1) - \beta\overline{\psi}_{1x} - (f_o/h_1)\overline{w}_2$$

$$+h_1^{-1}\mathrm{curl}_z\tau(y) + A_m\nabla^4\overline{\psi}_1 - \overline{J(\psi_1', \zeta_1')} \ , \tag{4-48}$$

$$\overline{A}_{1LB} = -((f - f_o)/h_1)\overline{w}_2 - \beta\overline{\chi}_{1y}, \tag{4-49}$$

$$\bar{A}_{1FB} = -\nabla\bar{\chi}_1\cdot\nabla\bar{\zeta}_1 - (2/h_1)\bar{\zeta}_1\bar{w}_2$$

$$+h_1^{-1}\bar{w}_2\bar{\zeta}^* - h_1^{-1}(\nabla\bar{w}_2\cdot\nabla\bar{\psi}^*)$$

$$-h_1^{-1}(\nabla\bar{\psi}_1)\bar{w}_2 - \overline{\nabla\chi_1'\cdot\nabla\zeta_1'}$$

$$-(2/h_1)\overline{\zeta_1'w_2'} + h_1^{-1}\overline{w_2'\zeta^{*\prime}}$$

$$-h_1^{-1}\overline{(\nabla w_2'\cdot\nabla\psi^{*\prime})} - h_1^{-1}\overline{((\nabla\psi_1')w_2')} \quad , \tag{4-50}$$

$$\bar{A}_{1PE} = h_1^{-1}J(\bar{w}_2,\bar{\chi}^*) - h_1^{-1}J(\bar{\chi}_1,\bar{w}_2)$$

$$+h_1^{-1}\overline{J(w_2',\chi^{*\prime})} - h_1^{-1}\overline{J(\chi_1',w_2')}, \tag{4-51}$$

$$\bar{A}_{2QG} = -J(\bar{\psi}_2,\bar{\zeta}_2) - \beta\bar{\psi}_{2x} + (f_o/h_2)\bar{w}_2$$

$$+A_m\nabla^4\bar{\psi}_2 - C_B\nabla^2\bar{\psi}_2 - \overline{J(\psi_2',\zeta_2')} \quad , \tag{4-52}$$

$$\bar{A}_{2LB} = ((f - f_o)/h_2)\bar{w}_2 - \beta\bar{\chi}_{2y} \quad , \tag{4-53}$$

$$\bar{A}_{2FB} = -\nabla\bar{\chi}_2\cdot\nabla\bar{\zeta}_2 + (2/h_1)\bar{\zeta}_2\bar{w}_2$$

$$-h_2^{-1}\bar{w}_2\bar{\zeta}^* + h_2^{-1}(\nabla\bar{w}_2\nabla\bar{\psi}^*)$$

$$+h_2^{-1}(\nabla\bar{\psi}_2)\bar{w}_2 - \overline{\nabla\chi_2'\cdot\nabla\zeta_2'}$$

$$+(2/h_1)\zeta_2'w_2' - h_2^{-1}\ w_2'\zeta^{*\prime}$$

$$+h_2^{-1}(\nabla w_2'\nabla\psi^{*\prime}) + h_2^{-1}(\nabla\psi_2)w_2 \ , \qquad (4\text{-}54)$$

and

$$\bar{A}_{2PE} = -h_2^{-1}J(\bar{w}_2,\bar{\chi}^*) + h_2^{-1}J(\bar{\chi}_2,\bar{w}_2)$$

$$-h_2^{-1}\overline{J(w_2',\chi^{*\prime})} + h_2^{-1}\overline{J(\chi_2',w_2')} \ . \qquad (4\text{-}55)$$

We note that for the statistically steady state, $(\nabla^2\bar{\psi}_1)_t$ and $(\nabla^2\bar{\psi}_2)_t$ are zero and a balance will exist for the various terms on the right-hand side of Eq. (4-46) and Eq. (4-47). For each layer we will examine the geographical distributions of these terms as well as the mean relative vorticity itself.

4.3 Potential vorticity

In the present experiments, two sets of potential vorticity equations are used. The first set is written in terms of time-dependent potential vorticity, and the second in terms of time-averaged motions.

4.3.1 Time-dependent potential vorticity equations

The potential vorticity equation for the upper layer is obtained by: 1) substituting Eq. (3-69) into Eq. (3-80); 2) multiplying the resulting equation by $(-f^2/g'h_1)$, and 3) adding the resulting equation to the relative vorticity equation (3-45);

$$\frac{DQ_1}{Dt} \equiv \frac{D(Q_{1QG})}{Dt} + \frac{D(Q_{1LB})}{Dt} \ , \qquad (4\text{-}56)$$

where

$$\frac{D(Q_{1QG})}{Dt} = h_1^{-1}\,\mathrm{curl}_z\tau(y) + A_m\nabla^4\psi_1 + (f_o^2/g'h_1)B_H\nabla^4(\psi_1 - \psi_2) - (f_o^2/g'h_1)F_{PE}\,, \tag{4-57}$$

$$\frac{D(Q_{1LB})}{Dt} = ((f^2-f_o^2)/g'h_1)B_H\nabla^4(\psi_1 - \psi_2) - ((f^2- f_o^2)/g'h_1)F_{PE} + A_{1LB} + A_{1FB} + A_{1PE}, \tag{4-58}$$

$$Q_{1QG} \equiv \nabla^2\psi_1 + f - (f_o^2/g'h_1)(\psi_1 - \psi_2)\,, \tag{4-59}$$

$$Q_{1LB} \equiv ((f^2-f_o^2)/g'h_1)(\psi_1 - \psi_2)\,, \tag{4-60}$$

$$Q_1 \equiv \nabla^2\psi_1 + f - (f^2/g'h_1)(\psi_1 - \psi_2)\,, \tag{4-61}$$

$$\frac{D(Q_{1QG})}{Dt} = (Q_{1QG})_t + J(\psi_1, Q_{1QG})\,, \tag{4-62}$$

and

$$\frac{D(Q_{1LB})}{Dt} = (Q_{1LB})_t + J(\psi_1, Q_{1LB})\,. \tag{4-63}$$

The potential vorticity for the lower layer is obtained by: 1) substituting Eq. (3-69) into Eq. (3-80), 2) multiplying the resulting equation by $(f^2/g'h_2)$, and 3) adding the resulting equation to the relative vorticity equation (3-46);

$$\frac{DQ_2}{Dt} \equiv \frac{D(Q_{2QG})}{Dt} + \frac{D(Q_{2LB})}{Dt}\,, \tag{4-64}$$

where

$$\frac{D(Q_{2QG})}{Dt} = A_m\nabla^4\psi_2 - C_B\nabla^2\psi_2$$

$$-(f_o^2/g'h_2)B_H\nabla^4(\psi_1 - \psi_2)$$

$$+(f_o^2/g'h_2)F_{PE} \ , \tag{4-65}$$

$$\frac{D(Q_{2LB})}{Dt} = -((f^2 - f_o^2)/g'h_1)B_H\nabla^4(\psi_1 - \psi_2)$$

$$+((f^2 - f_o^2)/g'h_2)F_{PE}$$

$$+A_{2LB} + A_{2FB} + A_{2PE} \ , \tag{4-66}$$

$$Q_{2QG} \equiv \nabla^2\psi_2 + f + (f_o^2/g'h_2)(\psi_1 - \psi_2) \ , \tag{4-67}$$

$$Q_{2LB} \equiv ((f^2 - f_o^2)/g'h_2)(\psi_1 - \psi_2) \ , \tag{4-68}$$

$$Q_2 \equiv \nabla^2\psi_2 + f + (f^2/g'h_2)(\psi_1 - \psi_2) \tag{4-69}$$

$$\frac{D(Q_{2QG})}{Dt} = (Q_{2QG})_t + J(\psi_2, Q_{2QG}) \ , \tag{4-70}$$

and

$$\frac{D(Q_{2LB})}{Dt} = (Q_{2LB})_t + J(\psi_2, Q_{2LB}) \ . \tag{4-71}$$

4.3.2 Time-mean potential vorticity equations

Averaging the potential vorticity equations (4-56) and (4-64) in time, we can obtain

$$\frac{D\bar{Q}_1}{Dt} = \frac{D(\bar{Q}_{1QG})}{Dt} + \frac{D(\bar{Q}_{1LB})}{Dt} \tag{4-72}$$

and

$$\frac{D\bar{Q}_2}{Dt} = \frac{D(\bar{Q}_{2QG})}{Dt} + \frac{D(\bar{Q}_{2LB})}{Dt} \ , \tag{4-73}$$

where

$$\frac{D\overline{Q}_{1QG}}{Dt} = h_1^{-1}\,\mathrm{curl}_z\tau(y) + A_m\nabla^4\overline{\psi}_1$$

$$+(f_o^2/g'h_1)B_H\nabla^4(\overline{\psi}_1 - \overline{\psi}_2)$$

$$-(f_o^2/g'h_1)\overline{F}_{PE} \quad , \tag{4-74}$$

$$\frac{D\overline{Q}_{1LB}}{Dt} = ((f^2-f_o^2)/g'h_1)B_H\nabla^4(\overline{\psi}_1 - \overline{\psi}_2)$$

$$-((f^2-f_o^2)/g'h_1)\overline{F}_{PE}$$

$$+\overline{A}_{1LB} + \overline{A}_{1FB} + \overline{A}_{1PE} \quad , \tag{4-75}$$

$$\overline{Q}_{1QG} = \nabla^2\overline{\psi}_1 + f - (f_o^2/g'h_1)(\overline{\psi}_1 - \overline{\psi}_2) \quad , \tag{4-76}$$

$$\overline{Q}_{1LB} = ((f^2-f_o^2)/g'h_1)(\overline{\psi}_1 - \overline{\psi}_2) \quad , \tag{4-77}$$

$$\overline{Q}_1 = \nabla^2\overline{\psi}_1 + f - (f^2/g'h_1)(\overline{\psi}_1 - \overline{\psi}_2) \tag{4-78}$$

$$\frac{D(\overline{Q}_{1QG})}{Dt} = (\overline{Q}_{1QG})_t + J(\overline{\psi}_1,\overline{Q}_{1QG})$$

$$+\overline{J(\psi_1',Q_{1QG}')} \quad , \tag{4-79}$$

$$\frac{D(\overline{Q}_{1LB})}{Dt} = (\overline{Q}_{1LB})_t + J(\overline{\psi}_1,\overline{Q}_{1LB})$$

$$+\overline{J(\psi_1',Q_{1LB}')} \quad , \tag{4-80}$$

$$\frac{D(\overline{Q}_{2QG})}{Dt} = A_m\nabla^4\overline{\psi}_2 - C_B\nabla^2\overline{\psi}_2$$

$$-(f_o^2/g'h_2)B_H\nabla^4(\overline{\psi}_1 - \overline{\psi}_2)$$

$$+(f_o^2/g'h_2)\overline{F}_{PE} \quad , \tag{4-81}$$

$$\frac{D(\overline{Q}_{2LB})}{Dt} = -((f^2-f_o^2)/g'h_1)B_H\nabla^4(\overline{\psi}_1 - \overline{\psi}_2)$$

$$+((f^2-f_o^2)/g'h_2)\overline{F}_{PE}$$

$$+\overline{A}_{2LB} + \overline{A}_{2FB} + \overline{A}_{2PE} \quad , \tag{4-82}$$

$$\overline{Q}_{2QG} = \nabla^2\overline{\psi}_2 + f + (f_o^2/g'h_2)(\overline{\psi}_1 - \overline{\psi}_2) \quad , \tag{4-83}$$

$$\overline{Q}_{2LB} = ((f^2-f_o^2)/g'h_2)(\overline{\psi}_1 - \overline{\psi}_2) \quad , \tag{4-84}$$

$$\overline{Q}_2 = \nabla^2\psi_2 + f + (f^2/g'h_2)(\overline{\psi}_1 - \overline{\psi}_2) \quad , \tag{4-85}$$

$$\frac{D}{Dt}(\overline{Q}_{2QG}) = (\overline{Q}_{2QG})_t + J(\overline{\psi}_2, \overline{Q}_{2QG})$$

$$+\overline{J(\psi_2', Q_{2QG}')} \quad , \tag{4-86}$$

and

$$\frac{D}{Dt}(\overline{Q}_{2LB}) = (\overline{Q}_{2LB})_t + J(\overline{\psi}_2, \overline{Q}_{2LB})$$

$$+\overline{J(\psi_2', Q_{2B}')} \quad . \tag{4-87}$$

We note that for the statistically steady state $(\bar{Q}_1)_t$, $(\bar{Q}_{1QG})_t$, $(\bar{Q}_{1LB})_t$, $(\bar{Q}_{2QG})_t$, $(\bar{Q}_{2LB})_t$ are zero and a balance exists for the various terms of Eqs. (4-74), (4-75), (4-81), and (4-82). For each layer we will examine the geographical distributions of the mean potential vorticity.

4.4 Summary

We have now obtained from the PE and QG model equations a set of basic comparison quantities that will be used extensively in the following chapters. For the convenience of the reader, we present in Table 4.1 a summary of these basic quantities, including text references. Some of the quantities listed need additional explanation, which we now present.

For the PE model, we obtain ψ and χ as follows: From Eqs. (3-33a) and (3-33b) we can obtain

$$\nabla^2\psi = v_x - u_y$$

and

$$\nabla^2\chi = u_x + v_y \ ,$$

which in semi-discrete form is

$$\nabla^2\psi_1 = v_{1x} - u_{1y} \qquad (4\text{-}88a)$$

$$\nabla^2\psi_2 = v_{2x} - u_{2y} \qquad (4\text{-}88b)$$

$$\nabla^2\chi_1 = u_{1x} + v_{1y} \qquad (4\text{-}89a)$$

$$\nabla^2 \chi_2 = u_{2x} + v_{2y} \quad . \tag{4-89b}$$

Eqs. (4-88a) and (4-88b) are solved with $\psi_1 = 0$ and $\psi_2 = 0$, respectively, on the lateral boundaries; Eqs. (4-89a) and (4-89b) are solved with $\chi_{1n} = 0$ and $\chi_{2n} = 0$ on the lateral boundaries, where n is the derivative of χ perpendicular to the boundary.

For the QG model, the quantity $(\psi_1 - \psi_2)$ changes in time along the lateral boundary (see Holland, 1978). In order to compare with the PE model, we need to subtract this changing boundary value, so we use ψ^* in place of ψ as follows:

$$\psi_1^* \equiv \psi_1 - \psi_{1 \text{ boundary}} \tag{4-90a}$$

and

$$\psi_2^* \equiv \psi_2 - \psi_{2 \text{ boundary}} \quad . \tag{4-90b}$$

The vector velocity fields $\vec{v}_1$, $\vec{v}_{1D}$, $\vec{v}_{1R}$, $\vec{v}_2$, $\vec{v}_{2D}$, and $\vec{v}_{2R}$ are obtained by combining the x and y components:

$$\vec{v}_1 = (u_1, v_1) \tag{4-91a}$$

$$\vec{v}_{1D} = (\chi_{1x}, \chi_{1y}) \quad , \tag{4-91b}$$

$$\vec{v}_{1R} = (-\psi_{1y}, \psi_{1x}) \quad , \tag{4-91c}$$

$$\vec{v}_2 = (u_2, v_2) \quad , \tag{4-91d}$$

$$\vec{v}_{2D} = (\chi_{2x}, \chi_{2y}) \quad , \tag{4-91e}$$

and

$$\vec{v}_{2R} = (-\psi_{2y}, \psi_{2x}) \quad . \tag{4-91f}$$

The vertical velocity field w_2 in the QG model is obtained diagnostically from the semi-discrete form of Eq. (3-8):

$$w_2 = -(f_o/g')(J(\psi_1 - \psi_2, \psi^*) - (\psi_1 - \psi_2)_t) \ . \qquad (4\text{-}92)$$

Finally, the horizontal pressure variants $\tilde{p}_1$ and $\tilde{p}_2$ are obtained by 1) horizontally averaging Eqs. (A-19) and (A-20), and 2) subtracting the horizontal average of p_1 and p_2.

Table 4.1 Basic comparison quantities

PE MODEL QUANTITY No.	Symbol	TEXT REF. Eq. No.	QG MODEL QUANTITY No.	Symbol	TEXT REF. Eq. No.
1a	ψ_1	(4-88a)	1b	ψ_1^*	(4-90a)
2a	ψ_2	(4-88b)	2b	ψ_2^*	(4-90b)
3a	χ_1	(4-89a)			
3b	χ_2	(4-89b)			
4a	u_1	(4-21)			
4b	χ_{1x}	(3-33a)			
4c	$-\psi_{1y}$	(3-33a)	4d	$-\psi_{1y}$	(3-34a)
5a	u_2	(4-22)			
5b	χ_{2x}	(3-33a)			
5c	$-\psi_{2y}$	(3-33a)	5d	$-\psi_{2y}$	(3-34a)
6a	v_1	(4-23)			
6b	χ_{1y}	(3-33b)			
6c	ψ_{1x}	(3-33b)	6d	ψ_{1x}	(3-34b)
7a	v_2	(4-24)			
7b	χ_{2y}	(3-33b)			
7c	ψ_{2x}	(3-33b)	7d	ψ_{2x}	(3-34b)
8a	$\vec{v}_1$	(4-91a)			
8b	$\vec{v}_{1D}$	(4-91b)			
8c	$\vec{v}_{1R}$	(4-91c)	8d	$\vec{v}_{1R}$	(4-91c)
9a	$\vec{v}_2$	(4-91d)			
9b	$\vec{v}_{2D}$	(4-91e)			

Table 4.1 (continued)

PE MODEL QUANTITY No.	Symbol	TEXT REF. Eq. No.	QG MODEL QUANTITY No.	Symbol	TEXT REF. Eq. No.
9c	$\vec{v}_{2R}$	(4-91f)	9d	$\vec{v}_{2R}$	(4-91f)
10a	w_2	(3-74)	10b	w_2	(4-92)
11a	$\tilde{p}_1$	(A-19)			
11b	$f_o\tilde{\psi}_1$	(3-59)			
11c	$\tilde{p}_1-f_o\tilde{\psi}_1$		11d	$f_o\tilde{\psi}_1$	(3-59)
12a	$\tilde{p}_2$	(A-20)			
12b	$f_o\tilde{\psi}_2$	(3-64)			
12c	$\tilde{p}_2-f_o\tilde{\psi}_2$		12d	$f_o\tilde{\psi}_2$	(3-64)
13a	T_1	(4-29a)			
13b	T_2	(4-29b)			
14	T^*	(3-68)			
15a	σ	(3-77)			
15b	σ_o	(3-87)	15c	σ_o	(3-87)
15d	σ'	(3-83)			
16a	$\nabla^2 T^*$	(3-69)			
16b	$(2f_o/\alpha gH)$		16c	$(2f_o/\alpha gH)$	
	$*\nabla^2(\psi_1-\psi_2)$	(3-70)		$*\nabla^2(\psi_1-\psi_2)$	(3-70)
17a	K_1	(4-34a)			
17b	K_{1D}	(4-11)			
17c	K_{1R}	(4-3)	17d	K_{1R}	(4-3)

Table 4.1 (continued)

PE MODEL QUANTITY No.	Symbol	TEXT REF. Eq. No.	QG MODEL QUANTITY No.	Symbol	TEXT REF. Eq. No.
18a	K_2	(4-34b)			
18b	K_{2D}	(4-12)			
18c	K_{2R}	(4-4)	18d	K_{2R}	(4-4)
19a	P_R	(4-43)			
19b	P_{RQG}	(4-43a)	19c	P_{RQG}	(4-43a)
19d	P_{RLB}	(4-43b)			
20a	$\nabla^2\psi_1$	(3-45)	21a	$\nabla^2\psi_1$	(3-45)
20b	$\nabla^2\psi_2$	(3-46)	21b	$\nabla^2\psi_2$	(3-46)
22a	Q_1	(4-61)			
22b	Q_{1QG}	(4-59)	22c	Q_{1QG}	(4-59)
22d	Q_{1LB}	(4-60)			
23a	Q_2	(4-69)			
23b	Q_{2QG}	(4-67)	23c	Q_{2QG}	(4-67)
23d	Q_{2LB}	(4-68)			

CHAPTER 5. RESULTS OF THE SINGLE-GYRE EXPERIMENT

Two-layer versions of the QG and PE models were spun-up with fine-grid horizontal resolution (20 km) using a single-gyre wind-forcing in a 1000 x 1000 km basin. Both models used lateral Laplacian diffusion and no bottom friction. Biharmonic heat diffusion was used in the PE model. A summary of the parameters used in the experiment is given in Table 5.1. In this table, R_d is the internal radius of deformation, which, following Holland (1978), is defined as

$$R_d \equiv ((h_1 h_2 g')/(H f_o^2))^{1/2} \quad . \tag{5-1}$$

The initial state of the experiment consisted of a horizontally uniform temperature stratification with no motion. Eq. (4-44) provided the basis for making the stratifications consistent in the two models. Using the Holland (1978) choice of g' and the standard values g and α (given in Table 5.1), we find that the initial temperatures in the PE system are constrained by:

$$(T_1 - T_2)_o \equiv 13.06°C \quad . \tag{5-2}$$

We chose an initial temperature of 16.06°C for the upper layer and 3°C for the lower layer.

Table 5.1 Summary of parameters used in the single-gyre experiment

PARAMETER Symbol	Units	VALUE	MODEL
h_1	m	1000	Both
h_2	m	4000	Both
Δ	km	20	Both
L	km	1000	Both
D	km	1000	Both
A_M	$m^2 s^{-1}$	330	Both
B_H	$10^{-10} m^4 s^{-1}$	1.0	PE
B_H	$10^{-10} m^4 s^{-1}$	0.0	QG
C_B	$10^{-7} s^{-1}$	0.0	Both
τ_o	$10^{-4} m^2 s^{-1}$	1.0	Both
g'	$10^{-2} ms^{-2}$	2.0	QG
g	ms^{-2}	9.8	PE
α	$10^{-4} °C^{-1}$	2.0	PE
f_o	$10^{-5} \Delta^{-1}$	8.365	Both
β_o	$10^{-11} m^{-1} s^{-1}$	1.875	Both
R_d	km	48	Both
κ	$10^{-4} m^2 s^{-1}$	1.0	PE

5.1 Spin-up and statistical equilibrium

Figs. 5.1 and 5.2 show the time-dependent behavior of the energetics for the QG and PE models, respectively. Figs. 5.1A-C and 5.2A-C show the energetics for the total model simulation time, while Figs. 5.1D-F and 5.2D-F show the energetics for the final 1000 days. In Figs. 5.1A,D and 5.2A,D the kinetic energies in the two layers are shown as a function of time. Figs. 5.1B,E and 5.2B,E show the rates of energy transfer in the upper layer, and Figs. 5.1C,F and 5.2C,F the rates of energy transfer in the lower layer.

At time zero the wind stress is applied to the surface layer and the ocean begins to spin up. Because an impulsive start of the full wind stress excited high-amplitude Kelvin waves in the PE model, the wind stress was slowly increased in both models to its full amplitude over the first 30 days. This resulted in smaller-amplitude Kelvin waves in the PE model.

During the first 600 days the spin-up process is characterized by an increase in both the upper layer kinetic energy and the available potential energy (not shown). The lower layer remains nearly motionless. At about 600 days the available potential energy and the upper layer circulation have built up sufficiently for the flow to become baroclinically unstable. After ~600 days the release of available potential energy gives rise to eddy motions. As in Experiment 1 of Holland (1978), the eddies generate deep mean flows in the lower layer

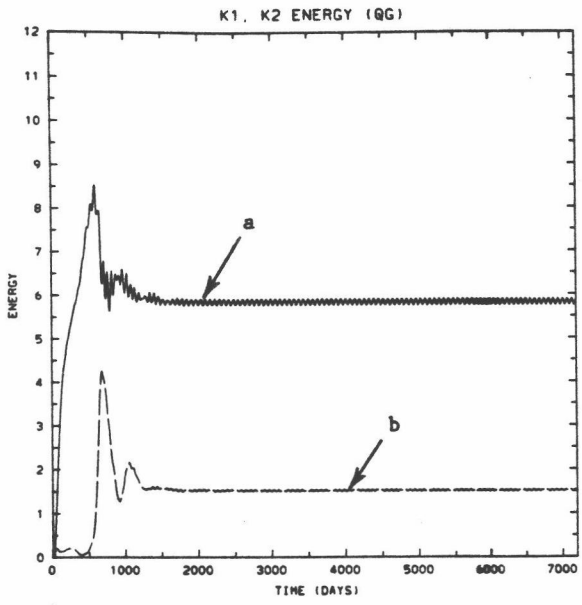

A

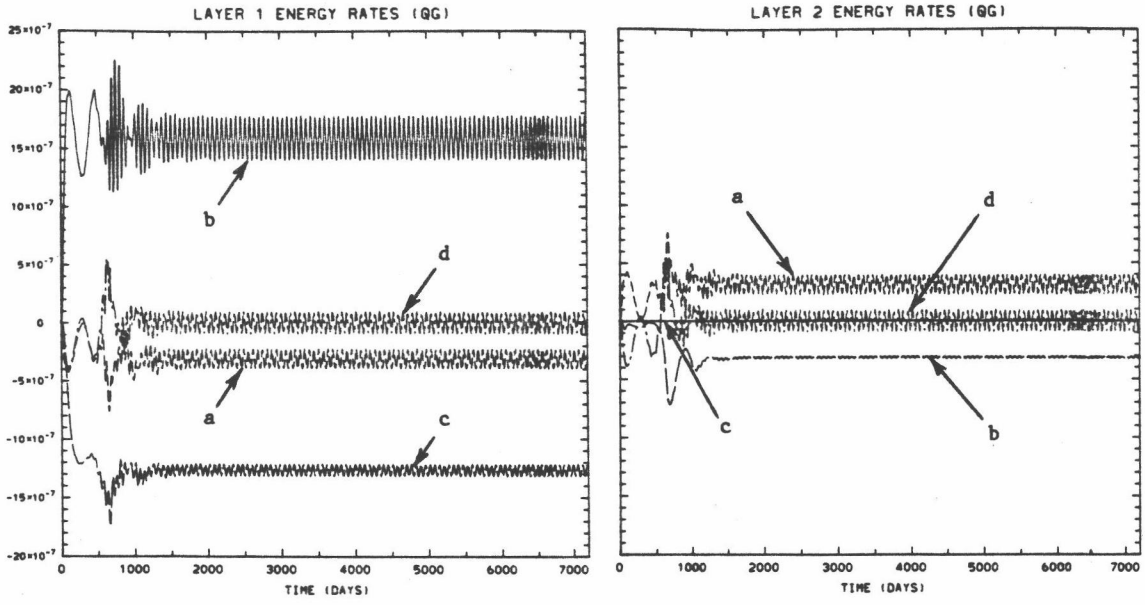

B C

Fig. 5.1 The time-dependent energetics for the QG single-gyre experiment. A) Energy per unit area showing: upper layer kinetic energy (a), lower layer kinetic energy (b). B) Energy fluxes into the upper layer: (a) $\{K_2 \rightarrow K_1\}$, (b) $\{\tau \rightarrow K_1\}$, (c) $\{K_1 \rightarrow D_{H1}\}$, (d) $\{P \rightarrow K_1\}$. C) Energy fluxes into the lower layer: (a) $\{K_1 \rightarrow K_2\}$, (b) $\{K_2 \rightarrow D_{H2}\}$, (c) $\{K_2 \rightarrow D_B\}$ (zero in this experiment) (d) $\{P \rightarrow K_2\}$.

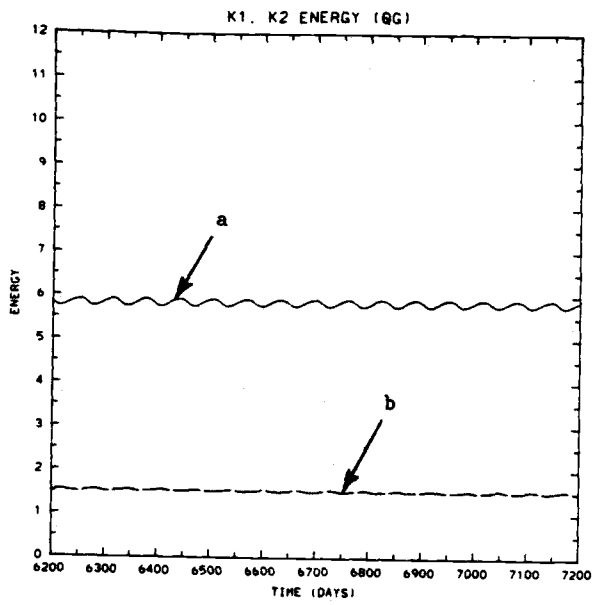

D

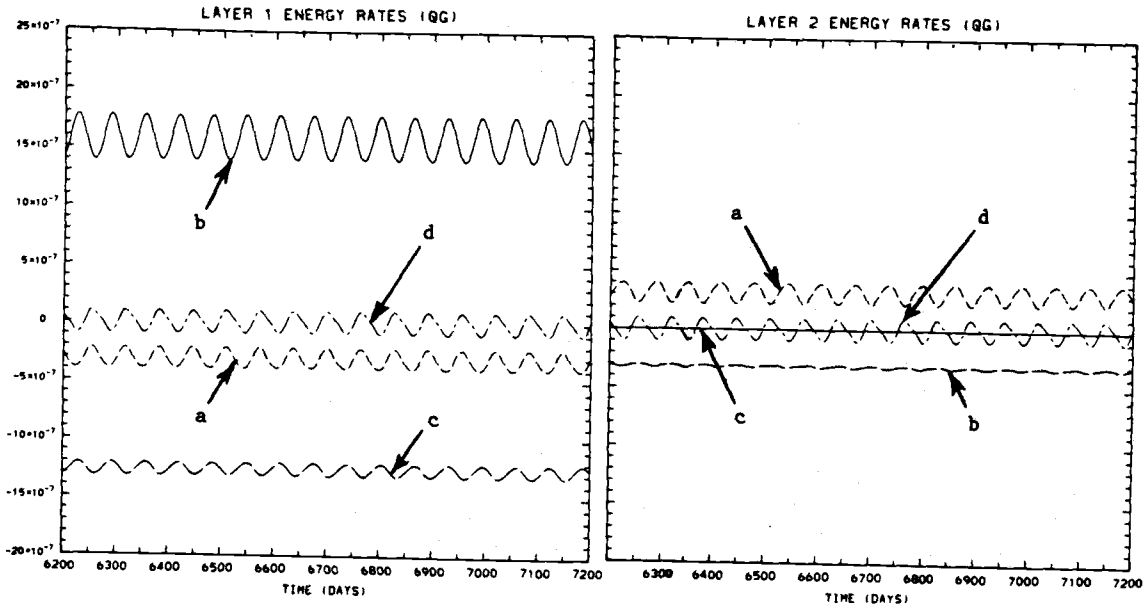

E F

Fig. 5.1 (cont.)
D), E), F) Same as A), B), C) but expanded time scale for the last 1000 days.

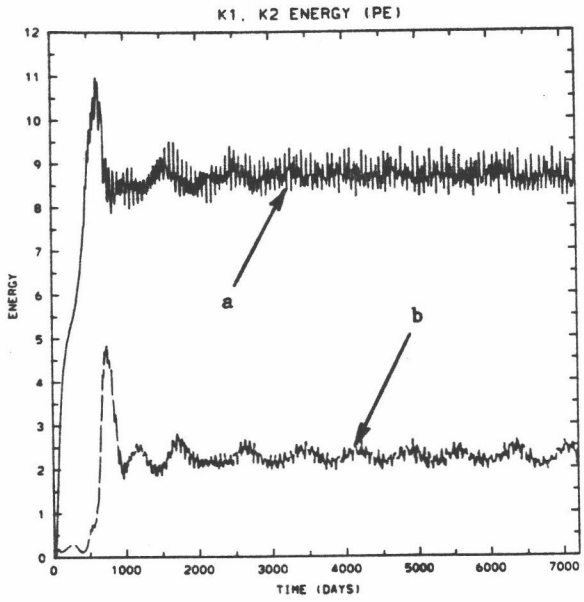

A

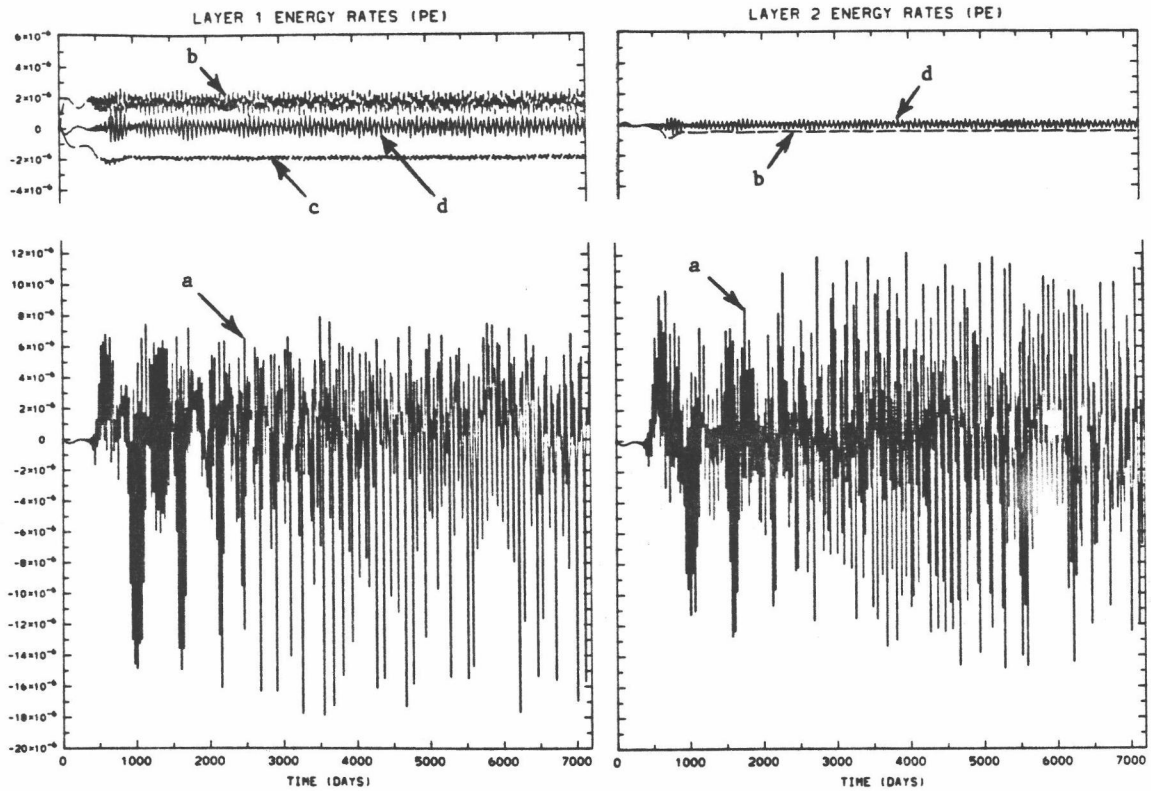

B C

Fig. 5.2 Same as Fig. 5.1, but for the PE experiment.

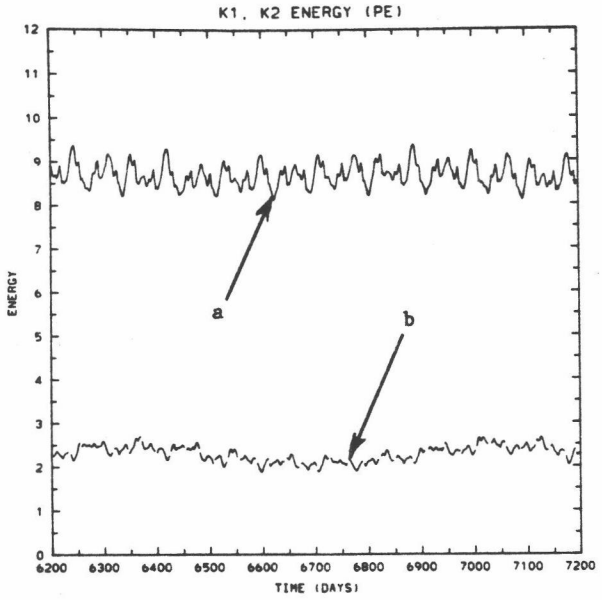

D

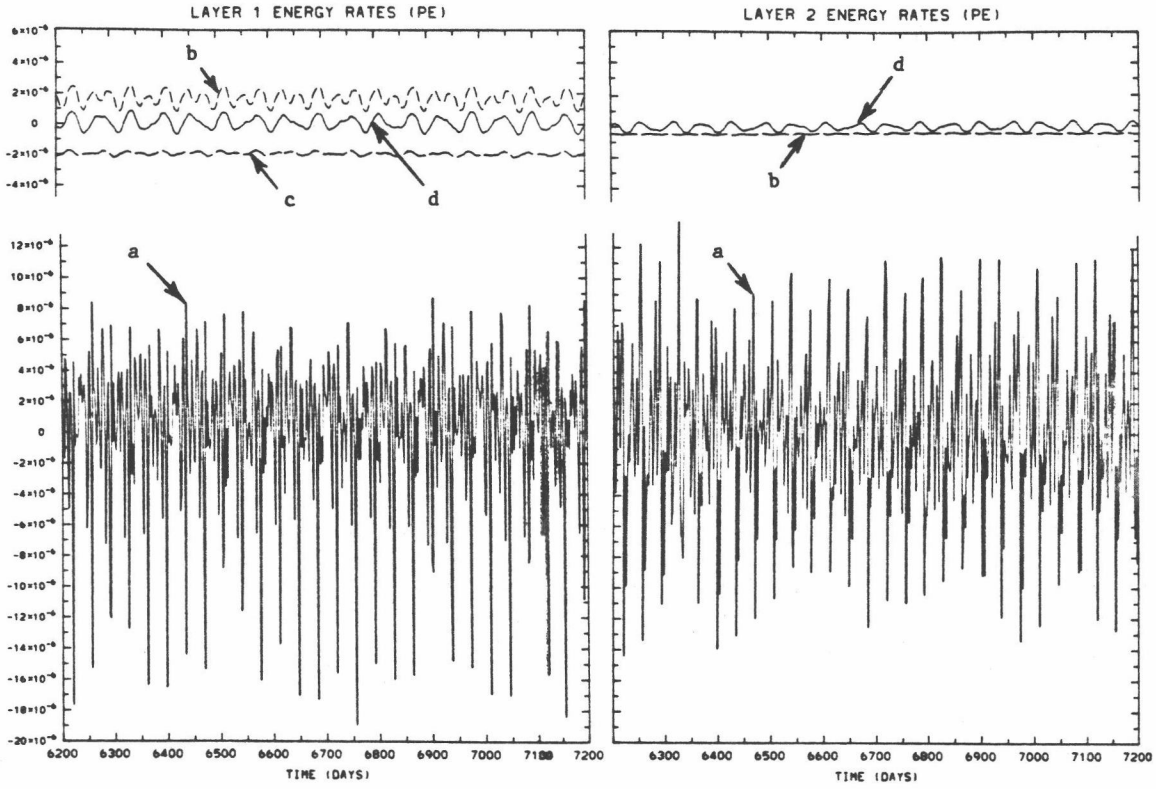

E F

Fig. 5.2 (cont.)

via energy transfers from the upper to the lower layer. After ~1500 days the system has come into statistical equilibrium in which eddies and the mean flow are in mutual balance.

The time scale for the energetic oscillations can be readily estimated from the expanded horizontal scale shown in Fig. 5.1D-F. Using the cyclic behavior of the wind energy input $\{\tau \rightarrow K_1\}$, we estimate a period of oscillation of about 62 days. This is close to the 64-day period both Holland and Lin (1975a) and Holland (1978) (Experiment 1) obtained, using eddy energy spectra.

A comparison of Figs. 5.1 and 5.2 shows similar energies and energy transfer rates. The main differences are: 1) the upper and lower layer kinetic energies are higher by about 35% for the PE model, and 2) the PE model has high frequency oscillations, due to the presence of Kelvin waves. Using the expanded horizontal scale in Fig. 5.2D-F, we estimate the periods of these oscillations to be 1.9 days. The low frequency oscillation of 62 days can also be seen in these figures. These results will be further analyzed in Section 5.4.

It should be noted that there are two time scales in the PE model, a fast-time and a long-term scale. The statistical equilibrium shown in Fig. 5.2 is for the fast-time scale adjustment process, i.e., at ~1500 days, the level of PE kinetic energy has reached a state of statistical equilibrium. On the long-term time scale, however, the PE experiment is not in equilibrium. The horizontally-averaged temperatures in each layer are

changing at constant rates throughout the experiment, i.e., 0.014°C per year for the upper layer and -0.003°C per year for the lower layer. The calculations of Bryan and Lewis (1979) have indicated that the ocean's diffusive relaxation scale is of the order of 1000 years, which is considerably longer than this experiment's time integration of 20 years.

5.2 Basic comparison quantities

The basic time-averaged PE and QG quantities are compared with each other in order to assess similarities and differences. The mean has been calculated as an average over the last five years using two-day sampling intervals. For the convenience of the reader, the quantities are presented in the order listed in Table 4.1, which also cites text references. Notes on the processing and plotting of the data can be found in Appendix B.

Fig. 5.3 shows the time-averaged upper layer streamfunctions. In both models the circulation patterns are quite similar. The subtropical anticyclonic gyre shows up as expected from the imposed surface wind stress pattern. Comparable nonlinear circulations near the northern wall are obtained. Over most of the basin interior, comparable, linear Sverdrup circulations are also obtained. The basic difference in the plots is the greater intensity of the subtropical high in the PE model.

Fig. 5.4 shows the time-averaged lower layer stream-

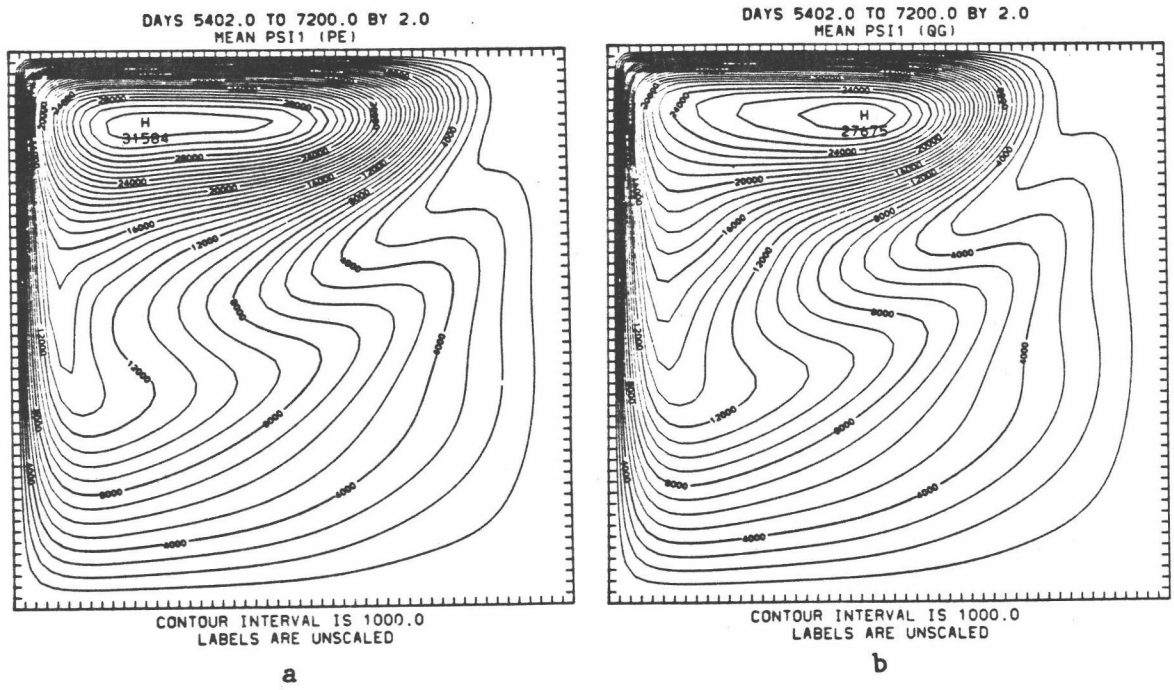

Fig. 5.3 Time-mean of entry 1 in Table 4.1: ψ_1 for a) PE, b) QG.

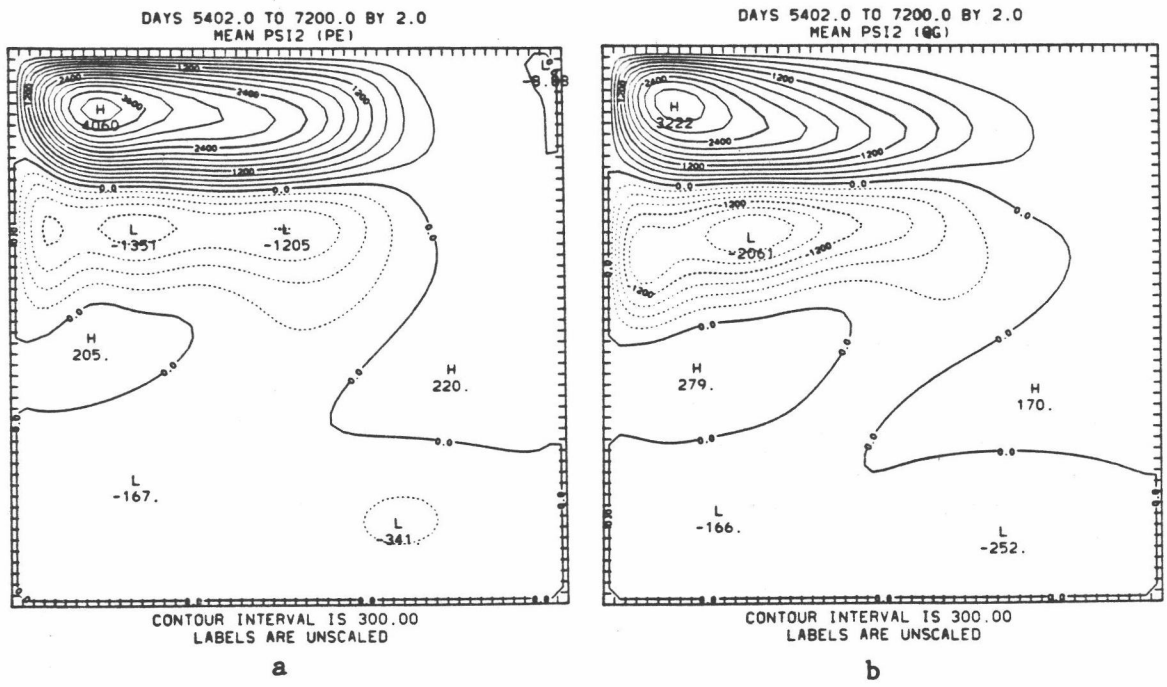

Fig. 5.4 Time-mean of entry 2 in Table 4.1: ψ_2 for a) PE, b) QG.

functions. Again, the circulation patterns are quite similar. As Holland (1978) has pointed out, since neither external stress nor interfacial friction acts on the lower layer, the deep mean circulation is driven entirely by the eddies. According to Holland and Rhines (1980), the lower layer is driven from above by inviscid pressure forcing at the interface; this is accompanied by downgradient potential vorticity flux everywhere in the lower layer.

The dominant feature in Figs. 5.4a and b is the presence of two gyres with alternating northward and southward flowing boundary layers. This feature of abyssal gyres is seen in many of Holland's (1978) experiments. Holland and Rhines (1980) have noted that the point on the western boundary dividing the northward and southward flowing boundary currents corresponds to where $\kappa \cdot \nabla \overline{Q}_2$ (here κ is the Lagrangian diffusivity and $\overline{Q}_2$ is the time-mean potential vorticity for the lower layer) takes its maxima, and assert that the presence of the two gyres arises from this maxima.

Fig. 5.5 shows the time-averaged velocity potential for the upper and lower layers of the PE model. Except for sign and scaling, χ_1 and χ_2 are really just the same quantity, and do not give independent information. Maximum values of the velocity potential are seen on the lateral boundaries. These are associated with counterclockwise-traveling Kelvin waves which 1) propagate along the boundaries with the phase speed of inertia-gravity waves, i.e., $c = (g' h_1 h_2 / H)^{1/2} = 4 \text{ m s}^{-1} \sim 400$

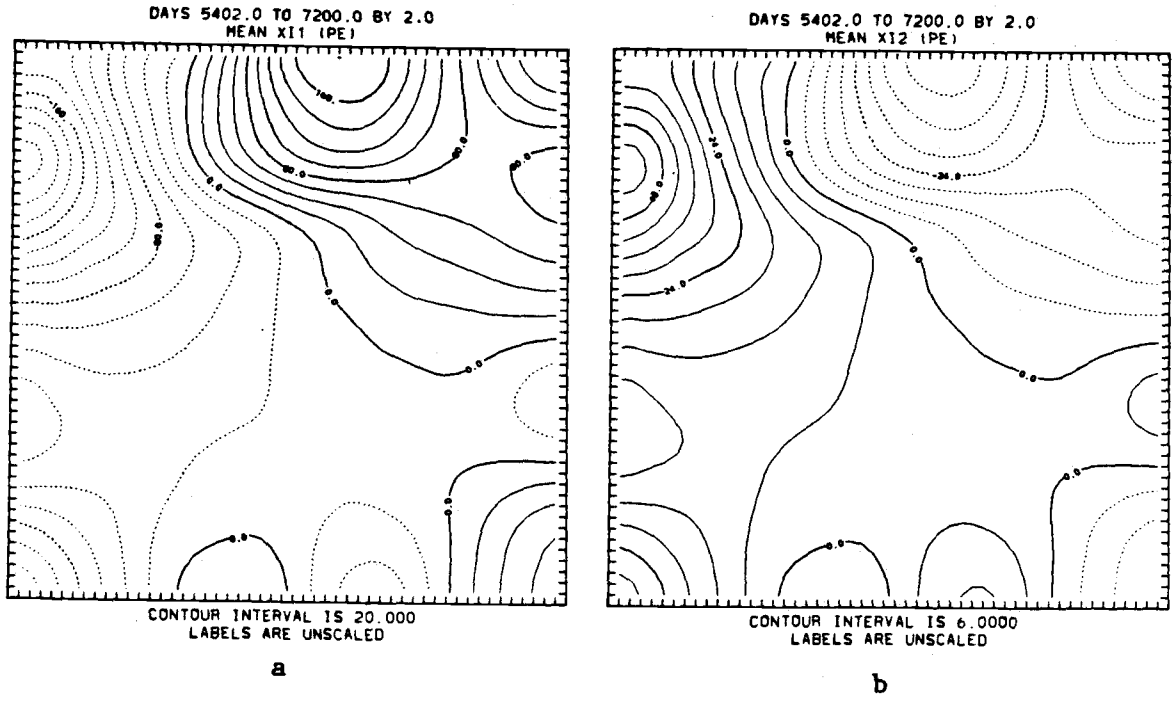

Fig. 5.5 Time-mean of entry 3 in Table 4.1: a) χ_1, b) χ_2.

km/day, and 2) decay exponentially away from the coast. A comparison of Fig. 5.5 with Figs. 5.3 and 5.4 shows that the velocity potential is much smaller in magnitude than either the upper or lower layer streamfunction.

It is not clear whether the patterns in Fig. 5.5 are the residual after time averaging or reflect aliasing due to the two-day sampling of 1.9-day period Kelvin waves. A longer time series and more frequent sampling may show that this divergence pattern will become even smaller upon time averaging.

Figs. 5.6 and 5.7 show the time-averaged zonal velocity for the upper and lower layer, respectively. Again, virtually all the same patterns are present in both models and only a slight difference (i.e., a few percent) in amplitude occurs. This difference is not due to an important divergent component of flow in the PE case.

Figs. 5.8 and 5.9 show the time-averaged meridional velocity for the upper and lower layers, respectively. In both layers there is comparable northward flow along the western boundary, and in the upper layer southward flow, indicative of a linear Sverdrup circulation, over most of the rest of the basin. In the lower layer there is also a comparable southward flow along the western boundary, indicative of deep western boundary currents that close the eddy-driven gyres. The divergent flow is still less than 1% of the total PE flow, and for all practical purposes is unimportant.

Figs. 5.10 and 5.11 show the time-averaged horizontal

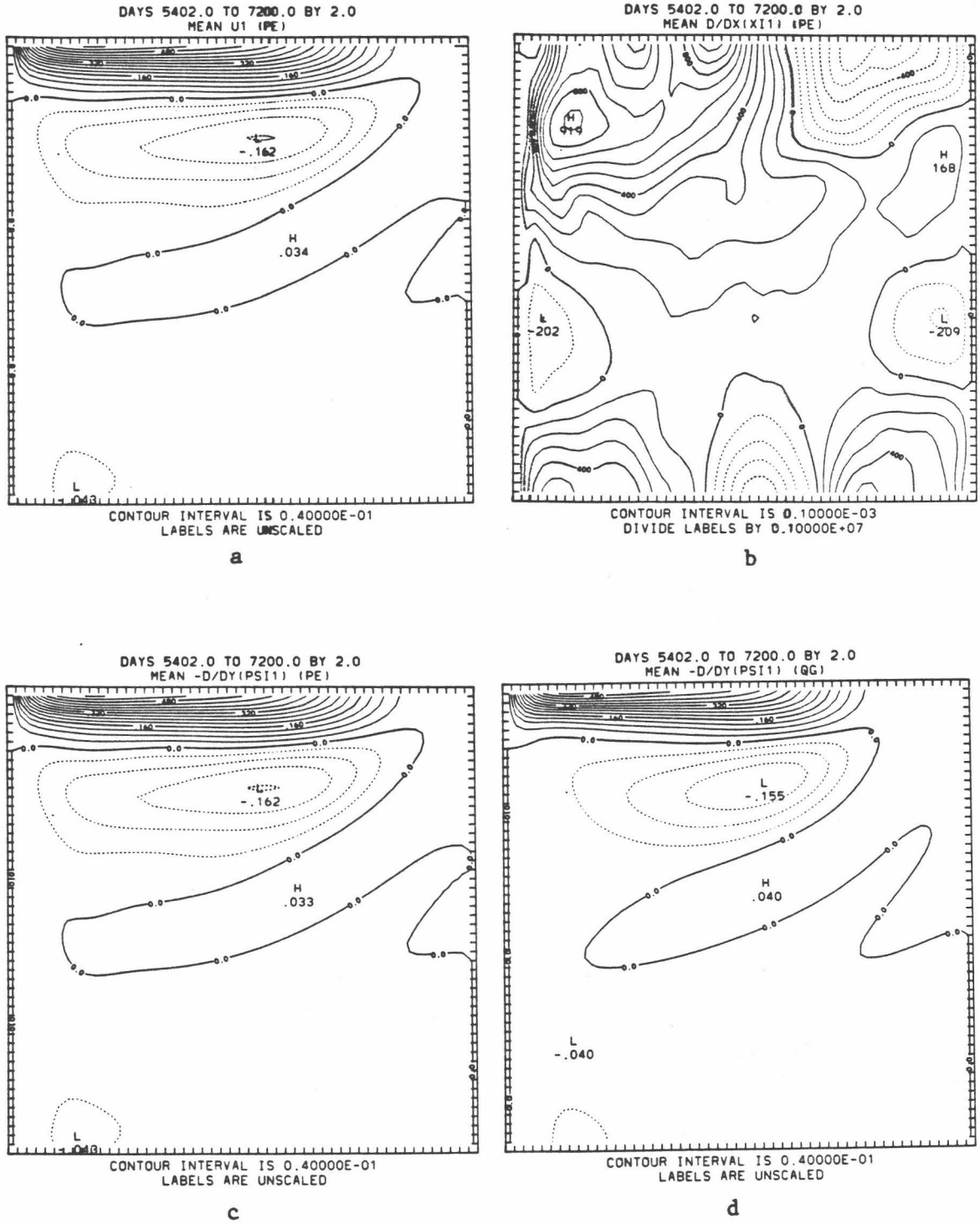

Fig. 5.6 Time-mean of entry 4 in Table 4.1: a) u_1, b) χ_{1x}, c) $-\psi_{1y}$ (PE), (d) $-\psi_{1y}$ (QG).

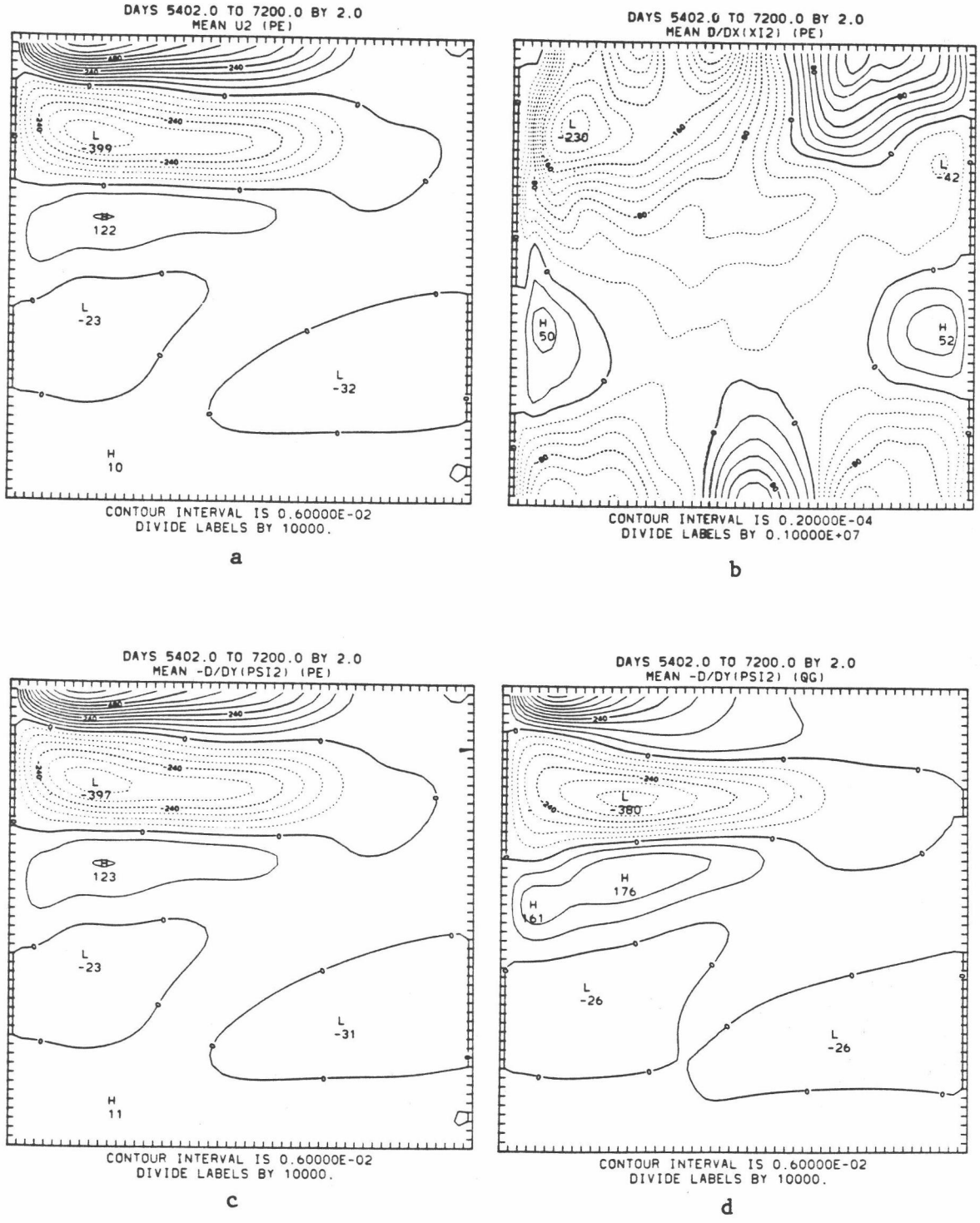

Fig. 5.7 Time-mean of entry 5 in Table 4.1: a) u_2, b) χ_{2x}, c) $-\psi_{2y}$ (PE), d) $-\psi_{2y}$ (QG).

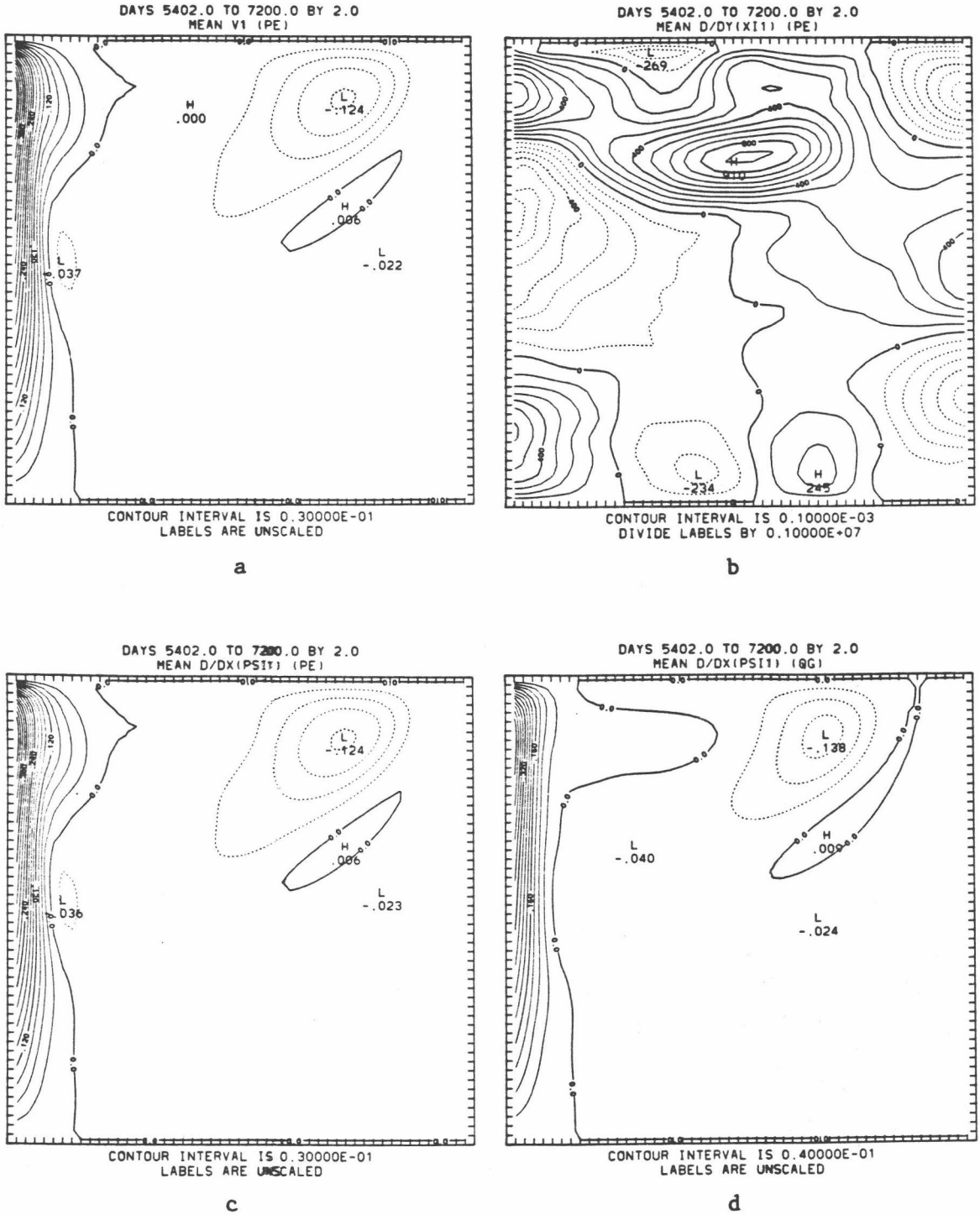

Fig. 5.8 Time-mean of entry 6 in Table 4.1: a) v_1, b) χ_{1y}, c) ψ_{1x} (PE), d) ψ_{1x} (QG).

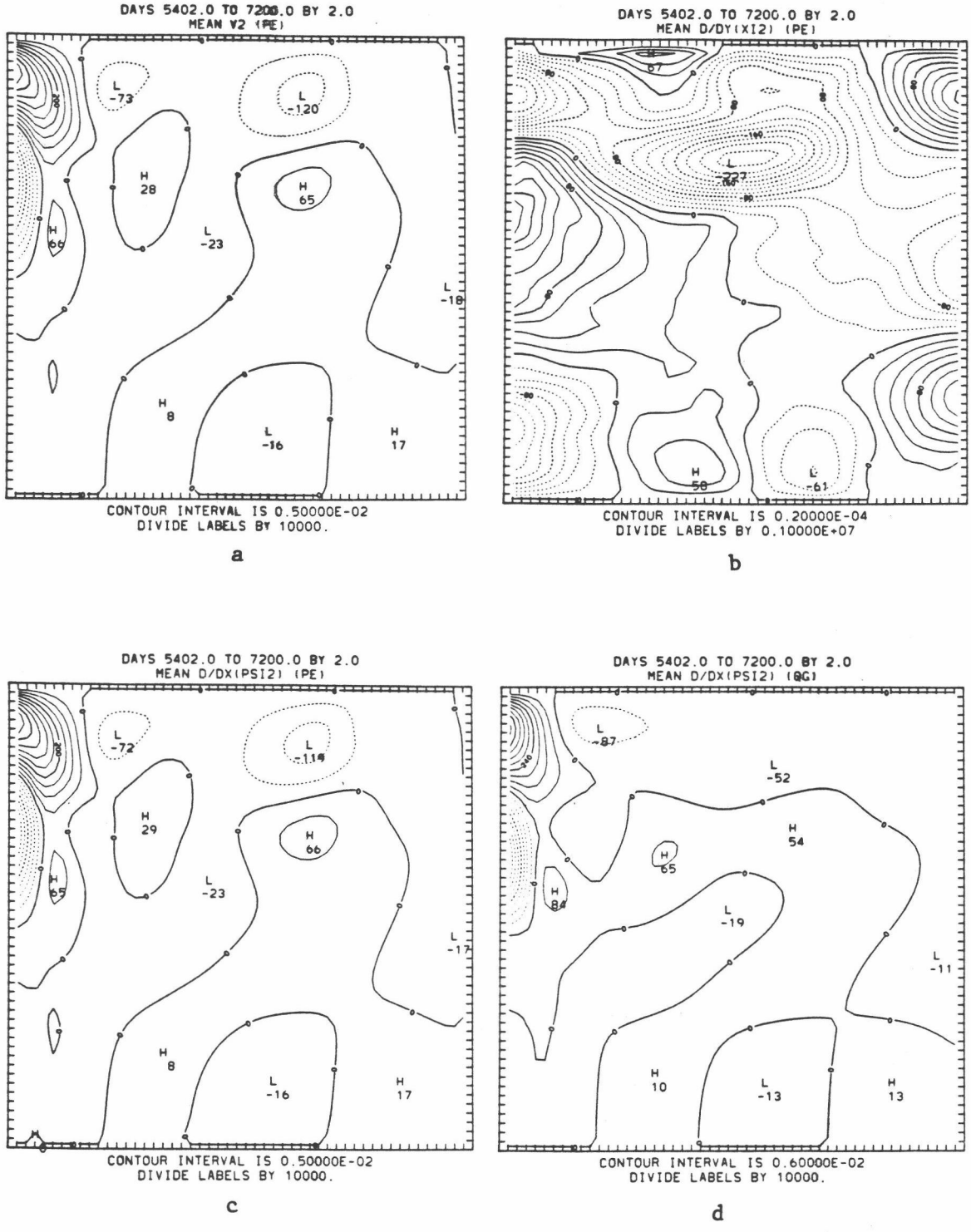

Fig. 5.9 Time-mean of entry 7 in Table 4.1: a) v_2, b) χ_{2y}, c) ψ_{2x} (PE), d) ψ_{2x} (QG).

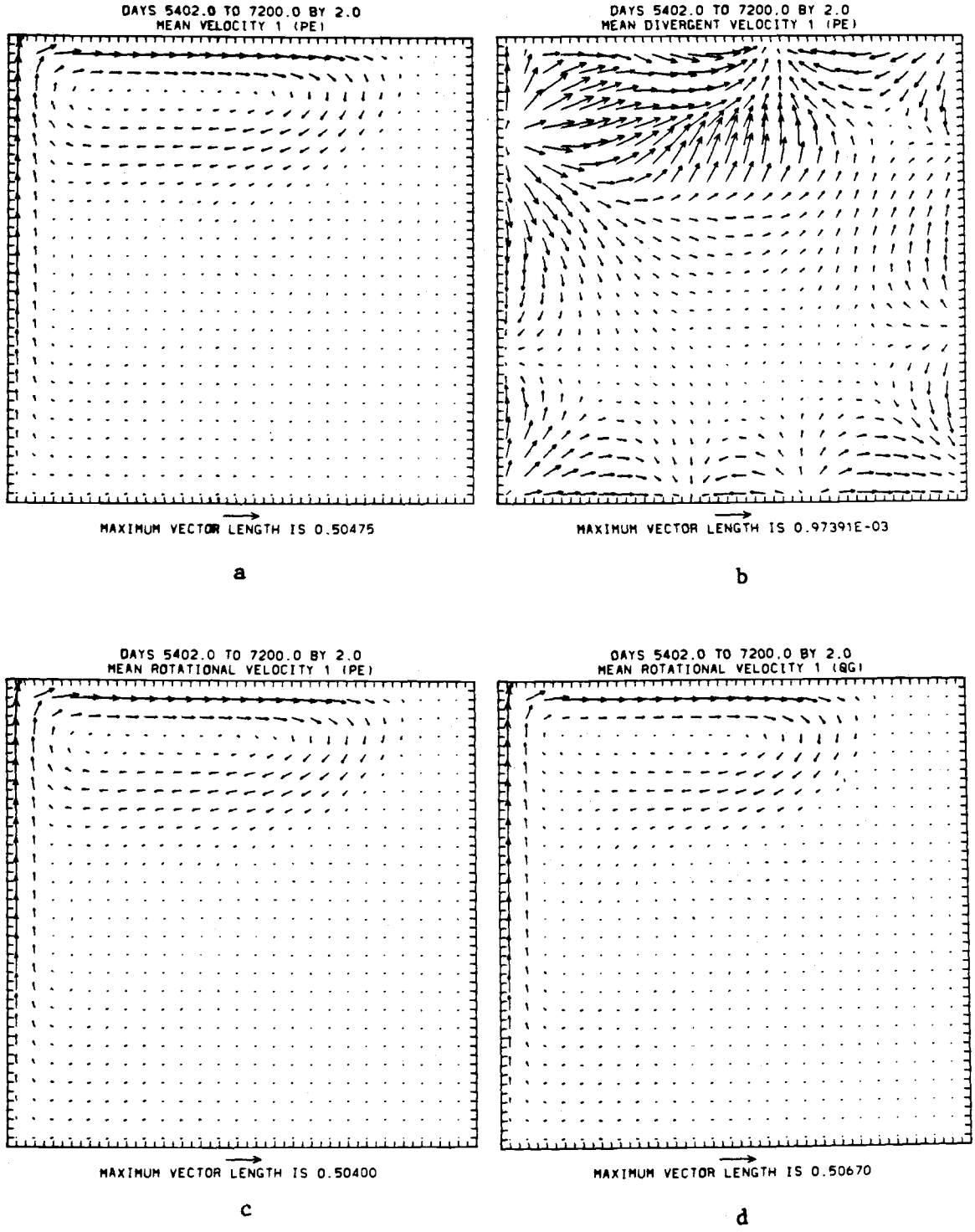

Fig. 5.10 Time-mean of entry 8 in Table 4.1: a) $\vec{v}_1$, b) $\vec{v}_{1D}$, c) $\vec{v}_{1R}$ (PE), d) $\vec{v}_{1R}$ (QG). Only every other velocity vector is plotted.

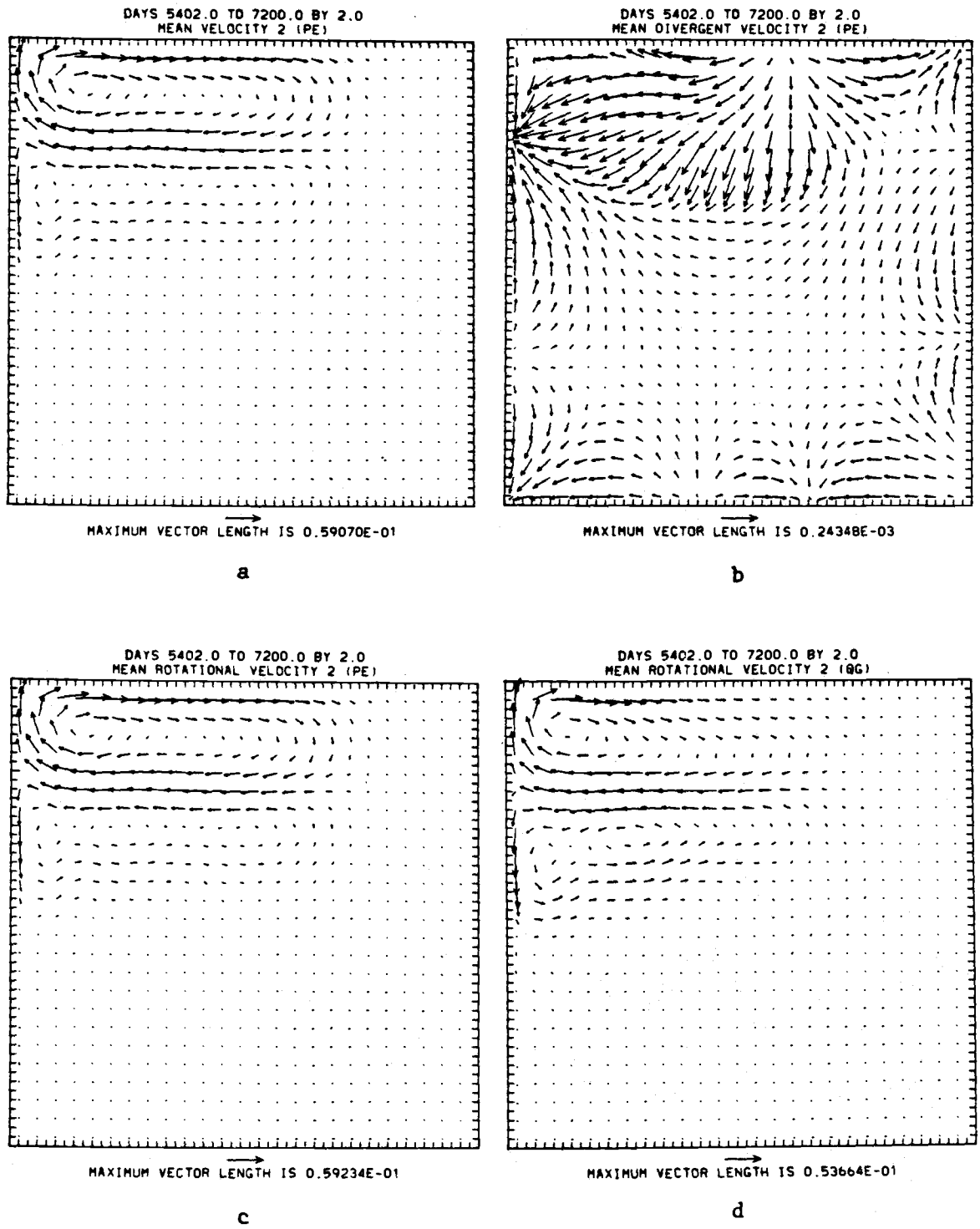

Fig. 5.11 Time-mean of entry 9 in Table 4.1: a) $\vec{v}_2$, b) $\vec{v}_{2D}$, c) $\vec{v}_{2R}$ (PE), d) $\vec{v}_{2R}$ (QG). Only every other velocity vector is plotted.

vector velocity fields for the upper and lower layers, respectively. In both layers, the same features discernible in the streamfunction plots are shown in vector form.

The vertical velocity is shown in Fig. 5.12. The strong upwelling on the southern edge of the recirculation region agrees with the results of McWilliams (1983), who analyzed the time-mean vertical velocity field on the southern edge of the Gulf Stream Recirculation Zone from data taken in the POLYMODE Local Dynamics Experiment. The upwelling and downwelling patterns seen in the westward recirculation region are consistent with baroclinic instability (Holland, 1978). The alternation of upwelling and downwelling near the western boundary could be related to offshore meanderings of the time-averaged flow (Han, 1975). The presence of alternating upwelling and downwelling areas on the southern and eastern boundaries in the PE model (Fig. 5.12a) could be due to either the time-averaged effects of the Kelvin waves of to strong aliasing with a two-day frequency.

The upper and lower layer pressure fields are shown in Figs. 5.13 and 5.14, respectively. Most of the upper and lower layer PE pressure fields are explained by the geostrophic streamfunction, shown in Figs. 5.13b and 5.14b. In the recirculation region, Figs. 5.13c and 5.14c suggest that other terms could become significant. In particular, terms with variable f could become important. Due to the small north-south extent of the basin, however, this is only a small effect here. A

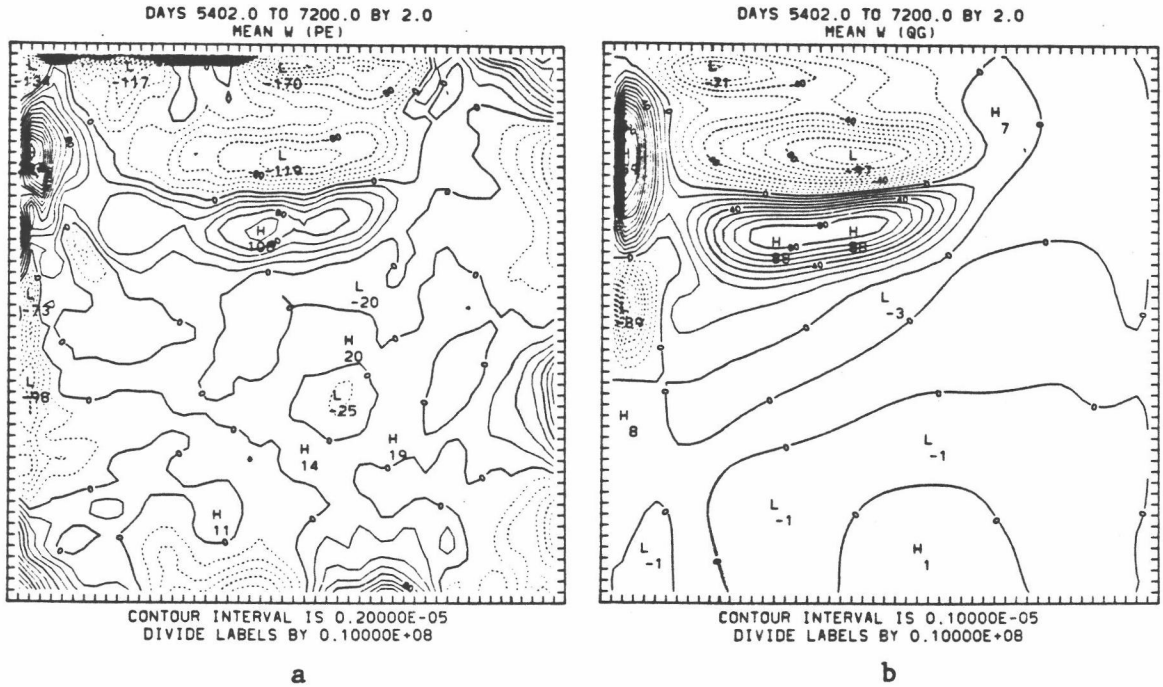

Fig. 5.12 Time-mean of entry 10 in Table 4.1: a) w_2 (PE), b) w_2 (QG).

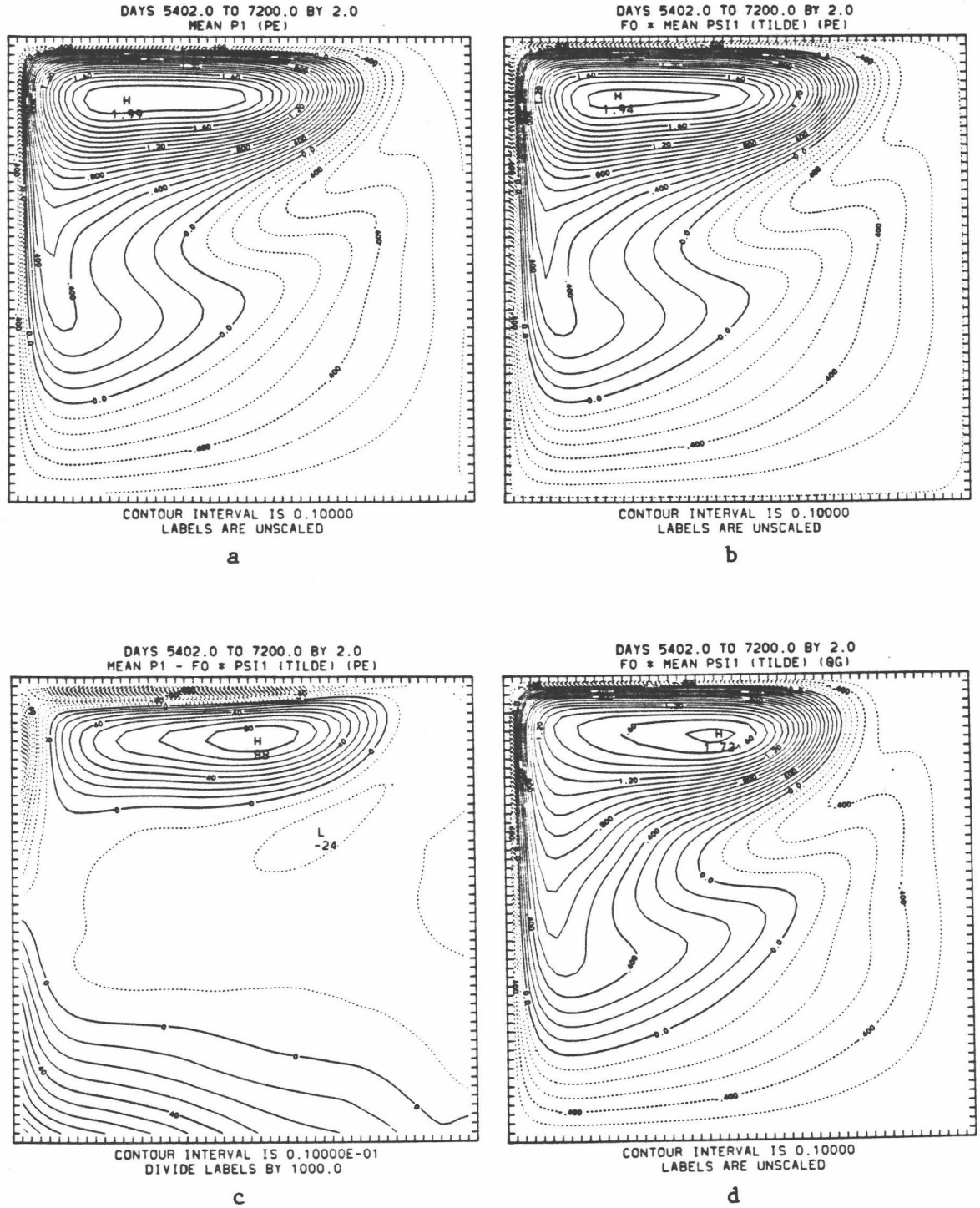

Fig. 5.13 Time-mean of entry 11 in Table 4.1: a) $\tilde{p}_1$, b) $f_o\tilde{\psi}_1$ (PE), c) $\tilde{p}_1 - f_o\tilde{\psi}_1$, d) $f_o\tilde{\psi}_1$ (QG).

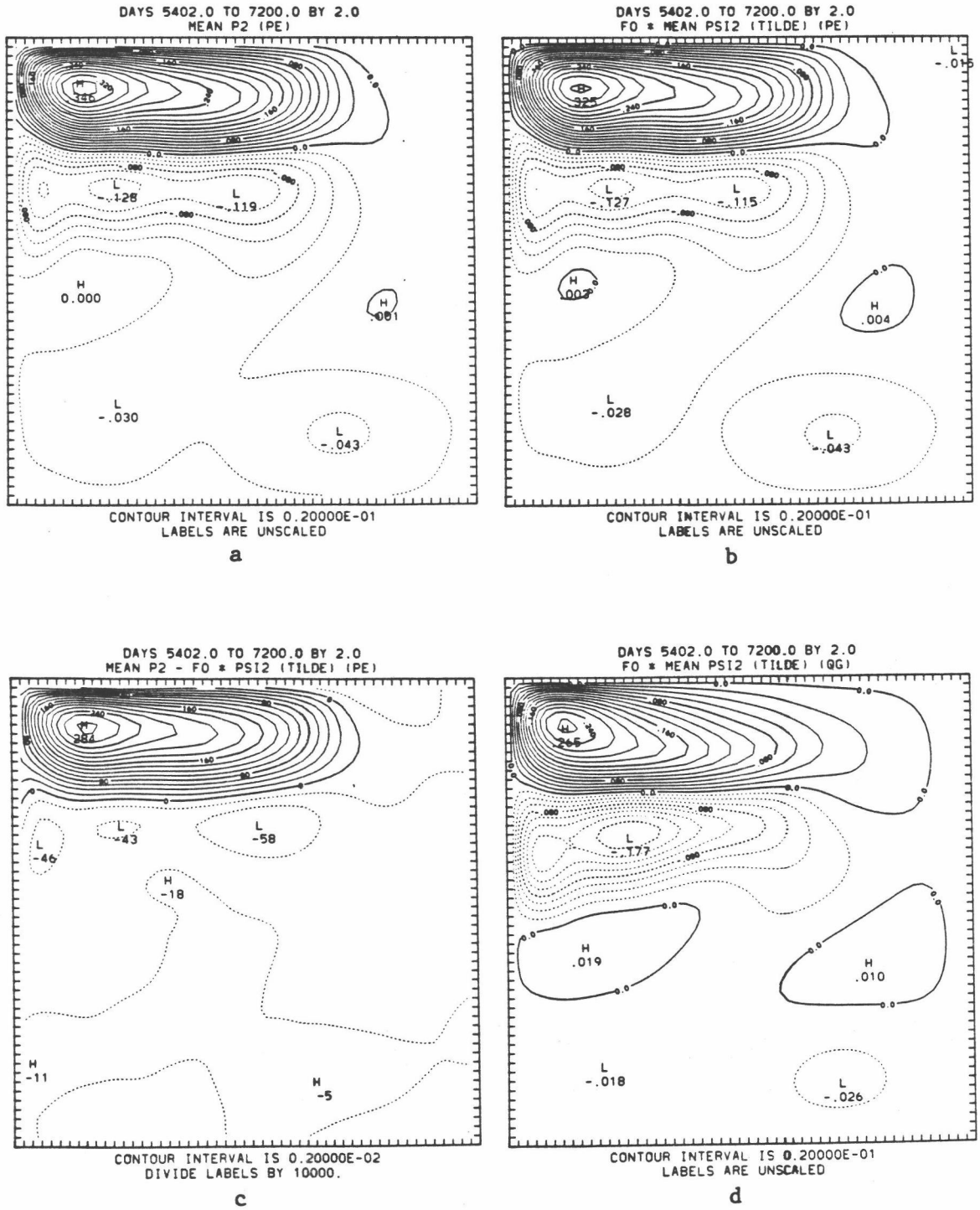

Fig. 5.14 Time-mean of entry 12 in Table 4.1: a) $\tilde{p}_2$, b) $f_o\tilde{\psi}_2$ (PE), c) $\tilde{p}_2 - f_o\tilde{\psi}_2$, d) $f_o\tilde{\psi}_2$ (QG).

comparison of Figs. 5.13 and 5.14 with Figs. 5.10 and 5.11, respectively, confirm the expected high degree of geostrophy.

The upper and lower layer time-averaged PE temperature fields are shown in Fig. 5.15, along with the average PE temperature and the per cent time change of PE static stability since the beginning of the experiment. In general, the temperature distribution in each layer corresponds to the streamfunction pattern (see Figs. 5.3 and 5.4). Notable exceptions to the dynamically-induced temperature distribution are seen in the areas of changing static stability (see Fig. 5.15d). The areas of changing static stability are simply a reflection of the fact that a long-term temperature adjustment is occurring, as discussed previously.

Lastly, the time-averaged thermal wind relationship is shown in Fig. 5.16. To a good approximation the thermal wind relationship is explained by the QG contribution (compare Figs. 5.16a and 5.16b).

5.3 Instantaneous, time mean and eddy fields

Fig. 5.17 shows the QG instanteous, time mean, and eddy fields for $f_o\psi_1$, $f_o\psi_2$, $\vec{v}_{1R}$ and $\vec{v}_{2R}$ at a particular instant in time. The mean has been calculated as an average over the last five years. A comparison of the upper layer mean and eddy quantities shows that the eddies and mean flow have about the same amplitude. A comparison of the lower layer

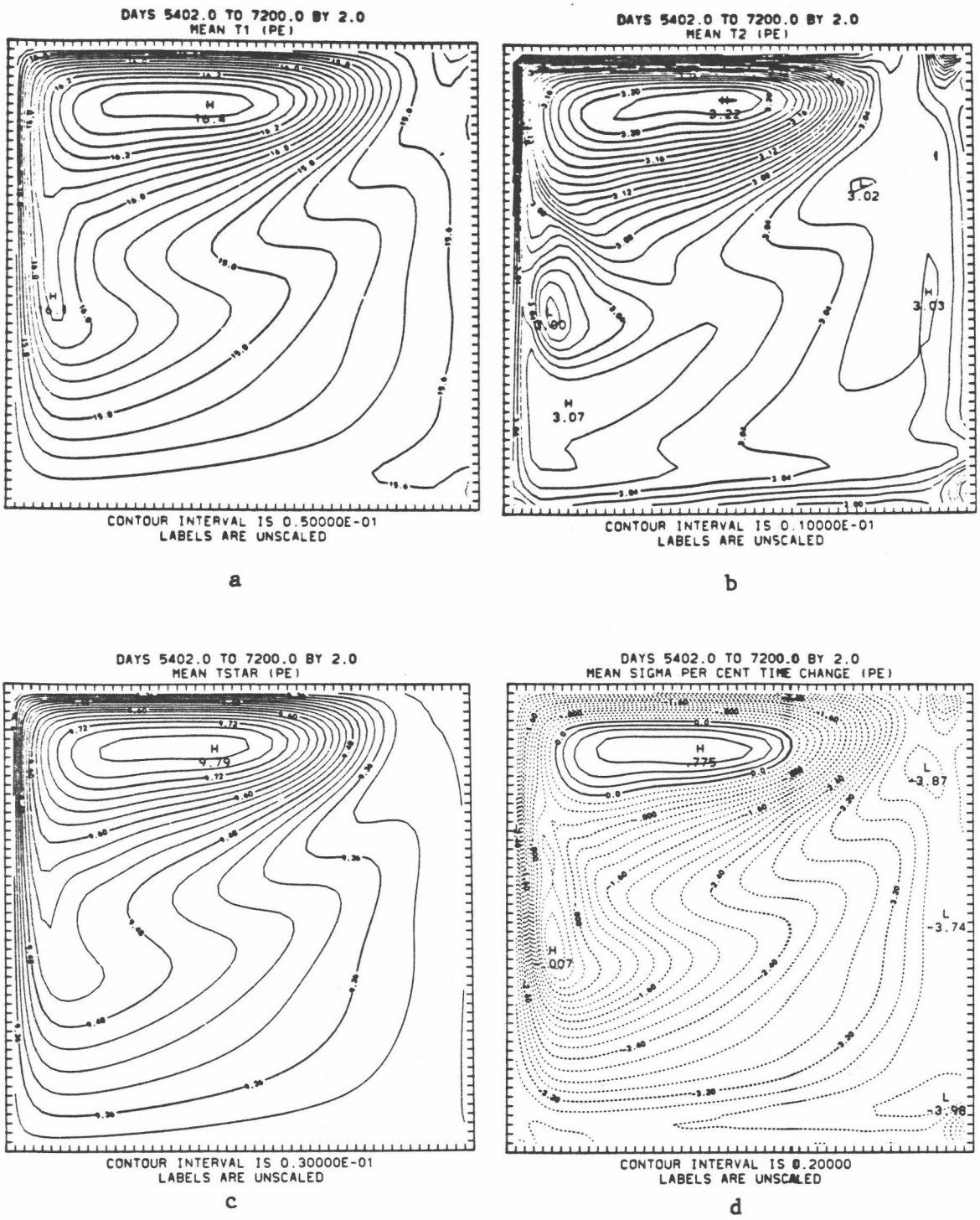

Fig. 5.15 Time-mean of entry 13 in Table 4.1: a) T_1, b) T_2, c) T* (entry 14 in Table 3.1), d) σ (entry 15 in Table 4.1).

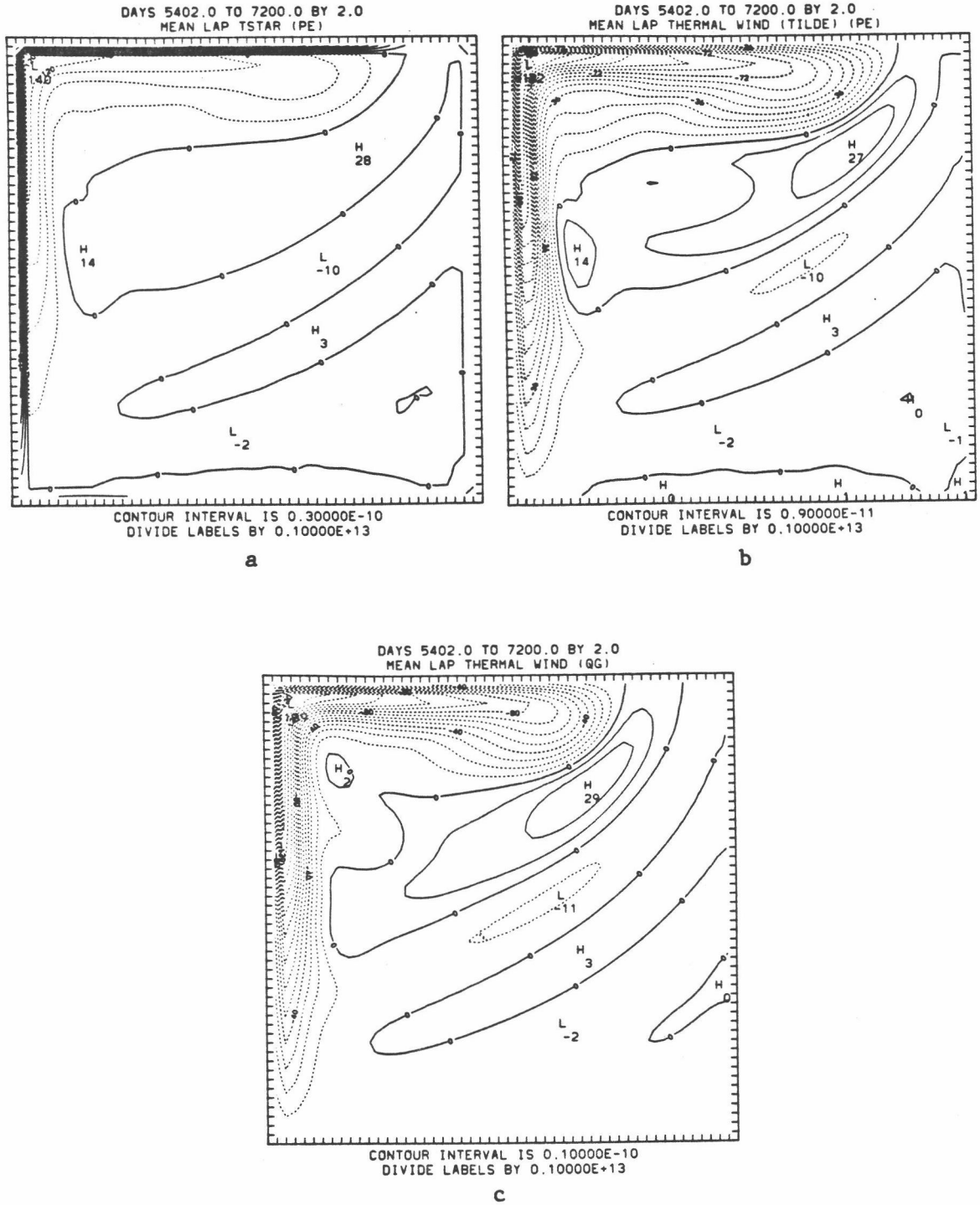

Fig. 5.16 Time-mean of entry 16 in Table 4.1: a) $\nabla^2 T^*$, b) $(2f_o/\alpha gH)\nabla^2(\psi_1-\psi_2)$ (PE), c) same as b) but for the QG model.

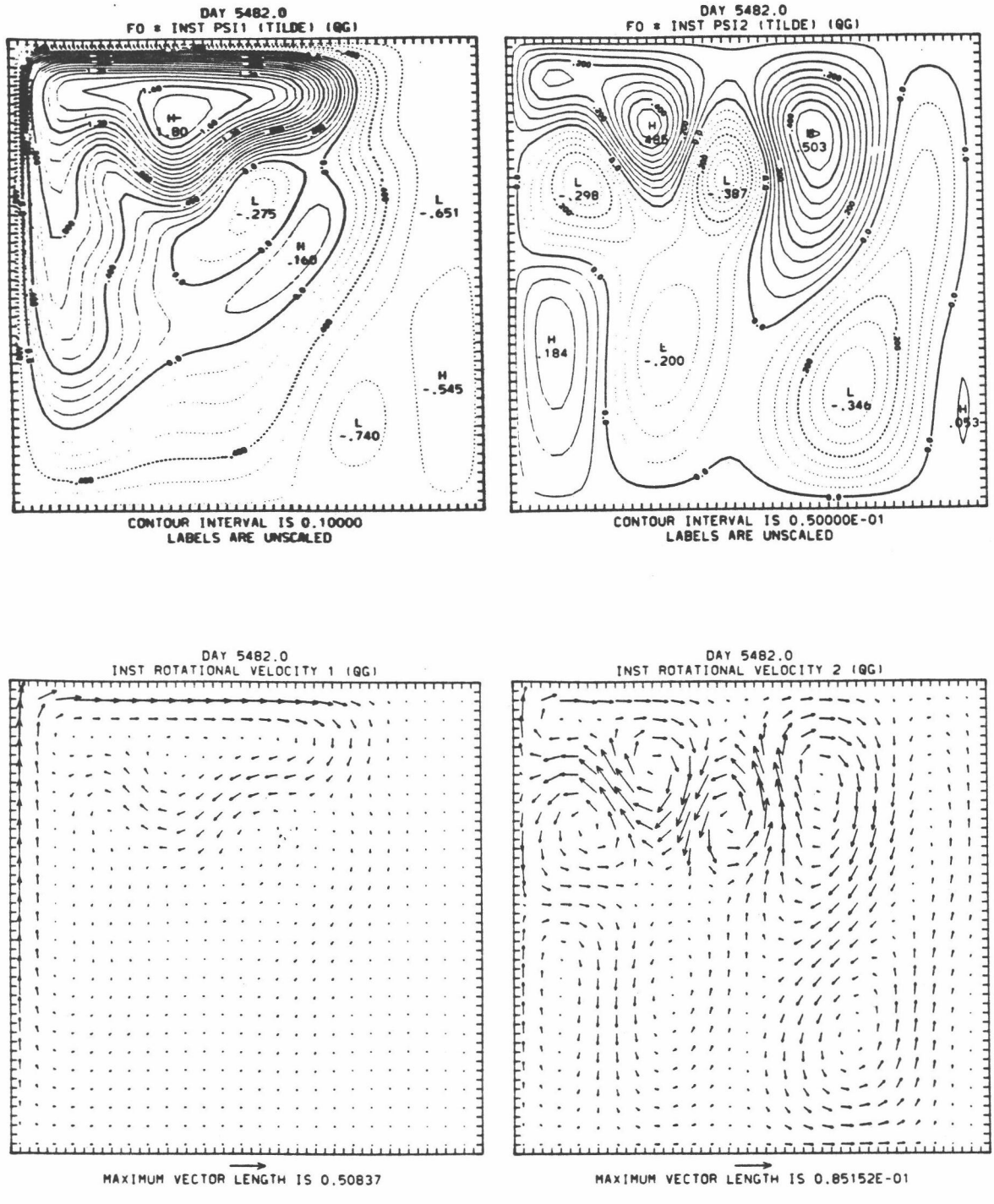

a

Fig. 5.17 The $f_o\psi_1$, $f_o\psi_2$, $\vec{v}_{1R}$, v_{2R} fields for the QG model: a) instantaneous, b) time mean, and c) eddy.

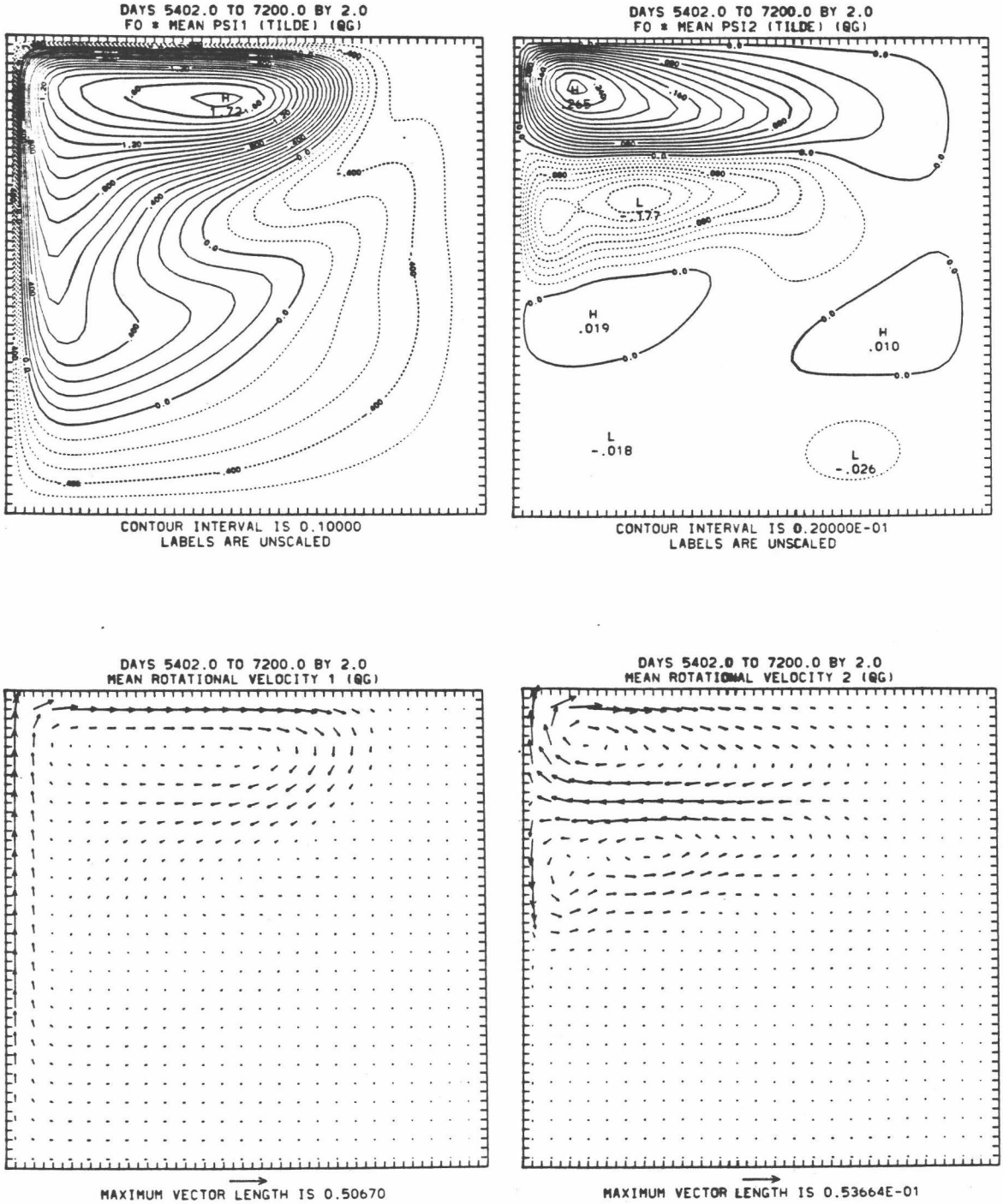

b

Fig. 5.17 (cont.)

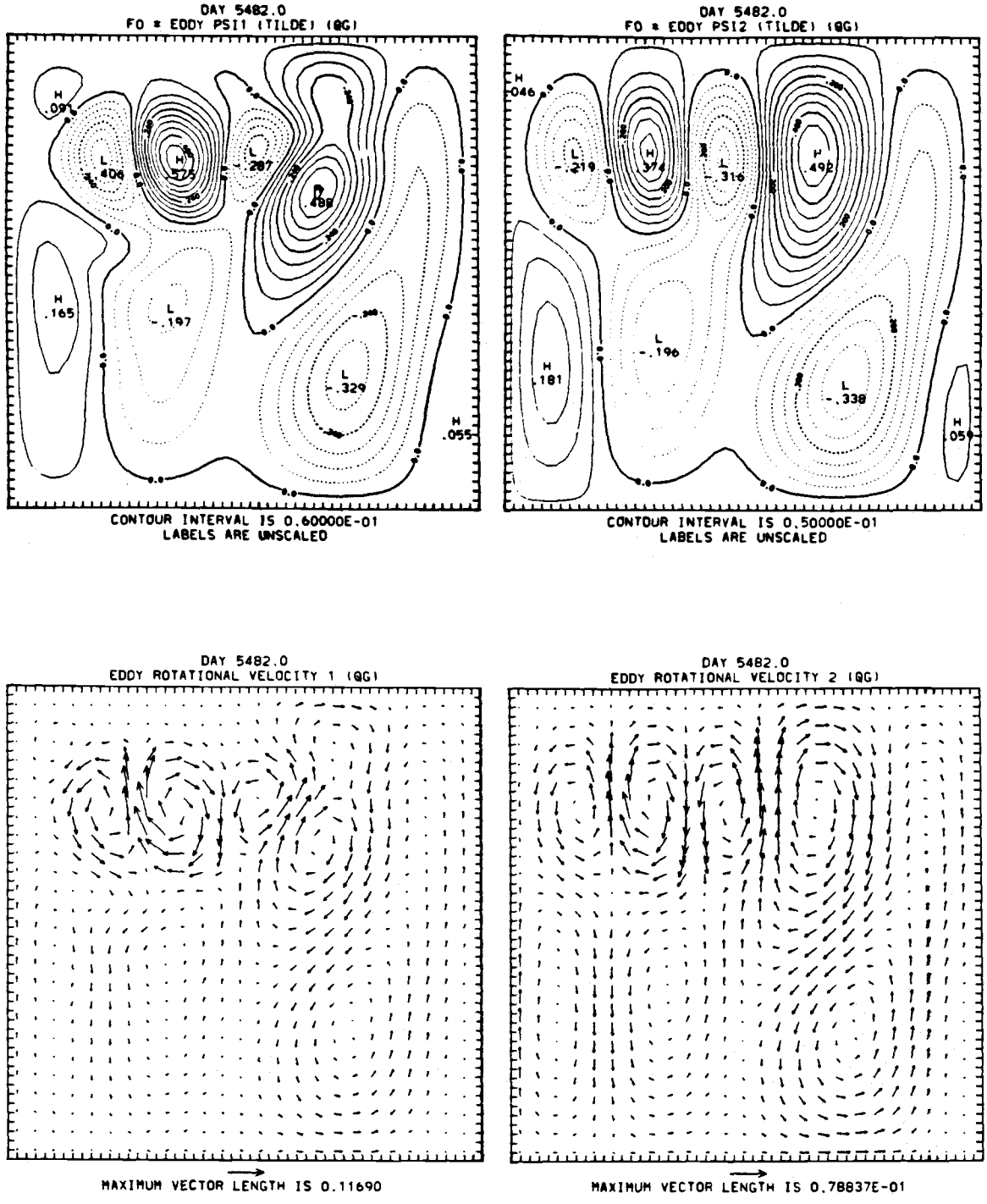

c

Fig. 5.17 (cont.)

quantities show that the eddies are dominant. As stated previously and as Holland (1978) and Holland and Lin (1975a) have noted, since there is no direct mean driving of the lower layer, the lower layer mean circulation is driven by the eddies.

Fig. 5.18 shows the PE instantaneous, time mean, and eddy fields for p_1, p_2, $\vec{v}_1$ and $\vec{v}_2$ at a particular instant in time. A comparison of Figs. 5.17 and 5.18 shows similar patterns, except that the boundary-trapped Kelvin waves in the PE experiment are absent in the QG experiment. The mean horizontal velocities show no hint of a divergent component. This is to be expected since the mean dynamical velocity is much smaller than the mean rotational velocity. In the eddy velocity fields, however, the Kelvin waves are comparable to the mesoscale eddies.

Fig. 5.19 shows eddy maps of $f_o\psi_1$, $f_o\psi_2$, $v_{1\vec{R}}$, and $\vec{v}_{2R}$ at 8-day intervals for the QG model. The mesoscale eddies propagate westward at ~5.5 km per day. In the northern half of the basin, the eddies have a basic wavelength of ~450 km (eddy diameter ~225 km), while in the southern half of the basin, the eddies have a larger wavelength. If Figs. 5.19a and 5.19b are overlaid, it is seen that 1) in the northern half of the basin, there is a tilt in the vertical, consistent with baroclinic instability, with the upper layer eddies lagging the lower layer eddies, and 2) in the southern half, there is little, if any, tilt, so that the eddies are very nearly barotropic. This basic eddy structure agrees well with that of Holland (1978) and Holland and Lin (1975a).

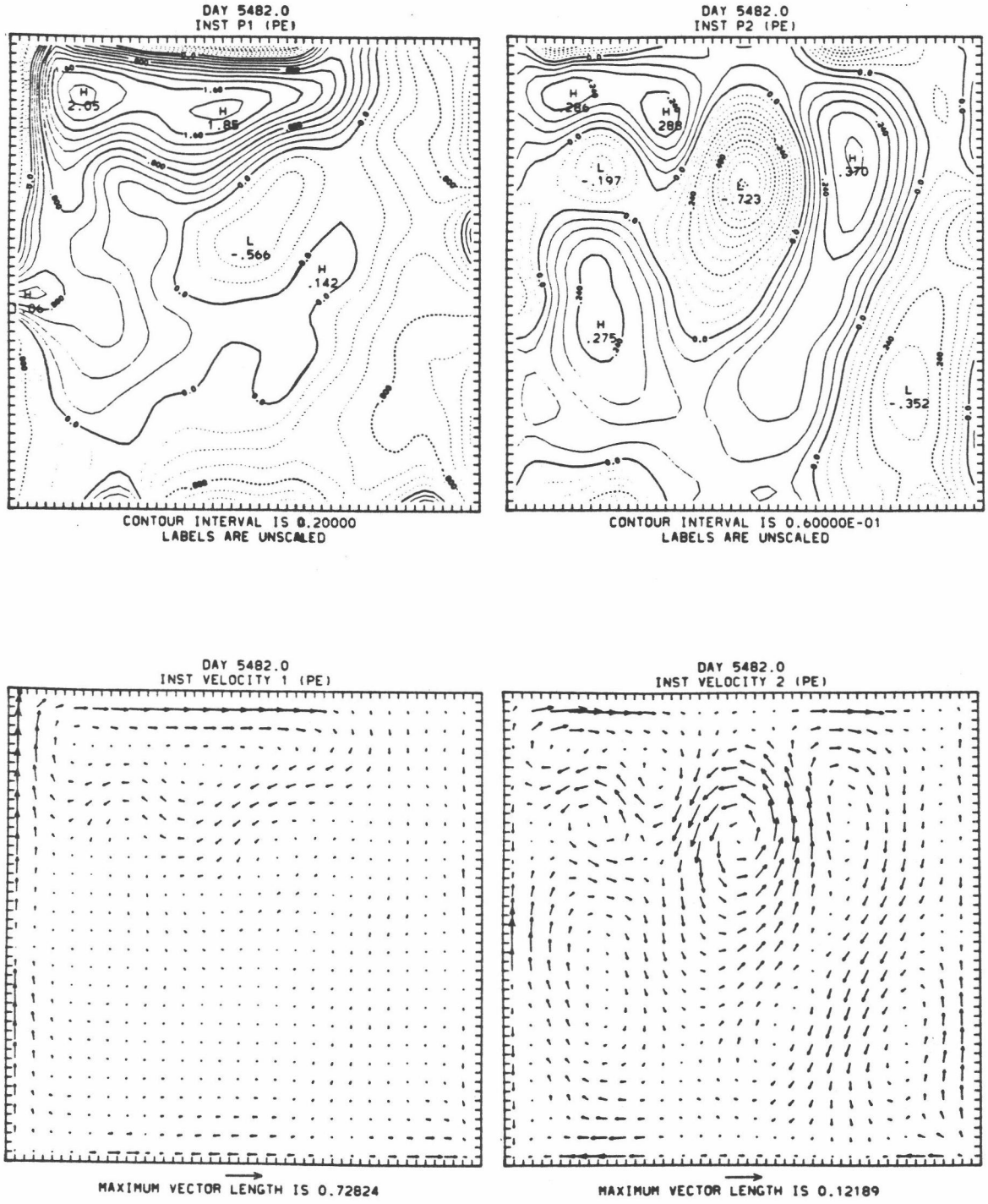

a

Fig. 5.18 The p_1, p_2, $\hat{\mathbf{v}}_1$, $\hat{\mathbf{v}}_2$ fields for the PE model: a) instantaneous, b) time mean, and c) eddy.

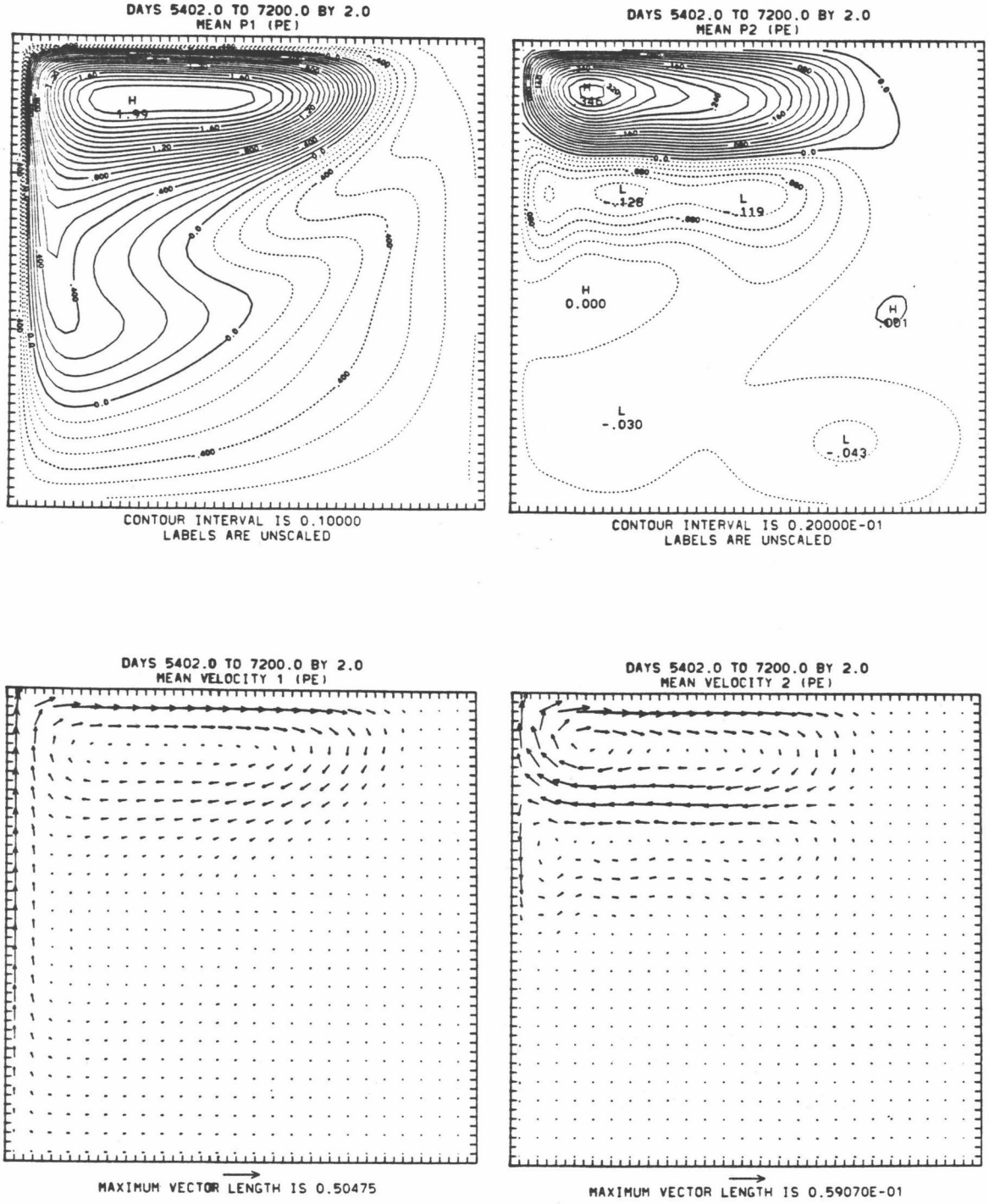

b

Fig. 5.18 (cont.)

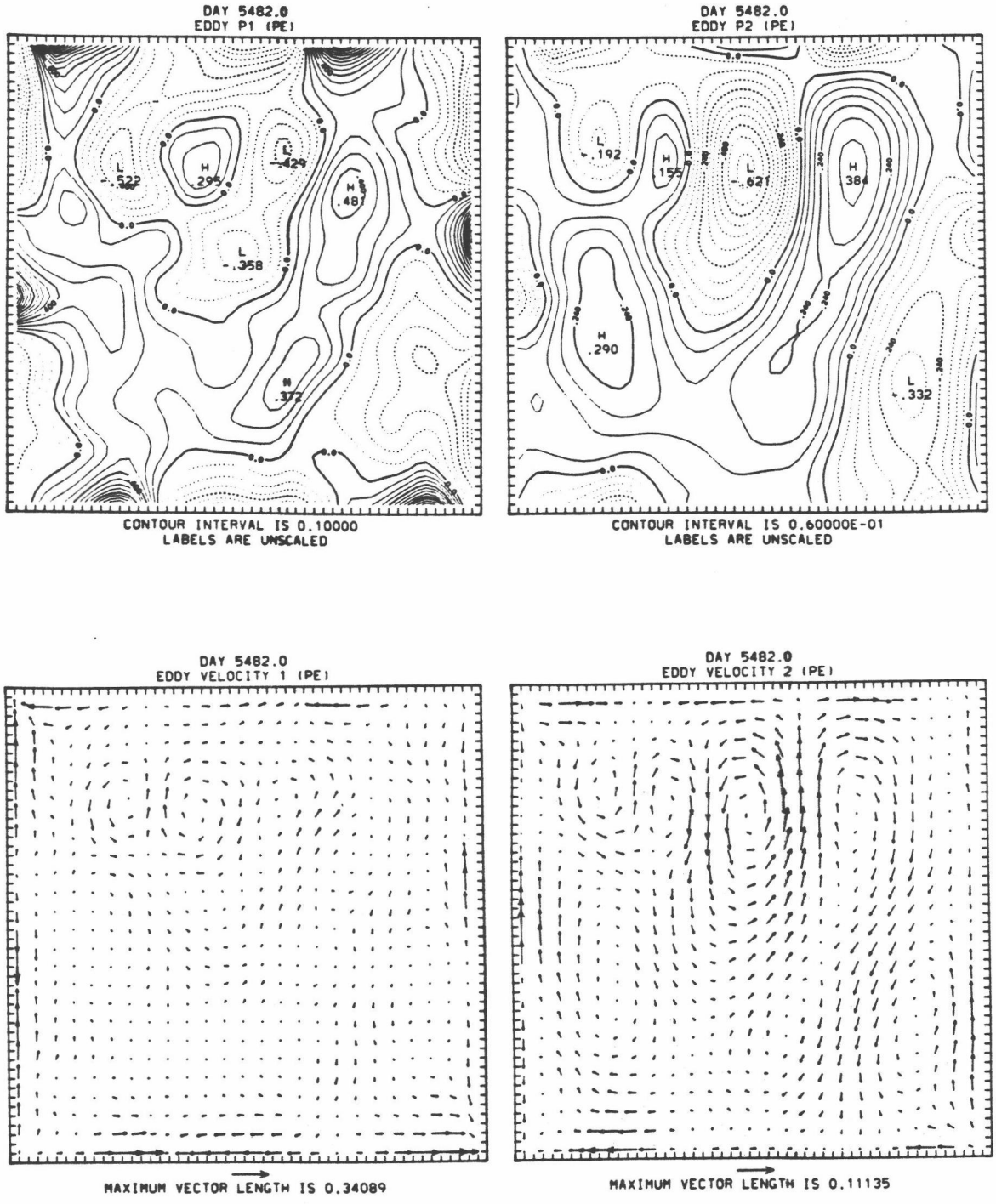

c

Fig. 5.18 (cont.)

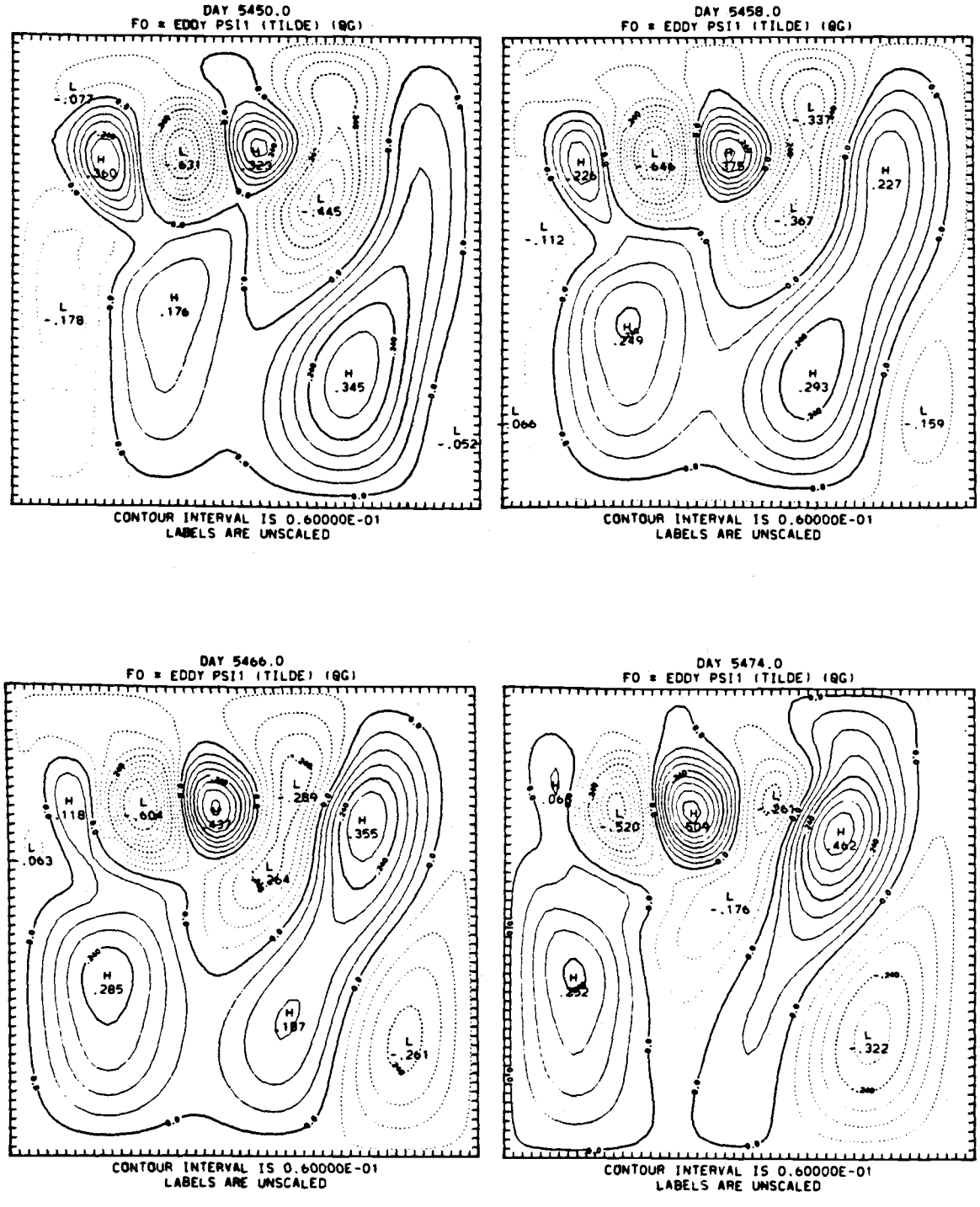

a

Fig. 5.19 The QG eddy fields at 8-day intervals for a) $f_o\psi_1$, b) $f_o\psi_2$, c) $\vec{v}_{1R}$, d) $\vec{v}_{2R}$.

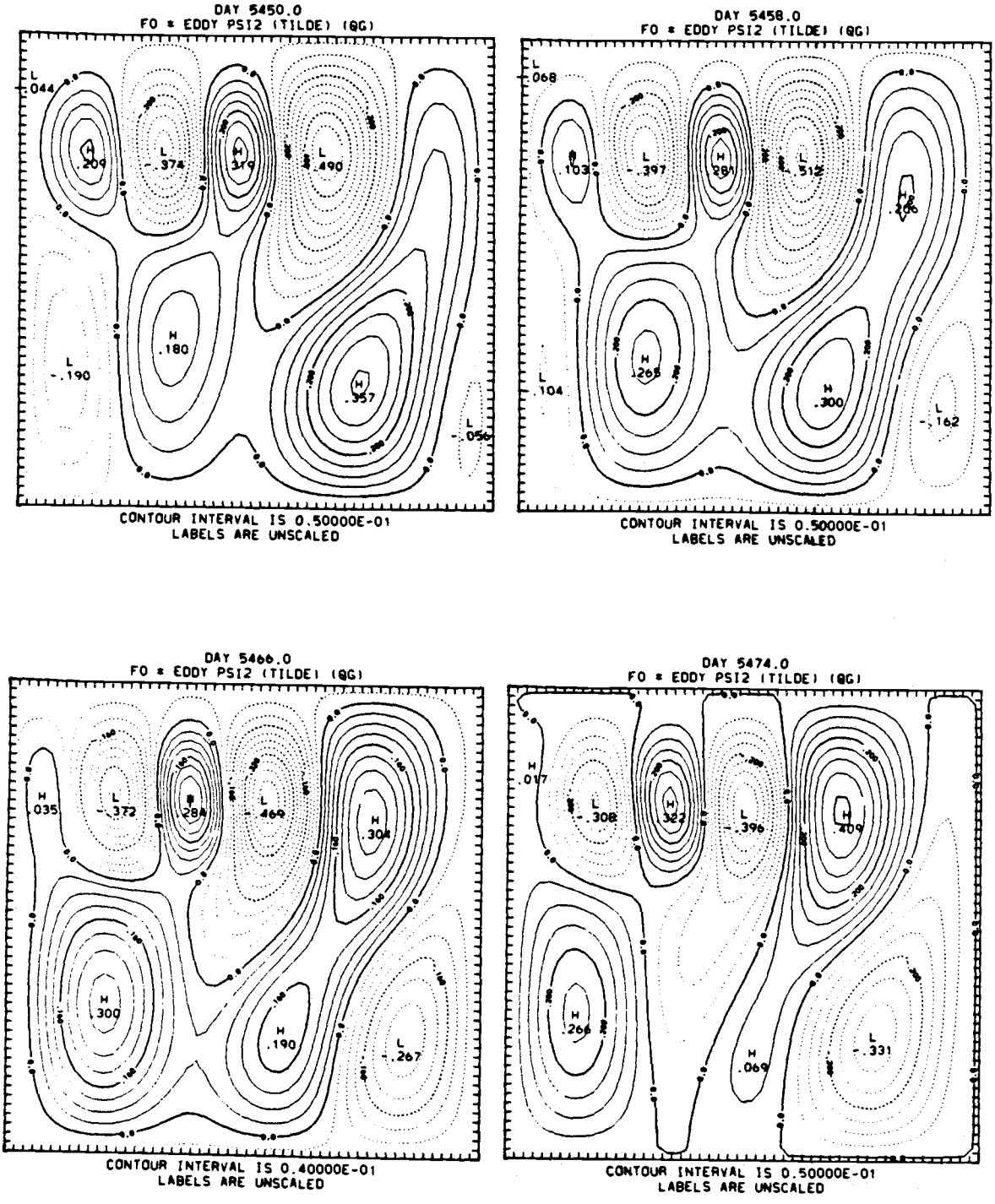

b

Fig. 5.19 (cont.)

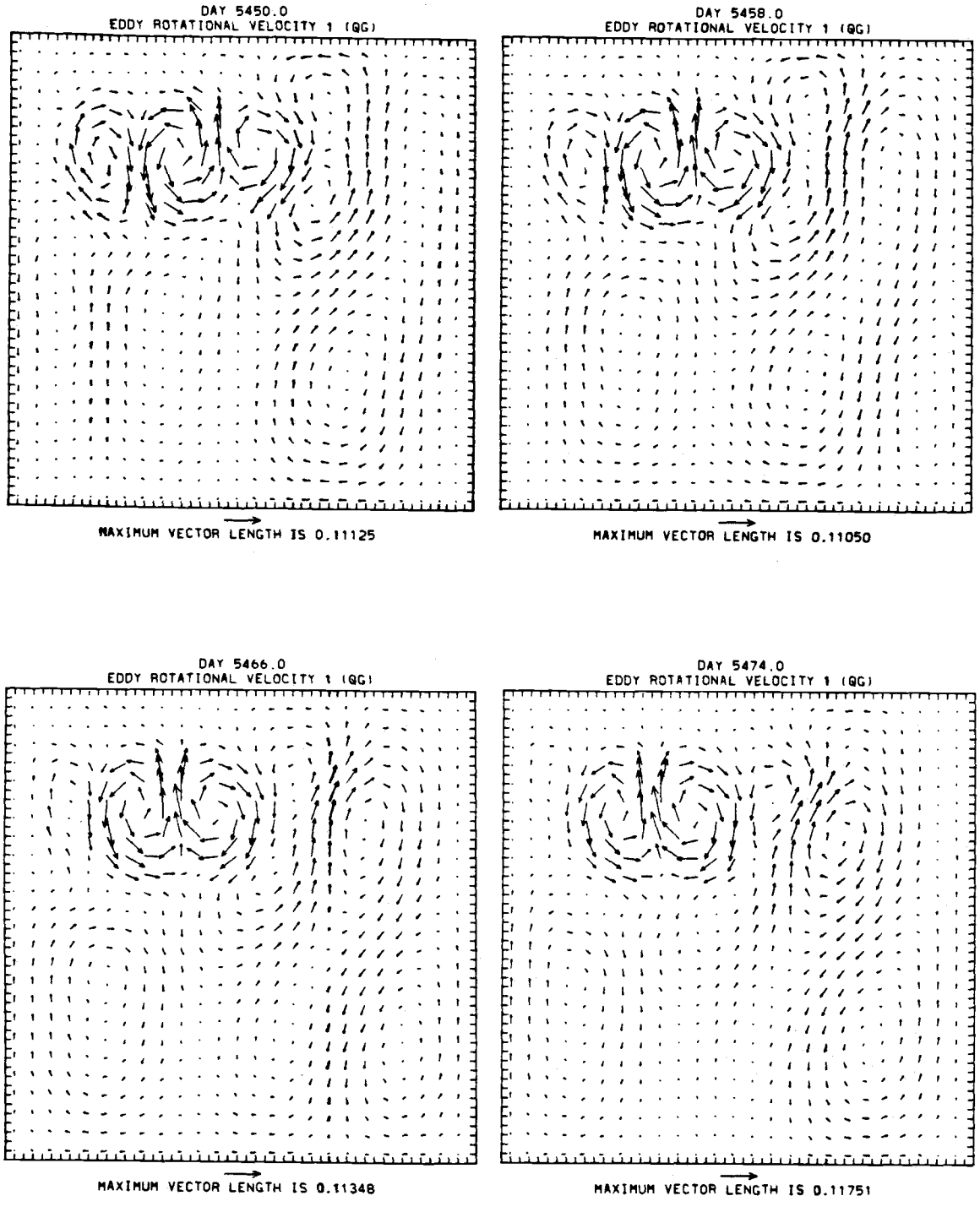

c

Fig. 5.19 (cont.)

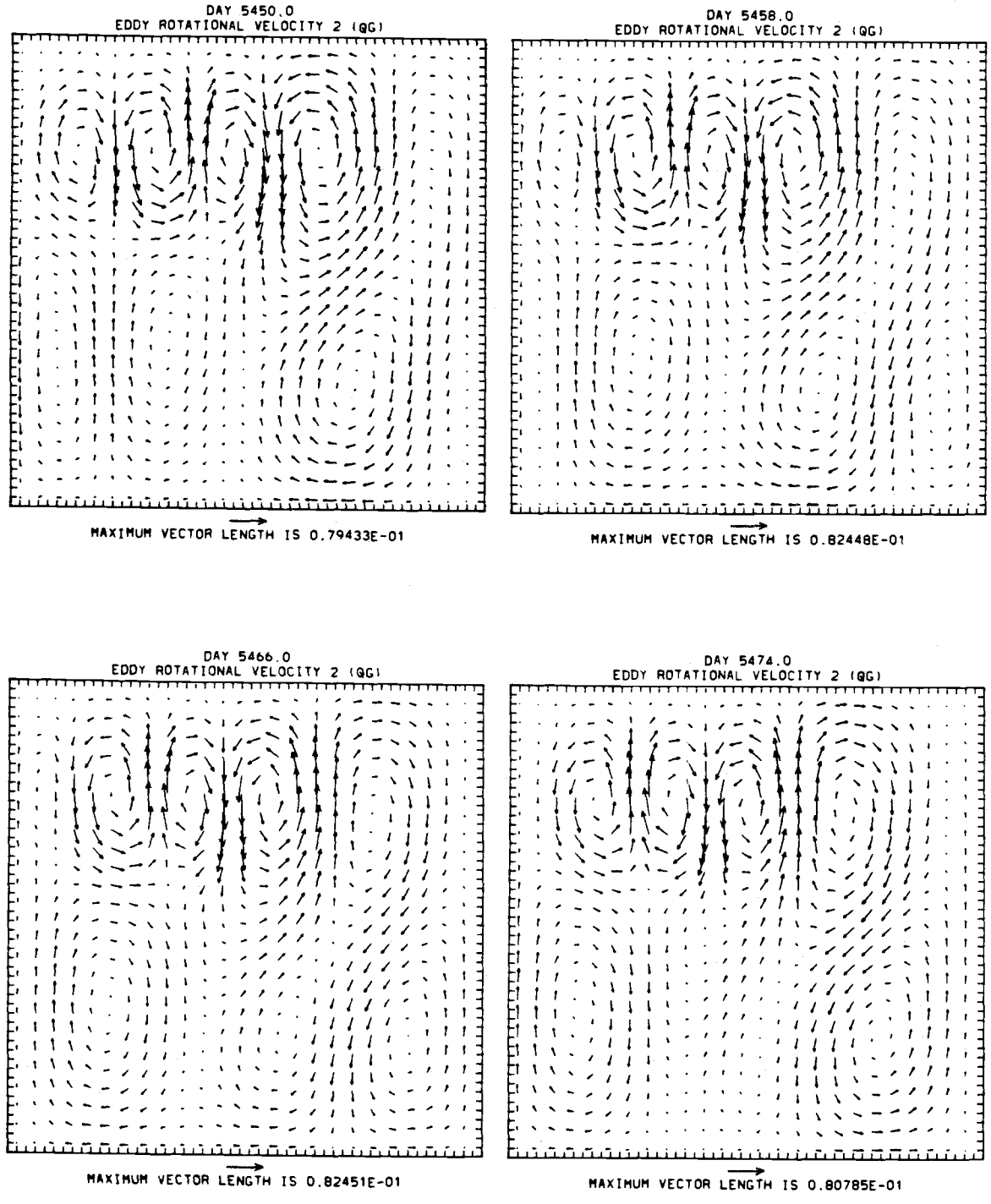

d

Fig. 5.19 (cont.)

Fig. 5.20 shows maps of p_1, p_2, $\vec{v}_1$, and $\vec{v}_2$ at the same time intervals, but for the PE model. The mesoscale eddies in these plots have basically the same properties as the QG eddies. These plots also show the Kelvin waves traveling counterclockwise around the lateral boundaries of the basin. (Note that this 8-day sampling frequency severely aliases these waves which travel completely around the basin in about 10 days.)

5.4 Energetics

Table 5.2 lists the horizontally-averaged, time-mean and eddy kinetic energies for both models. In the PE model, the total kinetic energy is listed, along with the breakdown into the rotational and divergent components. The PE total and rotational kinetic energy components are consistently higher than the QG kinetic energy components. The divergent component of K_1', contributes almost 50% to the total. Instead of being a few percent of the total kinetic energy, as the mean streamfunction and velocity potential (Figs. 5.3-5.5) would suggest, the mean divergent component for each layer contributes ~13%. This can be explained by the large areal extent: since the Kelvin waves are confined to within the Rossby radius of deformation, which is ~50 km in this experiment, the areal extent of the Kelvin waves covers ~10% of the total in this small basin.

The geographical distribution of the time-mean and eddy

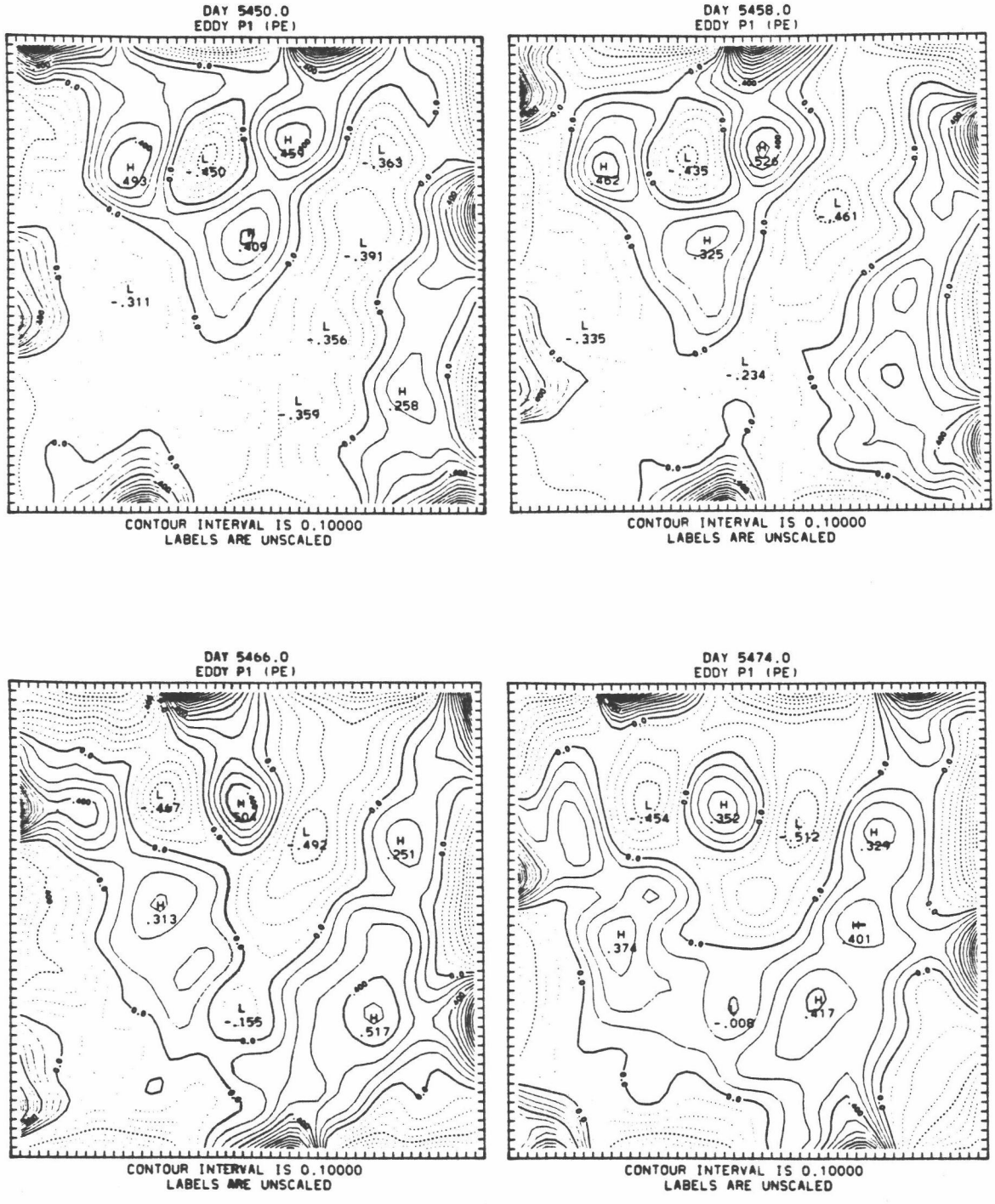

a

Fig. 5.20 The PE eddy fields at 8-day intervals for a) p_1, b) p_2, c) $\vec{v}_1$, d) $\vec{v}_2$.

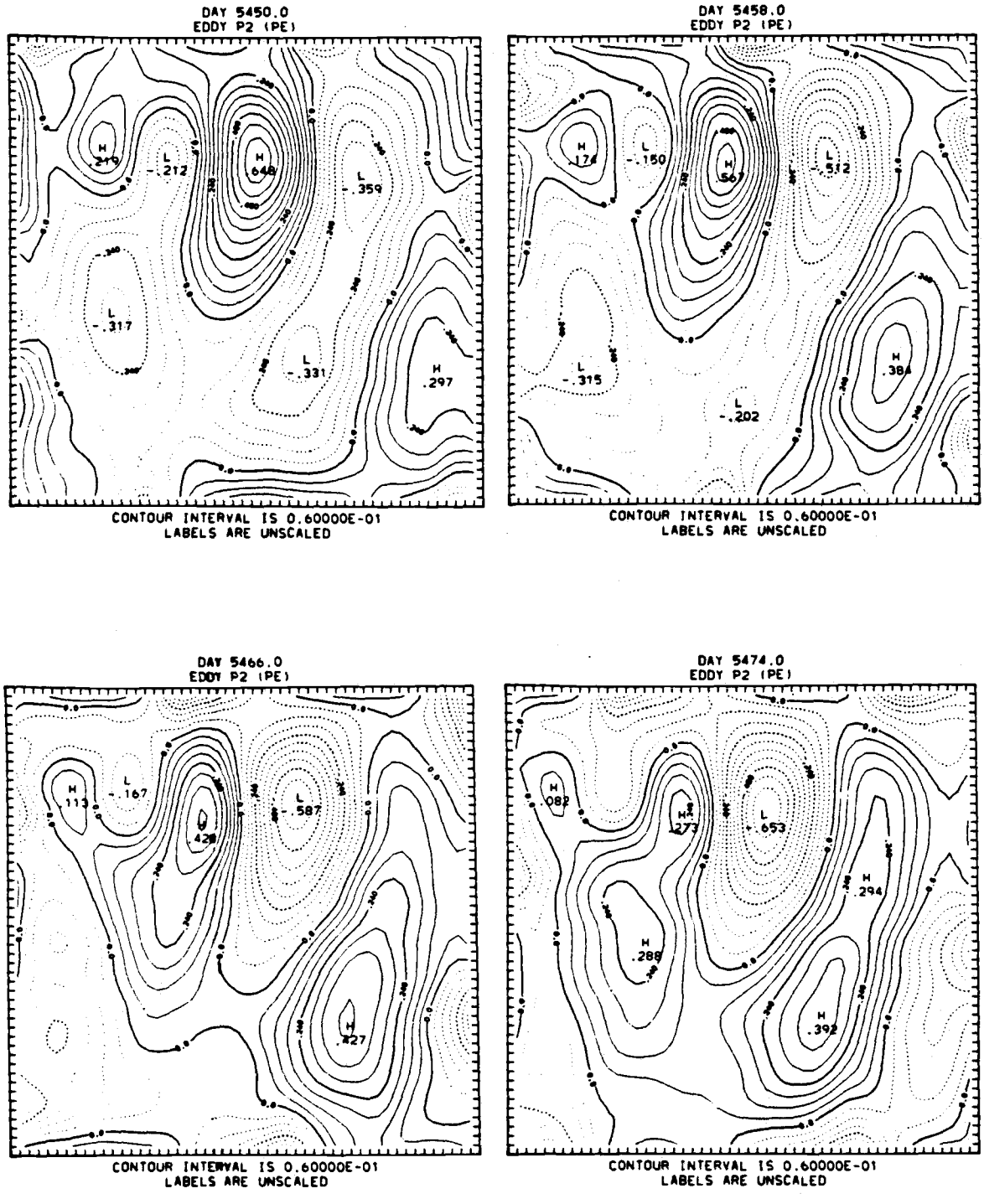

b

Fig. 5.20 (cont.)

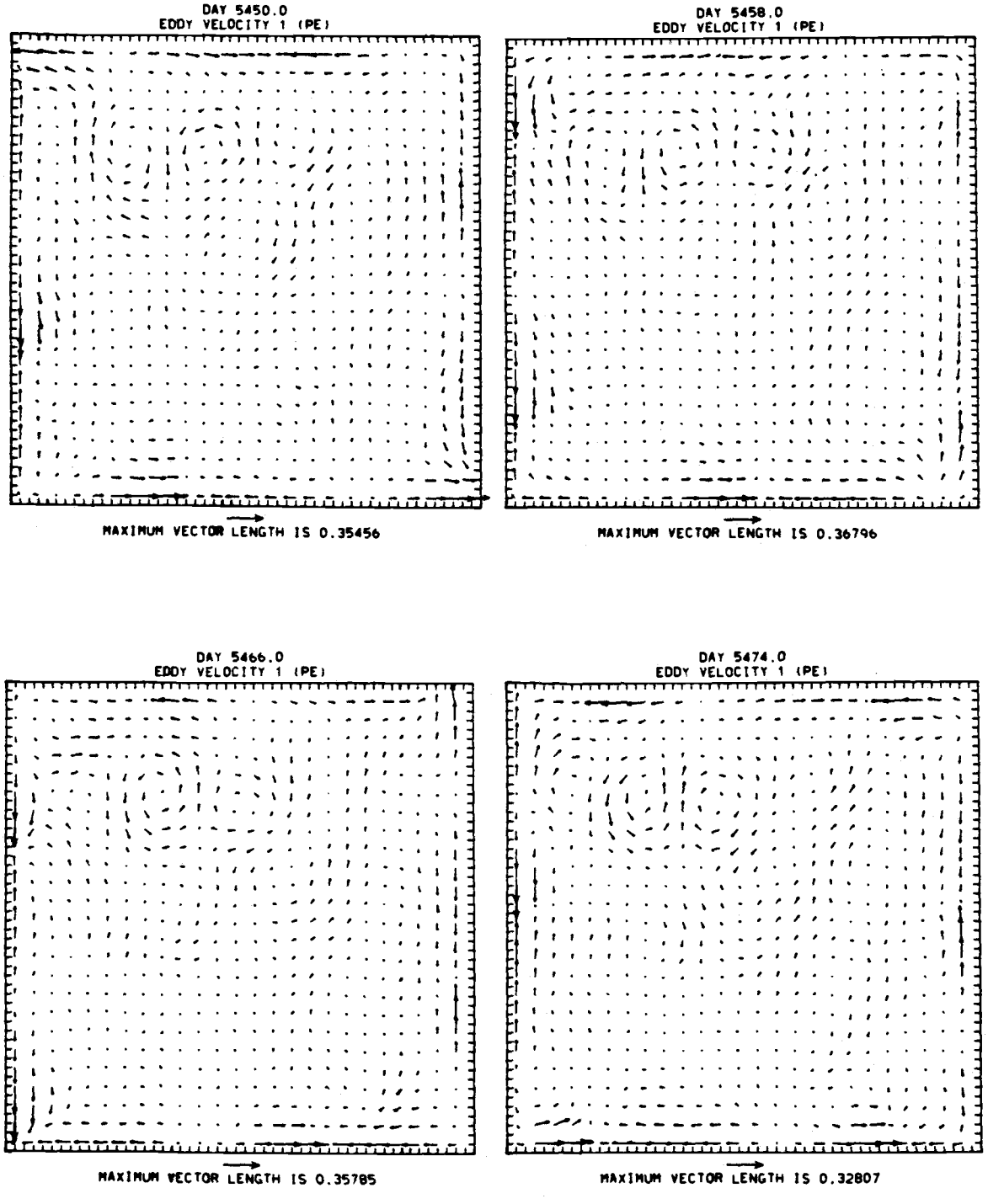

c

Fig. 5.20 (cont.)

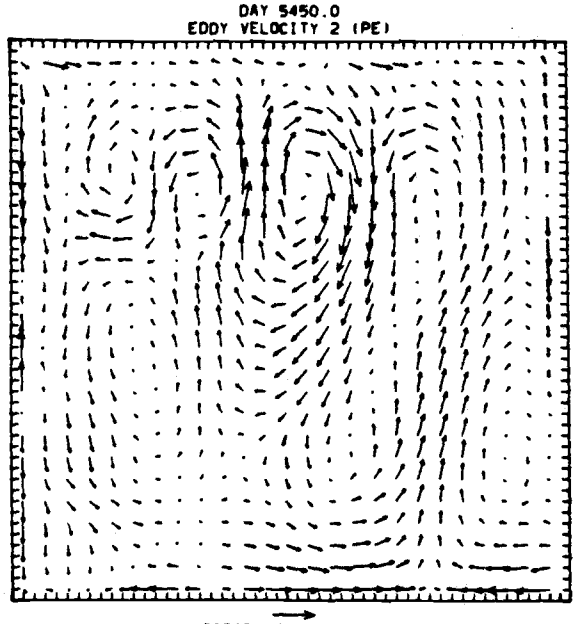

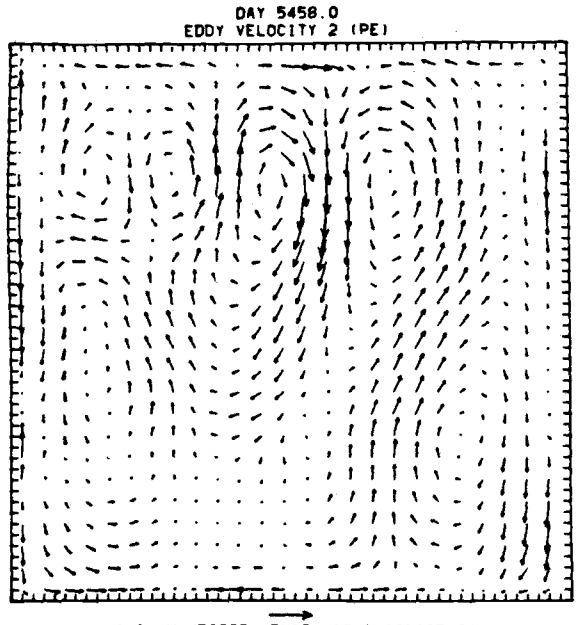

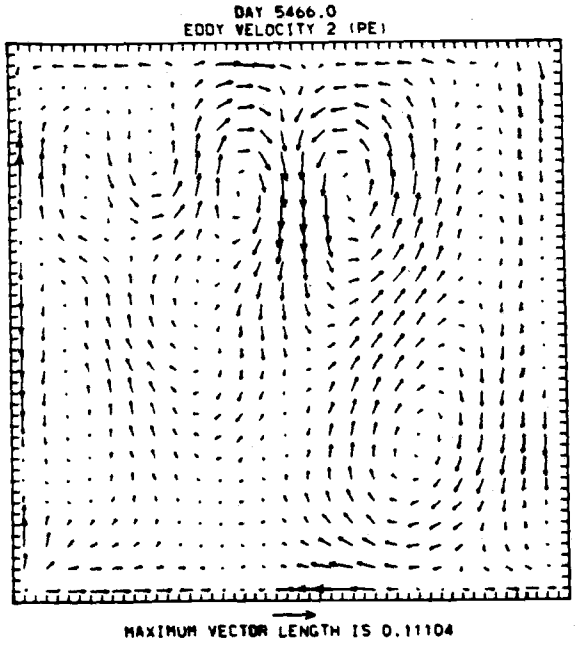

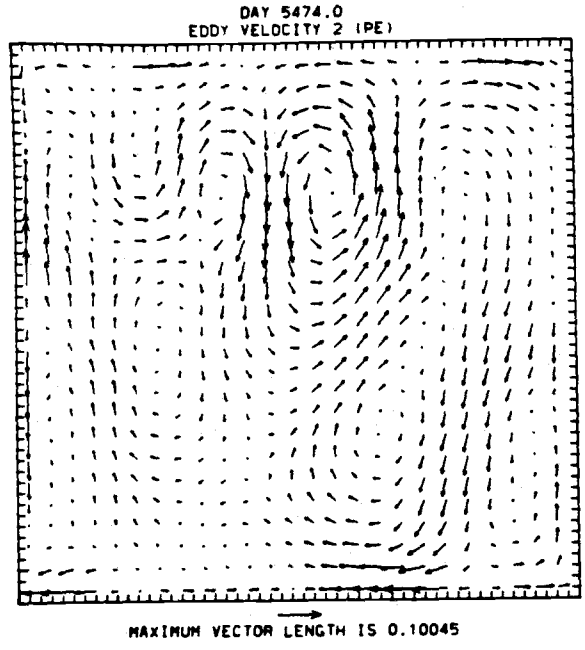

d

Fig. 5.20 (cont.)

Table 5.2 Horizontally-averaged time-mean and eddy kinetic energy for the single-gyre experiment

		$\overline{K}_1$		$\overline{K}_2$		K_1'		K_2'	
No.	Energy	Quantity (k J m^{-2})	% of PE total	Quantity (k J m^{-2})	% of PE total	Quantity (k J m^{-2})	% of PE total	Quantity (k J m^{-2})	% of PE total
1)	Total PE	8.70	100%	2.27	100%	2.29	100%	1.93	100%
1a)	Rotational component	7.57	87%	2.00	88%	1.16	51%	1.64	85%
1b)	Divergent component	1.13	13%	0.27	12%	1.13	49%	0.28	15%
2)	QG	5.82	67%	1.52	67%	0.43	19%	1.26	65%

kinetic energy for each layer is shown in Figs. 5.21-5.24. As in Fig. 12 of Holland and Lin (1975a), large local values of the mean kinetic energy are present. The PE eddy kinetic energy maps (Figs. 5.23a and 5.24a) suggest two regions of active transience: 1) the boundary, where Kelvin waves are present, and 2) the recirculation region, where the mesoscale eddies are driven by baroclinic instability processes. In the QG model only the latter region is present.

The geographical distribution of the time-mean and eddy rotational available potential energy for each model is shown in Figs. 5.25 and 5.26. Most of the mean and eddy rotational available potential energies in both models is produced in the recirculation region. The PE mean available potential energy is greater than the QG, but the patterns are very similar. Again, much of the eddy energy in the PE model occurs in the boundary regions, due to the presence of Kelvin waves. The linear balance component (Figs. 5.25d and 5.26d) contributes ~10% to the PE mean rotational available potential energy. This term would probably play a more important role if a larger basin size were used. The small basin size used here tends to diminish one of the important differences between PE and QG models, namely, the variation of the Coriolis parameter in some terms.

The energetic properties of the mean and eddy motions for the final, statistically steady state for the QG and PE models are shown in Figs. 5.27 and 5.28, respectively. These diagrams show the energy (units k J m^{-2}) and the rates of energy transfer

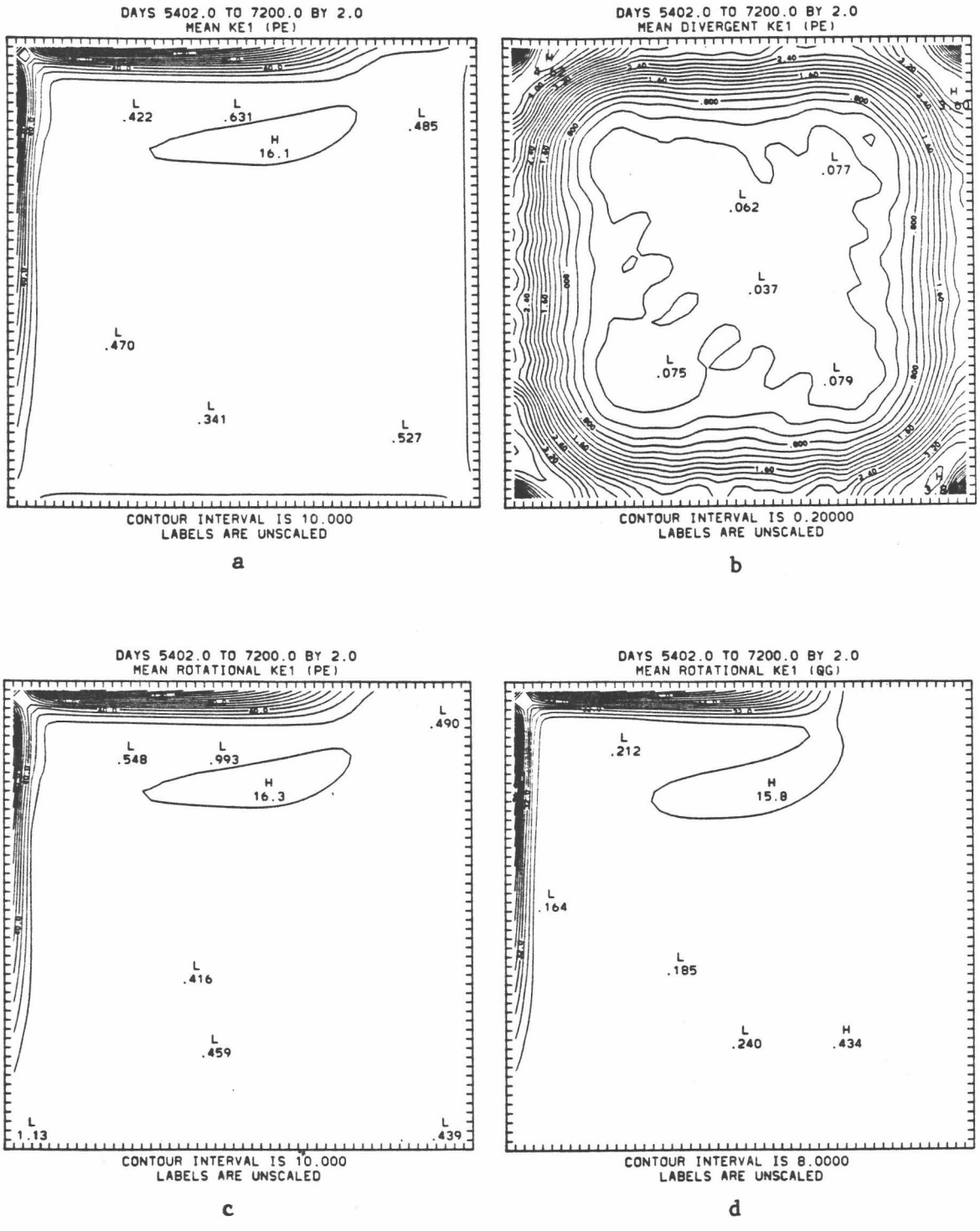

Fig. 5.21 Time-mean of entry 17 in Table 4.1: a) K_1, b) K_{1D}, c) K_{1R} (PE), d) K_{1R} (QG).

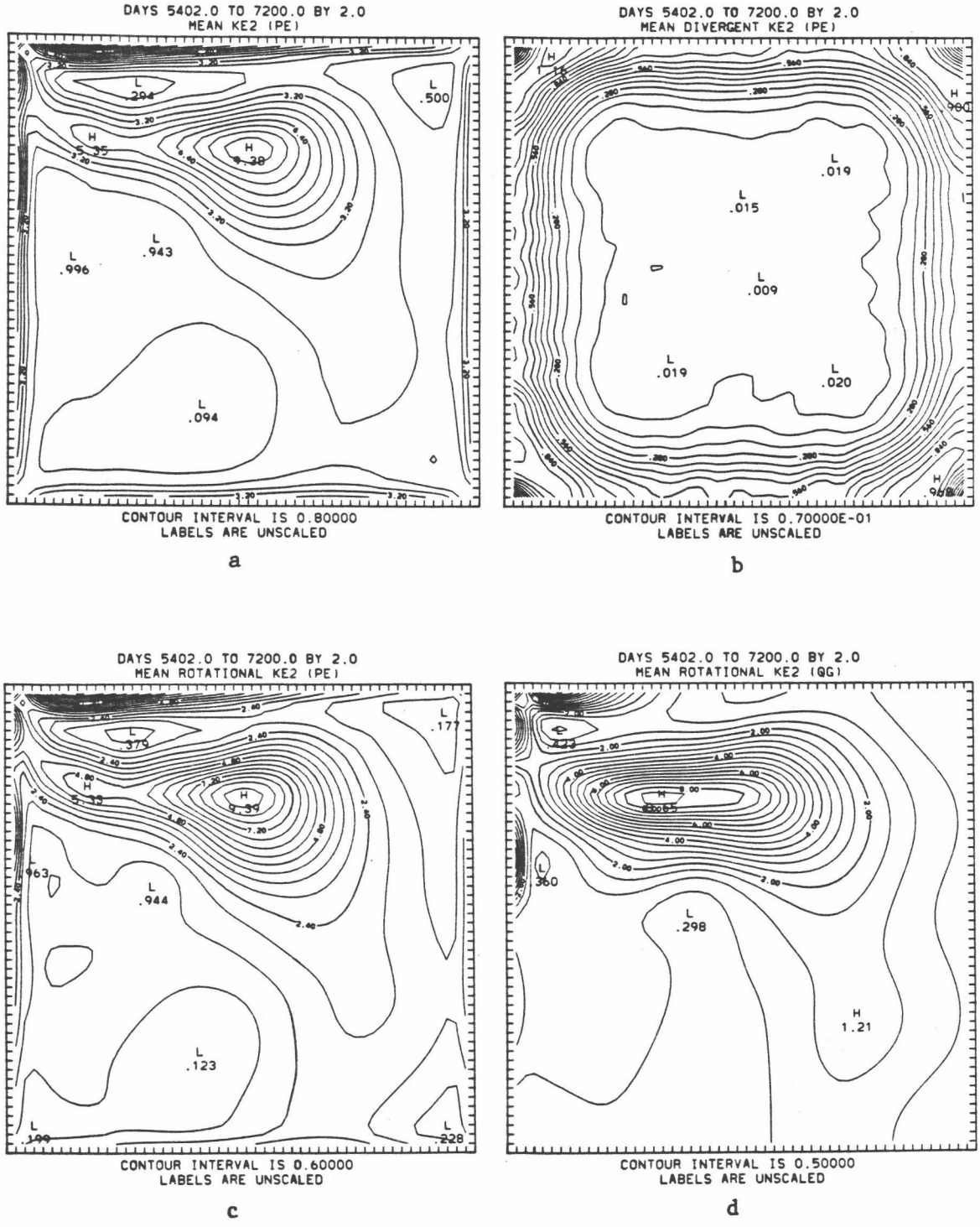

Fig. 5.22 Time-mean of entry 18 in Table 4.1: a) K_2, b) K_{2D}, c) K_{2R} (PE), d) K_{2R} (QG).

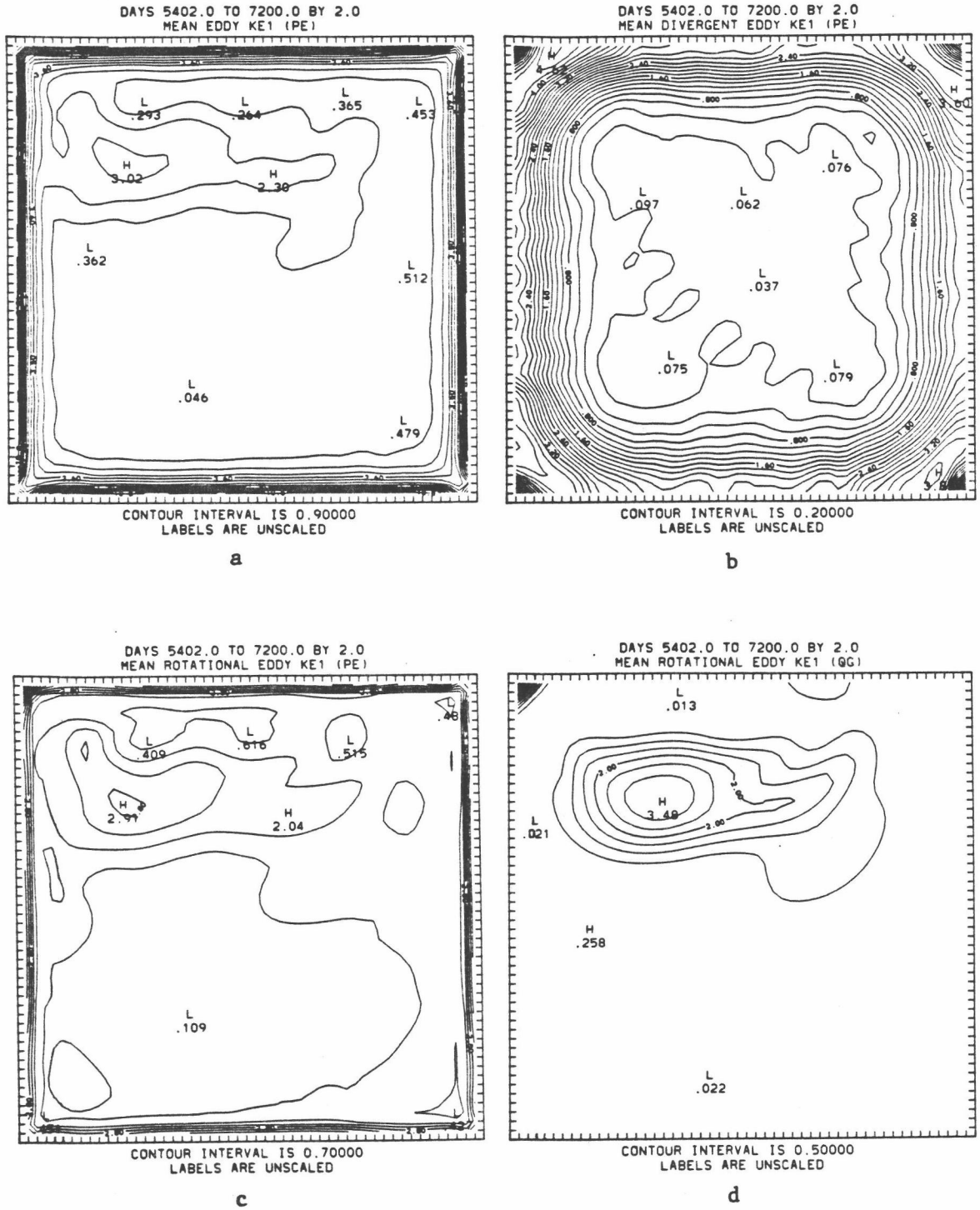

Fig. 5.23 Time-deviation of entry 17 in Table 4.1: a) K_1, b) K_{1D}, c) K_{1R} (PE), d) K_{1R} (QG).

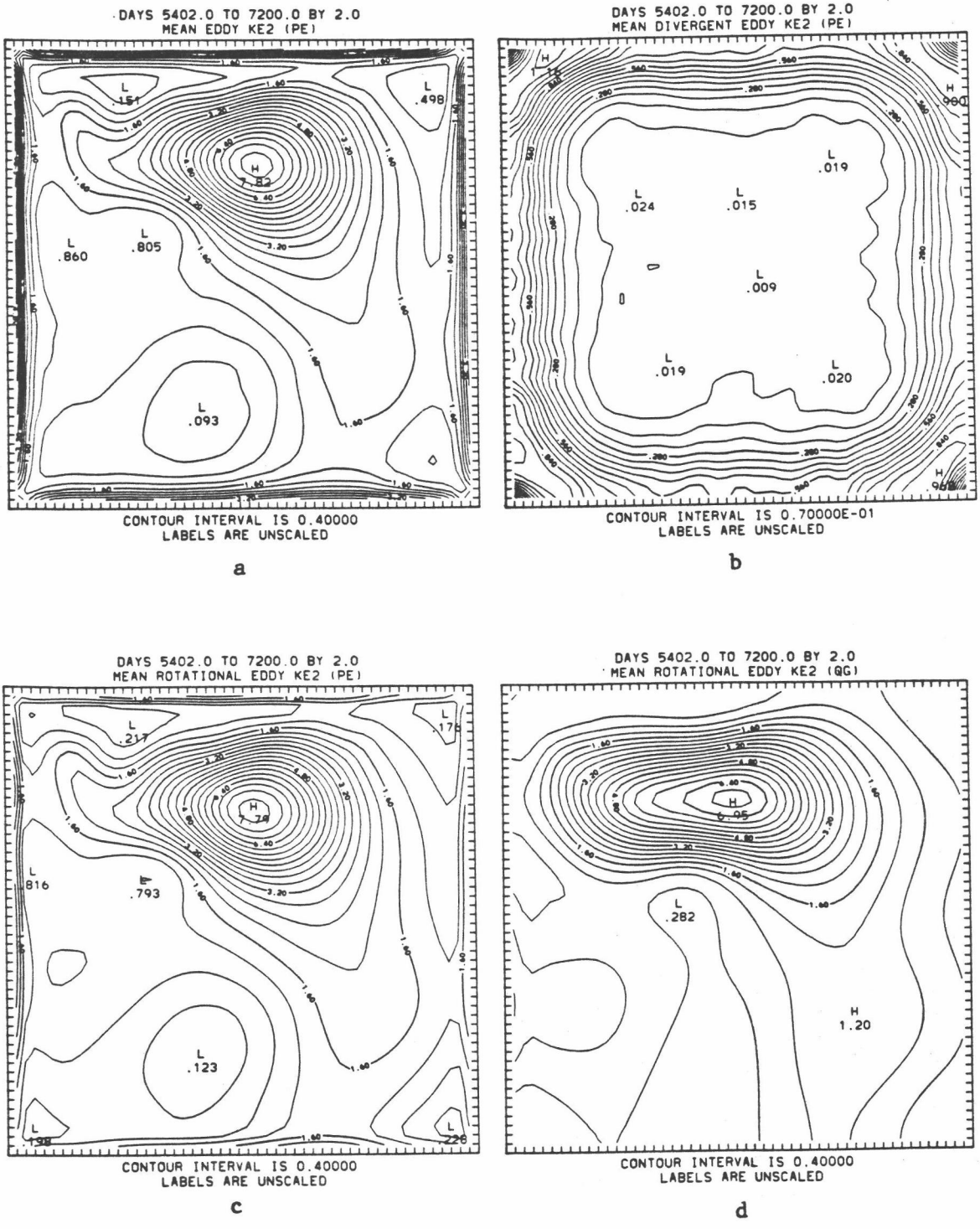

Fig. 5.24 Time-deviation of entry 18 in Table 4.1: a) K_2, b)K_{2D}, c) K_{2R} (PE), d) K_{2R} (QG).

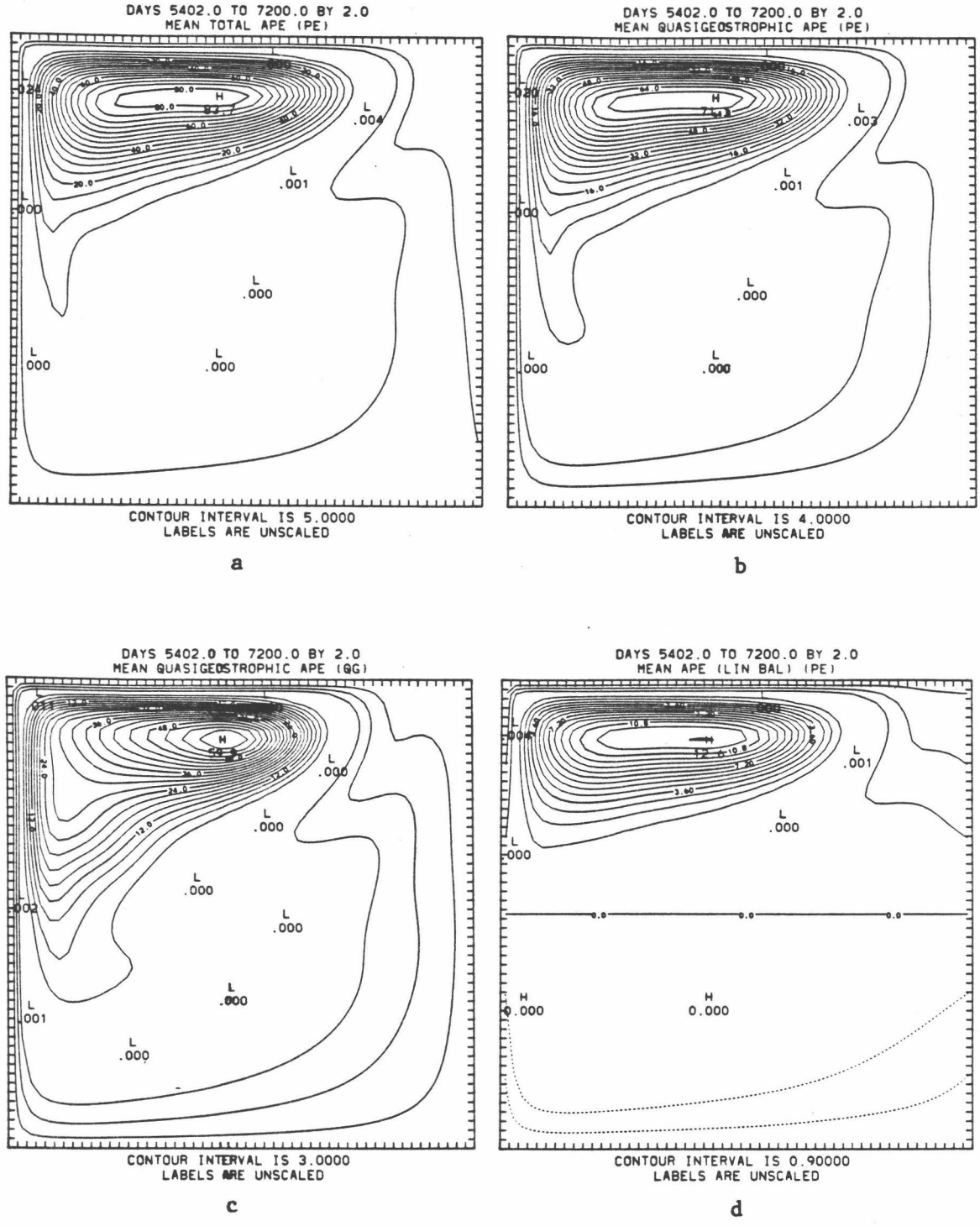

Fig. 5.25 Time-mean of entry 19 in Table 4.1: a) P_R, b) P_{RQG} (PE), c) P_{RQG} (QG), d) P_{RLB}.

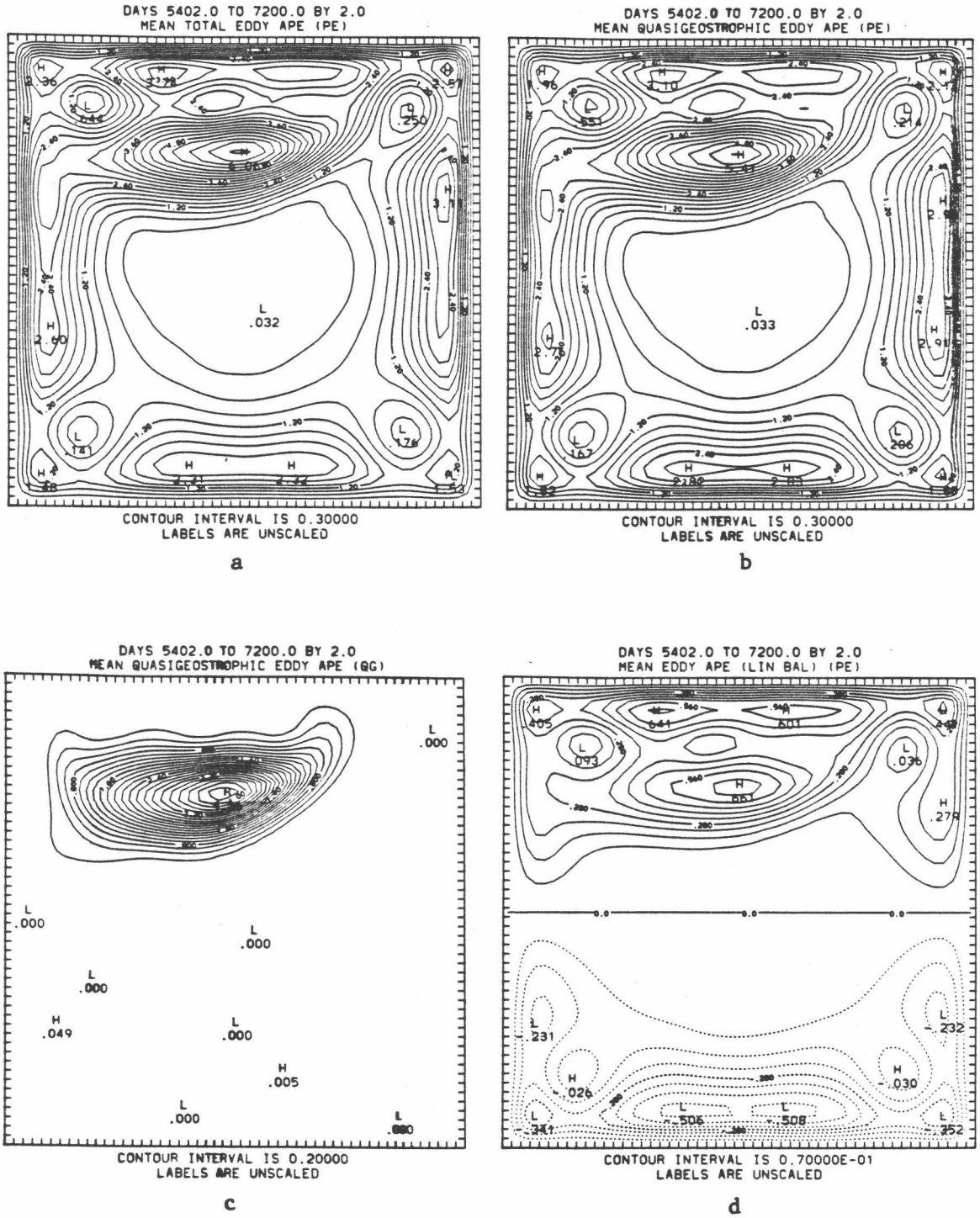

Fig. 5.26 Time-deviation of entry 19 in Table 4.1: a) P_R, b) P_{RQG} (PE), c) P_{RQG} (QG), d) P_{RLB}.

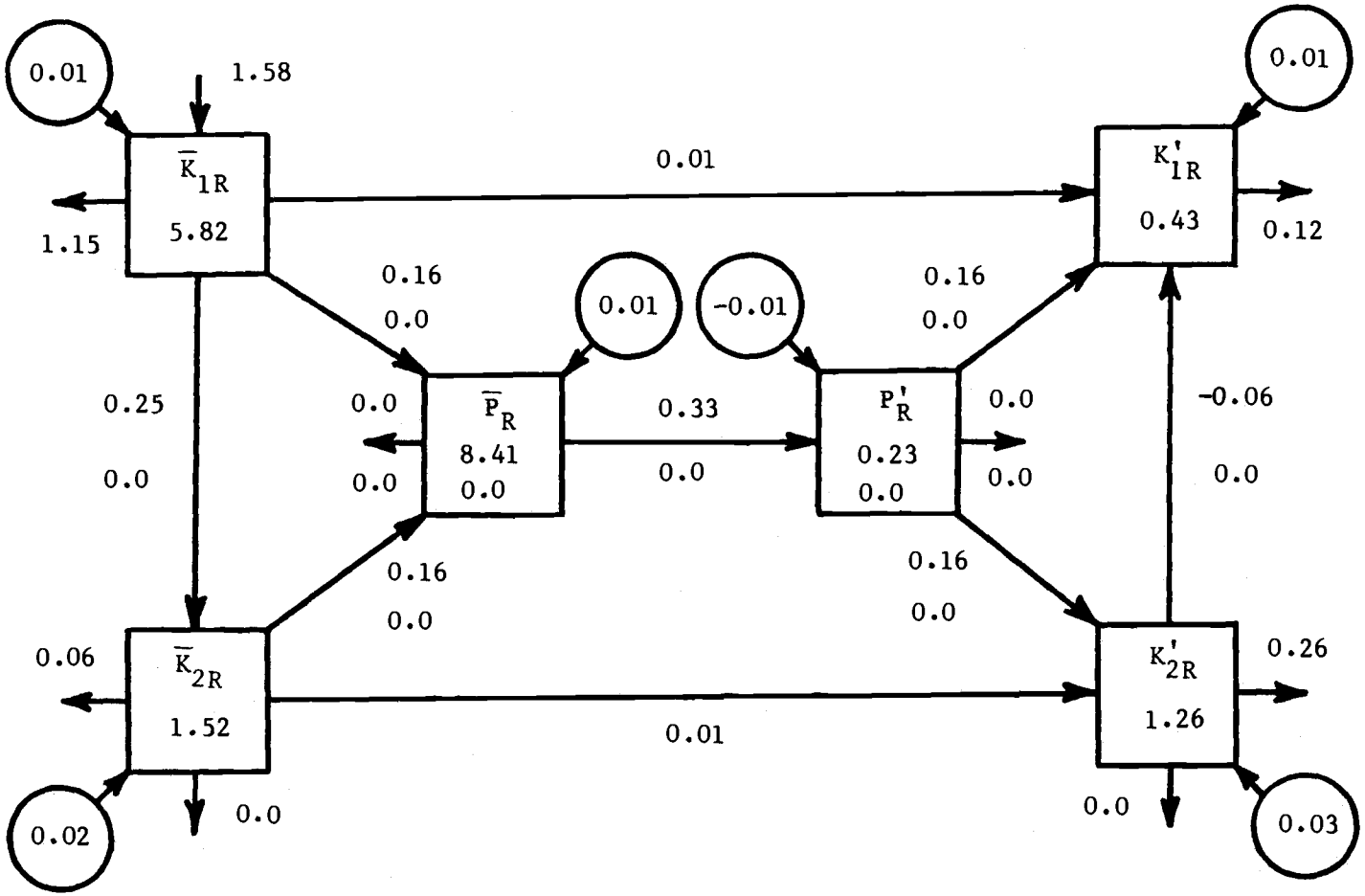

Fig. 5.27. The QG global energetics (the energy box diagram shown in Fig. 4.2) for the single-gyre experiment. The numbers within the boxes are the energy levels of the various components (units k J m^{-2}), and the numbers on the arrows show the energy transfers (units 10^6 k J m^{-2} s^{-1}), described by Eq. (4-45). Unless indicated by a negative sign, the arrow head shows the direction of energy flow.

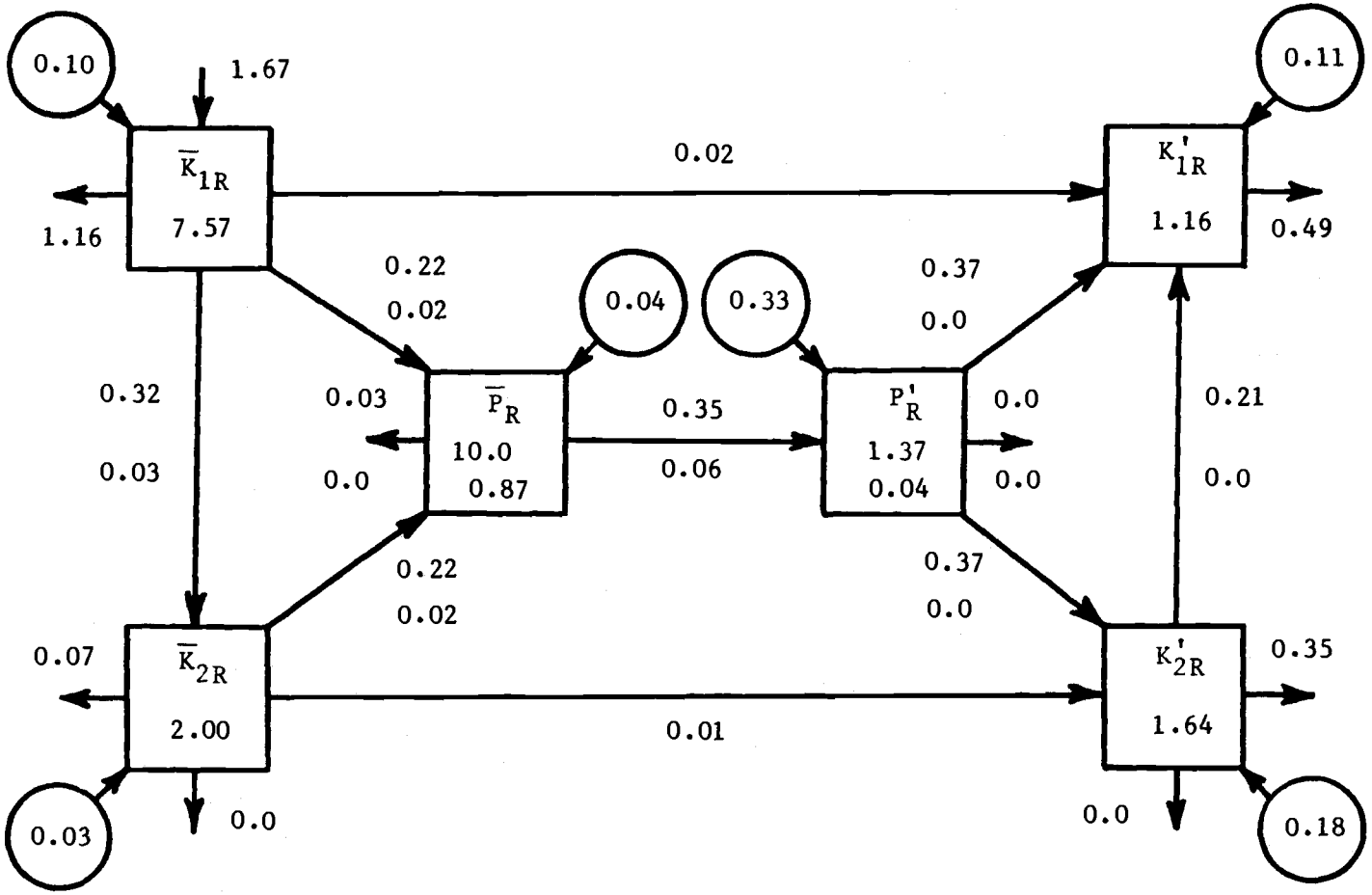

Fig. 5.28 Same as for Fig. 5.27, but for the PE model.

(units 10^6 k J m^{-2} s^{-1}) for the rotational mean and eddy available potential and kinetic energies, as shown in Eq. (4-45).

Fig. 5.27 shows that the wind puts on the average 1.58×10^6 k J m^{-2} s^{-1} into the upper layer mean kinetic energy. About 75% of this is dissipated by lateral friction, primarily in the western and northern boundary layers. The other 25% of the energy put in by the wind participates in the eddy generation process. Work done by the pressure forces transfers 0.25×10^6 k J m^{-2} s^{-1} from the upper layer to the lower layer. Work done by buoyancy forces transfers 0.16×10^6 k J m^{-2} s^{-1} from each layer to maintain the mean available potential energy of the system, which is continually releasing energy to supply to the eddies. Buoyancy forces transform eddy potential energy into eddy kinetic energy in order to maintain the eddy field, which would otherwise be dissipated by lateral friction. A very small amount of energy goes directly from mean to eddy kinetic energy. Thus the eddy field receives its energy mainly as a result of baroclinic instability processes. This transfer of energy occurs almost entirely in the recirculation region. These results are similar to those in Experiment 1 of Holland (1978).

A comparison of Fig. 5.28 with Fig. 5.27 shows that 1) the QG energy transfer rates are similar, but in general, higher for the PE model, 2) little energy is dissipated by biharmonic heat diffusions, 3) the work done by pressure forces in transferring eddy energy from the lower to upper layer is of opposite sign,

and 4) the LB transfer rates are generally small, due to the small basin size.

The small residuals shown for the QG eddy energy terms in Fig. 5.27 would be identically zero if longer time averaging were used. The large residuals shown for the PE eddy energy terms in Fig. 5.28 imply important FB and PE energy transfers (which were not explicitly computed in this study). These terms presumably represent transfers between rotational and divergent components. A more complete analysis of the total PE energetics, necessary to explain the underlying dynamics, has not been done here.

5.5 Vorticity

5.5.1 Relative vorticity

The geographical distributions of the time-averaged relative vorticity (i.e., $\nabla^2\overline{\psi}$) for both the PE and QG models are shown in Figs. 5.29 and 5.30, respectively. The vorticity patterns are similar, but the QG model has, in general, larger values of both clockwise and counterclockwise vorticity.

In order to examine the local vorticity transfers, plots of the geographical distribution of various terms on the right-hand side of Eqs. (4-46) and (4-47) are shown in Figs. (5-31)-(5-36). We first examine the spatial distribution of the $\overline{A}_{1QG}$

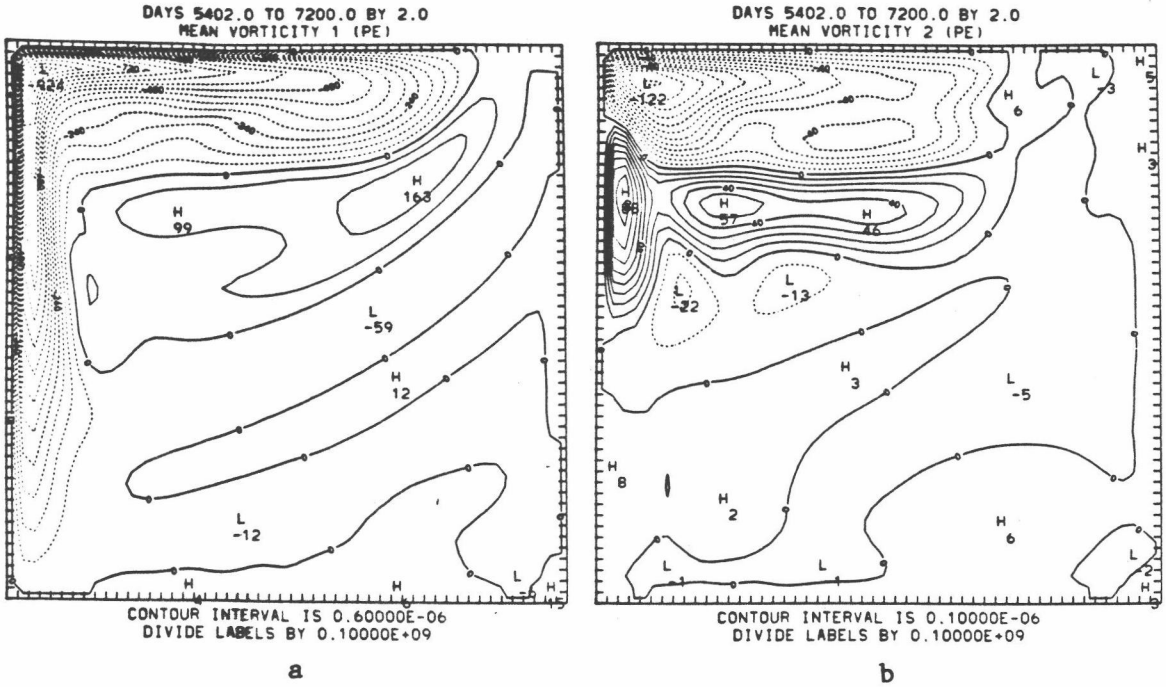

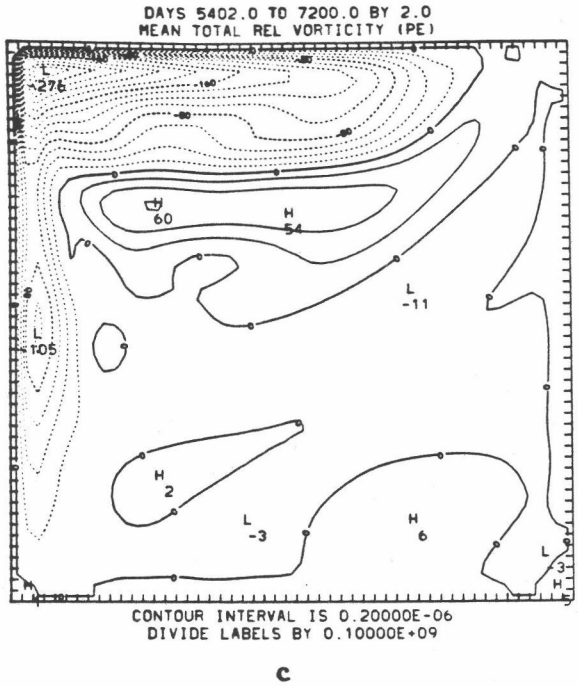

Fig. 5.29 Time-mean of entry 20 in Table 4.1: a) $\nabla^2\psi_1$, b) $\nabla^2\psi_2$, c) $H^{-1}(h_1\nabla^2\psi_1 + h_2\nabla^2\psi_2)$ (not shown in Table 4.1).

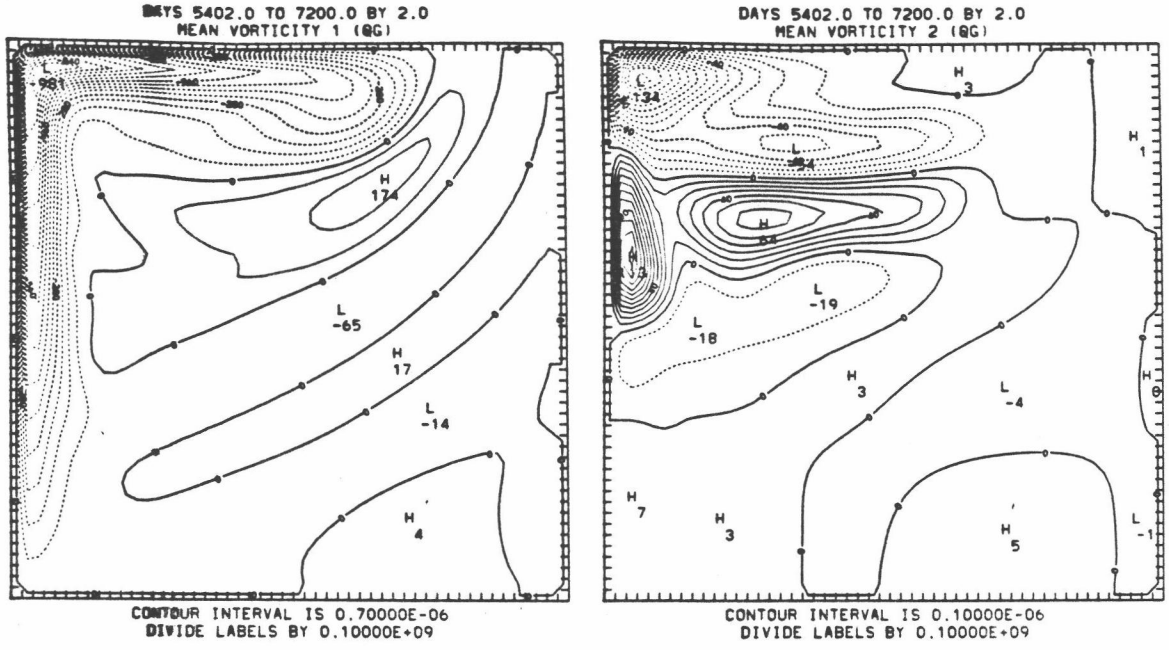

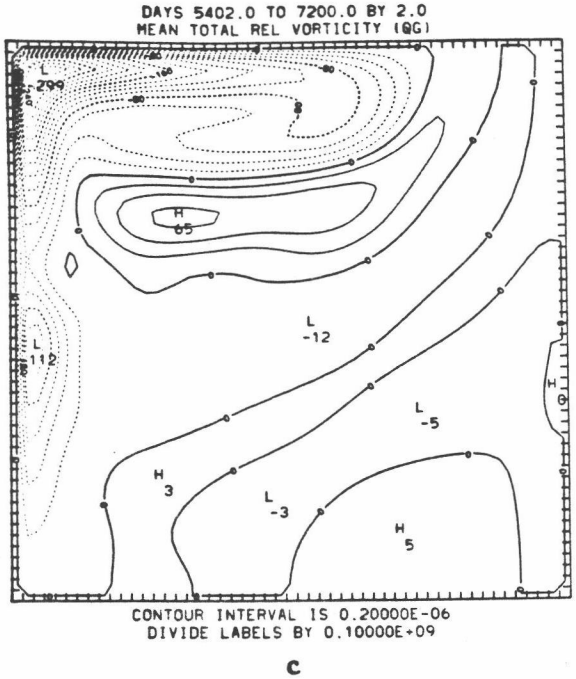

Fig. 5.30 Time-mean of entry 21 in Table 4.1: a) $\nabla^2\psi_1$, b) $\nabla^2\psi_2$, c) $H^{-1}(h_1\nabla^2\psi_1 + h_2\nabla^2\psi_2)$ (not shown in Table 4.1).

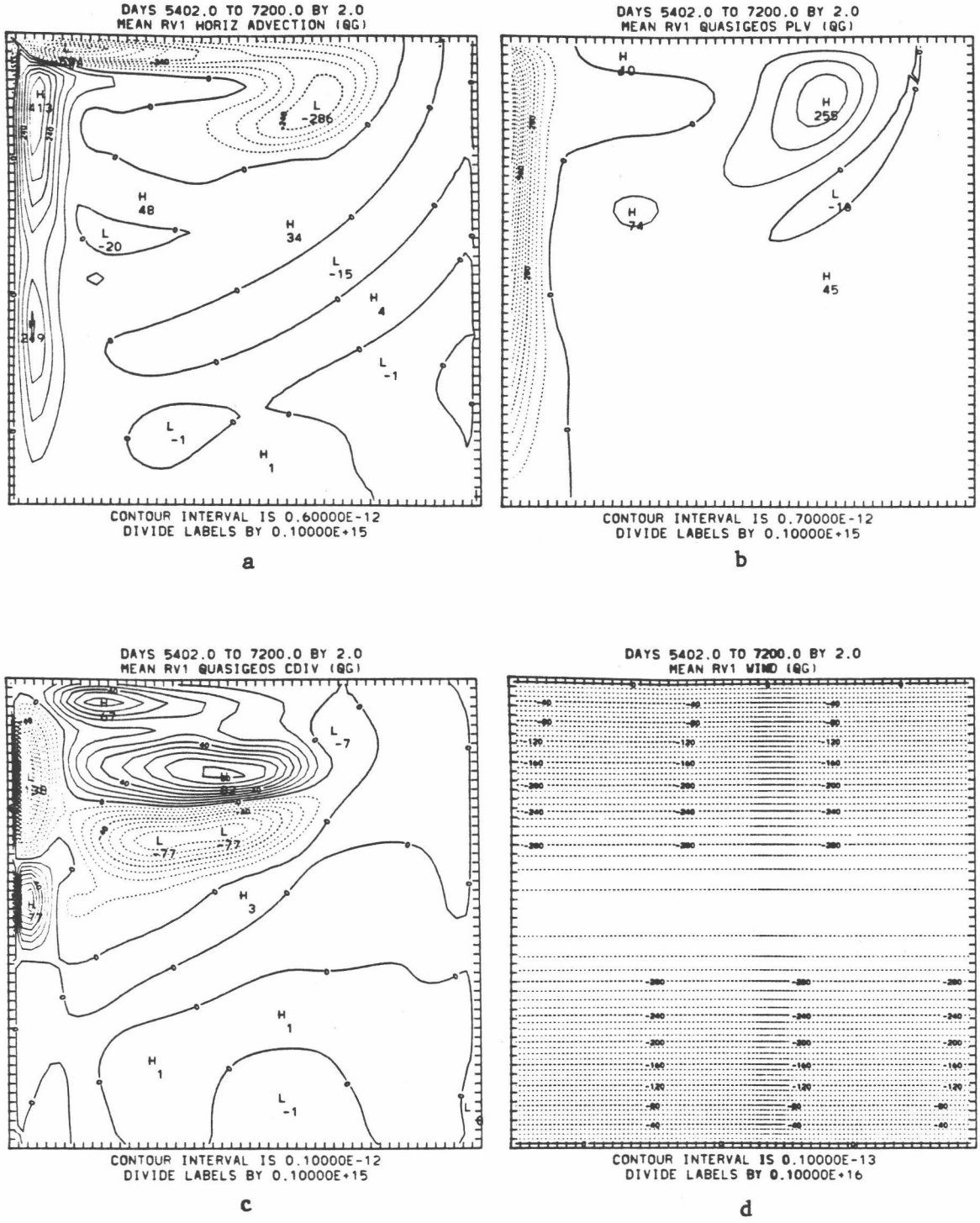

Fig. 5.31 QG spatial distributions of the time-averages of the A_{1QG} terms on the right-hand side of Eq. (4-46): a) $-J(\psi_1, \zeta_1)$, b) $-\beta\psi_{1x}$, c) $-(f_o/h_1)w_2$, d) $h_1 \mathrm{curl}_z \tau(y)$, e) $A_m\nabla^4\psi_1$, f) $-J(\psi_1', \zeta_1')$.

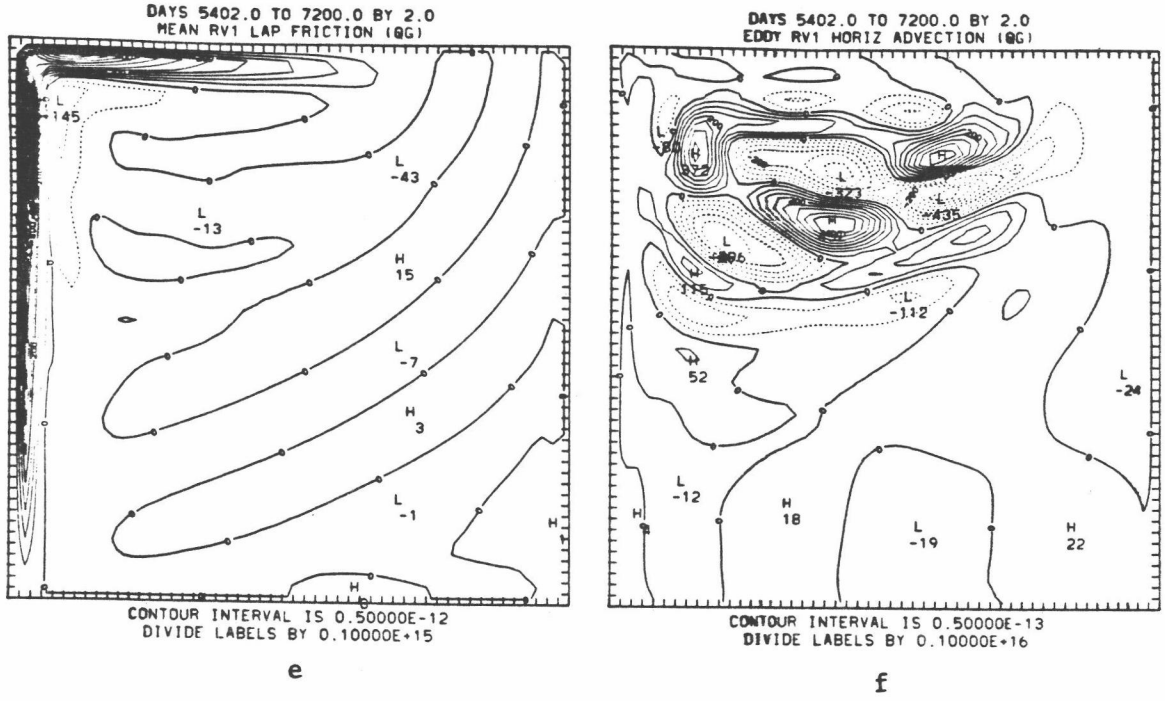
DAYS 5402.0 TO 7200.0 BY 2.0
MEAN RV1 LAP FRICTION (@G)
L
-145
L
-43
L
-13
H
15
L
-7
H
3
L
-1
H
H
CONTOUR INTERVAL IS 0.50000E-12
DIVIDE LABELS BY 0.10000E+15
e
DAYS 5402.0 TO 7200.0 BY 2.0
EDDY RV1 HORIZ ADVECTION (@G)
L
-435
L
-112
H
52
L
-24
L
-12
H
18
L
-19
H
22
CONTOUR INTERVAL IS 0.50000E-13
DIVIDE LABELS BY 0.10000E+16
f

Fig. 5.31 (cont.)

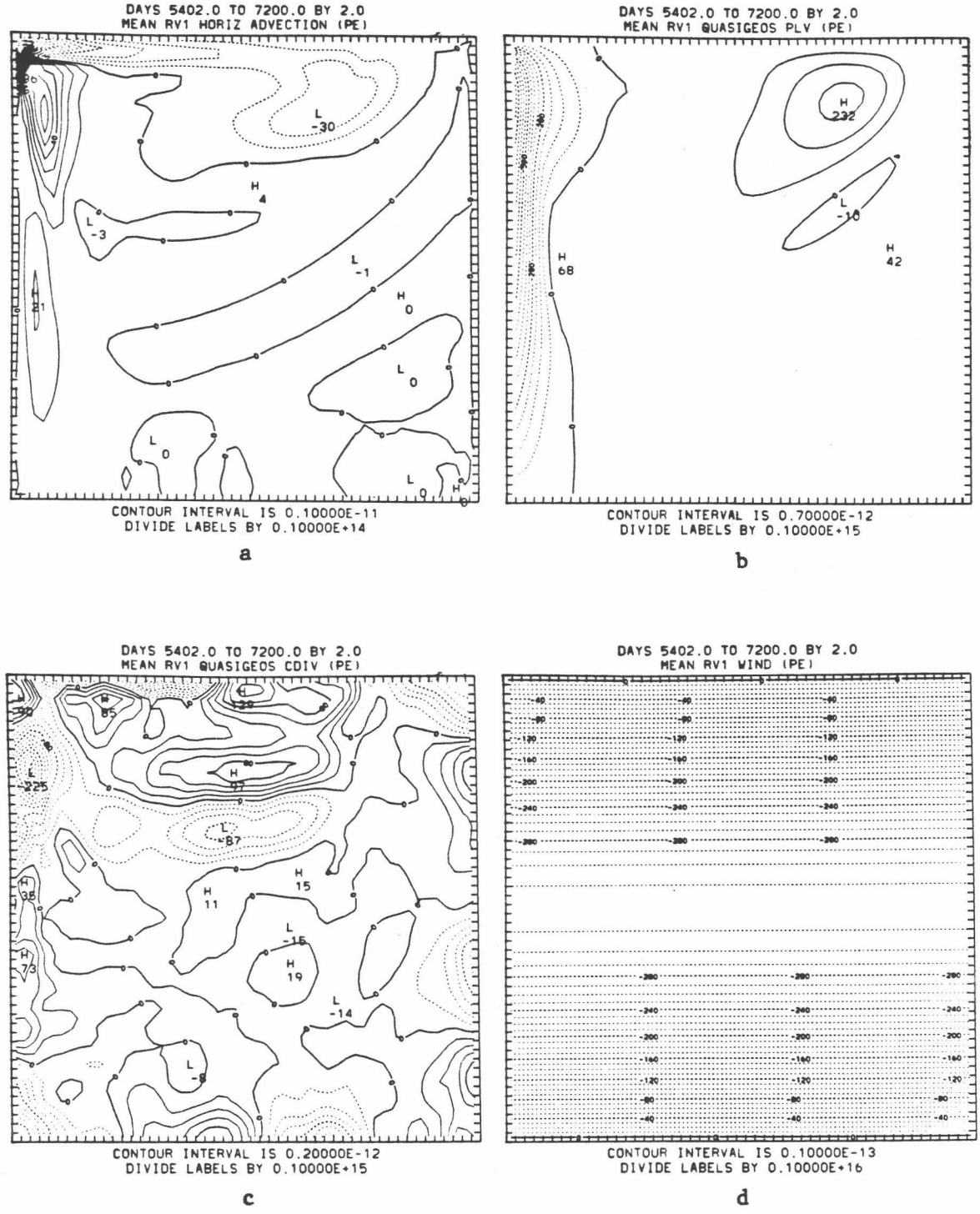

Fig. 5.32 Same as Fig. 5.31, but for the PE model.

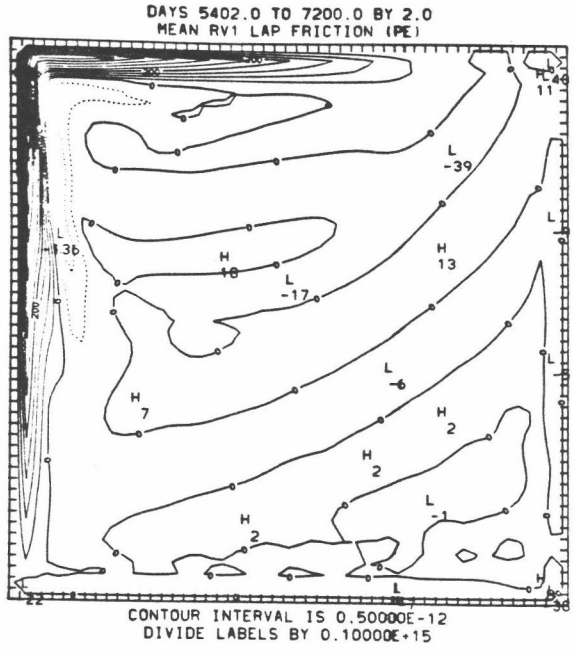

e

f

Fig. 5.32 (cont.)

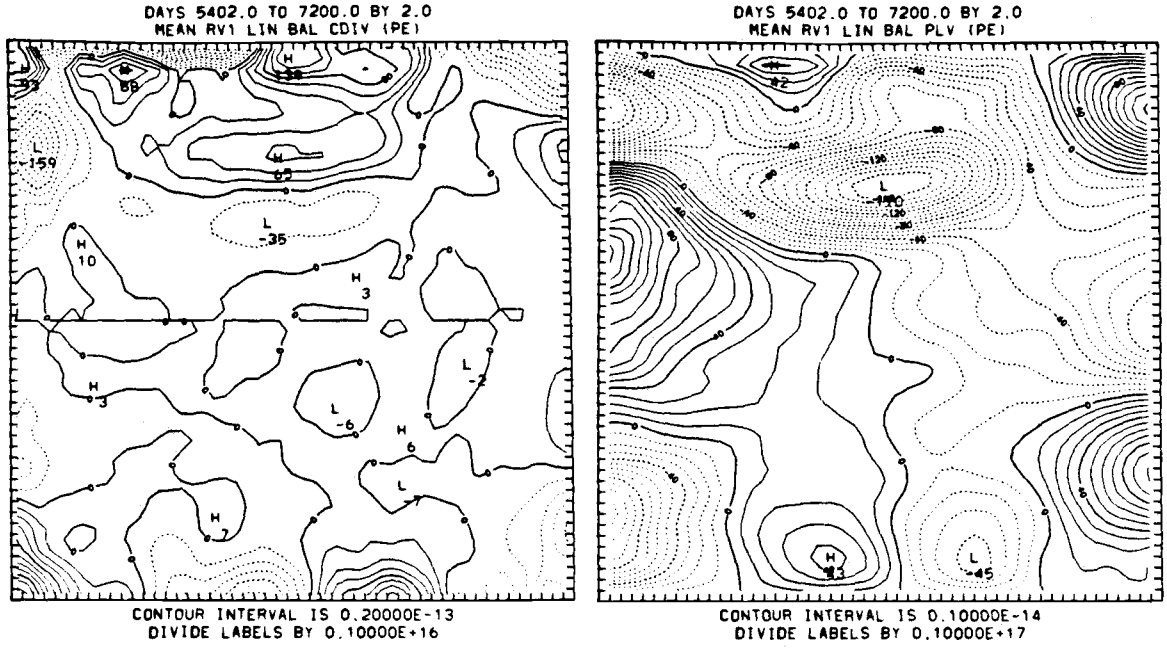

Fig. 5.33 PE spatial distribution of the time-averages of the A_{1LB} terms in Eq. (4-46): a) $-(f-f_o)/h_1)w_2$, b) $-\beta\chi_{1y}$.

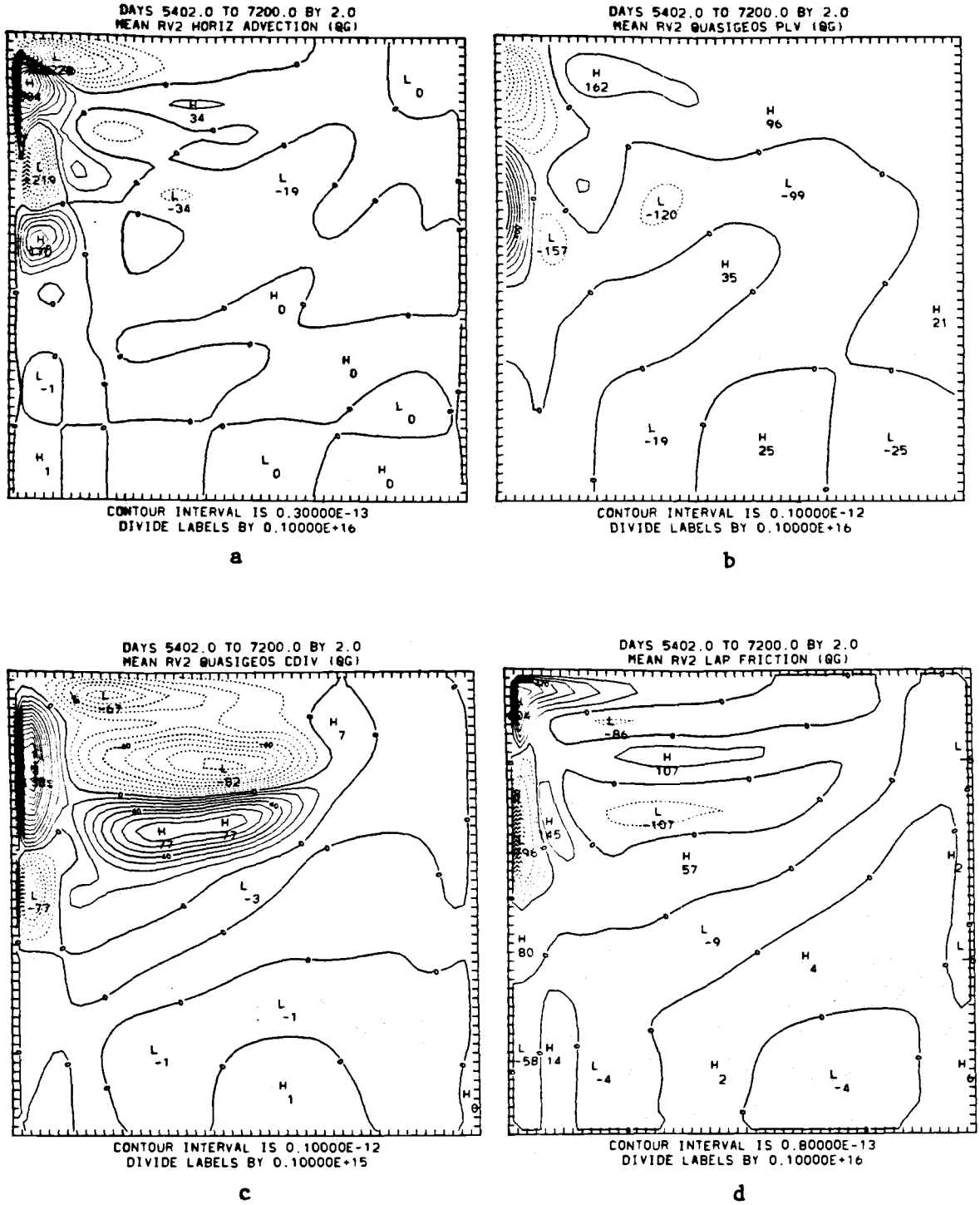

Fig. 5.34 QG spatial distribution of the time-averages of the time-averages of the A_{2QG} terms on the right-hand side of Eq. (4-47): a) $-J(\psi_2,\zeta_2)$, b) $-\beta\psi_{2x}$, c) $(f_o/h_2)w_2$, d) $A_m\nabla^4\psi_2$, e) $-J(\psi_2',\zeta_2')$.

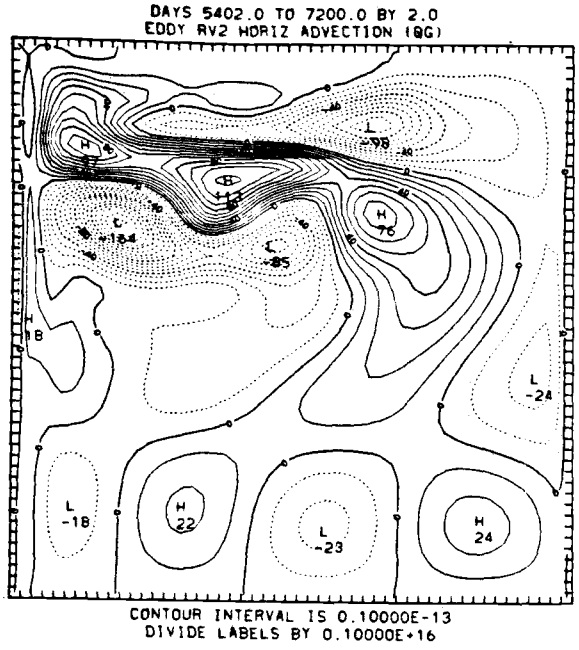

e

Fig. 5.34 (cont.)

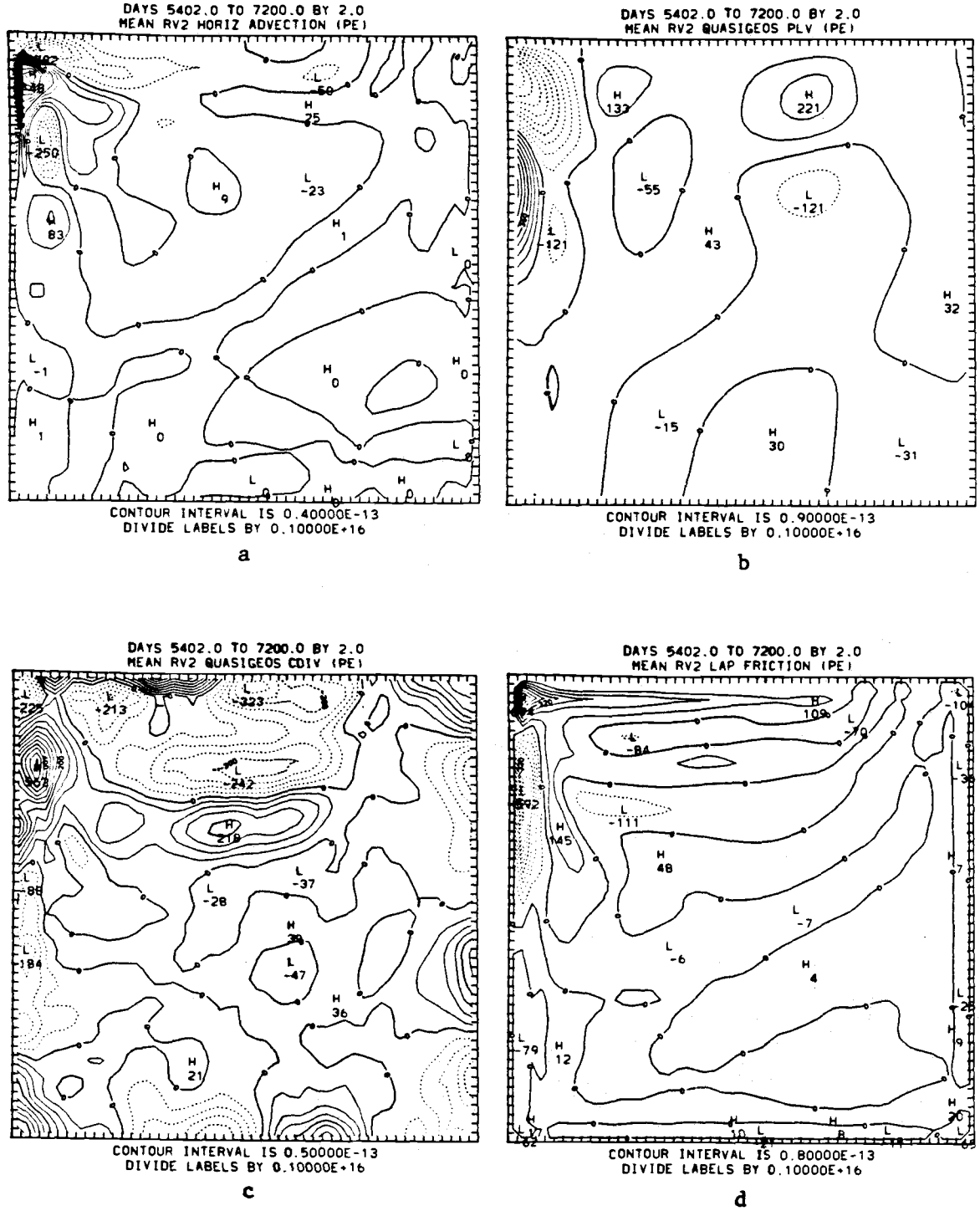

Fig. 5.35 Same as Fig. 5.34, but for the PE model.

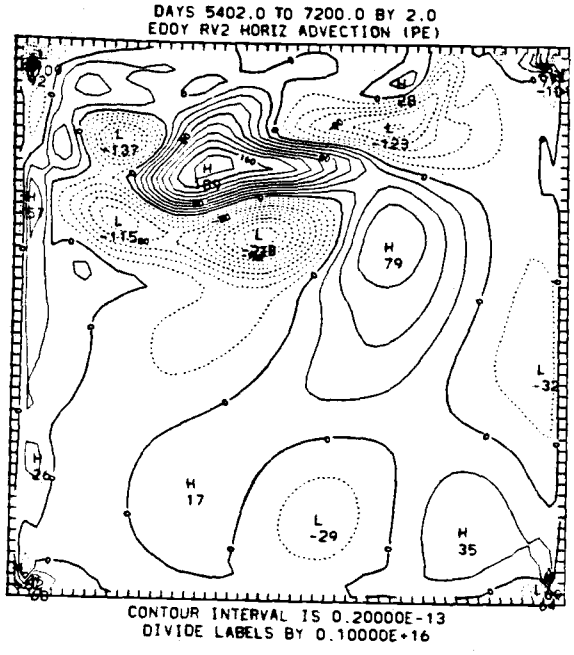

e

Fig. 5.35 (cont.)

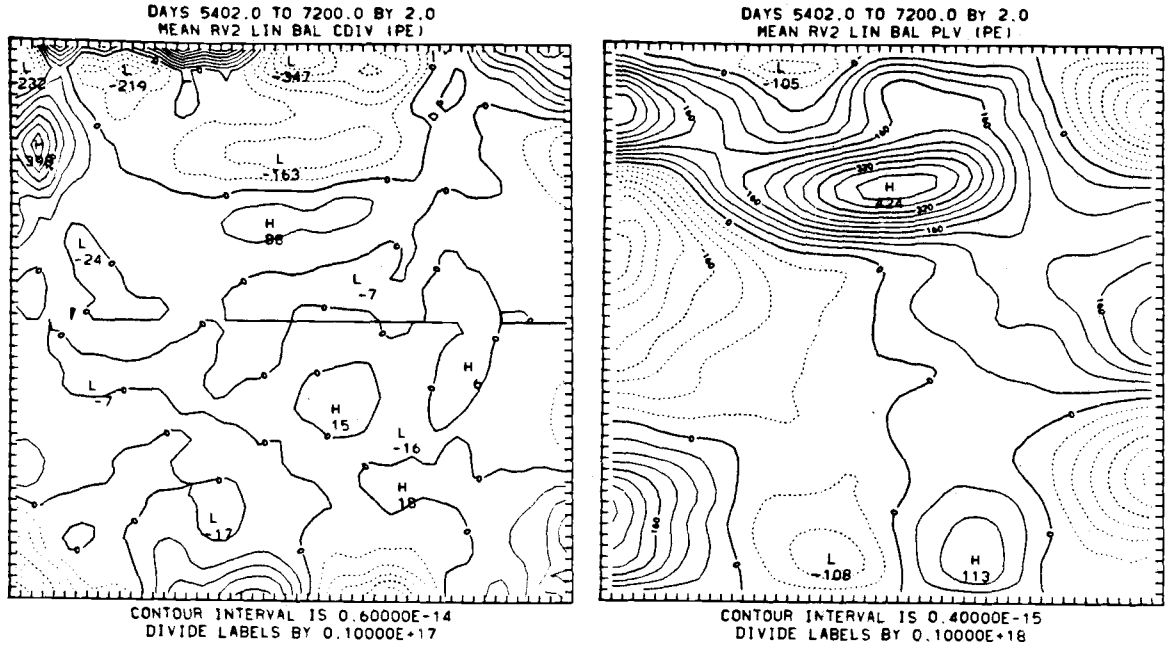

Fig. 5.36 PE spatial distributions of the time-average of the A_{2LB} terms in Eq. (4-47): a) $((f - f_o)/h_2)$, b) $-\beta\chi_{2y}$.

terms in Eq. (4-46) for the QG model (Fig. 5.31). In the western boundary region, the Laplacian friction (Fig. 5.31e) and horizontal advection (Fig. 5.31a) terms tend to increase the counterclockwise vorticity (see Fig. 5.29a), while the planetary vorticity (Fig. 5.31b) tends to decrease it. The stretching term (Fig. 5.31c) is ~15-20% of the other terms, and tends to decrease the vorticity in the northern portion of the western boundary region, and increase it in the southern portion.

In the northern boundary region, the main balances are as follows: 1) in the western portion of the northern boundary, Laplacian friction and the stretching tendency combine to increase the counterclockwise vorticity, while the horizontal advection tends to decrease it, 2) in the central portion of the northern boundary region (near the vicinity of the recirculation region) the planetary vorticity tends to increase the counterclockwise vorticity, while the horizontal advection tends to decrease it.

In the interior and southern portions of the basin, a Sverdrup balance exists, i.e., the planetary vorticity is balanced by the wind stress curl (Fig. 5.31d).

The change of vorticity due to the eddies (Fig. 5.31f) is concentrated in the recirculation region. In this area, the eddies both increase and decrease the vorticity, with the result that the net contribution to the vorticity is small. The maximum amplitudes are an order of magnitude smaller than amplitudes of other terms in the boundary currents, but are of comparable

amplitude in the middle of the recirculation region, where all terms are important (note the contour intervals in Fig. 5.31). These vorticity balances are similar to the vertically-averaged balances obtained by Holland and Lin (1975a), and in some respects to the steady-state cases with strong inertial effects in Veronis (1966).

Fig. 5.32 shows the spatial distribution of the $\overline{A}_{1QG}$ terms in Eq. (4-46) in the PE model. A comparison of Fig. 5.32 with Fig. 5.31 shows similar "mean vorticity tendencies", except for Kelvin wave effects in the boundary regions of the PE model.

Fig. 5.33 shows the geographical distribution of the time-averaged linear balance terms in Eq. (4-46). Except in the recirculation region, both of the linear balance terms are smaller than any of the $\overline{A}_{1QG}$ terms discussed previously. Much of the structure of these patterns is apparently determined by the Kelvin wave behavior, and severe aliasing may be a problem.

The terms $\overline{A}_{1FB}$ and $\overline{A}_{1PE}$ in Eq. (4-46) were calculated as a residual, and shown to be significant. Further analysis is necessary to determine what terms in particular are important. Such analysis also may help to explain why the PE vorticity pattern has generally smaller values of vorticity than the QG model.

The time average of the time rate of change of relative vorticity, i.e., $\nabla^2\overline{\psi}_{1t}$, was also calculated. This term was close to zero, which is to be expected in a statistically steady state.

Fig. 5.34 shows the geographical distribution of the $\overline{A}_{2QG}$ terms in Eq. (4-47) in the QG model. In the northwestern area of the basin, the main balance is between the Laplacian friction (Fig. 5.34d), horizontal advection (Fig. 5.34a), planetary vorticity (Fig. 5.34b), and the stretching term (Fig. 5.34c). The Laplacian friction term tends to increase the counterclockwise vorticity (see Fig. 5.31b), while the other terms tend to decrease it. In the western boundary region, the clockwise vorticity in general tends to be increased by the stretching term, planetary vorticity, and the mean advection terms, and decreased by the Laplacian friction. The clockwise vorticity in the recirculation area tends to be increased by the stretching tendency and eddies (Fig. 5.34e), and decreased by the planetary vorticity and Laplacian friction.

The change of vorticity due to the eddies (Fig. 5.34e) is concentrated in the vicinity of the recirculation region. Along the southeastern, southern and southwestern regions, smaller contributions are discernible. Like the upper layer, the eddies both increase and decrease the vorticity, with the result that the net contribution to the vorticity is small.

Fig. 5.35 shows the geographical distribution of the $\overline{A}_{2QG}$ terms in Eq. (4-47) in the PE model. Again a comparison of Fig. 5.35 with Fig. 5.34 shows similar mean vorticity tendencies, except for Kelvin wave effects in the PE model.

Fig. 5.36 shows the geographical distribution of the time-

averaged linear balance terms in Eq. (4-47). The linear balance planetary vorticity tendency (Fig. 5.36b) increases the vorticity primarily in the recirculation region. The linear balance Coriolis divergence (Fig. 5.36a) increases the vorticity in the northern boundary regions, and decreases it in the recirculation region. Both terms play a minor role in the net balance however.

The terms $\overline{A}_{2FB}$ and $\overline{A}_{2PE}$ in Eq. (4-47) were calculated as a residual. The time average of the time rate of change of relative vorticity for the lower layer, i.e., $\nabla^2\overline{\psi}_{2t}$, was also calculated. As in the upper layer, the residual terms were significant, whereas the latter term was small.

5.5.2 Potential vorticity

The geographical distributions of the QG and PE time-averaged quasigeostrophic potential vorticity for the upper and lower layers are shown in Figs. 5.37 and 5.38, respectively. In the upper layer the following features are discernible: 1) sharp gradients or "tongues" of potential vorticity near the western boundary and northeastern regions, 2) uniform regions of potential vorticity in the recirculation region, and 3) a gradual northward increase of potential vorticity in the eastern, interior, and southern portions of the basin. In the lower layer the following features can be seen: 1) a gradual northward increase of potential vorticity throughout most of the

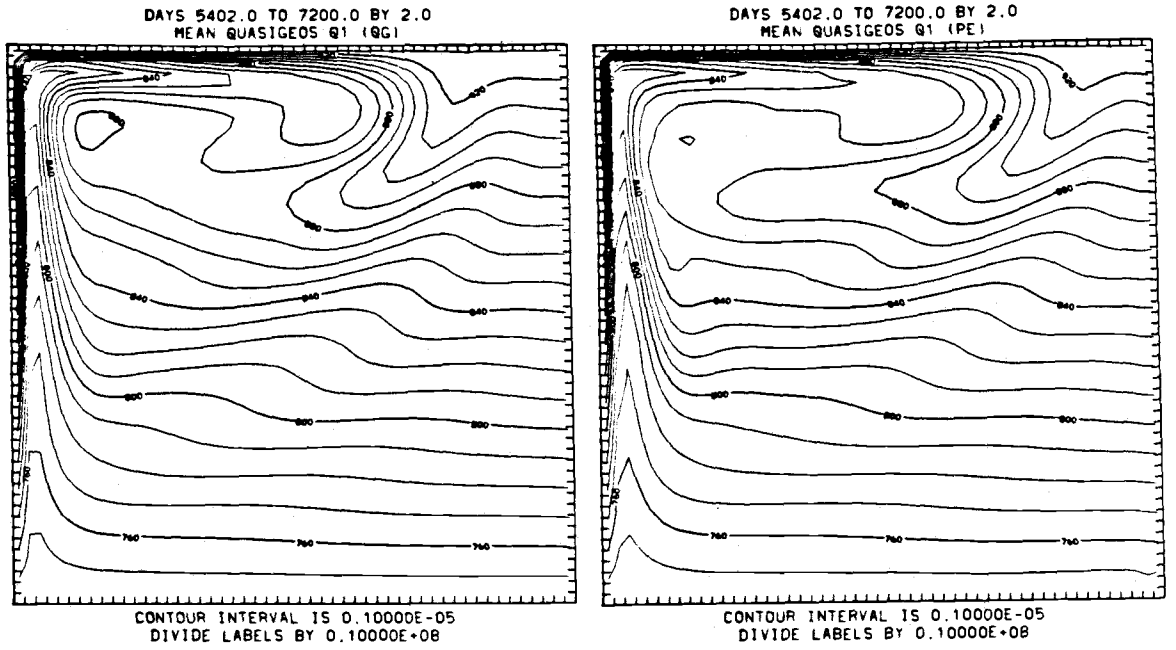

Fig. 5.37 Time-mean of Entry 22 in Table 4.1: a) Q_{1QG} (QG), b) Q_{1QG} (PE).

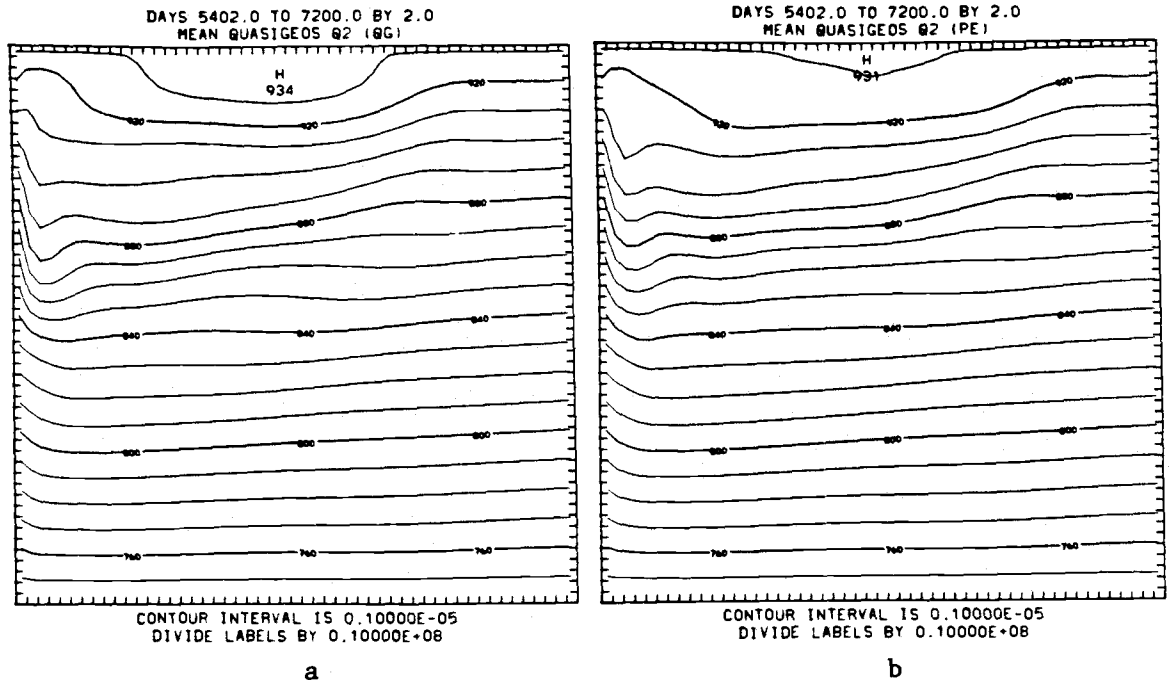

Fig. 5.38 Time-mean of Entry 23 in Table 4.1: a) Q_{2QG} (QG), b) Q_{2QG} (PE).

basin, 2) a uniform region of potential vorticity in the northern boundary region, and 3) a southward extending tongue of potential vorticity in the northern portion of the western boundary region. It should be noted that the reason that the potential vorticity patterns are so similar is that only the lowest order component (i.e., the quasigeostrophic) component has been calculated for the PE model. Analysis of the higher order components in the PE model is necessary in order to address differences.

5.6 Eddy momentum transports

The zonally-averaged off-diagonal component of the eddy momentum transports in each layer for both models are shown in Figs. 5.39 and 5.40. The main contribution in the PE model is by the rotational component, which is generally larger than the QG. In some areas the $\overline{u'v'}$ correlations tend to retard the mean flow, whereas in other areas they tend to drive it. Such correlations, as a result, may be unimportant as momentum transports, compared to other terms, but they are signatures of the instability.

5.7 PE heat transports

5.7.1 Meridional heat transports

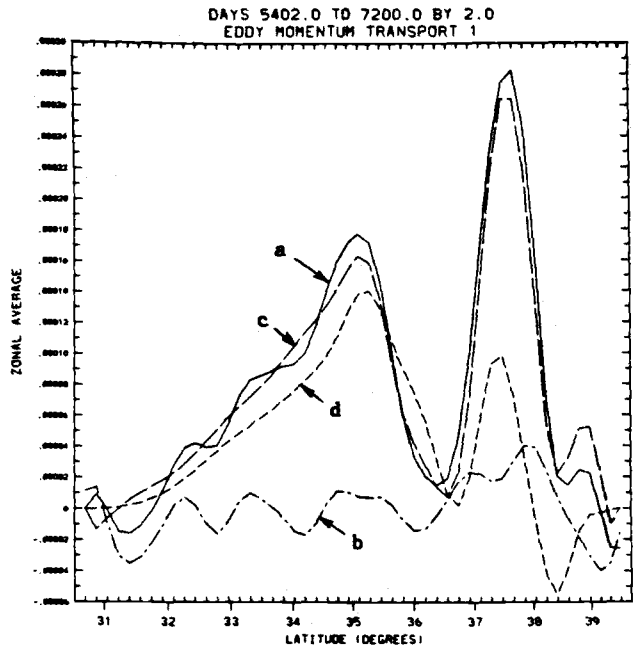

Fig. 5.39 Time-mean of the zonally-averaged eddy momentum transports in the upper layer: a) u_1v_1, b) $\chi_{1x}\chi_{1y}$, c) $-\psi_{1y}\psi_{1x}$ (PE), d) $-\psi_{1y}\psi_{1x}$ (QG).

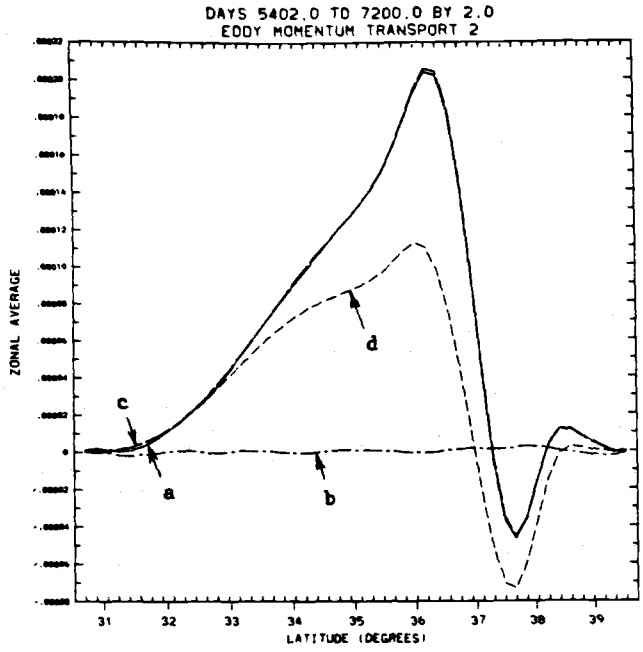

Fig. 5.40 Time-mean of the zonally-averaged eddy momentum transports in the lower layer: a) u_2v_2, b) $\chi_{2x}\chi_{2y}$, c) $-\psi_{2y}\psi_{2x}$ (PE), d) $-\psi_{2y}\psi_{2x}$ (QG).

The spatial distribution of the time-mean and eddy, meridional heat transports in each layer and for both layers is shown in Figs. 5.41-5.46. In general, the eddies act against the mean transport of heat. Eddy heat transport occurs in the recirculation regions, and along the western and eastern boundaries. For each layer, both divergent and rotational components are significant in local eddy heat transports.

The main contribution for eddy heat transport by the rotational component is in the recirculation region, an area noted by Gill (1983) to be of possible importance for eddy-equatorward transports of heat. Fig. 5.47, which shows the vertically-integrated and zonally-averaged, time-mean and eddy, meridional heat transports (obtained from vertically integrating and zonally averaging the PE temperature equations (4-29)) emphasizes the mean-poleward and eddy-equatorward transports of heat in this region. The slight imbalances seen in Fig. 5.47 are due to the transport of heat by biharmonic heat diffusion processes.

The main contribution for eddy meridional heat transport by the divergent component is along the western and eastern boundaries, and is due to the Kelvin waves. Since there would also be eddy zonal heat transports along the northern and southern boundaries by the Kelvin waves, these divergent components represent a "circular" flux around the basin perimeter and may play little role in the actual eddy heat transports. A more detailed discussion of these waves and their transports is given in Chapter 7.

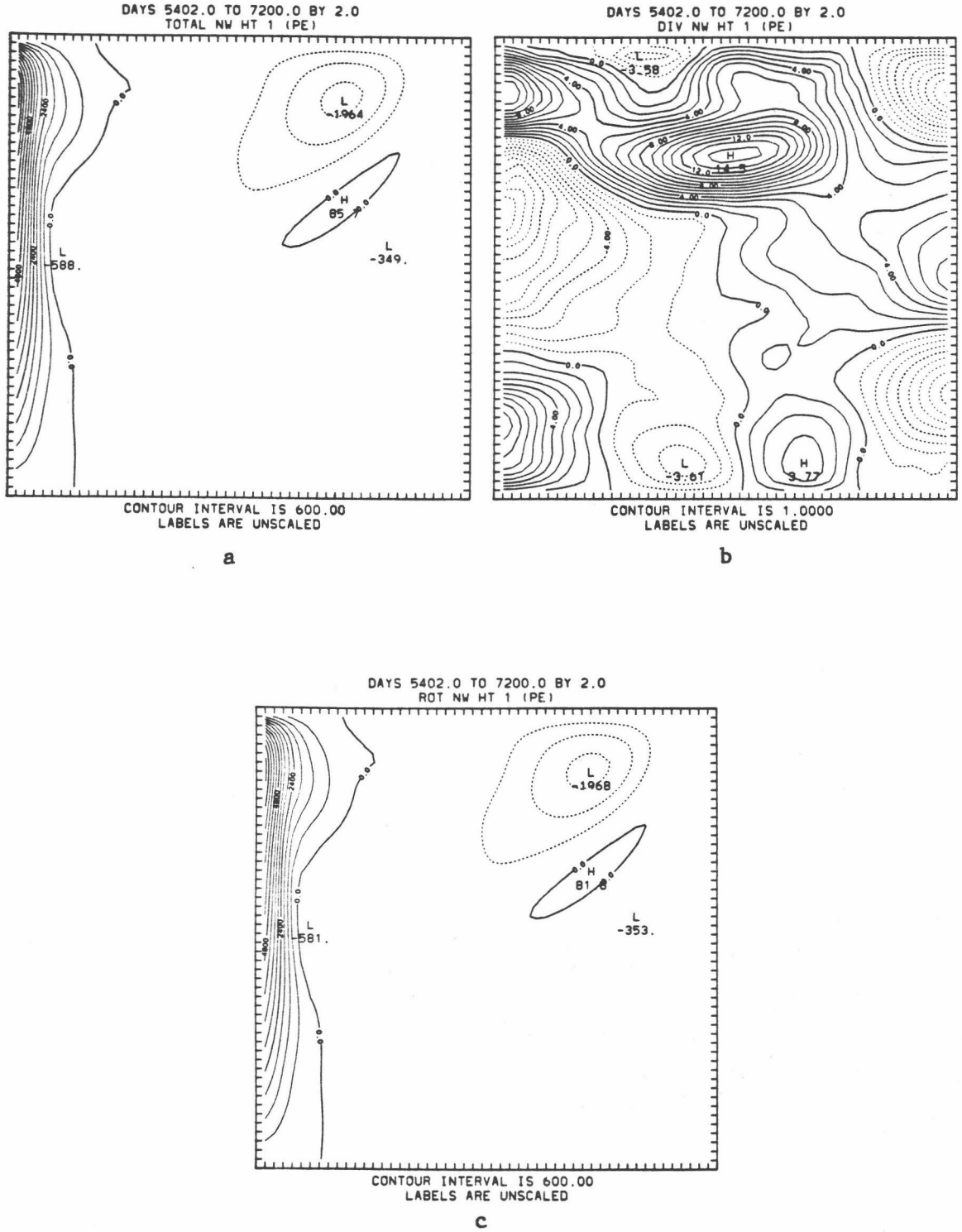

Fig. 5.41 Spatial distribution of the time-averaged, meridional heat transport in the upper layer: a) $h_1 v_1 T_1$, b) $h_1 \chi_{1y} T_1$, c) $h_1 \psi_{1x} T_1$.

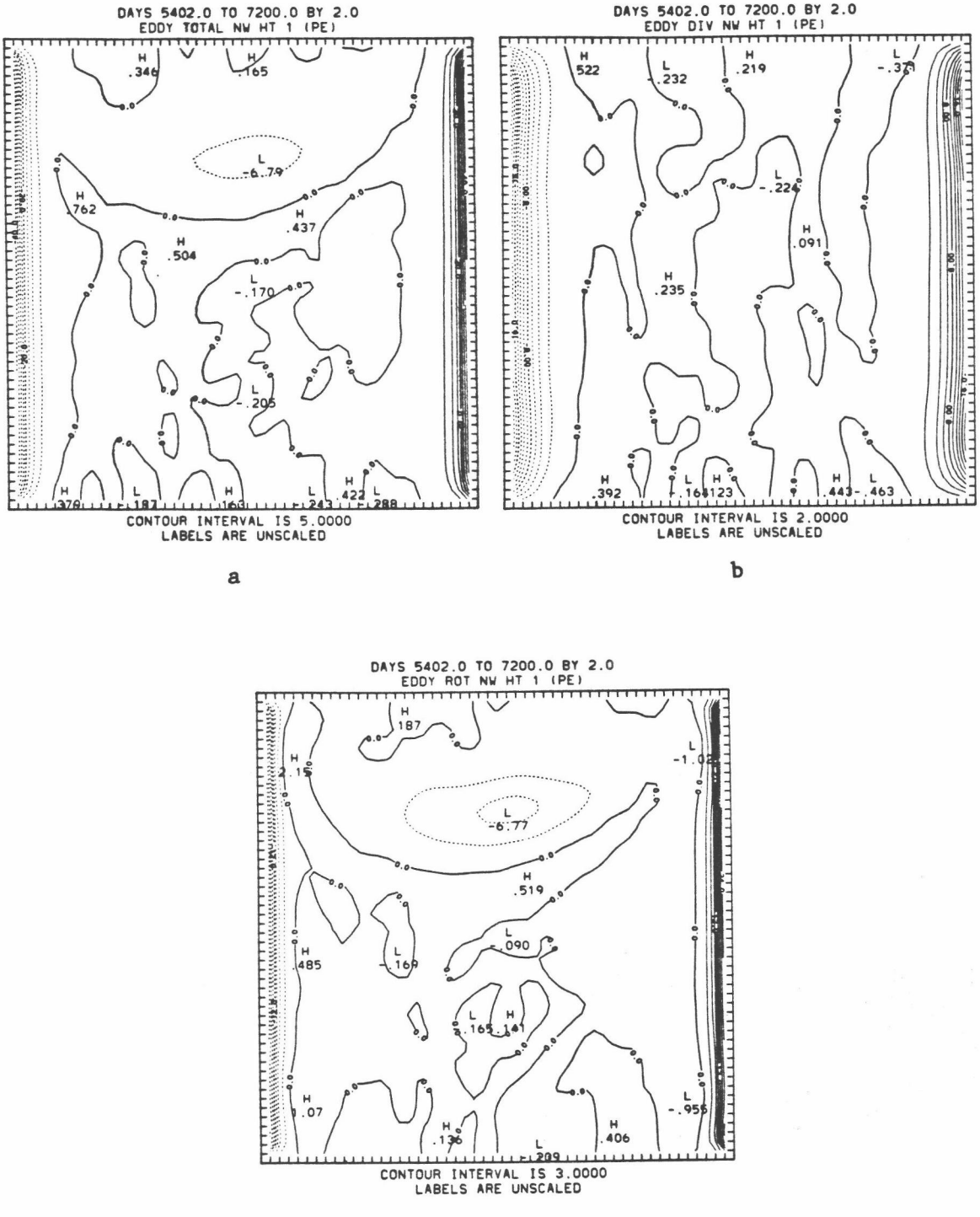

Fig. 5.42 Spatial distribution of the eddy meridional heat transport in the upper layer: a) $h_1 v_1 T_1$, b) $h_1 \chi_{1y} T_1$, c) $h_1 \psi_{1x} T_1$.

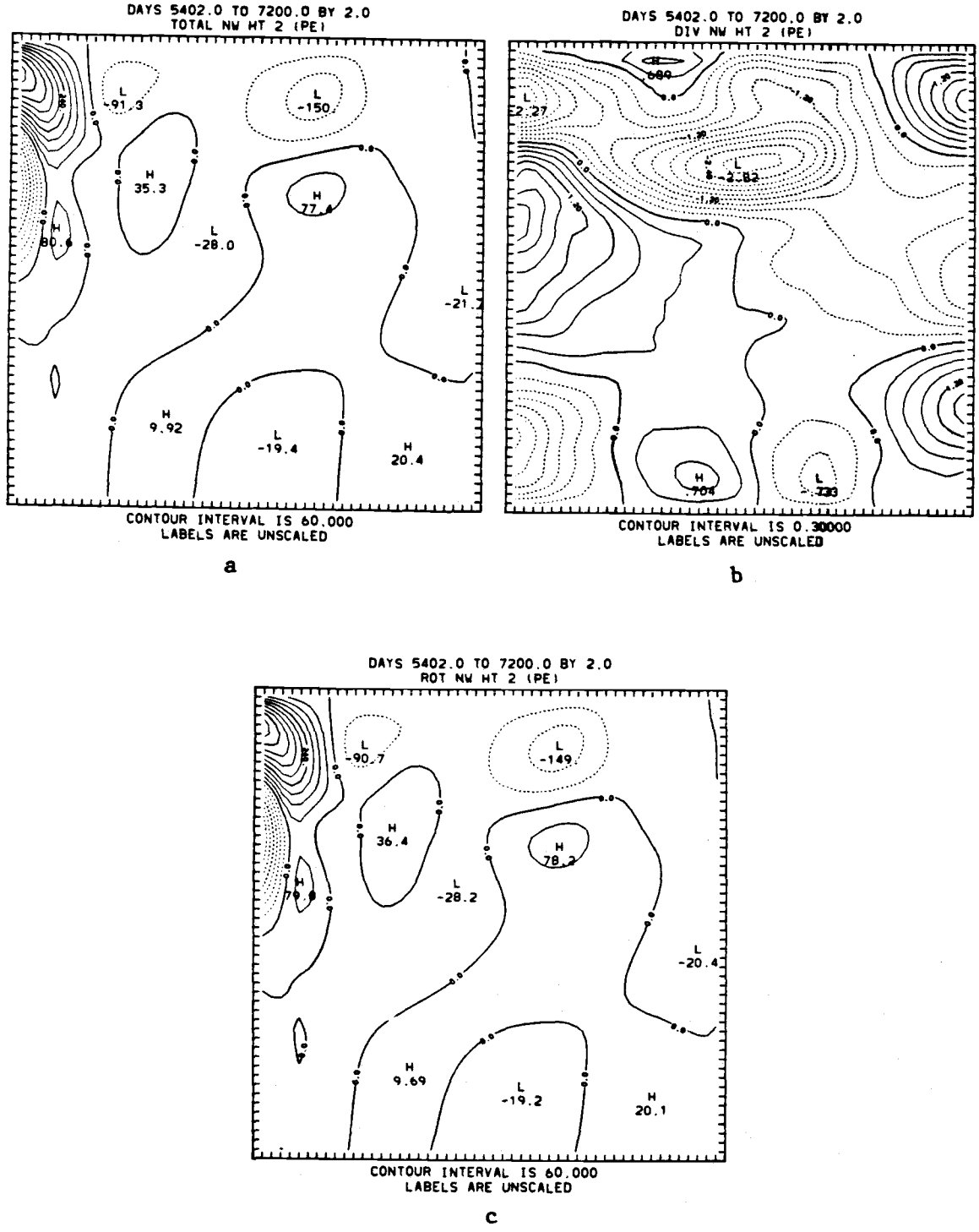

Fig. 5.43 Spatial distribution of the time-averaged meridional heat transport in the lower layer: a) $h_2 v_2 T_2$, b) $h_2 \chi_{2y} T_2$, c) $h_2 \psi_{2x} T_2$.

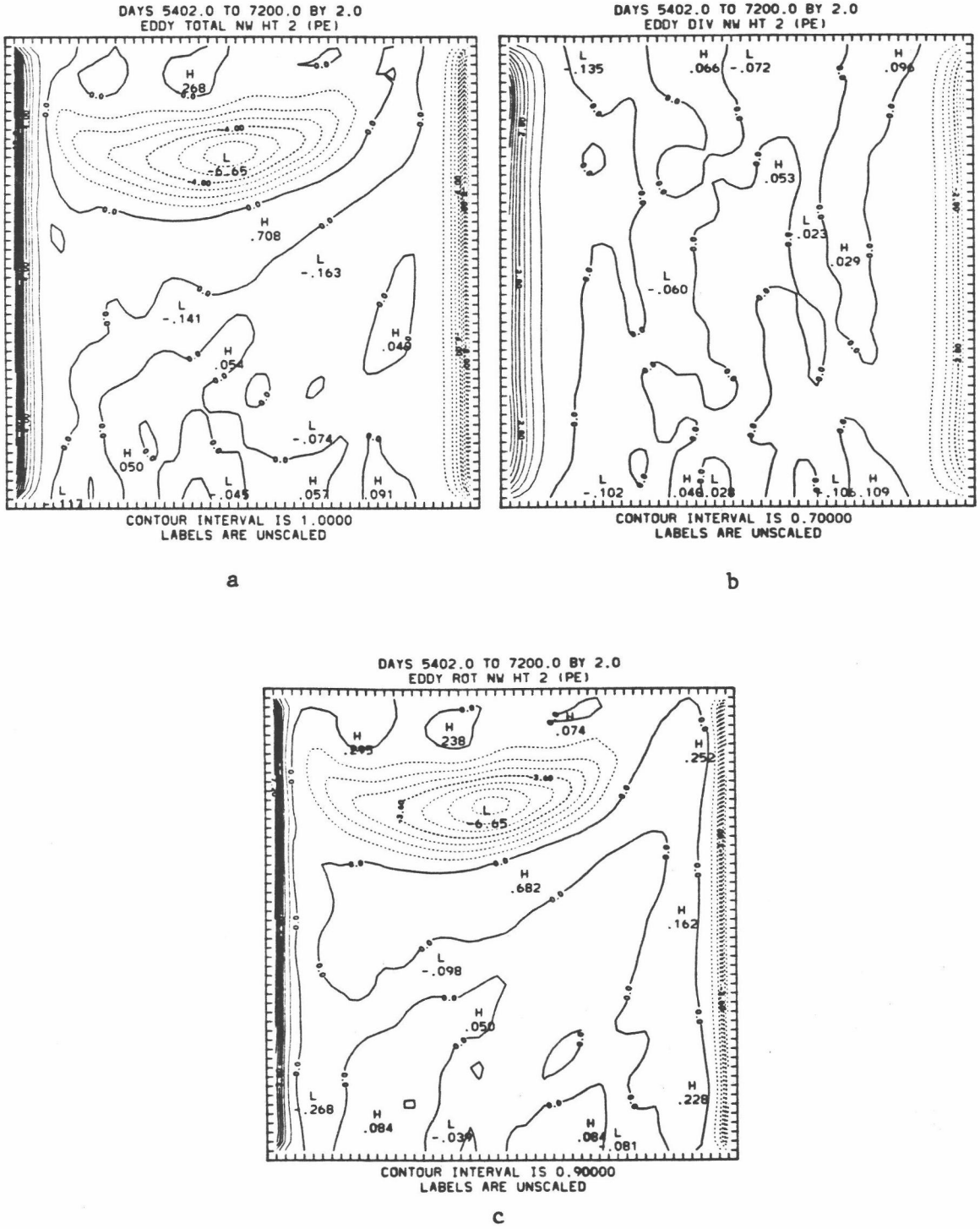

Fig. 5.44 Spatial distribution of the eddy meridional heat transport in the lower layer: a) $h_2 v_2 T_2$, b) $h_2 \chi_{2y} T_2$, c) $h_2 \psi_{2x} T_2$.

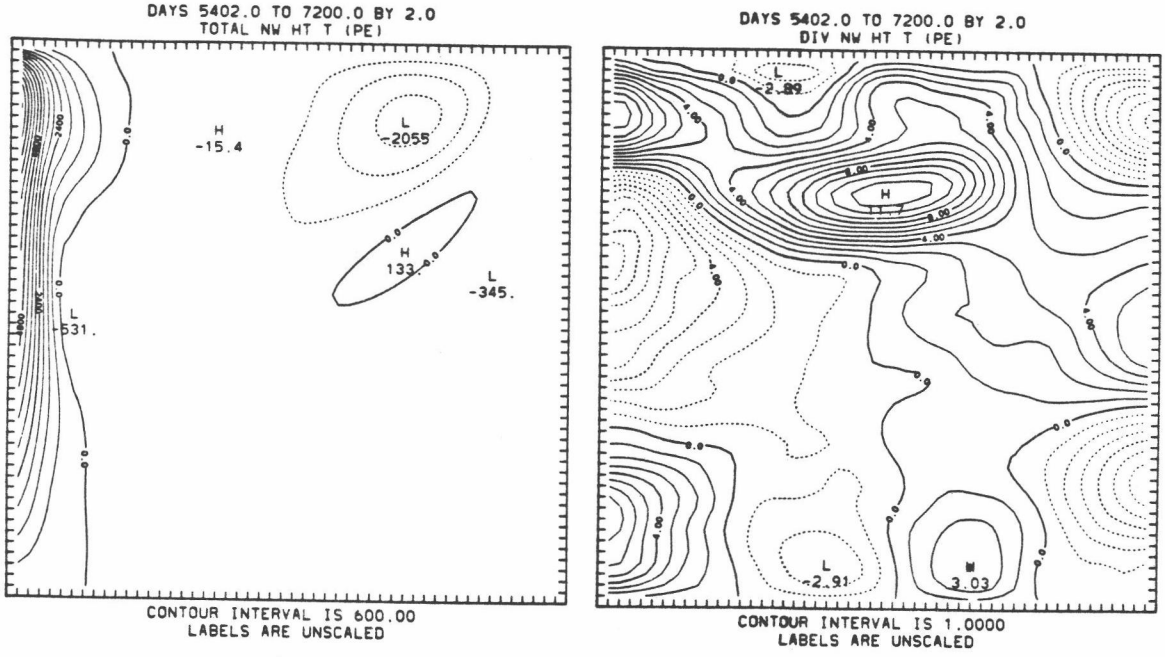

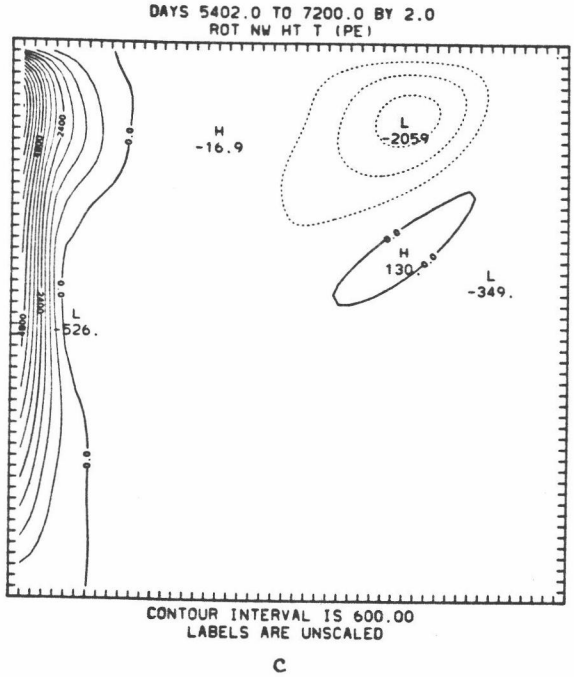

Fig. 5.45 Spatial distribution of the time-averaged, meridional heat transport summed for both layers: a) $h_1 v_1 T_1 + h_2 v_2 T_2$, b) $h_1 \chi_{1y} T_1 + h_2 \chi_{2y} T_2$, c) $h_1 \psi_{1x} T_1 + h_2 \psi_{2x} T_2$.

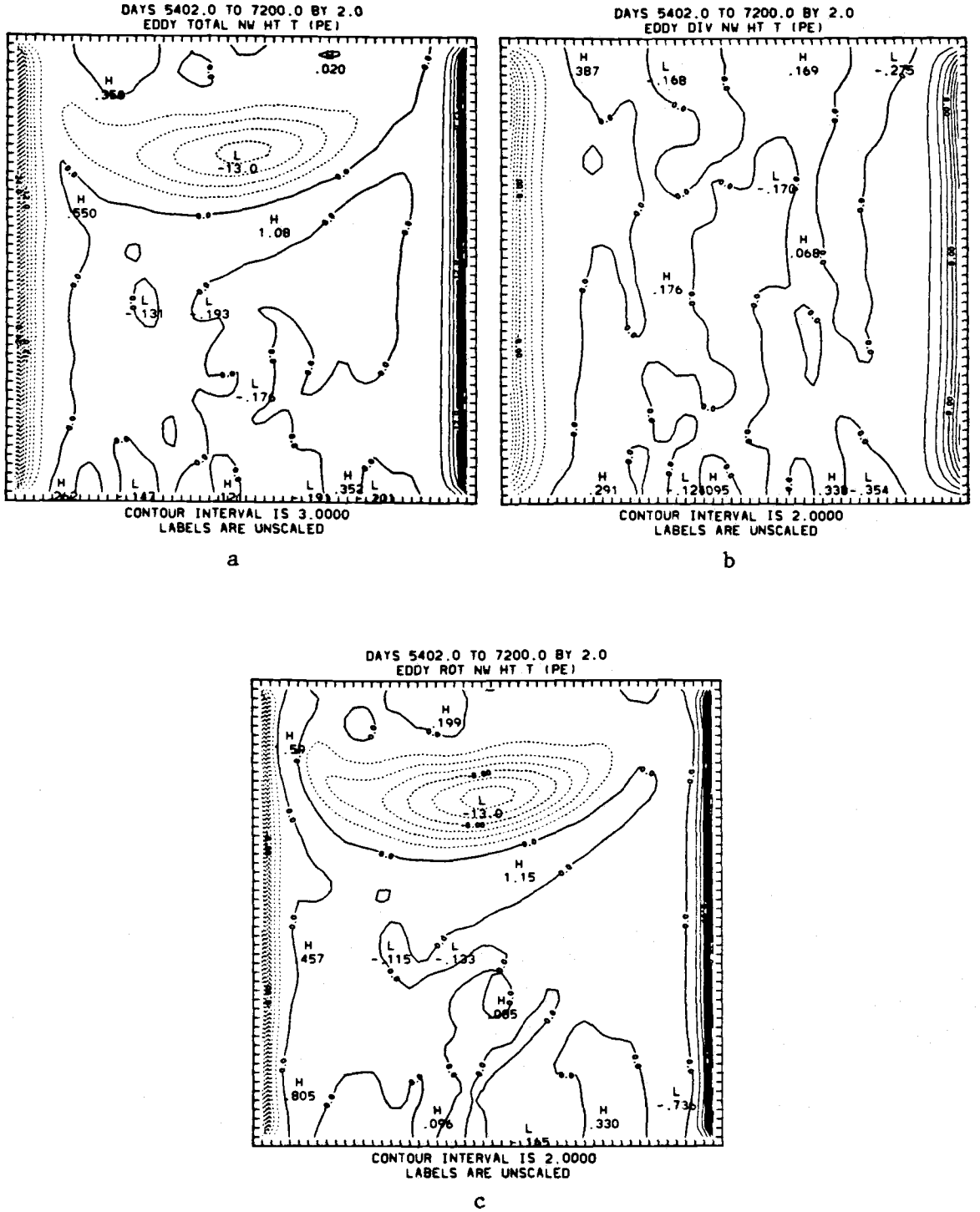

Fig. 5.46 Spatial distribution of the eddy meridional heat transport summed for both layers:
a) $h_1 v_1 T_1 + h_2 v_2 T_2$, b) $h_1 \chi_{1y} T_1 + h_2 \chi_{2y} T_2$,
c) $h_1 \psi_{1x} T_1 + h_2 \psi_{2x} T_2$.

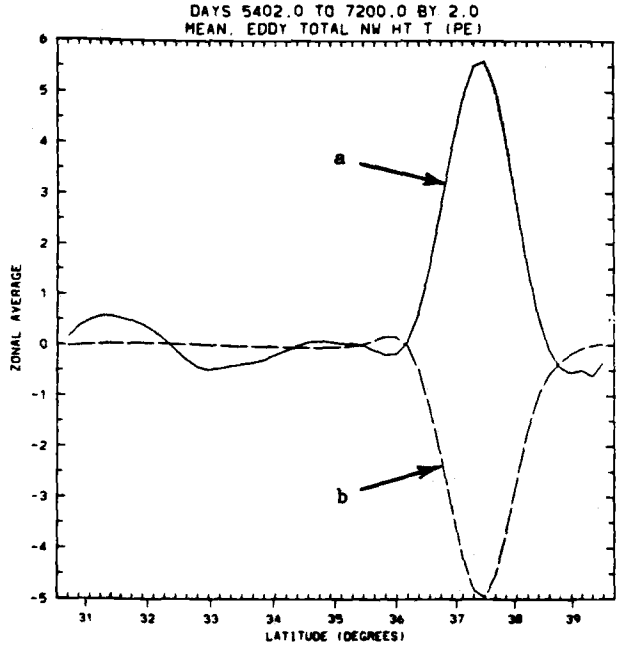

Fig. 5.47 Zonal average of the a) time-mean and b) eddy, vertically-integrated, meridional heat transport.

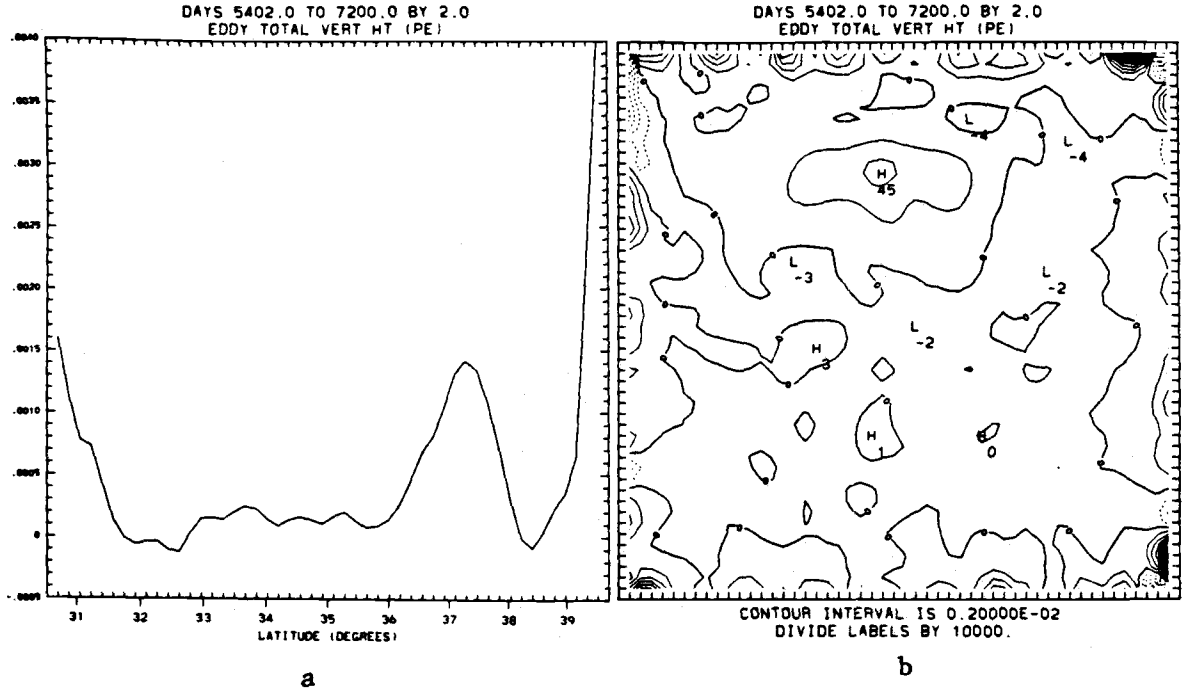

Fig. 5.48 Zonal average (a) and spatial distribution (b) of the time-mean, vertically-integrated, vertical heat transport.

5.7.2 Vertical heat transports

The vertically-integrated, time-mean vertical heat transport is shown in Fig. 5.48. The presence of positive vertical heat transport in the recirculation region is associated with baroclinic instability. The concentration of vertical heat transport in the northeastern portion of the basin is likely a reflection of the long-term adjustment process, in which the ocean temperature field is responding to long-time scale, vertical diffusion processes.

CHAPTER 6. RESULTS OF THE DOUBLE-GYRE EXPERIMENT

We now show some results from the double-gyre PE and QG experiments. These experiments differ from the previous experiments in the following respects: 1) a double-gyre wind forcing is used, with the result that the northern boundary of the single-gyre experiment is replaced by a free jet at mid-latitudes, 2) the north-south extent of the basin is increased from 1000 to 2000 kilometers, and 3) bottom friction is incorporated. A summary of the parameters used in the experiment is given in Table 6.1.

As in the single-gyre experiment, the initial state of the experiment consisted of a horizontally uniform temperature stratification with no motion. The same initial temperatures as in the single-gyre experiment were used, i.e., 16.06°C for the upper layer and 3°C for the lower layer.

6.1 Spin-up and statistical equilibrium

Figs. 6.1 and 6.2 show the time-dependent behavior of the energetics for the QG and PE models, respectively. As shown in Fig. 6.1, during the first 1300 days the spin-up process is characterized by an increase in both the upper layer kinetic energy and available potential energy (not shown). The lower layer remains nearly motionless. After ~1300 days available

Table 6.1 Summary of parameters used in the double-gyre experiment

PARAMETER Symbol	Units	VALUE	MODEL
h_1	m	1000	Both
h_2	m	4000	Both
Δ	km	20	Both
L	km	1000	Both
D	km	2000	Both
A_m	$m^2 s^{-1}$	330	Both
B_H	$10^{-10} m^4 s^{-1}$	1.0	PE
B_H	$10^{-10} m^4 s^{-1}$	0.0	QG
C_B	$10^{-7} s^{-1}$	1.0	Both
τ_o	$10^{-4} m^2 s^{-1}$	1.0	Both
g'	$10^{-2} ms^{-2}$	2.0	QG
g	ms^{-2}	9.8	PE
α	$10^{-4} °C^{-1}$	2.0	PE
f_o	$10^{-5} s^{-1}$	9.374	Both
β_o	$10^{-11} m^{-1} s^{-1}$	1.754	Both
R_d	km	13	Both
κ	$10^{-4} m^2 s^{-1}$	1.0	PE

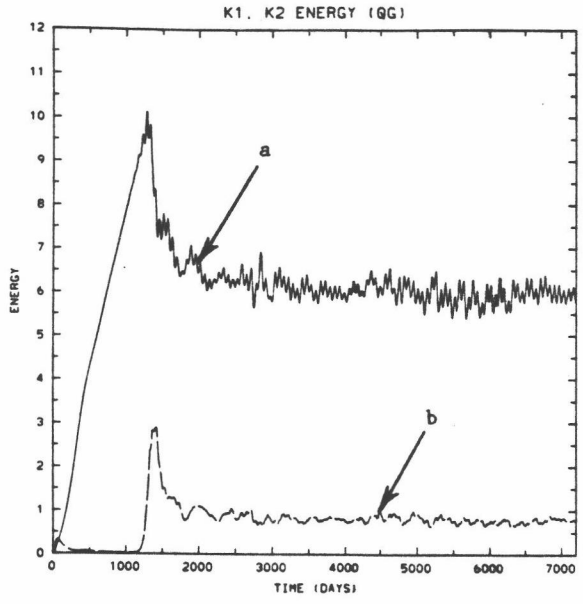

A

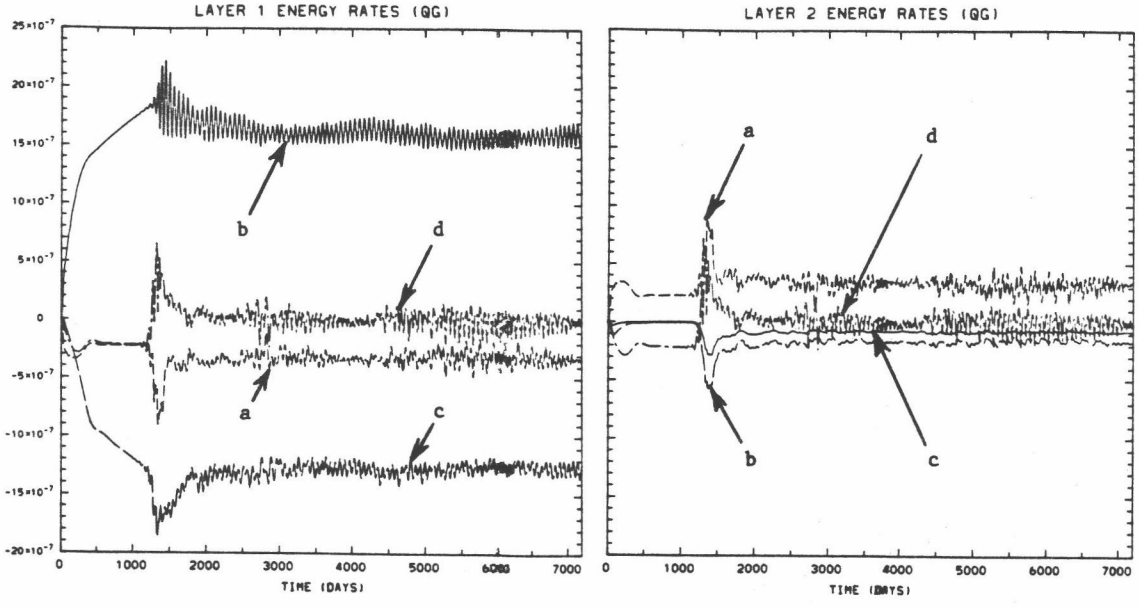

B C

Fig. 6.1 The time-dependent energetics for the QG double-gyre experiment. A) Energy per unit area showing: upper layer kinetic energy (a), lower layer kinetic energy (b). B) Energy fluxes into the upper layer: (a) $\{K_2 \rightarrow K_1\}$, (b) $\{\tau \rightarrow K_1\}$, (c) $\{K_1 \rightarrow D_{H1}\}$, (d) $\{P \rightarrow K_1\}$. C) Energy fluxes into the lower layer: (a) $\{K_1 \rightarrow K_2\}$, (b) $\{K_2 \rightarrow D_{H2}\}$, (c) $\{K_2 \rightarrow D_B\}$, (d) $\{P \rightarrow K_2\}$.

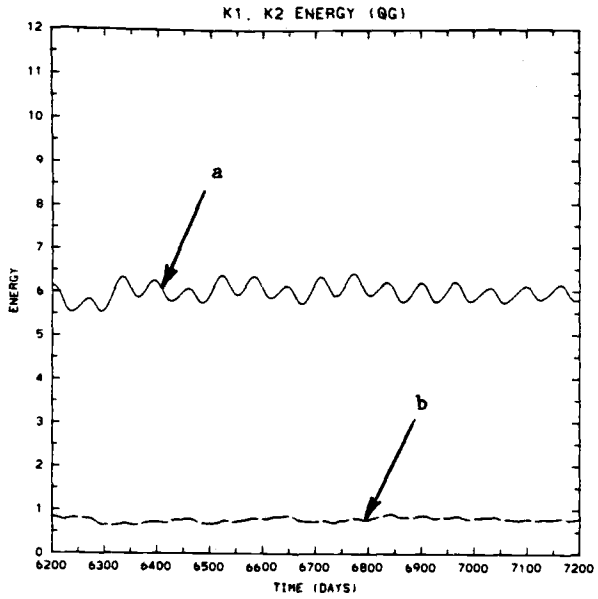

D

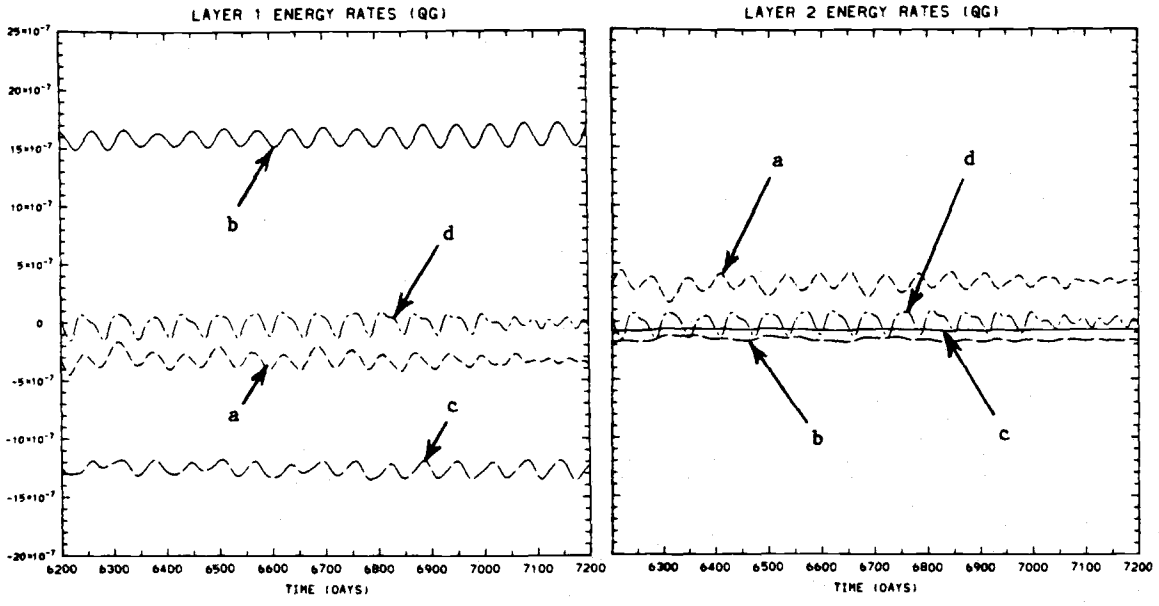

E F

Fig. 6.1 (cont.)
D), E), F) Same as A), B), C) but expanded time scale for last 1000 days.

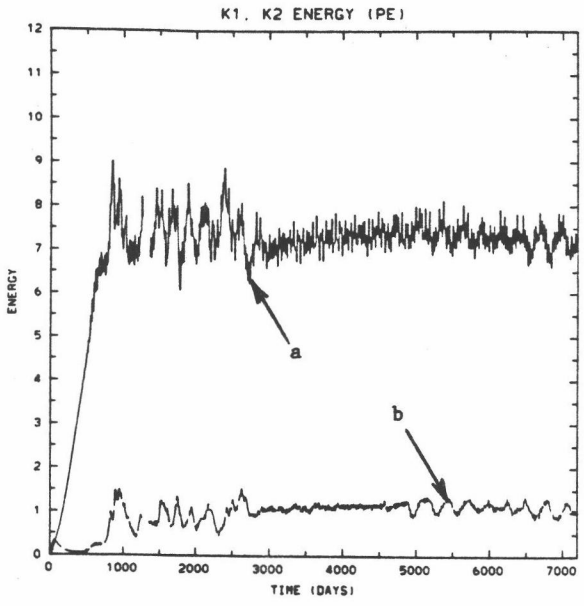

A

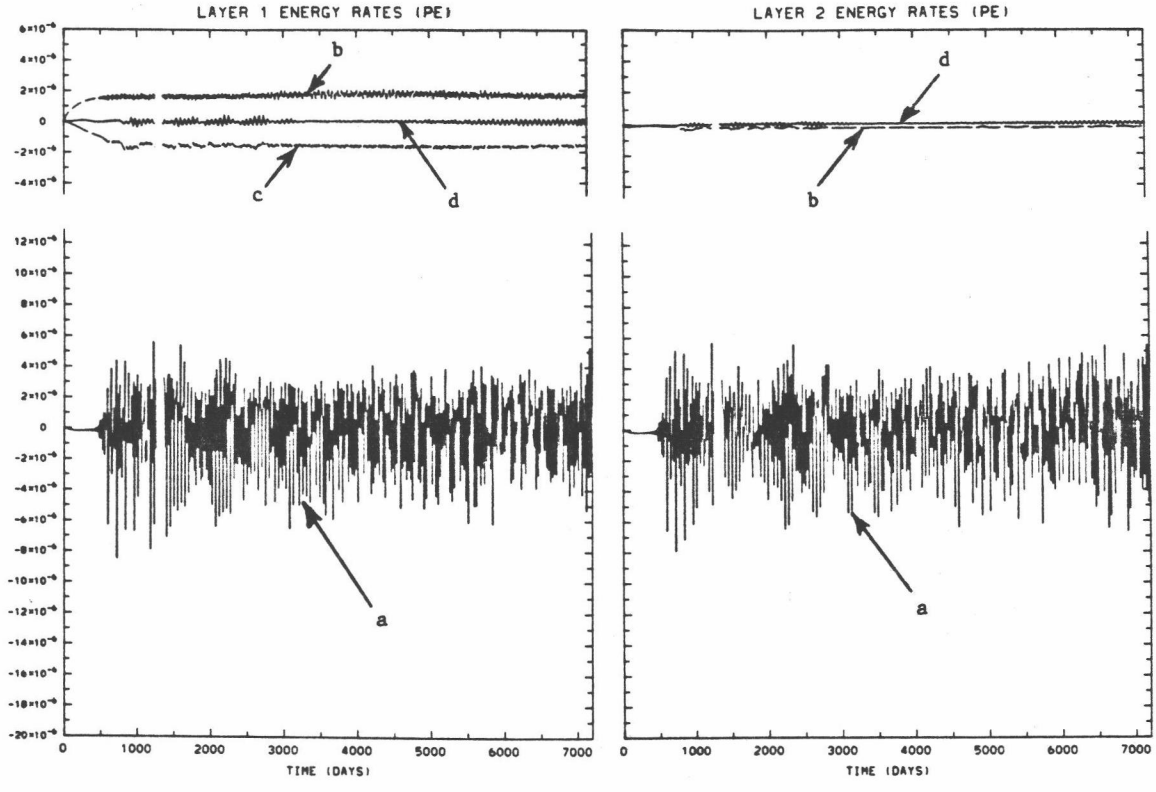

B C

Fig. 6.2 Same as Fig. 6.1, but for the PE experiment. The bottom friction is not plotted.

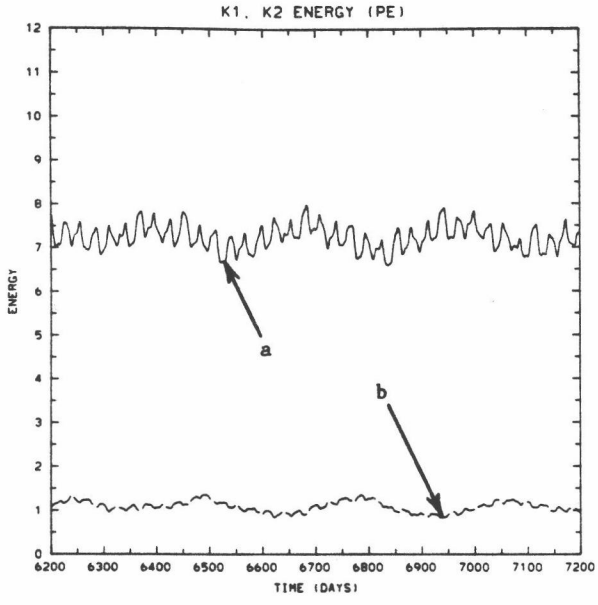

D

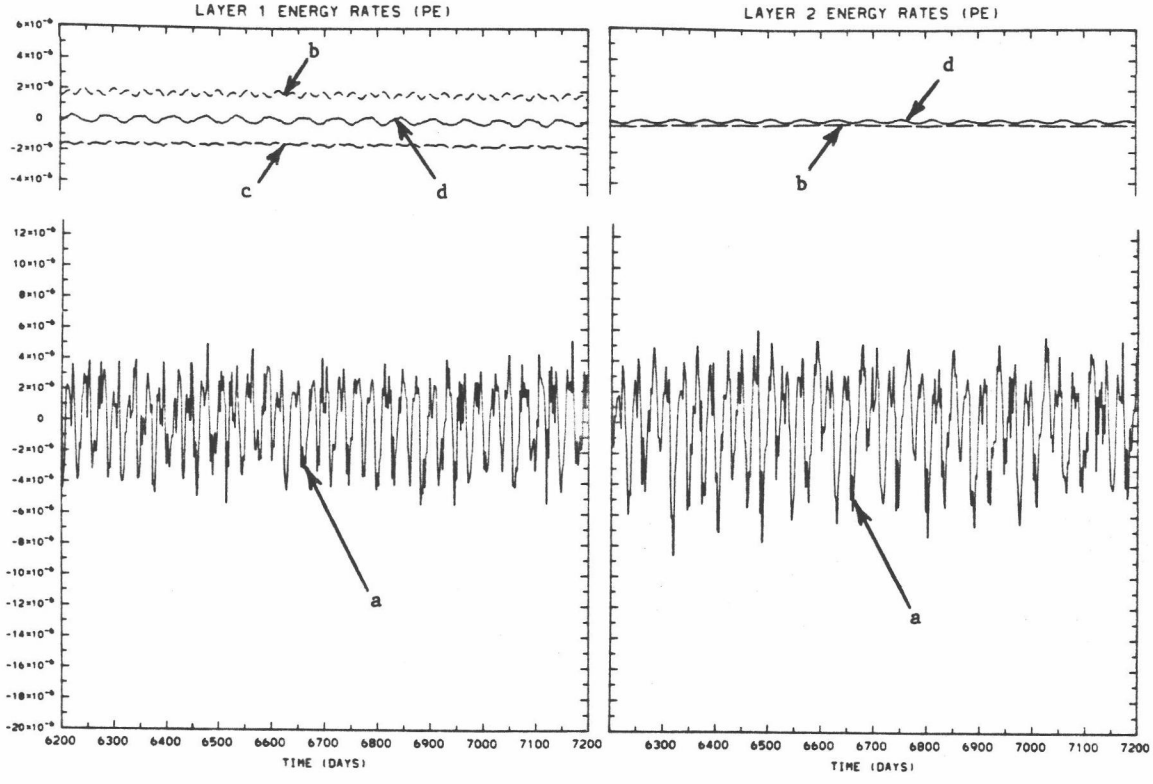

E F

Fig. 6.2 (cont.)

potential energy begins to be released and gives rise to eddy motions, which generate deep mean flows in the lower layer via energy transfers from the upper to the lower layer. After ~5000 days the system has come into a quasi-statistically steady state.

As in the single-gyre experiment, only the fast-time scale is in statistical equilibrium for the PE model. The long-term scale is not in equilibrium: there is a very slow continuing adjustment as the static stability changes on a long time scale.

A comparison of Figs. 6.1 and 6.2 shows similar energies and energy transfer rates. The main differences are: 1) the spin-up time for the PE model is shorter (~900 days compared to ~1300 days), 2) kinetic energies for both layers are slightly higher for the PE model, and 3) the PE model has high frequency oscillations.

A comparison of the QG single-gyre (Fig. 5.1) and double-gyre (Fig. 6.1) time-dependent energetics, which are horizontally-averaged over the respective basin, shows the following: 1) a much larger available potential energy level and a smaller lower layer kinetic energy level in the double-gyre, and 2) more irregular oscillations in the double-gyre energies and energy transfer rates. The irregularity in the equilibrium oscillations can be accounted for since Holland (1978) has shown that the free jet contributes an additional source of instability in double gyres; the eddy field is no longer so simple.

A comparison of the PE single-gyre (Fig. 5.2) and double-gyre (Fig. 6.2), time-dependent energetics shows similar energies and energy transfer rates. The main differences are : 1) much smaller amplitude in the variability of $\{P \rightarrow K_1\}$ and $\{P \rightarrow K_2\}$ transfer rates in the double gyre (note that the ordinates for both experiments have the same scales), and 2) smaller lower layer kinetic energy in the double gyre. These smaller values could be due to the additional dissipation mechanism, i.e., bottom friction, in the double-gyre experiment.

These results will be further analyzed in Section 6.4.

6.2 Basic comparison quantities

In order to assess similarities and differences, in both models and experiments, the basic time-averaged PE and QG quantities are compared with each other, and with the corresponding single-gyre quantities. Again the period of time averaging is for five years, using two-day sampling intervals.

Fig. 6.3 shows the time-averaged upper layer streamfunctions. Both subtropical anticyclonic and subpolar cyclonic gyres show up as expected from the imposed surface wind stress pattern. A comparable free jet exists at mid-latitudes, which draws off more boundary-current fluid to the south than to the north. As Holland (1978) has pointed out, barotropic instabilities are likely to occur in this free jet region, resulting in a different stability problem than in the single-gyre

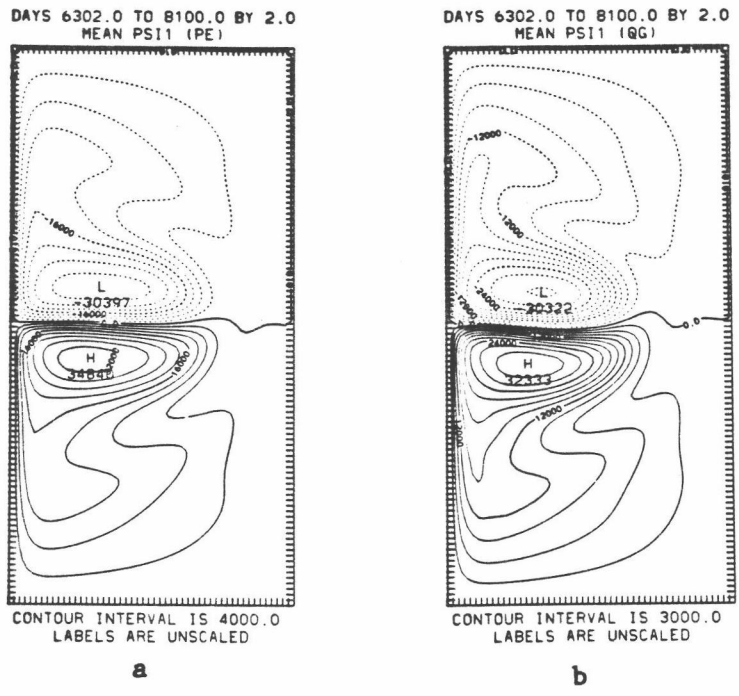

Fig. 6.3 Time-mean of entry 1 in Table 4.1: ψ_1 for a) PE, b) QG.

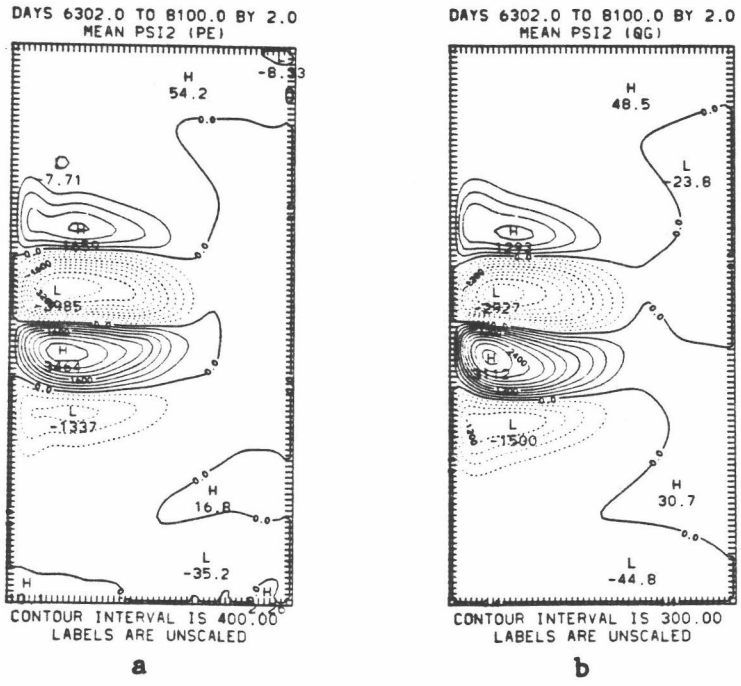

Fig. 6.4 Time-mean of entry 2 in Table 4.1: ψ_2 for a) PE, b) QG.

experiment. Comparable linear, Sverdrup circulations are obtained in the interior and eastern portions of the basin. The basic difference in the plots is the slightly greater intensity of the subpolar low and subtropical high in the PE model. A comparison of Figs. 5.3 and 6.3 for both models shows a similar anticyclonic gyre, which is more intense in the double-gyre case.

Fig. 6.4 shows the time-averaged lower layer streamfunctions. Again, the circulation patterns are quite similar. There is a pair of inertial gyres with non-linear circulations near the free jet region with counter-rotating cells adjacent to each gyre. Holland and Rhines (1980) have explained that the presence of the four gyres arises from the minimum of the lower layer eddy potential vorticity flux at mid-basin, which separates two broad maxima. This minimum is directly attributable to the "flat" region in the lower layer mean potential vorticity (see Fig. 6.29).

Fig. 6.5 shows the time-averaged velocity potential for the upper and lower layers of the PE model. Again it is important to note that χ_1 and χ_2 are really just the same except for sign and scaling. The largest values are in the western boundary current as it approaches separation. This same feature is discernible in the single-gyre velocity potential (Fig. 5.5), which is twice as intense as the double-gyre. As in the single-gyre case, the velocity potential is much smaller in magnitude than either the upper or lower layer streamfunction.

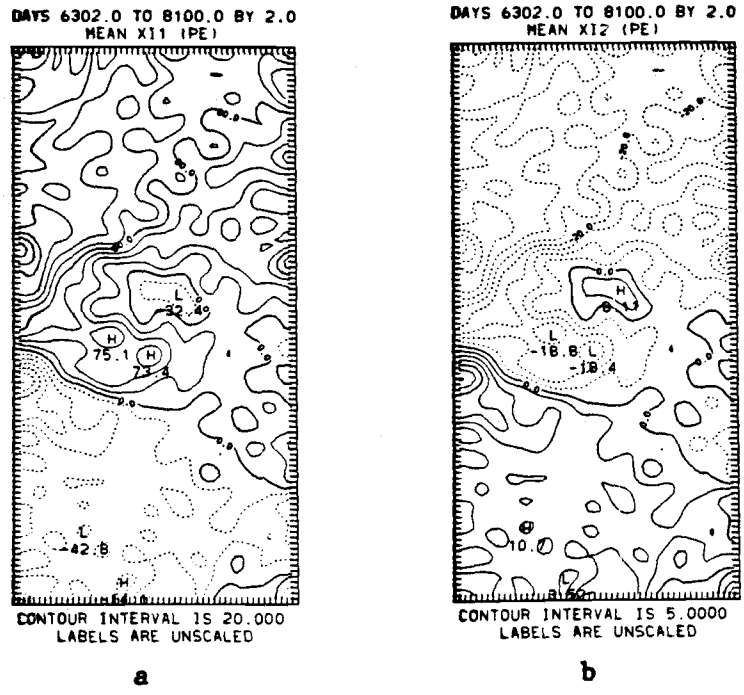

Fig. 6.5 Time-mean of entry 3 in Table 4.1: a) χ_1, b) χ_2.

Again it is not clear whether the velocity potential pattern is statistically well-determined. A longer time series and more frequent sampling may show that this divergence pattern will become even smaller upon time averaging.

The time-averaged horizontal vector velocity fields are shown in Figs. 6.6 and 6.7 for the upper and lower layers, respectively. Only every other point is plotted. In the PE model, the rotational component dominates the divergent by a factor of 50. Both the PE and QG models show similar horizontal velocity patterns. In both layers, the following features can be seen: 1) strong eastward flow in the area of the free jet, with strong recirculation regions to the north and south, 2) strong western boundary currents which flow northward (southward) in the southern (northern) half of the basin, 3) weak Sverdrup flow over most of the basin, and 4) very weak divergent flow which is strongest in the vicinity of the free jet and recirculation regions. In the lower layer, deep countercurrents near the western wall are evident. The basic difference in the PE and QG plots is the greater intensity of the PE subpolar low and anticyclonic high in the recirculating portions of the basin. Figs. 6.6 and 6.7 are similar to their single-gyre counterparts, i.e., Figs. 5.10 and 5.11.

The vertical velocity is shown in Fig. 6.8. The QG vertical velocity field shows the same areas of upwelling and downwelling in the southern half of the basin as in the single-gyre (compare Figs. 6.8b and 5.12b), and a mirror-image in the

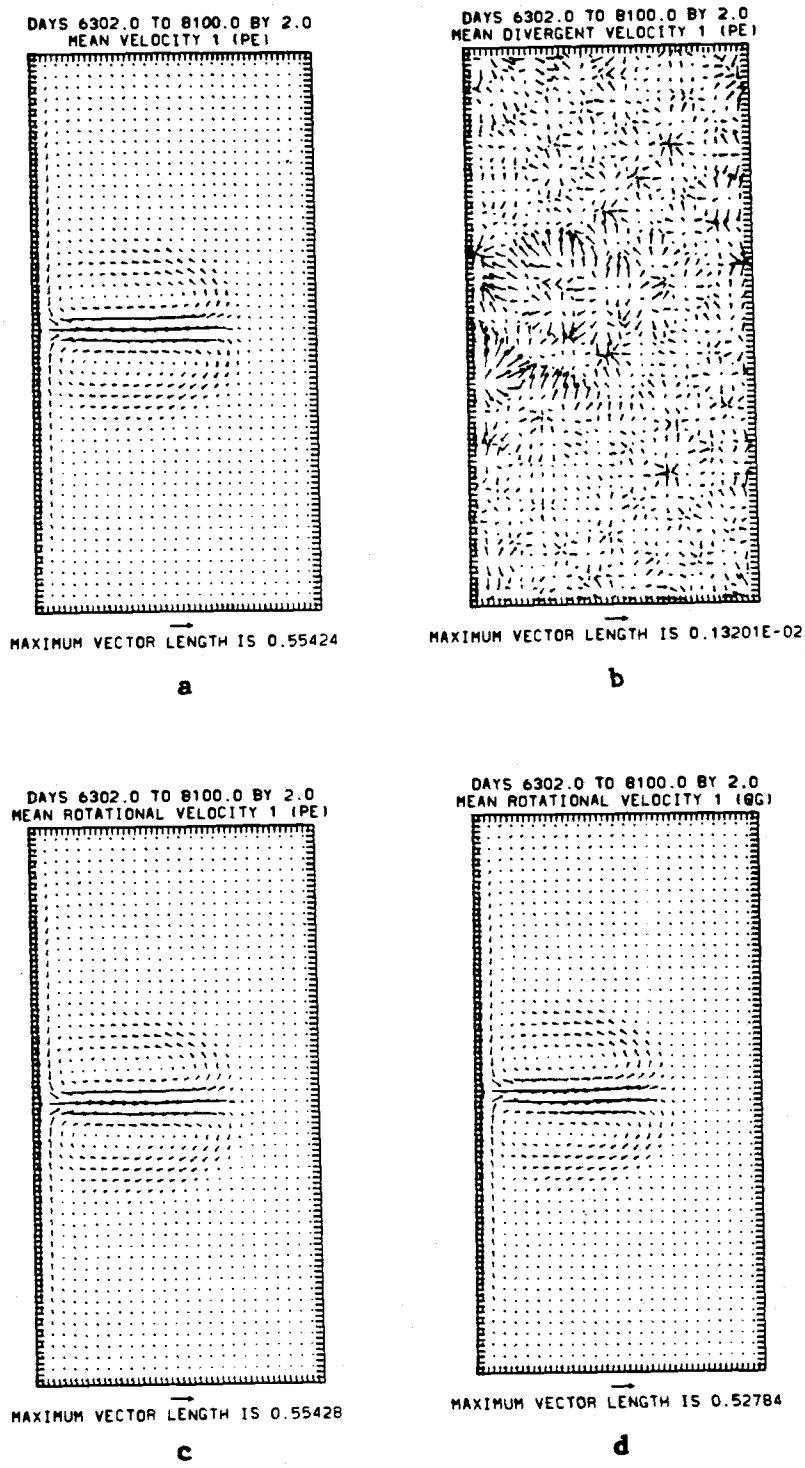

Fig. 6.6 Time-mean of entry 8 in Table 4.1: a) $\hat{\mathbf{v}}_1$, b) $\hat{\mathbf{v}}_{1D}$, c) $\hat{\mathbf{v}}_{1R}$ (PE), d) $\hat{\mathbf{v}}_{1R}$ (QG). Only every other velocity vector is plotted.

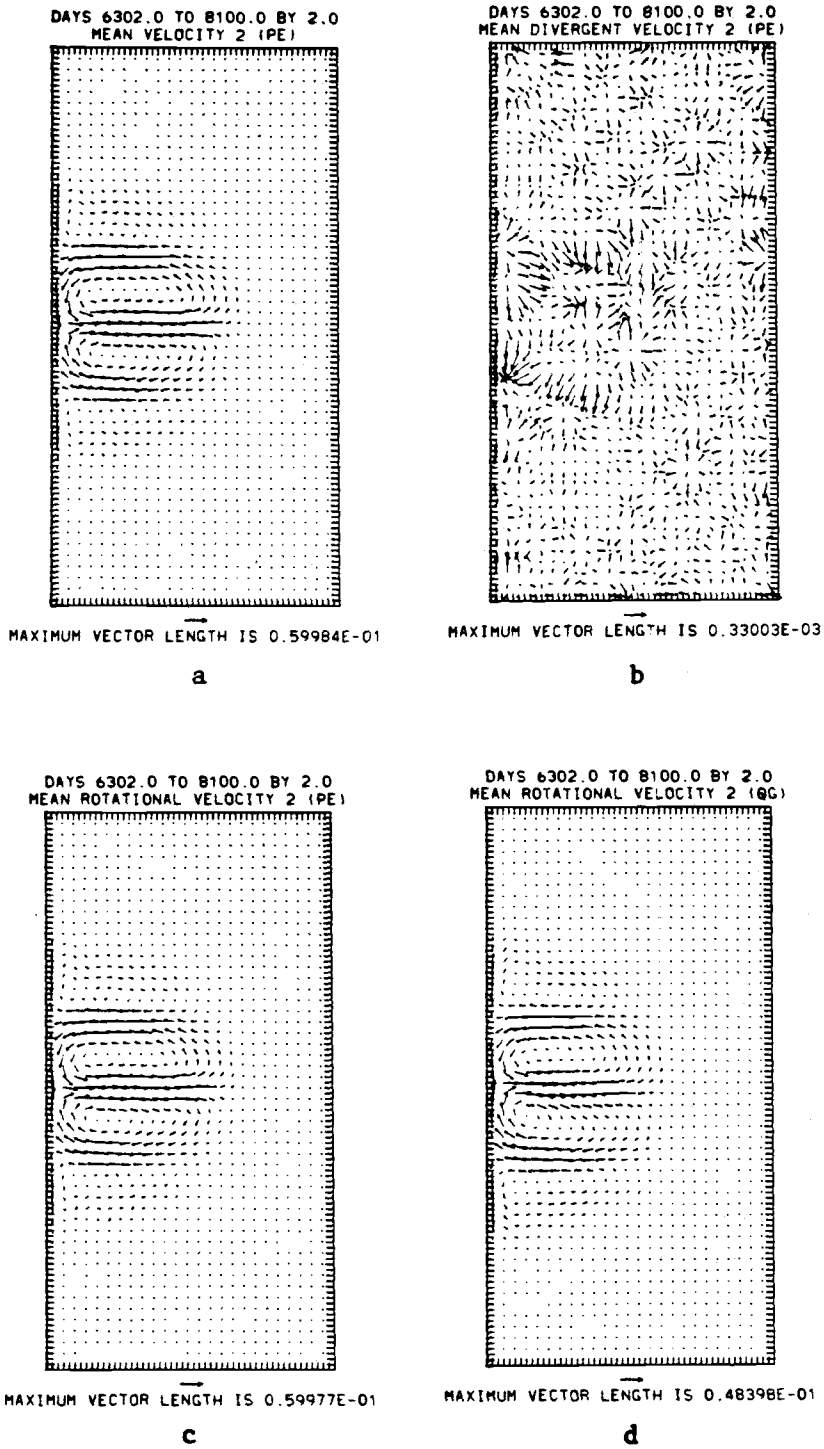

Fig. 6.7 Time-mean of entry 9 in Table 4.1: a) $\vec{v}_2$, b) $\vec{v}_{2D}$, c) $\vec{v}_{2R}$ (PE), d) $\vec{v}_{2R}$ (QG). Only every other velocity vector is plotted.

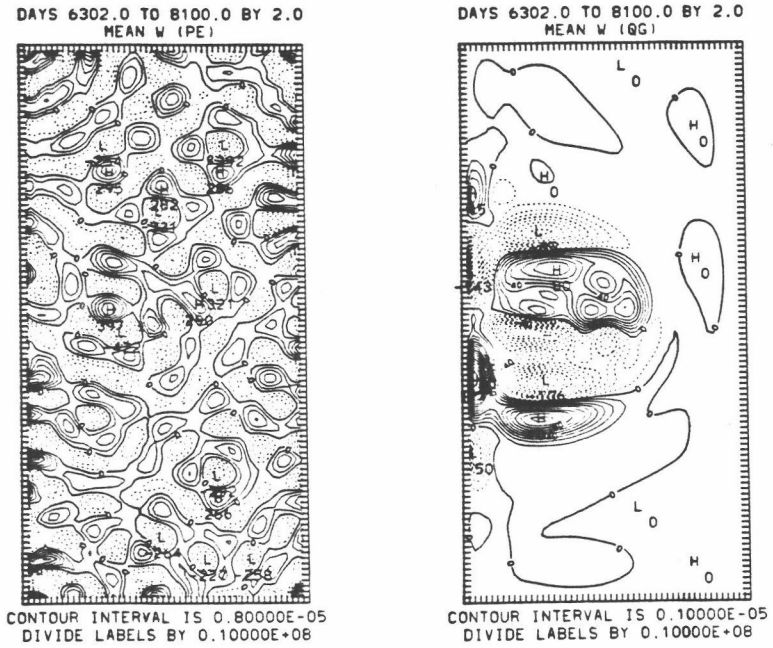

Fig. 6.8 Time-mean of entry 10 in Table 4.1: a) w_2 (PE), b) w_2 (QG).

northern half of the basin.

One would expect the PE mean vertical velocity field to resemble the QG, as in the single-gyre experiments. The presence of high frequency activity in the PE vertical velocity suggests that more time averaging may be necessary to average out these gravity waves in this experiment. A closer inspection of the PE time-dependent energetics for the double-gyre experiment (Fig. 6.2) suggests that trends could still be present, which could be affecting the results. In the PE upper layer kinetic energy there is a 32-day oscillation superimposed on a longer (~300-day) oscillation, neither of which is evident in the QG energetics.

The upper layer pressure field is shown in Fig. 6.9. The basic circulation patterns are similar, with the PE high pressure cell more intense than the QG geostrophic streamfunction. Fig. 6.9c shows that terms in addition to the PE geostrophic streamfunction are significant, but only at the 10% level. Fig. 6.9 cannot be readily compared with Fig. 5.13 because 1) these fields are deviations from their respective horizontal means, which are considerably different in the single-and double-gyre experiments, and 2) the choice of f_o is different in the two gyres.

Fig. 6.10 shows the lower layer pressures. Again the PE pressure cells are more intense than the QG geostrophic streamfunction cells. Fig. 6.10c shows that terms in addition to the PE geostrophic streamfunction can become important at the 10%

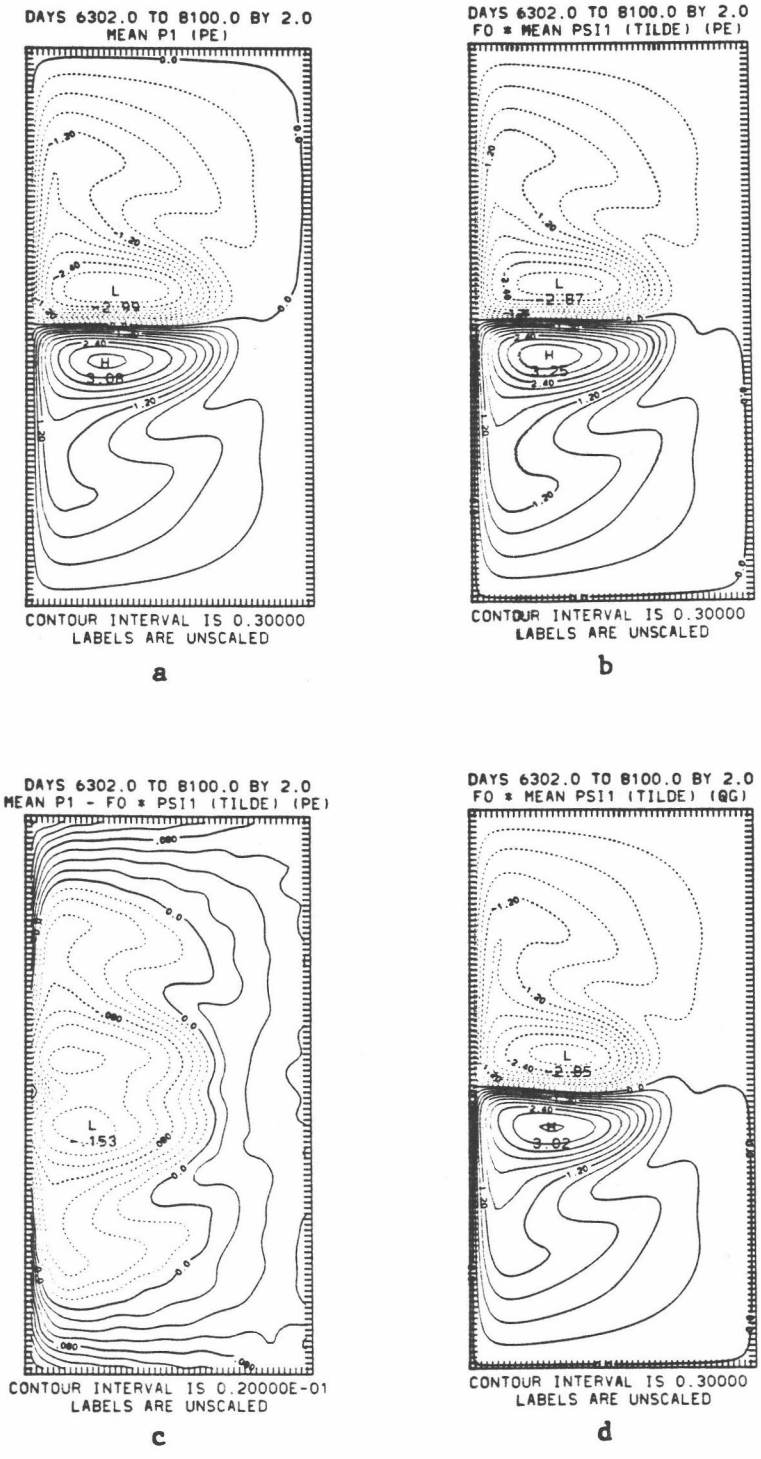

Fig. 6.9 Time-mean of entry 11 in Table 4.1: a) $\tilde{p}_1$, b) $f_o\tilde{\psi}_1$ (PE), c) $\tilde{p}_1 - f_o\tilde{\psi}_1$, d) $f_o\tilde{\psi}_1$ (QG).

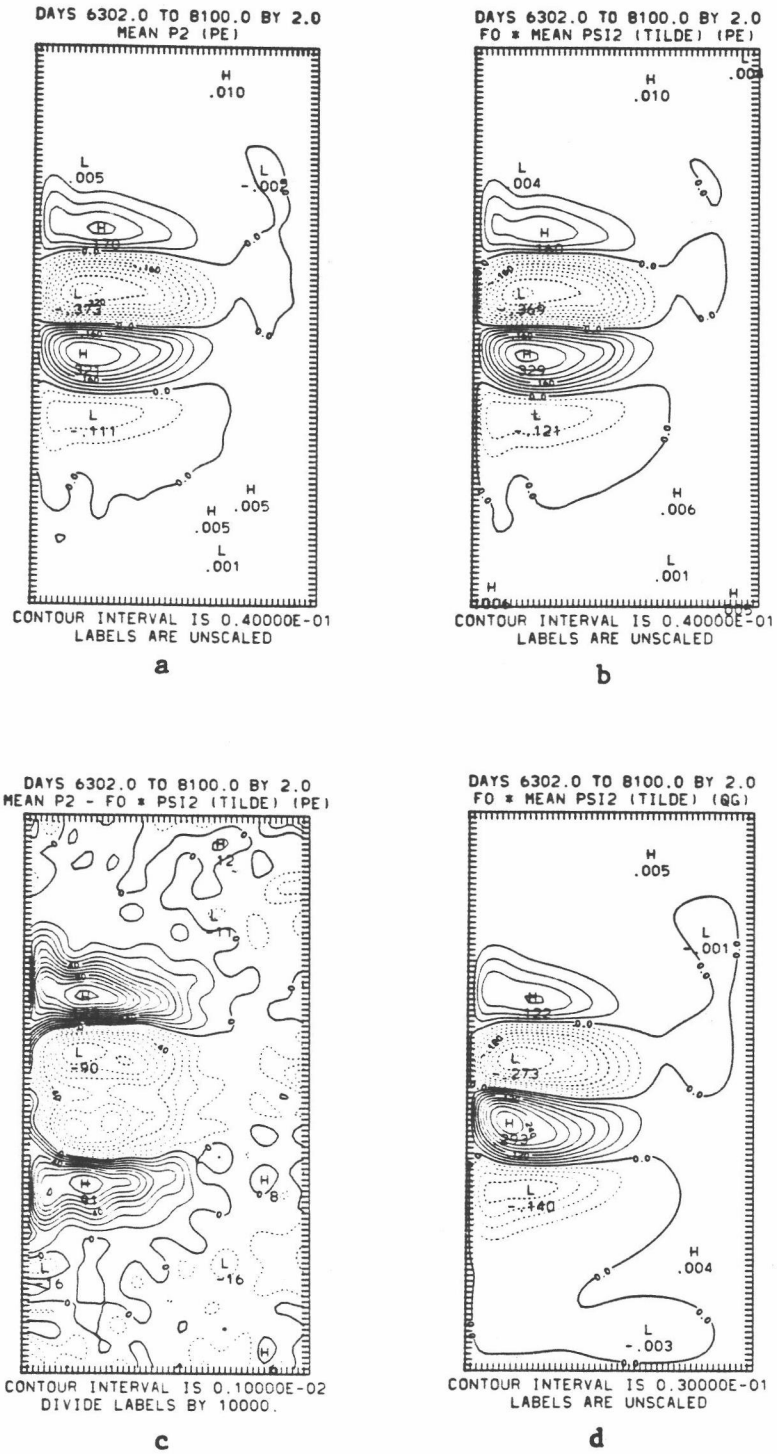

Fig. 6.10 Time-mean of entry 12 in Table 4.1: a) $\tilde{p}_2$, b) $f_o\tilde{\psi}_2$ (PE), c) $\tilde{p}_2 - f_o\tilde{\psi}_2$, d) $f_o\tilde{\psi}_2$ (QG).

level. As in the single-gyre experiment, there is a high degree of geostrophy.

Lastly, the upper and lower layer time-averaged temperature fields are shown in Fig. 6.11, along with the average PE temperature and the per cent time change of PE static stability since the beginning of the experiment. Evidence of the two time scales in the PE model can be seen. The temperature fields reflect the fast-time scale, i.e., baroclinic adjustments, while the slow continuing adjustment of the static stability (seen in Fig. 6.11d) reflects the long-time scale.

6.3 Instantaneous, time mean and eddy fields

Fig. 6.12 shows the QG instantaneous, time mean, and eddy fields for $f_o\psi_1$, $f_o\psi_2$, $\hat{v}_{1R}$ and $\hat{v}_{2R}$ at a particular instant in time. As in the single-gyre experiment, a comparison of the upper layer mean and eddy quantities shows that the eddies and mean flow have about the same amplitude. A comparison of the lower layer quantities shows that the eddies are dominant. Since there is no direct mean forcing of the lower layer, the lower layer mean circulation is again driven by the eddies.

Fig. 6.13 shows the PE instantaneous, time mean, and eddy fields for p_1, p_2, $\hat{v}_1$ and $\hat{v}_2$ at a particular instant in time. A comparison of Fig. 6.13 with Fig. 6.12 shows similar patterns, except that the boundary-trapped Kelvin waves in the PE

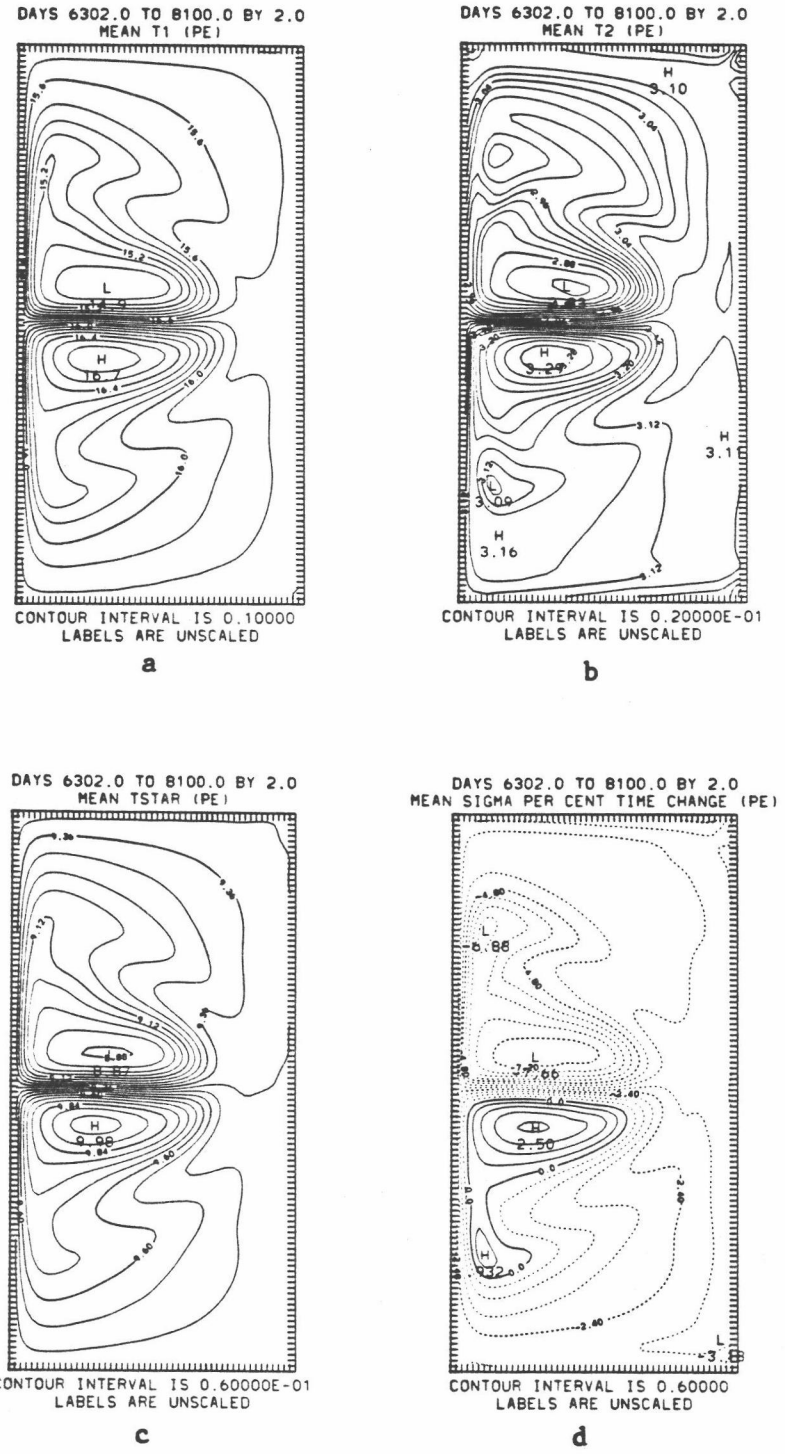

Fig. 6.11 Time-mean of entry 13 in Table 4.1: a) T_1, b) T_2, c) T* (entry 14 in Table 3.1), d) σ (entry 15 in Table 4.1).

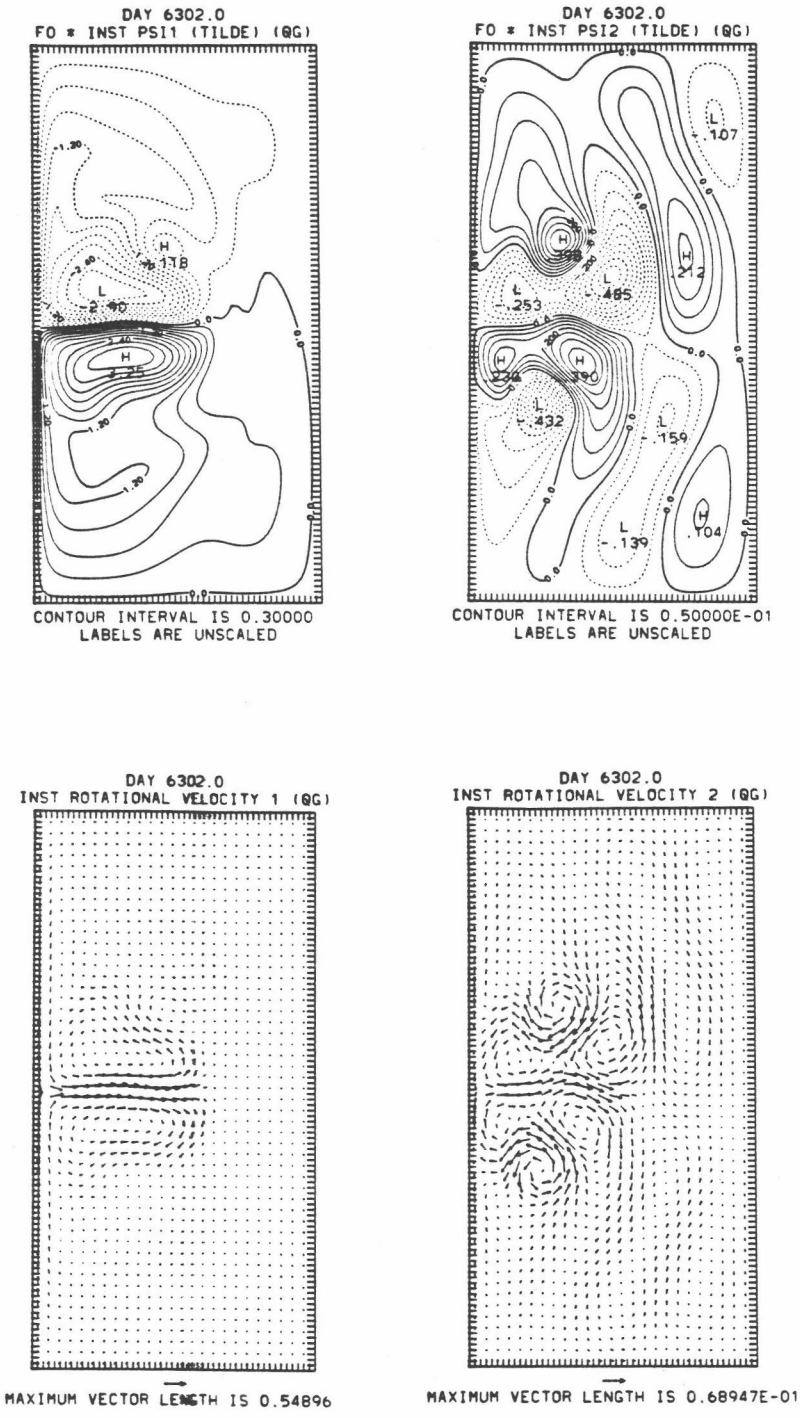

a

Fig. 6.12 The $f_o\psi_1$, $f_o\psi_2$, $\vec{v}_{1R}$, v_{2R} fields for the QG model: a) instantaneous, b) time mean, and c) eddy.

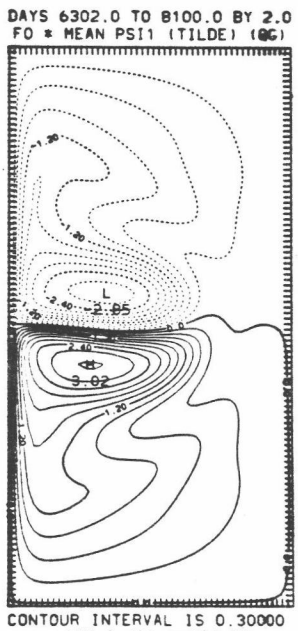

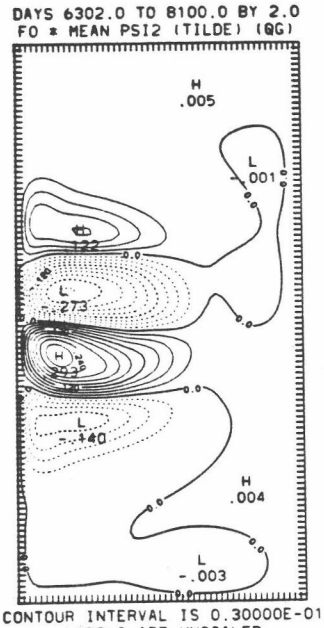

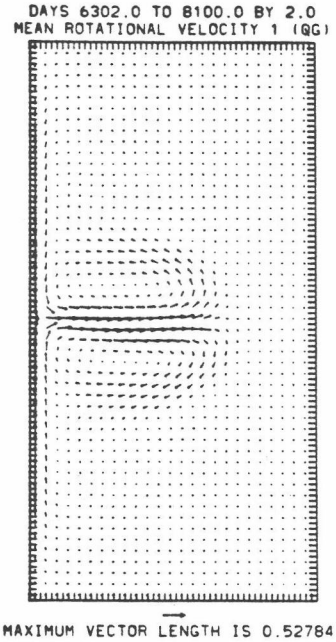

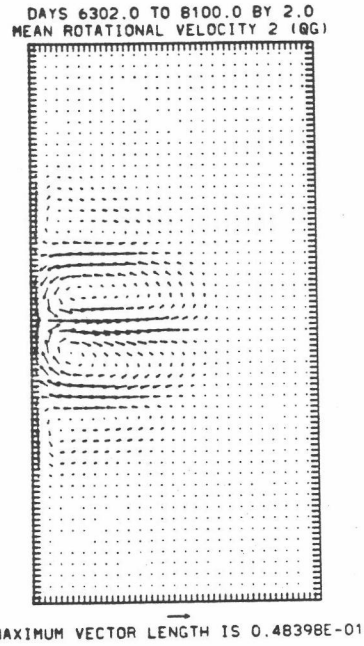

b

Fig. 6.12 (cont.)

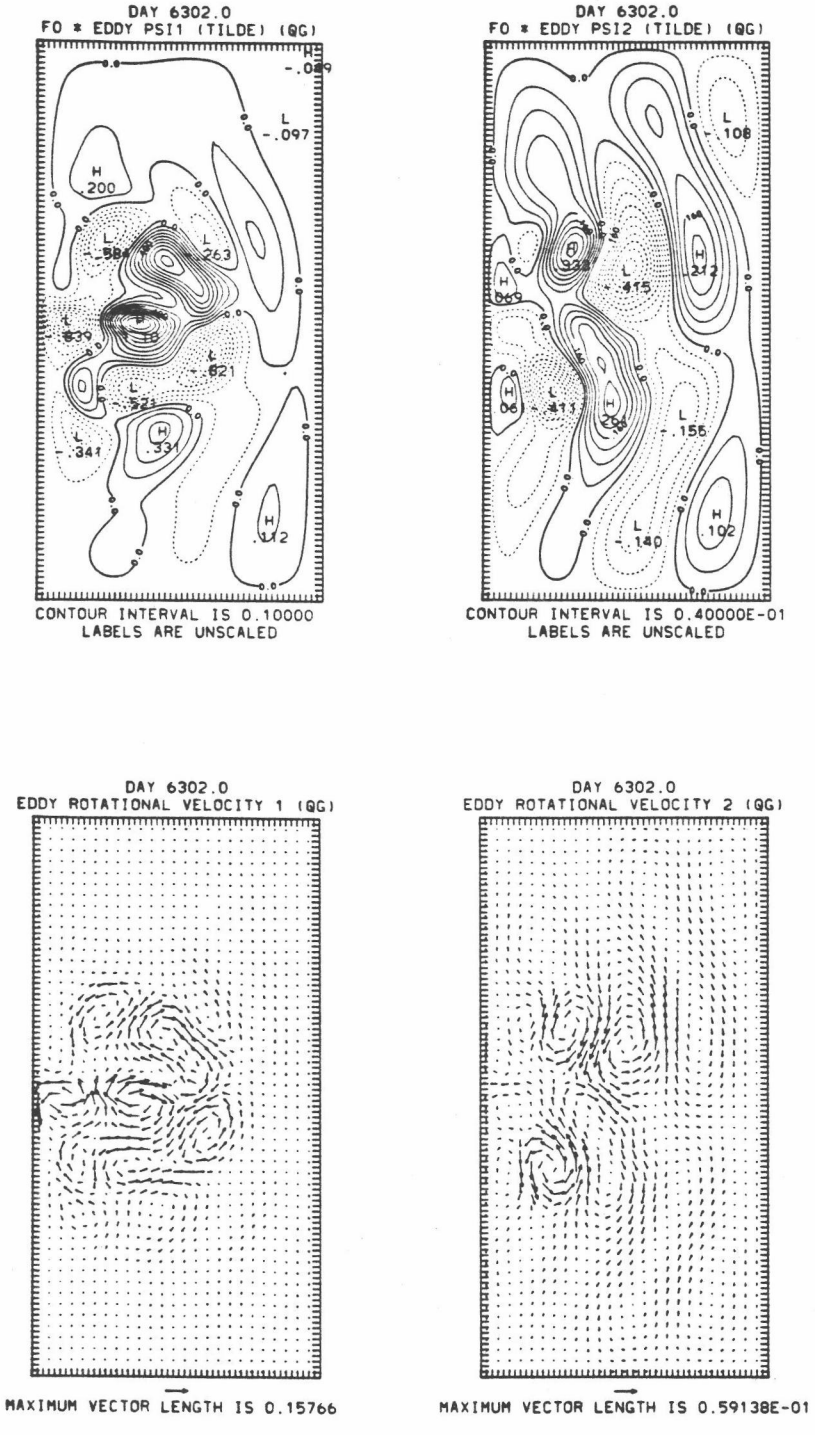

c

Fig. 6.12 (cont.)

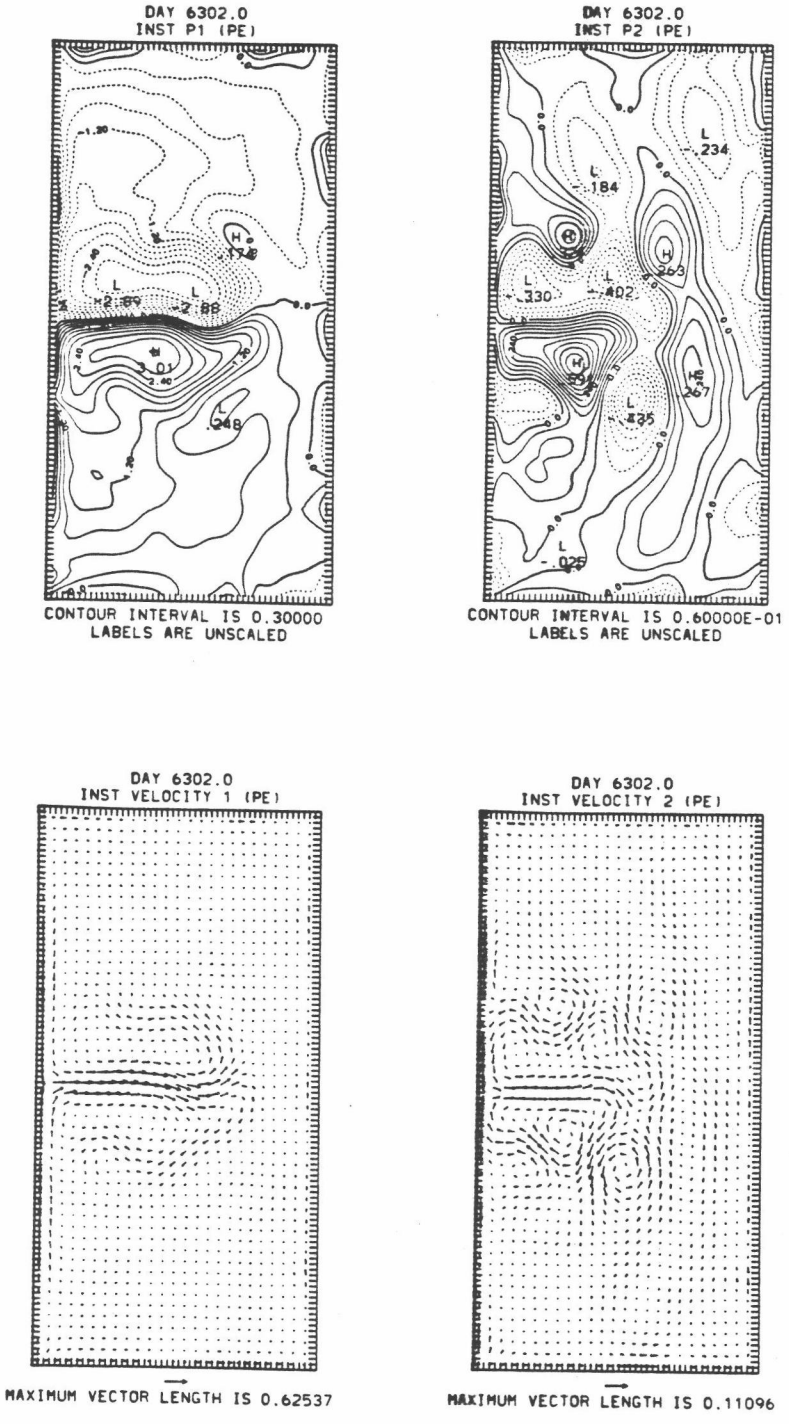

Fig. 6.13 The p_1, p_2, $\vec{v}_1$, $\vec{v}_2$ fields for the PE model: a) instantaneous, b) time mean, and c) eddy.

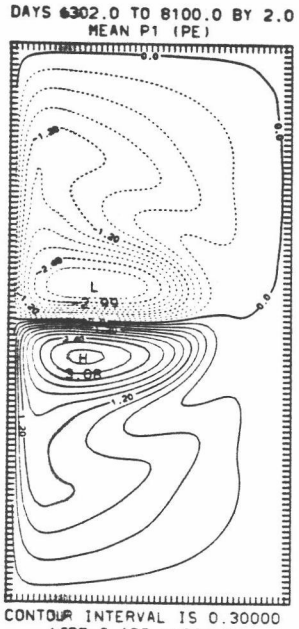

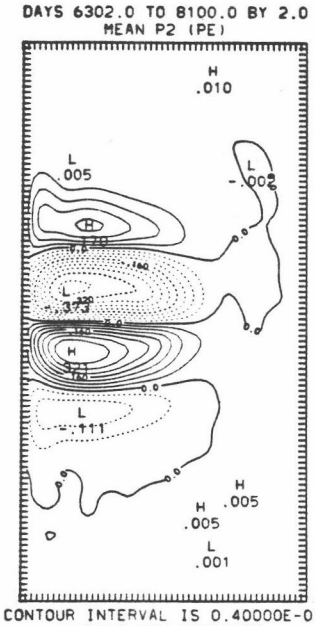

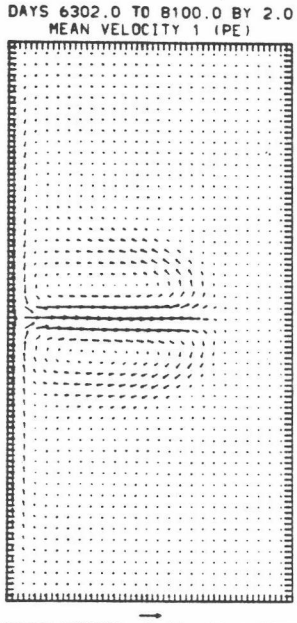

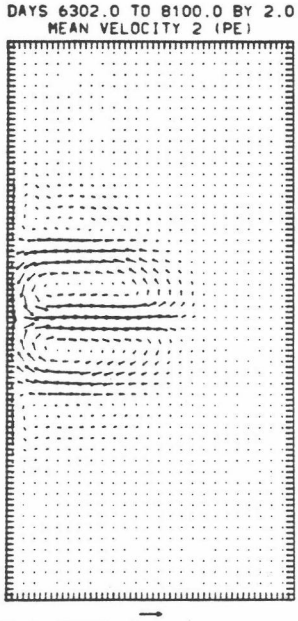

b

Fig. 6.13 (cont.)

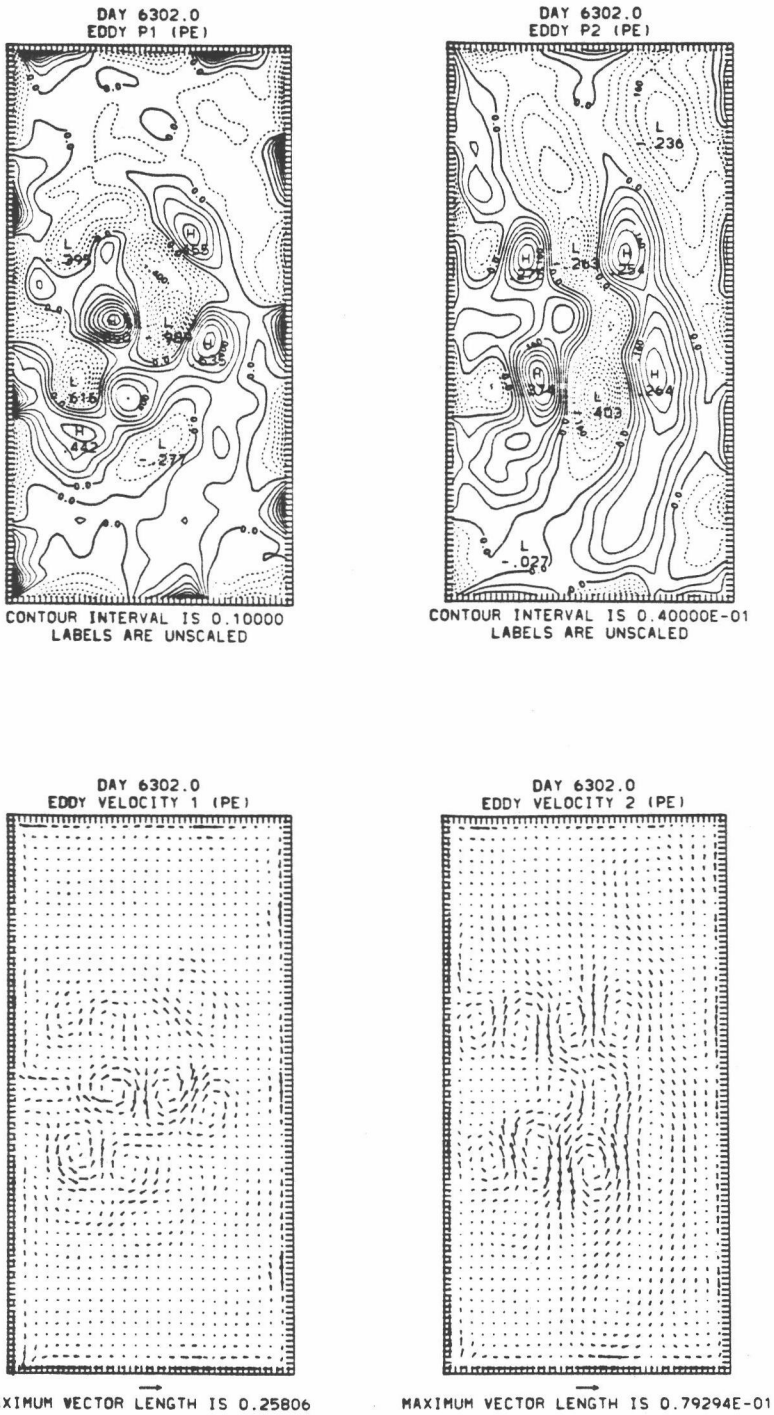

c

Fig. 6.13 (cont.)

experiment are absent in the QG experiment.

Fig. 6.14 shows eddy maps of $f_o\psi_1$, $f_o\vec{\psi}_2$, v_{1R},$^{\rightarrow}$and v_{2R} at 8-day intervals for the QG model. The eddies propagate westward at ~4 to 7 km per day. In the central portions of the basin, the eddies have a basic wavelength of ~450 km, while in the northern and southern areas of the basin, the eddies have a larger wavelength. If Figs. 6.14a and b are overlaid, it is seen, as in the single-gyre experiment, that 1) in the central portions of the basin, there is a tilt in the vertical, consistent with baroclinic instability, with the upper layer eddies lagging the lower layer eddies, and 2) in the northern and southern areas of the basin, there is little, if any, tilt, so that the eddies are very nearly equivalent barotropic.

Finally, Fig. 6.15 shows eddy maps of p_1, p_2, v_1, and v_2 at 8-day intervals for the PE model. In the interior, the PE and QG mesoscale eddies look similar and tend to be quite barotropic. The main difference between the PE and QG eddy fields is the additional eddy field propagating counterclockwise around the basin. This field, which is due to the Kelvin waves, is, unlike the interior, entirely baroclinic. A comparison with the single-gyre experiment shows the Kelvin waves to have the same wavelengths (~675 km). Further discussion of these Kelvin waves will be given in the following chapter.

6.4 Energetics

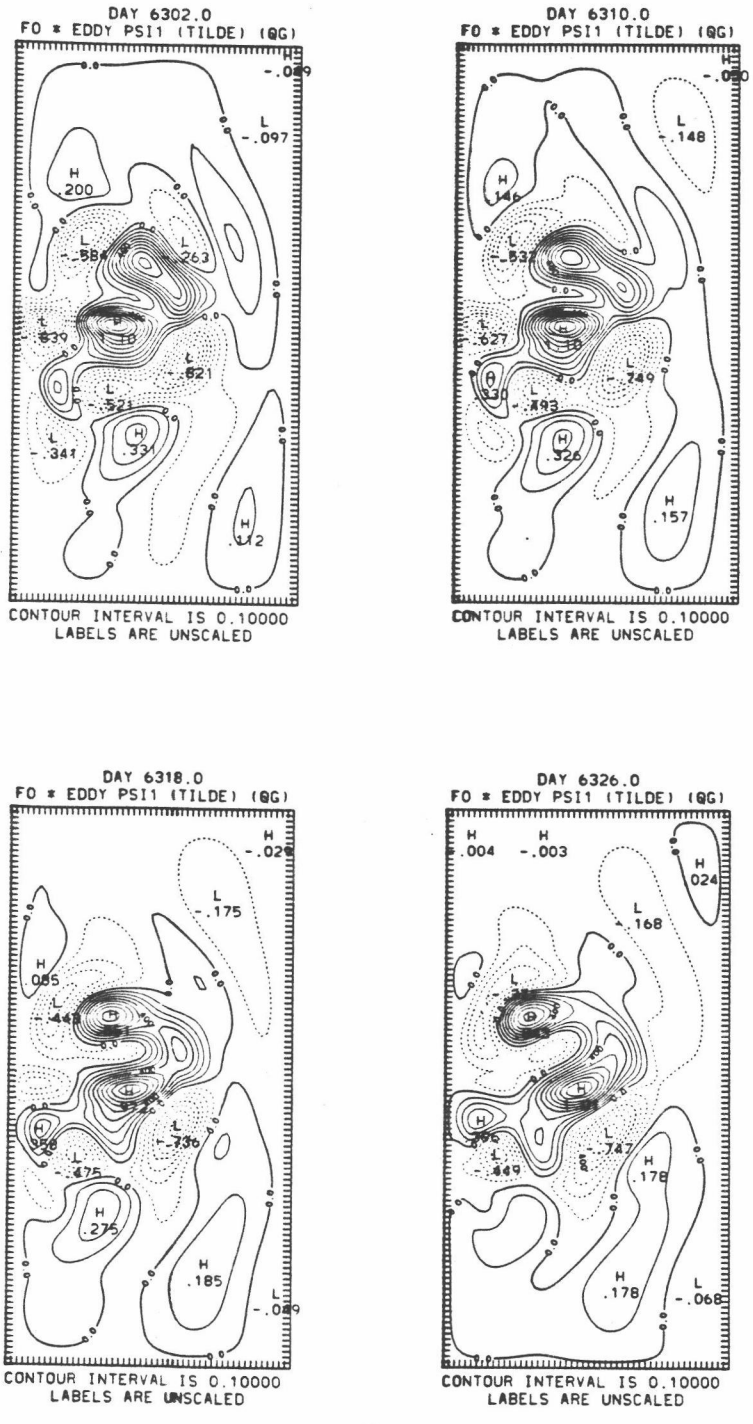

Fig. 6.14 The QG eddy fields at 8-day intervals for a) $f_o\psi_1$, b) $f_o\psi_2$, c) $\vec{v}_{1R}$, d) $\vec{v}_{2R}$.

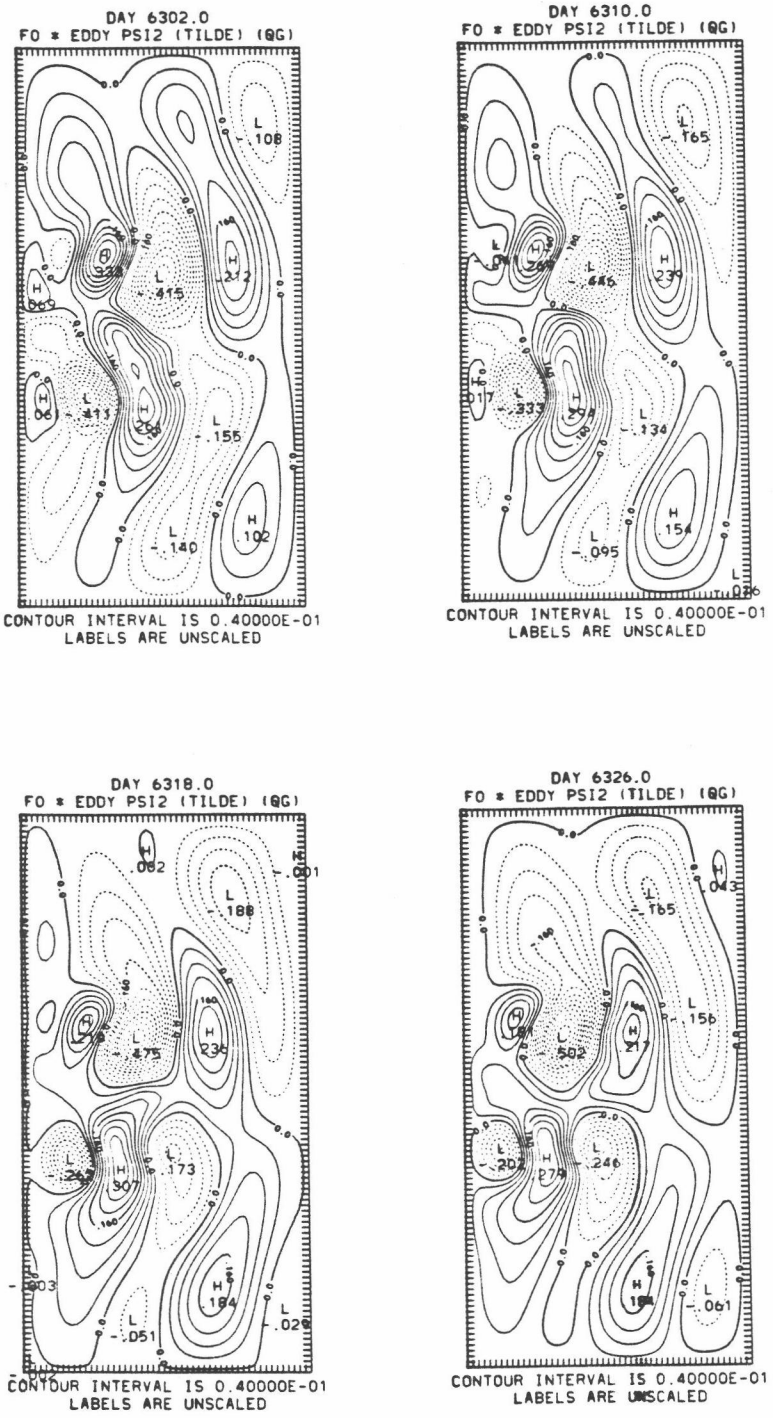

b

Fig. 6.14 (cont.)

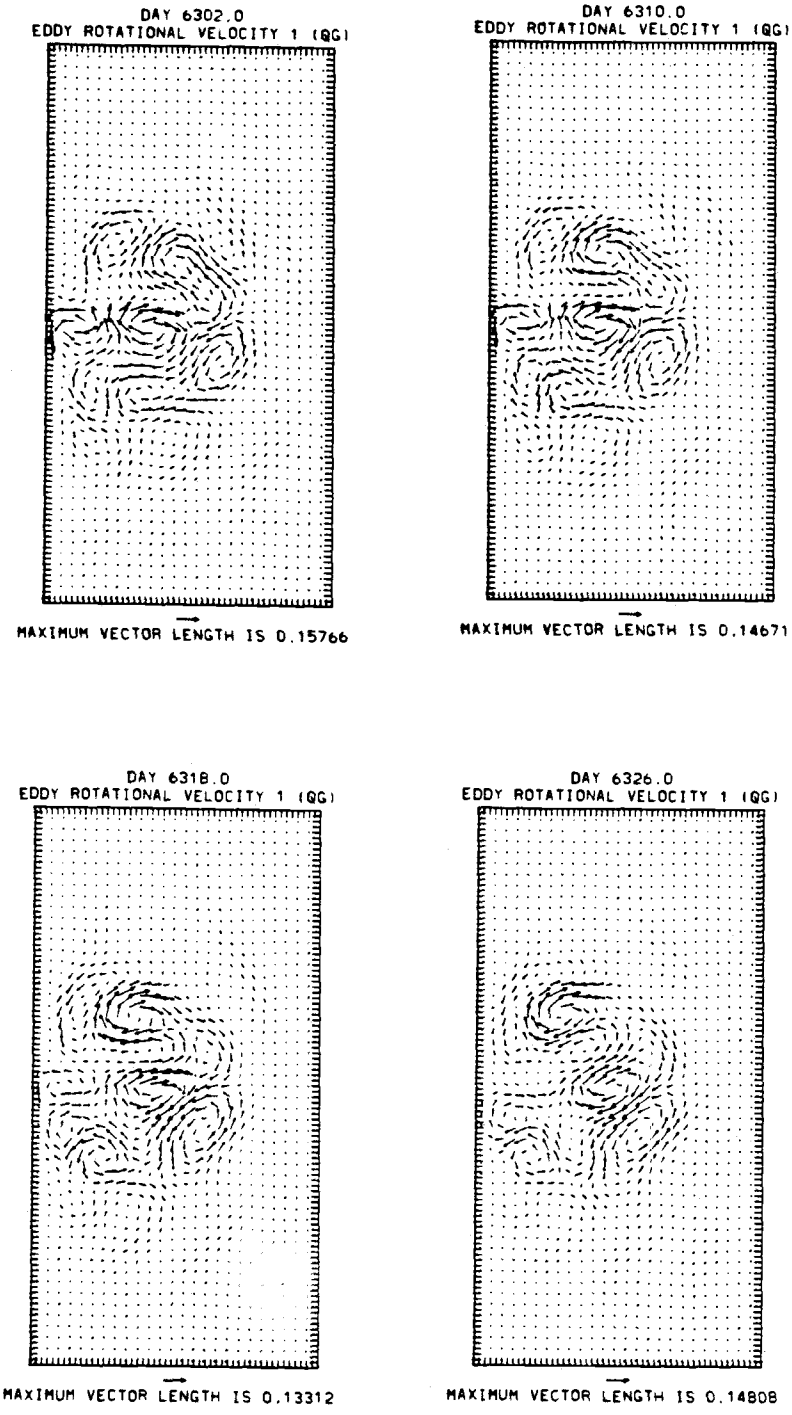

c

Fig. 6.14 (cont.)

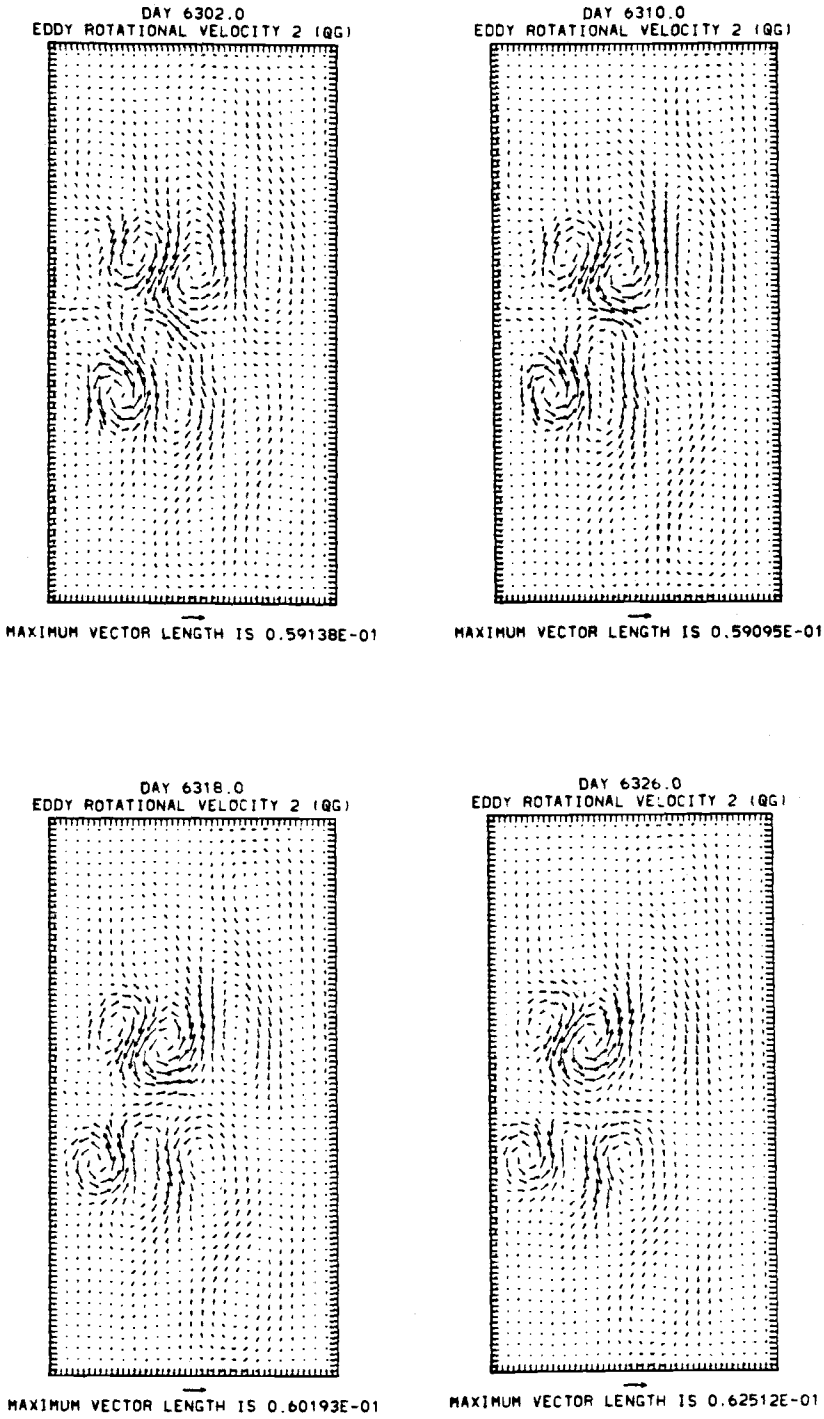

d

Fig. 6.14 (cont.)

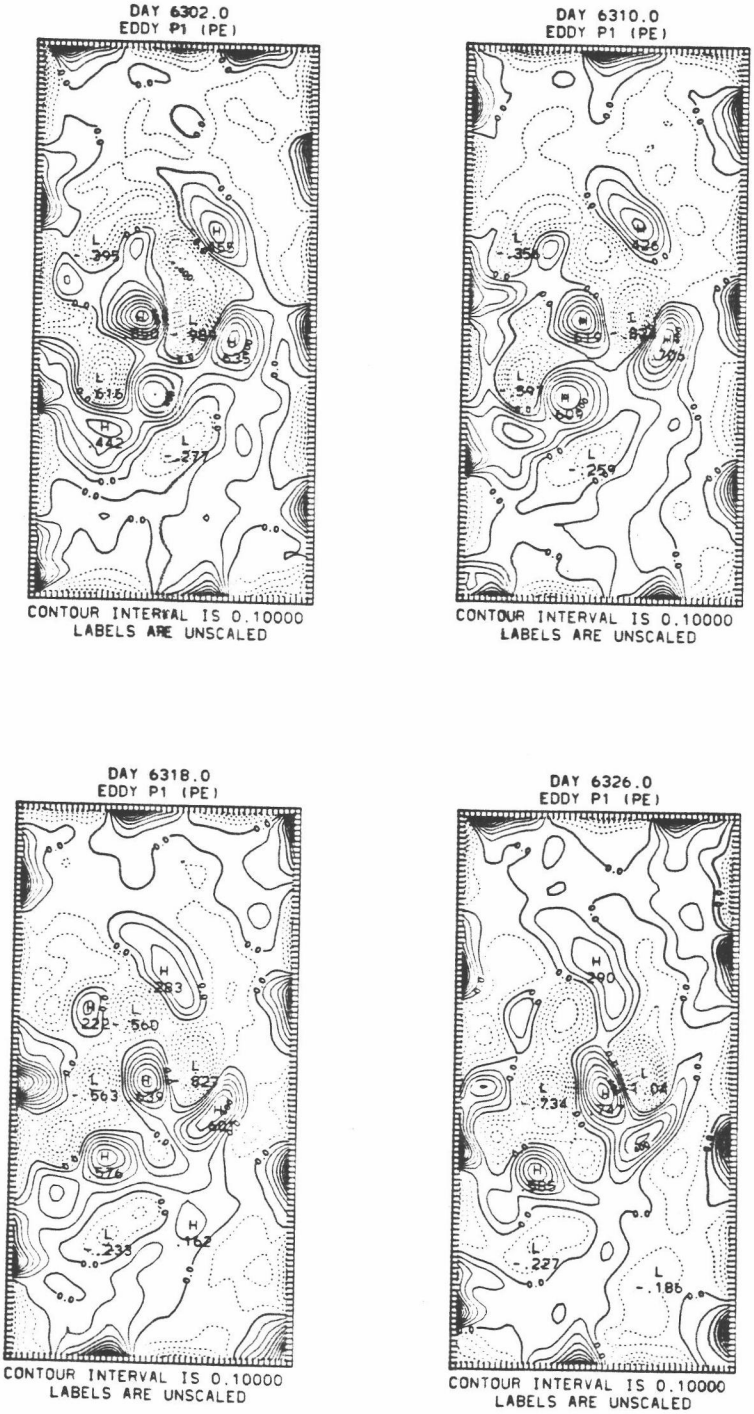

Fig. 6.15 The PE eddy fields at 8-day intervals for a) p_1, b) p_2, c) $\vec{v}_1$, d) $\vec{v}_2$.

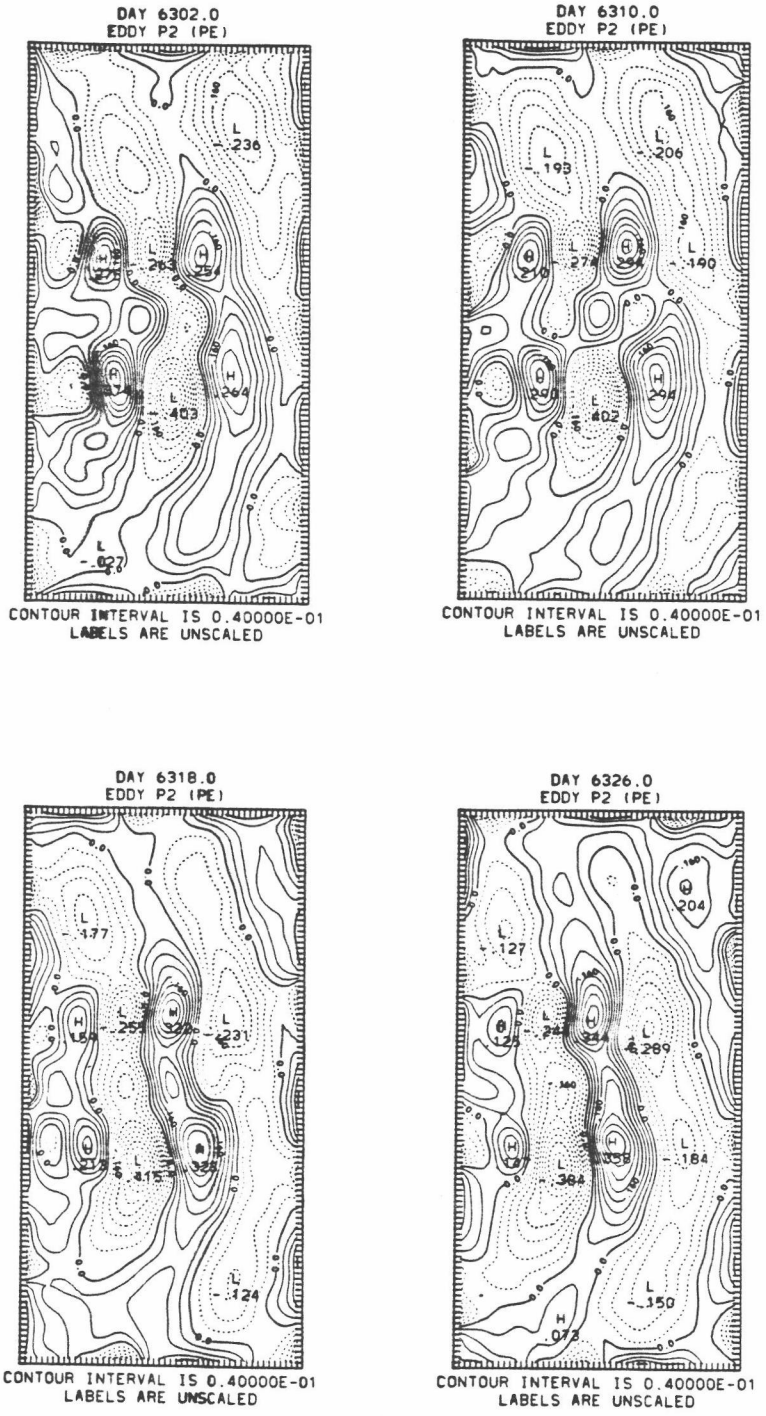

b

Fig. 6.15 (cont.)

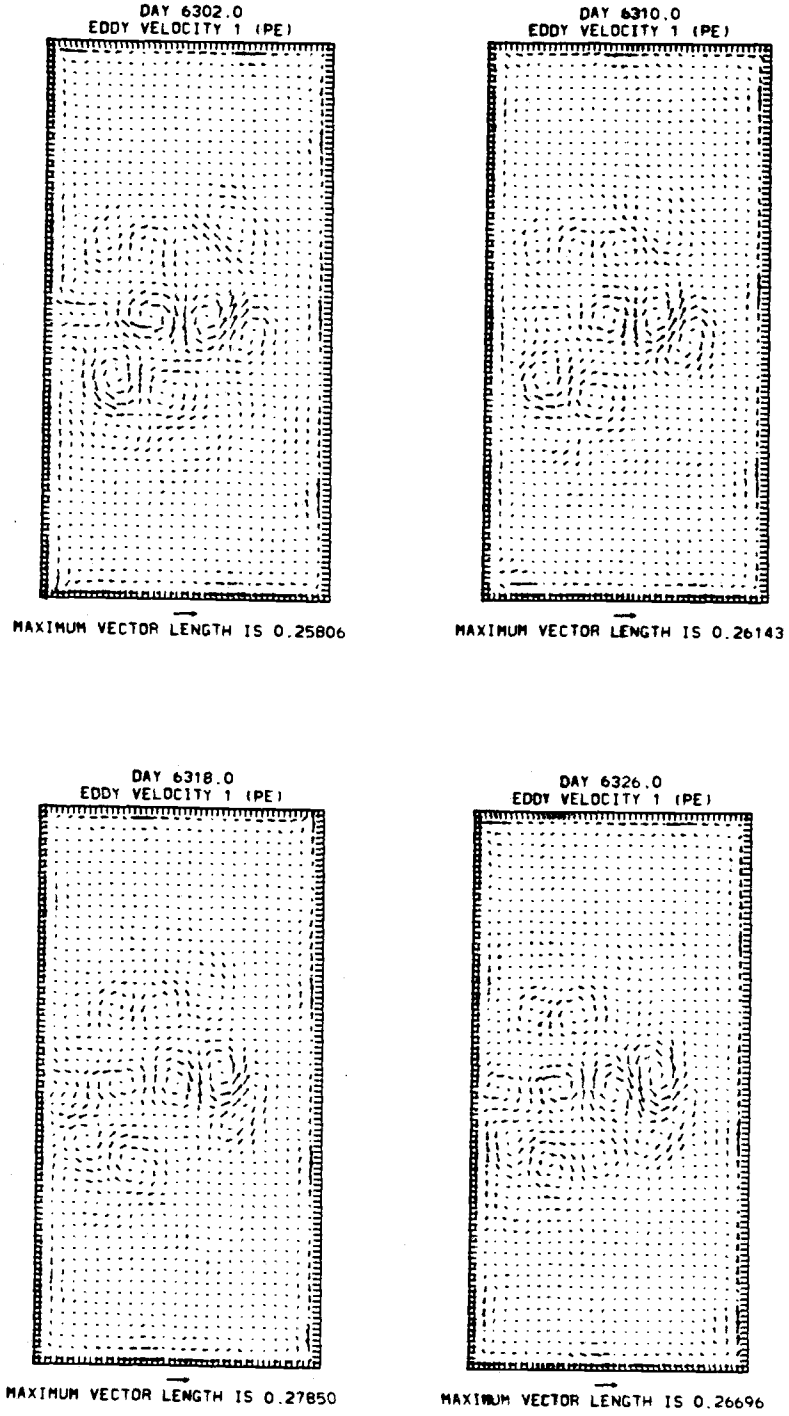

c

Fig. 6.15 (cont.)

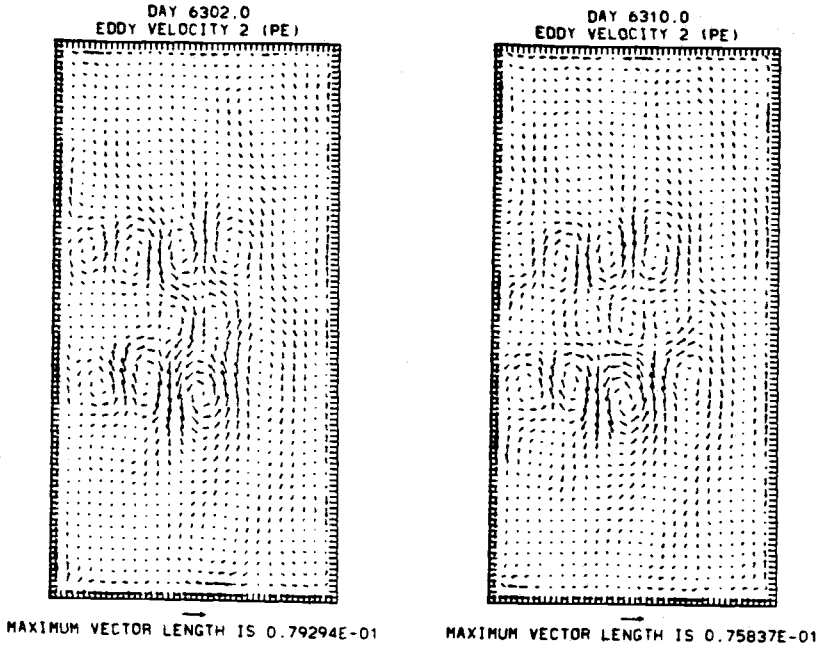

d

Fig. 6.15 (cont.)

Table 6.2 lists the horizontally-averaged, time-mean and eddy kinetic energies for both models. As in the single-gyre experiment, the PE total and rotational kinetic energy components are always higher than the QG kinetic energy components, and 2) the divergent component of the PE kinetic energy is small, except for K_1', where the divergent component contributes ~33% to the total. A comparison of Table 6.2 with Table 5.2 shows that the PE energies for the single-gyre experiment are higher. This is probably due to the added dissipation process, i.e, the bottom friction, in the double-gyre experiment. The divergent component in the double-gyre experiment is also smaller by about 30-50% than that in the single-gyre. This is likely due to the smaller ratio of radius of deformation size (the "trapping" scale for the Kelvin waves) to the horizontal domain.

The geographical distribution of the time-mean and eddy kinetic energy for each layer is shown in Figs. 6.16-6.19. Again very large local values of the mean kinetic energy are noted. The PE eddy kinetic energy maps (Figs. 6.18a and 6.19a) suggest three regions of active transience: 1) the boundary, where Kelvin waves are present, 2) the recirculation region, where the mesoscale eddies are driven by baroclinic instability processes, and 3) the area of the free jet, where the mesoscale eddies are driven by barotropic processes. In the QG model only the latter two regions are present.

Table 6.2 Horizontally-averaged time-mean and eddy kinetic energy for the single-gyre experiment

		$\overline{K}_1$		$\overline{K}_2$		K_1'		K_2'	
No.	Energy	Quantity (k J m^{-2})	% of PE total	Quantity (k J m^{-2})	% of PE total	Quantity (k J m^{-2})	% of PE total	Quantity (k J m^{-2})	% of PE total
1)	Total PE	7.20	100%	1.10	100%	1.3	100%	0.77	100%
1a)	Rotational component	6.77	94%	0.95	90%	0.86	67%	0.66	86%
1b)	Divergent component	0.43	6%	0.11	10%	0.43	33%	0.11	14%
2)	QG	6.08	90%	0.77	70%	0.60	46%	0.59	77%

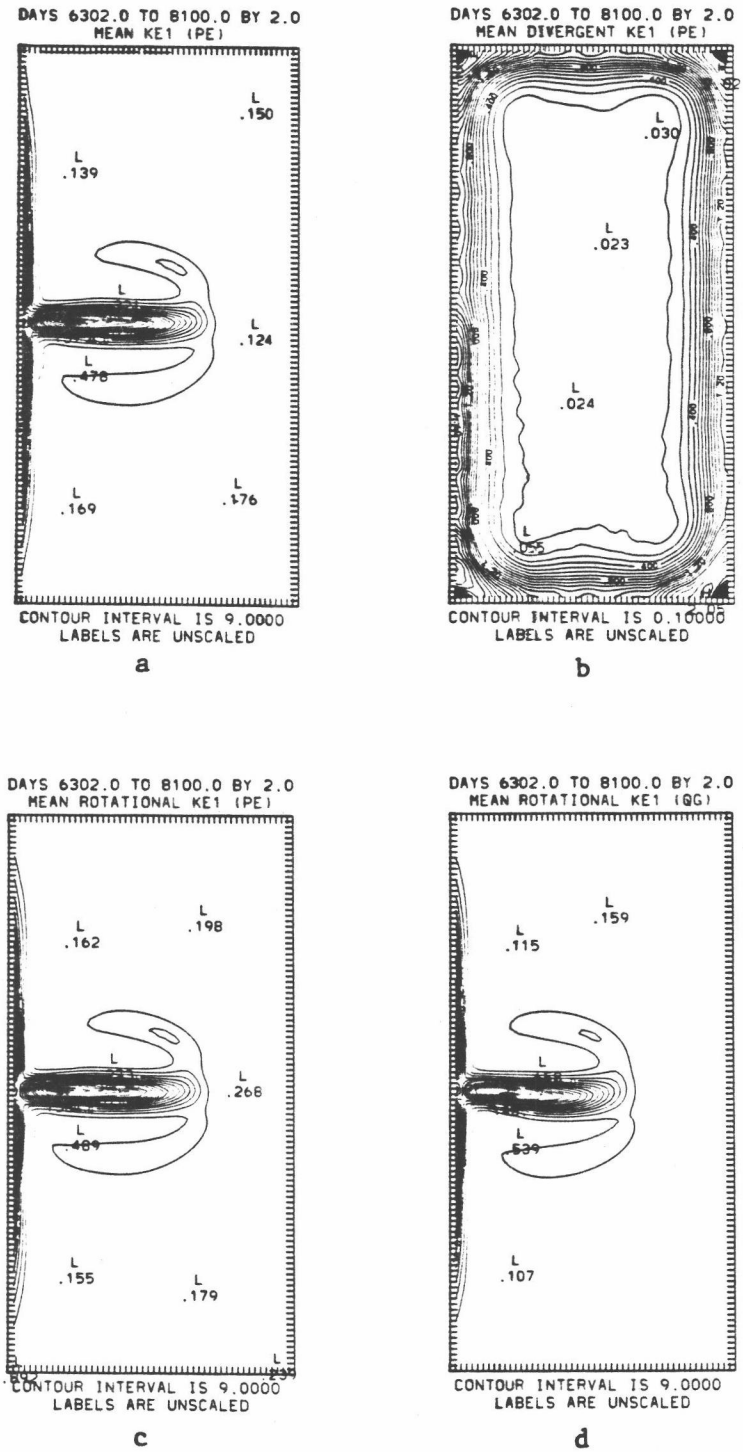

Fig. 6.16 Time-mean of entry 17 in Table 4.1: a) K_1, b) K_{1D}, c) K_{1R} (PE), d) K_{1R} (QG).

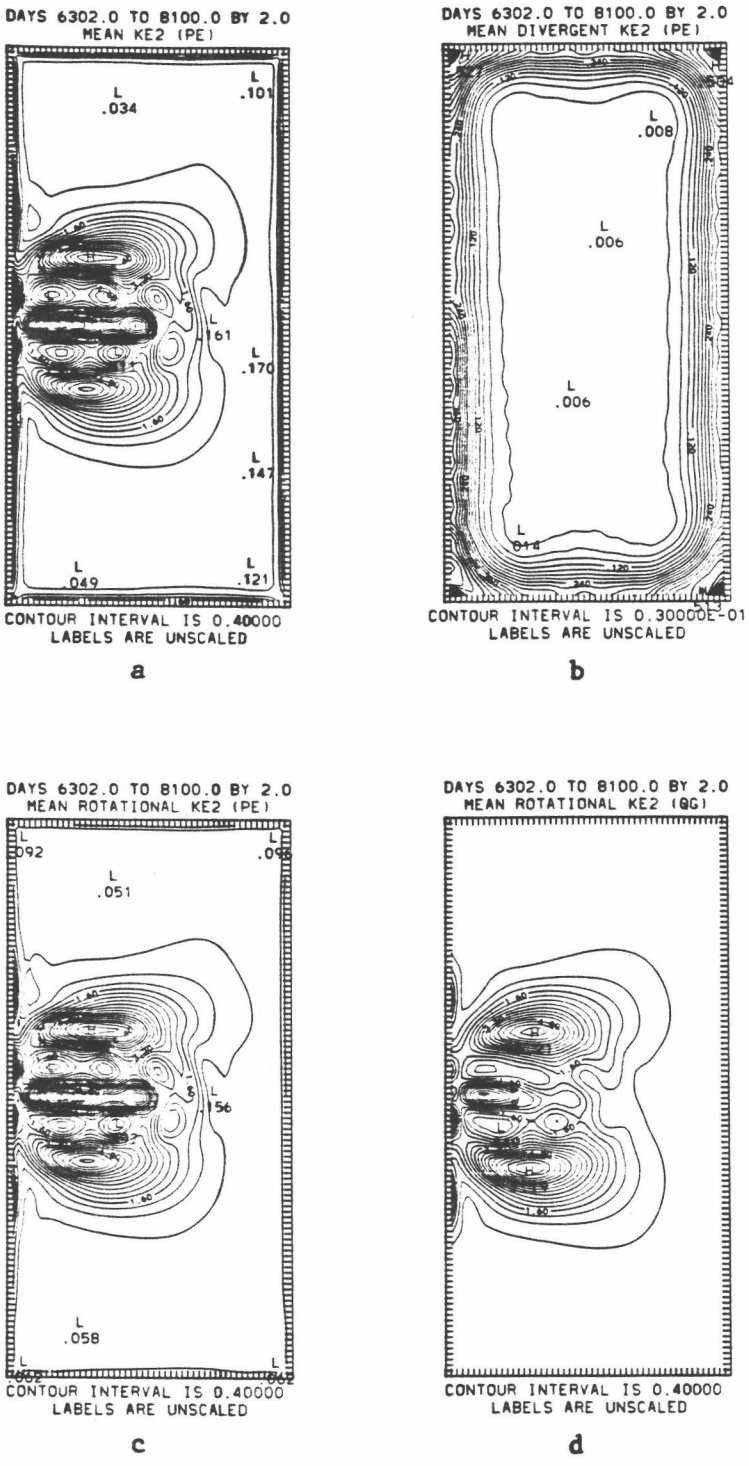

Fig. 6.17 Time-mean of entry 18 in Table 4.1: a) K_2, b) K_{2D}, c) K_{2R} (PE), d) K_{2R} (QG).

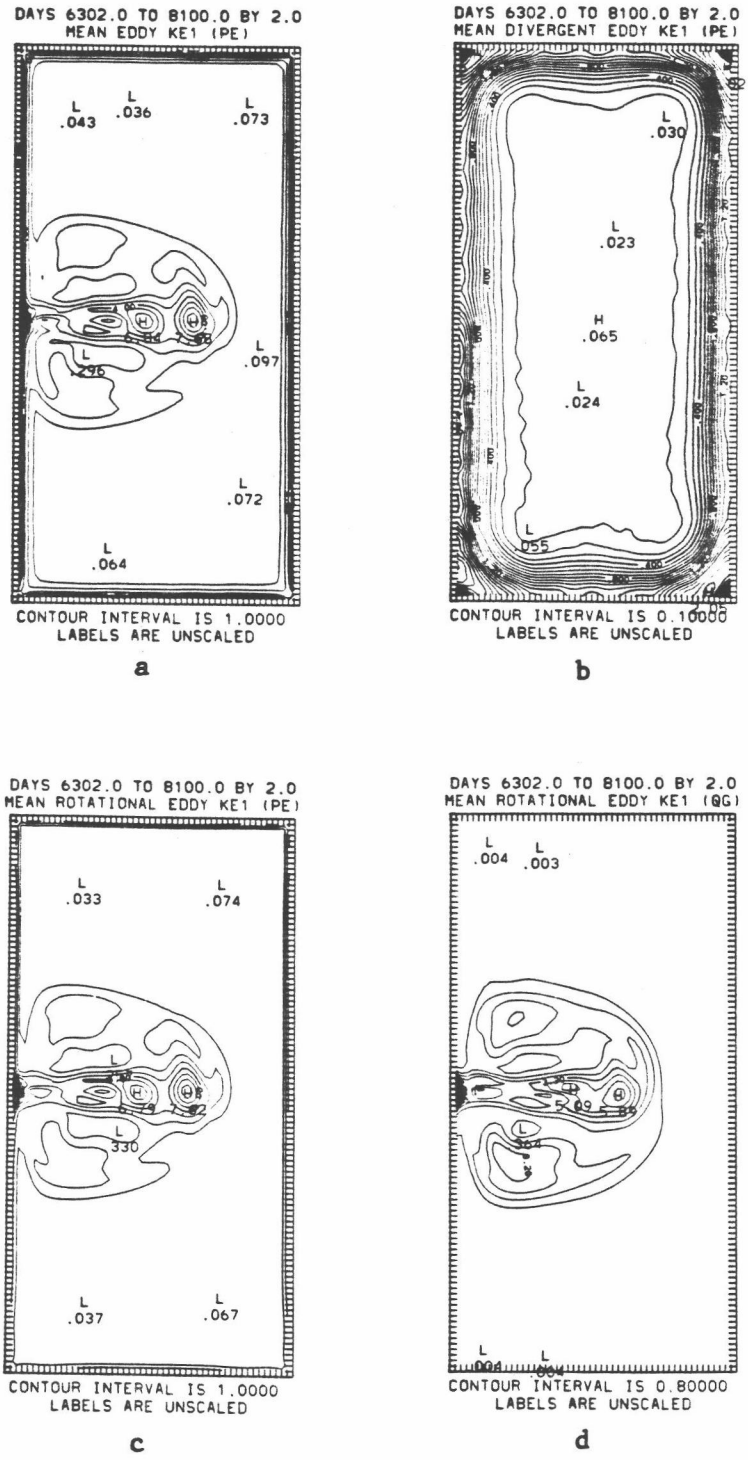

Fig. 6.18 Time-deviation of entry 17 in Table 4.1: a) K_1, b) K_{1D}, c) K_{1R} (PE), d) K_{1R} (QG).

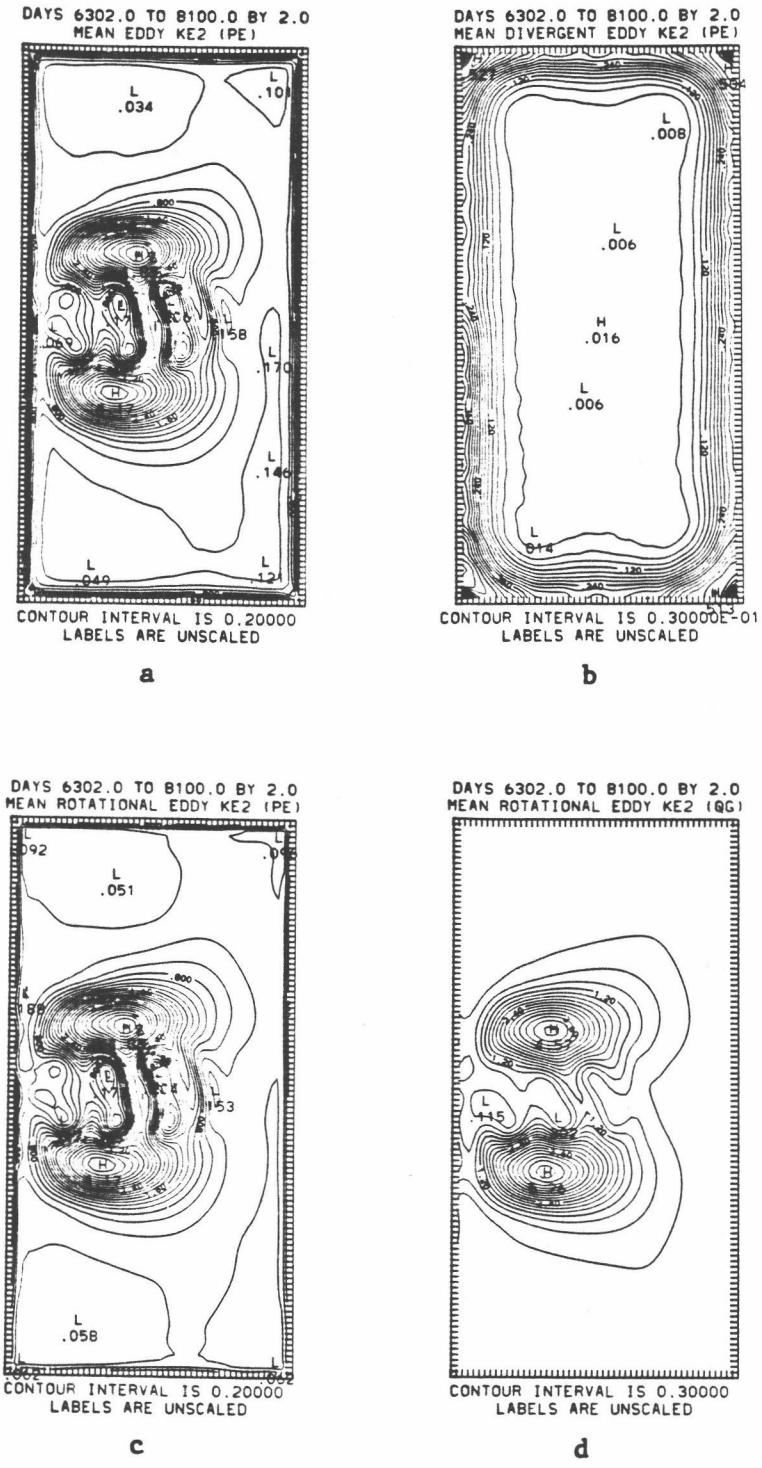

Fig. 6.19 Time-deviation of entry 18 in Table 4.1: a) K_2, b)K_{2D}, c) K_{2R} (PE), d) K_{2R} (QG).

A comparison of Figs. 6.18 and 6.19 with Figs. 5.23 and 5.24 shows that the maximum eddy kinetic energy has shifted from the recirculation regions and northwestern corner of the single-gyre experiment to the axis of the free jet. The presence of the eastward free jet can be conducive to the production of eddies by instability processes, whereas the presence of the northern boundary can inhibit eddy production (Holland, 1978).

The eddy divergent kinetic energy of the upper layer has also decreased considerably in the double-gyre case. This decrease could be due to several factors related to the Kelvin waves, which are the main reason for significant eddy divergent kinetic energy in these experiments. Since the Kelvin waves always travel counterclockwise (in the northern hemisphere) along the basin boundaries the change from single-gyre to double-gyre wind forcing could be affecting their propagation. These waves travel in the same direction as the wind in the northern half of the basin, but in the opposite direction in the southern half. Since the generation mechanism for the Kelvin waves is not known, it is possible that the mechanisms involved in their generation may have changed too. Other possible factors are the increased basin size and the incorporation of bottom friction in the double-gyre case. The latter could be acting to dissipate the Kelvin waves along the continental boundaries.

The geographical distributions of the time-mean and eddy rotational available potential energy for each model are shown in Figs. 6.20 and 6.21. Again most of the mean and eddy rotational available potential energy in both models is produced in the recirculation regions, where baroclinic instability occurs. The linear balance component still plays a lesser role than if a much larger basin size were used. Due to the dependence on symmetry about the mid-point of the basin, the linear balance terms in the single-gyre and double-gyre experiment are not readily comparable.

The energetic properties of the mean and eddy motions for the final, statistically steady state for the QG and PE models are shown in Figs. 6.22 and 6.23, respectively. Fig. 6.22 shows that the wind puts on the average 1.62×10^6 k J m^{-2} s^{-1} into the upper layer mean kinetic energy. About 65% of this is dissipated by lateral friction, primarily along the axis of the free jet and in the western boundary regions. The other 35% of the energy put in by the wind participates in the eddy generation process. Work done by the presure forces transfers 0.32×10^6 k J m^{-2} s^{-1} from the upper to the lower layer. Work done by buoyancy forces transfer 0.16×10^6 k J m^{-2} s^{-1} from each layer to maintain the mean available potential energy, which is continually supplying energy to the eddies. Buoyancy forces transform eddy potential energy into eddy kinetic energy in order to maintain the eddy field, which would otherwise be dissipated by both lateral and bottom friction. Thus the eddy

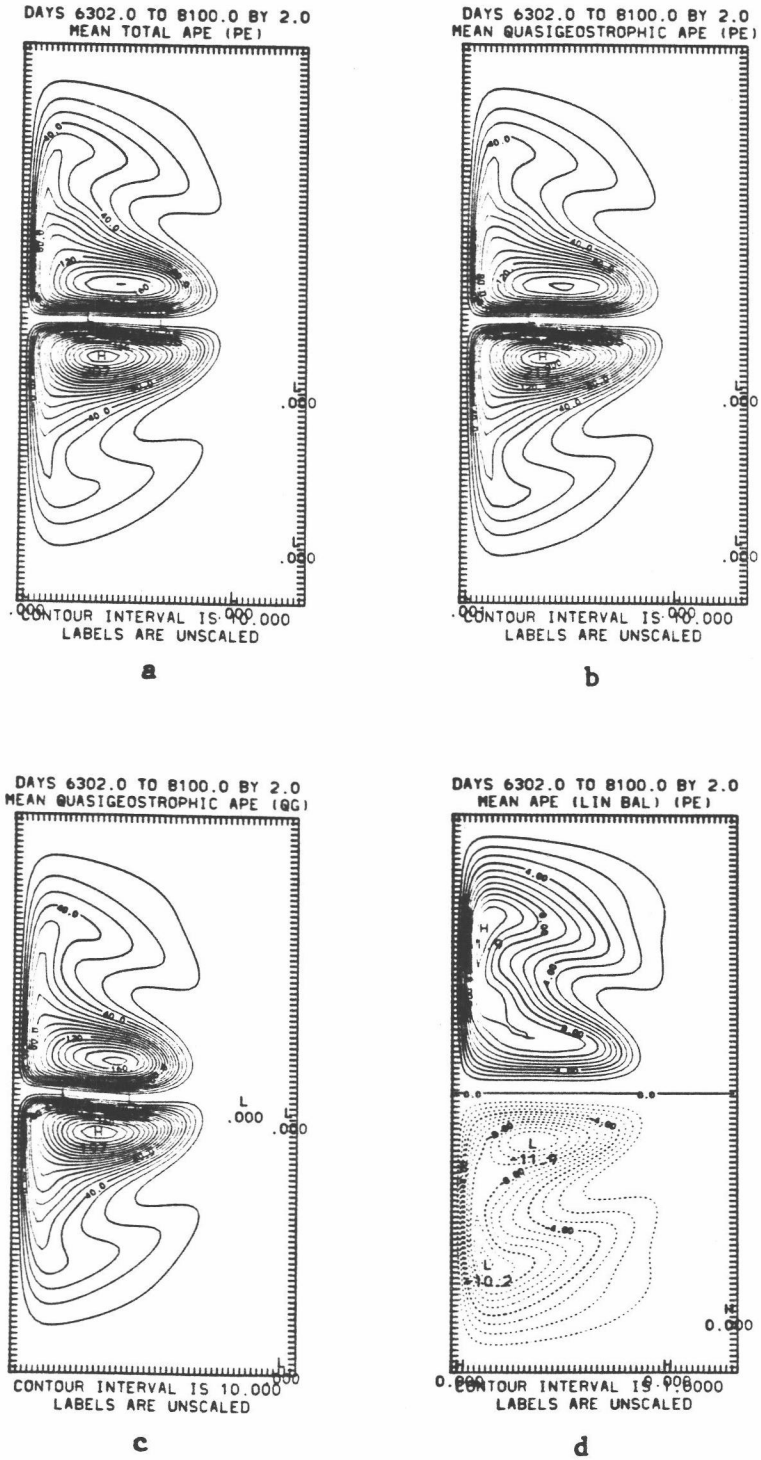

Fig. 6.20 Time-mean of entry 19 in Table 4.1: a) P_R, b) P_{RQG} (PE), c) P_{RQG} (QG), d) P_{RLB}.

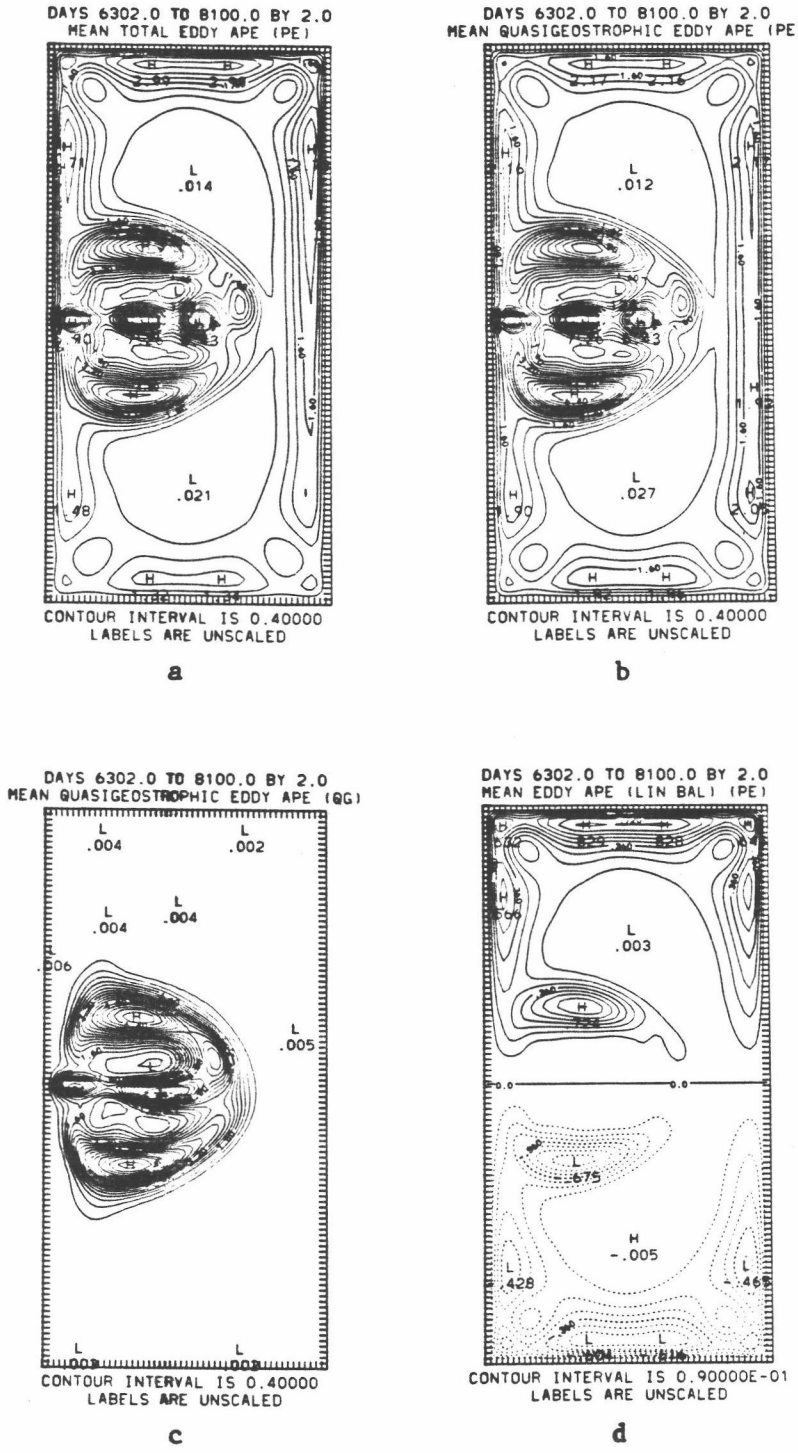

Fig. 6.21 Time-deviation of entry 19 in Table 4.1: a) P_R, b) P_{RQG} (PE), c) P_{RQG} (QG), d) P_{RLB}.

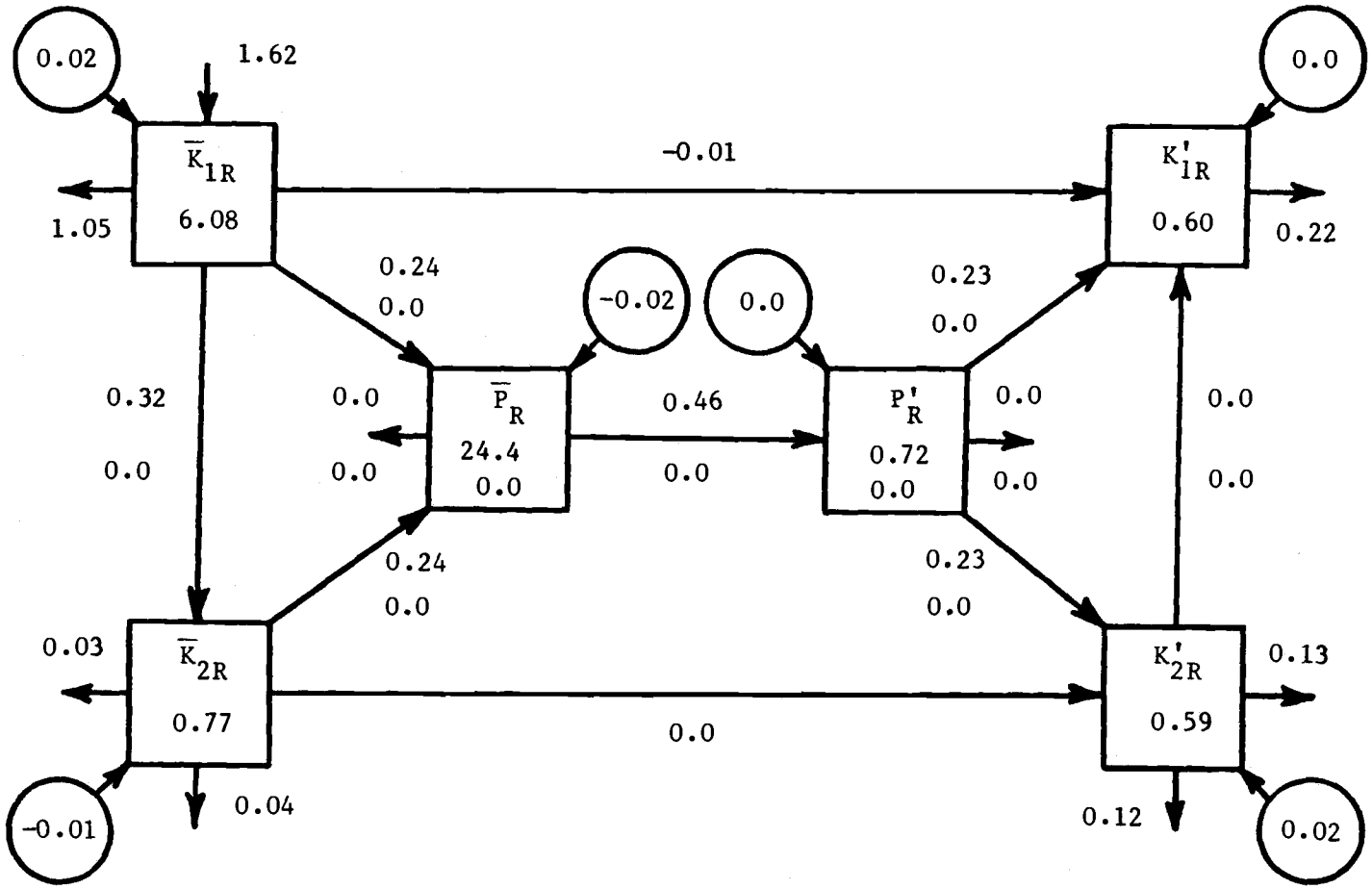

Fig. 6.22 The QG global energetics (the energy box diagram shown in Fig. 4.2) for the double-gyre experiment. The numbers within the boxes are the energy levels of the various components (units k J m^{-2}), and the numbers on the arrows show the energy transfers (units 10^6 k J m^{-2} s^{-1}), described by Eq. (4-45). Unless indicated by a negative sign, the arrow head shows the direction of energy flow.

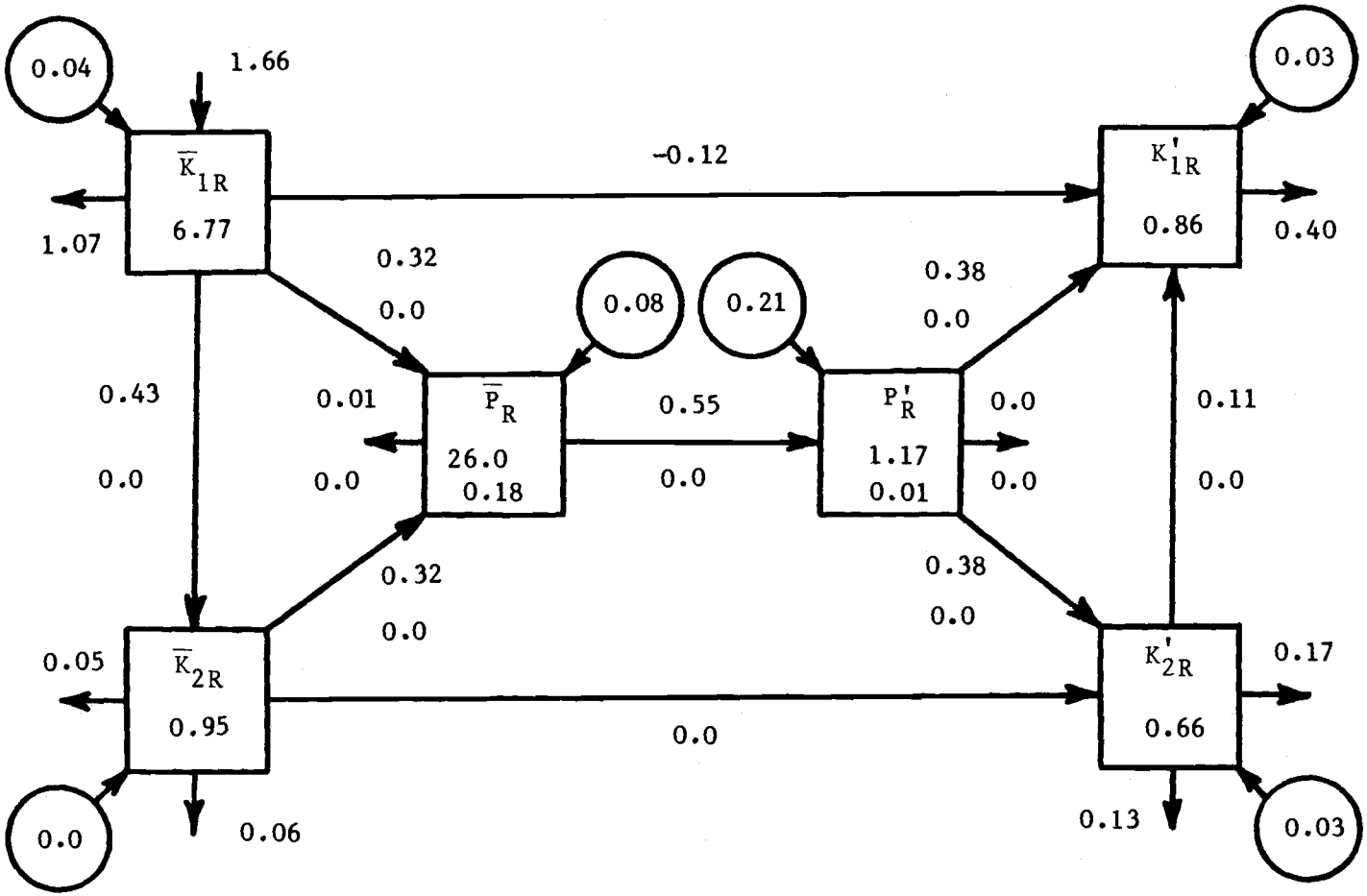

Fig. 6.23 Same as for Fig. 6.22, but for the PE model.

field receives its energy mainly as a result of baroclinic instability processes. The incorporation of bottom friction results in nearly equal amounts of lower layer kinetic energy being dissipated by lateral and bottom friction.

A comparison of Fig. 6.23 with Fig. 6.22 shows that 1) the QG energy transfer rates are similar, but generally higher for the PE model, 2) little energy is dissipated by biharmonic heat diffusion, 3) the work done by pressure forces in transferring eddy energy from the lower to upper layer is a significant pathway in the PE model, 4) a significant amount of energy goes directly from eddy to mean kinetic energy in the upper layer of the PE model, and 5) due to the small basin size, the LB terms are small.

The residuals for the QG model shown in Fig. 6.22 are small, implying that the five-year time-averaging is long enough to examine the eddy/mean breakdown in this model. Fig. 6.23 shows large residuals for the PE eddy energy, which could imply important FB and PE energy transfers, which were not explictly computed in this study. These residuals may represent real energy fluxes from the divergent component of flow to the rotational part (or vice versa). A more complete analysis of the total PE energy itself, necessary to explain the underlying dynamics, has not been done here.

A comparison of Figs. 5.27 and 5.28 with Figs. 6.22 and 6.23 shows that 65 to 75% of the upper layer mean kinetic energy input by the wind is dissipated by Laplacian friction, leaving

only 25 to 35% of the energy to participate in the eddy generation process. Thus the generally similar results between the single-gyre and double-gyre experiments can be most likely explained by the use of a rather large Laplacian friction coefficient. This suggests that in both experiments Laplacian friction dominates over eddy processes, with the result that rather weak instabilities and nonlinearities are observed. If the friction were reduced, the eddy processes could play a greater role, and stronger instabilities might be observed (see Holland, 1978). In particular, as stated previously, barotropic instabilities would be more likely to occur in the free jet of the double-gyre case, resulting in a different stability process than the single-gyre.

6.5 Vorticity

6.5.1 Relative vorticity

The geographical distributions of the time-averaged relative vorticity for both the QG and PE models are shown in Figs. 6.24 and 6.25, respectively. The vorticity patterns are similar. The QG model has slightly larger values of vorticity in the southern half of the basin, whereas the PE model has slightly larger values of vorticity in the northern half of the basin. The vertically-averaged vorticity, as in the single-gyre experiment, to a large extent resembles the upper layer vorti-

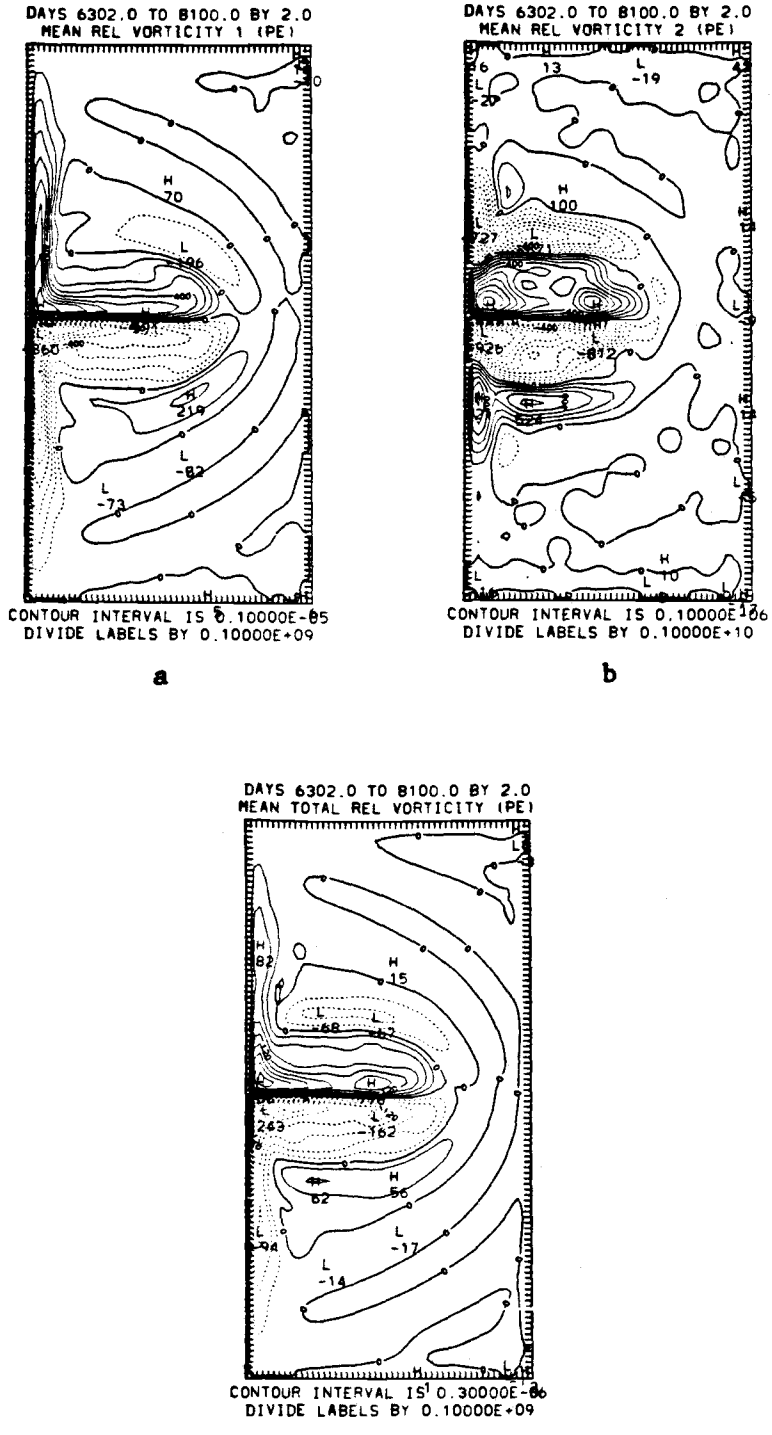

Fig. 6.24 Time-mean of entry 20a in Table 4.1: a) $\nabla^2\psi_1$, b) $\nabla^2\psi_2$, c) $H^{-1}(h_1\nabla^2\psi_1 + h_2\nabla^2\psi_2)$ (not shown in Table 4.1).

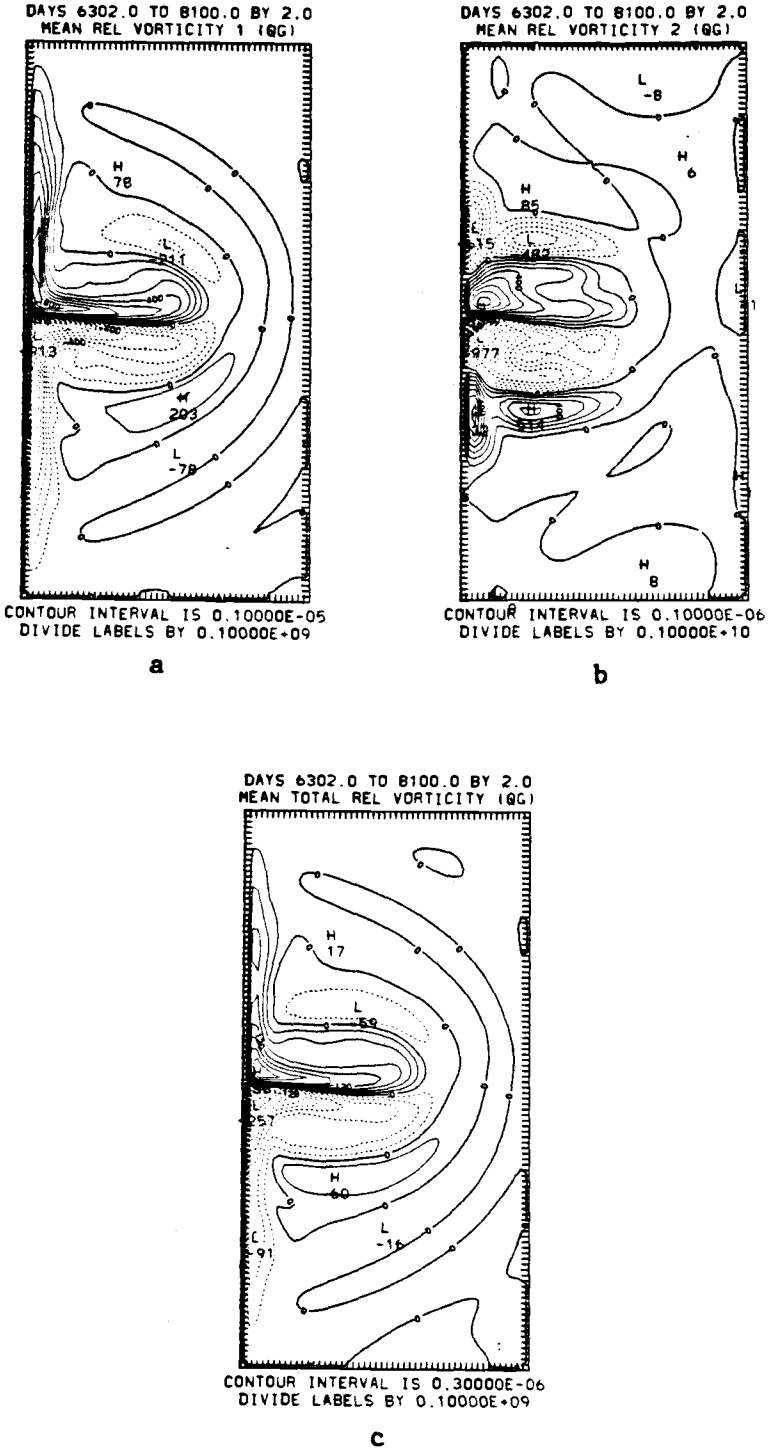

Fig. 6.25 Time-mean of entry 20b in Table 4.1: a) $\nabla^2\psi_1$, b) $\nabla^2\psi_2$, c) $H^{-1}((h_1\nabla^2\psi_1 + h_2\nabla^2\psi_2)$ (not shown in Table 4.1).

city, due to the generally larger values of vorticity in the upper layer.

In order to examine the local vorticity transfers, plots of the geographical distribution of the vertically-averaged relative vorticity are shown in Figs. (6.26)-(6.27). We first examine the spatial distribution of the vertical averages of the $\overline{A}_{1QG}$ and $\overline{A}_{2QG}$ terms in Eqs. (4-46) and (4-47), respectively, for the QG model (Fig. 6.26). In the western boundary regions, the main balance is between the Laplacian friction (Fig. 6.26d), planetary vorticity (Fig. 6.26b), and the horizontal advection (Fig. 6.26a). In the southern (northern) half of the basin, the Laplacian friction and horizontal advection terms tend to increase the counterclockwise (clockwise) vorticity, while the planetary vorticity tends to decrease it.

In the recirculation regions, the main balances are between the horizontal advection, the planetary vorticity, and to a lesser extent, the Laplacian friction. In the southern (northern) half of the basin, the planetary vorticity tends to increase the counterclockwise (clockwise) vorticity, while the horizontal advection and Laplacian terms tend to increase it.

To the south and north of the axis of the free jet, the main balance is between the horizontal advection and Laplacian friction. To the south (north) of the axis of the free jet, the horizontal advection tends to increase the counterclockwise (clockwise) vorticity, while the Laplacian friction tends to decrease it.

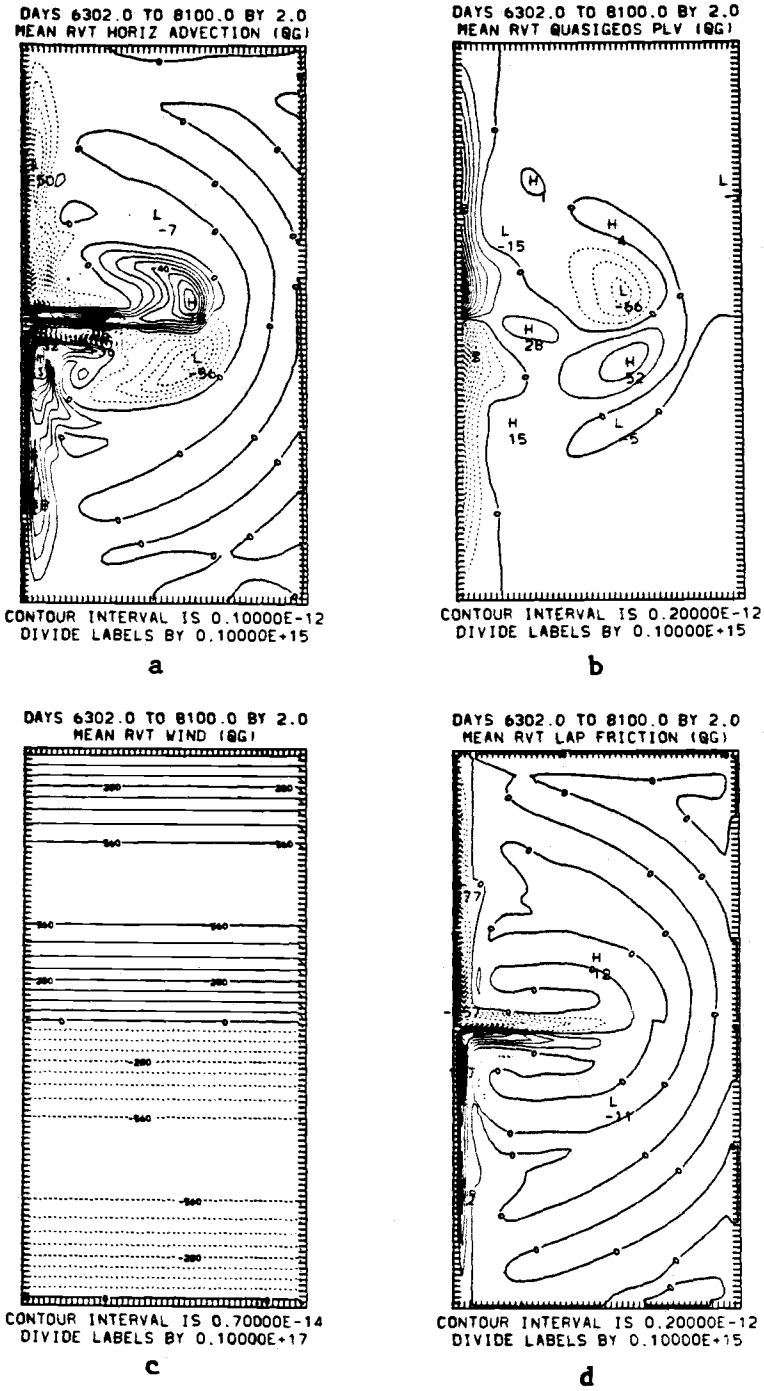

Fig. 6.26 QG spatial distribution of the time and vertical averages of the A_{1QG} and A_{2QG} terms on the right-hand sides of Eqs. (4-46) and (4-47):

a) $-(h_1 J(\psi_1,\zeta_1)+h_2 J(\psi_2,\zeta_2))/H$,

b) $-(h_1\beta\psi_{1x}+h_2\beta\psi_{2x})/H$, c) $(h_1/H)\mathrm{curl}_z\tau(y)$,

d) $(A_m/H)(h_1\nabla^4\psi_1+h_2\nabla^4\psi_2)$,

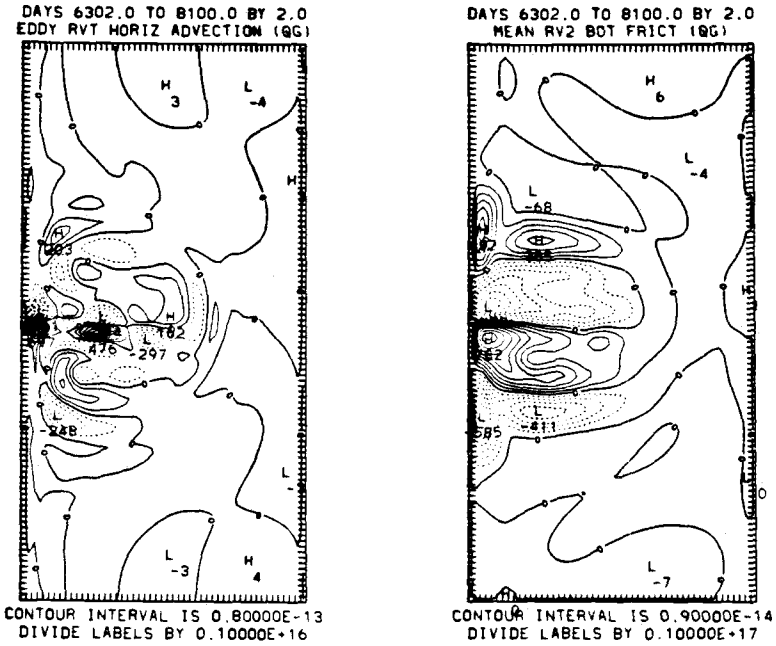

e f

Fig. 6.26 (cont.)

e) $-(h_1 J(\psi_1', \zeta_1') + h_2 J(\psi_2', \zeta_2'))/H,$

f) $-(h_2/H) C_B \nabla^2 \psi_2.$

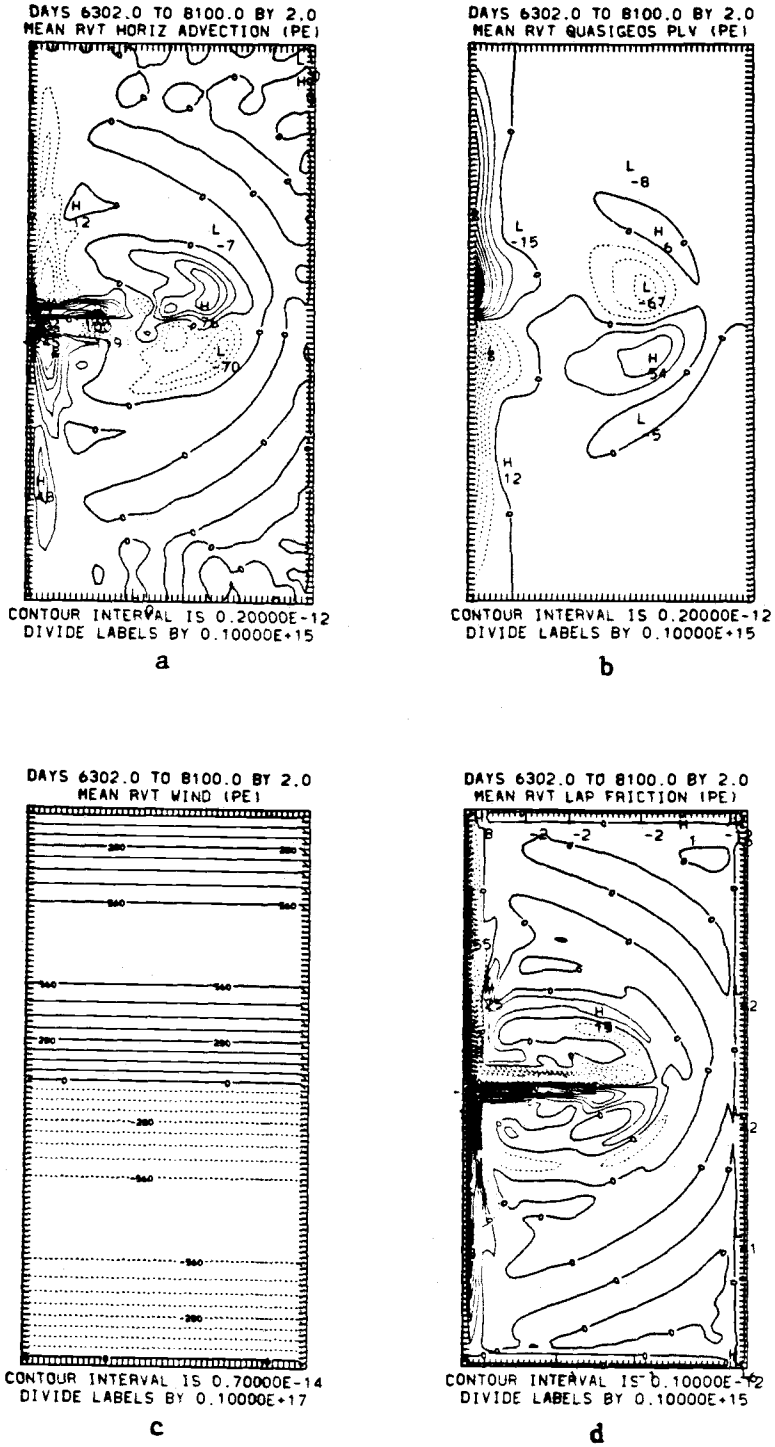

Fig. 6.27 Same as Fig. 6.26, but for the PE model.

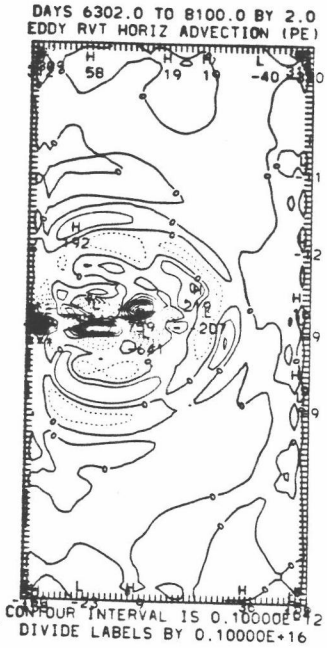

e

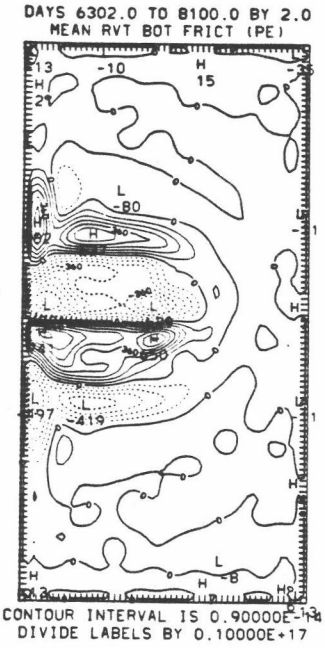

f

Fig. 6.27 (cont.)

In the interior and southern portions of the basin, a Sverdrup balance exists, i.e., the planetary vorticity is balanced by the wind stress curl (Fig. 6.26c).

The change of vorticity due to the eddies (Fig. 6.26e) is concentrated 1) along the axis of the free jet, and 2) to the north and south of the axis of the free jet. In these areas, the eddies both increase and decrease the vorticity, with the result that the net contribution to the vorticity is small.

The change of vorticity due to the bottom friction is shown in Fig. 6.26f. Alternate areas of clockwise and counterclockwise vorticity are seen along the western boundary, and to the north and south of the axis of the free jet. The bottom friction term is in general small compared to the other terms.

Fig. 6.27 shows the spatial distribution of the vertical averages of the $\overline{A}_{1QG}$ and $\overline{A}_{2QG}$ terms in Eqs. (4-46) and (4-47), respectively, for the PE model. A comparison of Fig. 6.27 with Fig. 6.26 shows similar "mean vorticity tendencies", except for Kelvin wave effects in the boundary regions of the PE model.

The vertical averages of the $\overline{A}_{1LB}$ and $\overline{A}_{2LB}$ terms in Eqs. (4-46) and (4-47) were calculated, and shown to be much smaller than any of the vertically-averaged $\overline{A}_{1QG}$ and $\overline{A}_{2QG}$ terms discussed previously. The vertical averages of the terms $\overline{A}_{1FB}$ and $\overline{A}_{1PE}$ in Eq. (4-46), and $\overline{A}_{2FB}$ and $\overline{A}_{2PE}$ in Eq. (4-47) were calculated as a residual, and shown to be significant, as in the single-gyre experiment. The time rate of change

of the horizontally-averaged vorticity, i.e., $((h_1\nabla^2\psi_{1t}+ h_2\nabla^2\psi_{2t})/H)$, was also calculated. This term was close to zero, which is to be expected in a statistically steady state.

The geographical distributions of the PE and QG vertically-averaged relative vorticity for the southern half of the double-gyre basin (the lower half of Figs. 6.26 and 6.27) are similar to those for the single-gyre basin (not shown). The main difference is that the change of vorticity due to the eddies is concentrated in the vicinity of the recirculation region in the single-gyre case, and near the axis of the free jet in the double-gyre experiment.

6.5.2 Potential vorticity

The geographical distributions of the QG and PE time-averaged potential vorticity for the upper and lower layers are shown in Figs. 6.28 and 6.29, respectively. In the upper layer (Fig. 6.28), the following features are discernible in both models, which are similar to the single-gyre results: 1) sharp gradients or "tongues" of potential vorticity in the western boundary regions, 2) in the southern (northern) half of the basin, a southwestward (northwestward) tongue of potential vorticity near the eastern side of the basin, 3) sharp gradients of potential vorticity along the axis of the free jet, and 4) a gradual northward increase of potential vorticity in the rest of the basin. In the lower layer, the following features, also

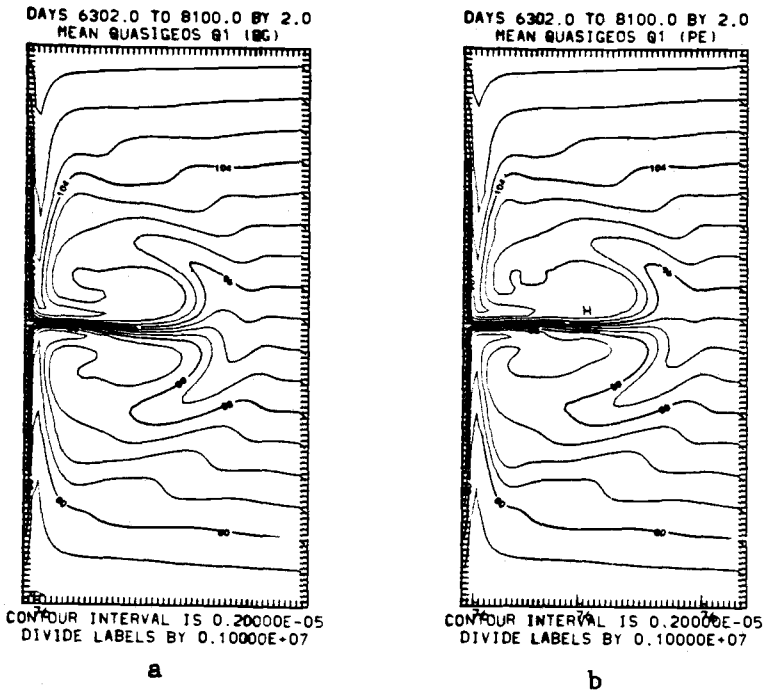

Fig. 6.28 Time-mean of Entry 22 in Table 4.1: a) Q_{1QG} (QG), b) Q_{1QG} (PE).

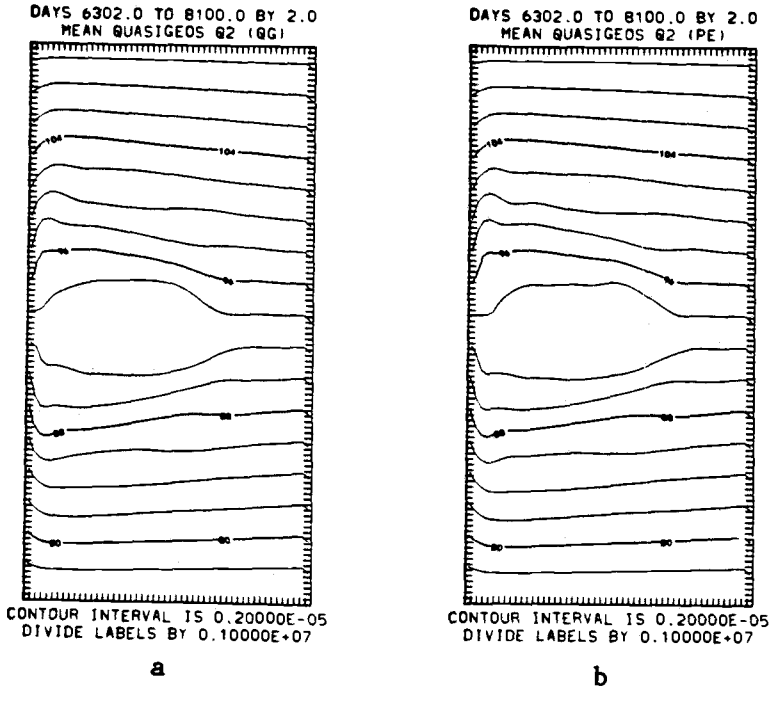

Fig. 6.29 Time-mean of Entry 23 in Table 4.1: a) Q_{2QG} (QG), b) Q_{2QG} (PE).

similar to the single-gyre results, can be seen in both models: 1) a gradual northward increase of potential vorticity throughout most of the basin, 2) a uniform region of potential vorticity in the central portion of the basin, and 3) in the southern (northern) half of the basin, a southward (northward) extending tongue of potential vorticity in the western boundary region.

Again, only the lowest order component has been calculated for the PE model, which explains why the QG and PE patterns are so similar. Analysis of the higher order components in the PE model is necessary to address the differences.

6.6 Eddy momentum transports

The zonally-averaged, off-diagonal components of the eddy momentum transports in each layer for both models are shown in Figs. 6.30 and 6.31. As in the single-gyre case, the main contribution to the eddy momentum transports or stresses in the PE model is by the rotational component, which is generally larger than the QG. The geographical distribution (not shown) of the off-diagonal components shows 1) adjacent regions of positive and negative eddy momentum transports along the axis of the free jet, and to the north and south of the free jet and 2) in the recirculation regions, positive (negative) transports in the southern (northern) half of the basin. A comparison of the southern half of Figs. 6.30 and 6.31 with Figs. 5.39 and 5.40 shows similar eddy transport patterns.

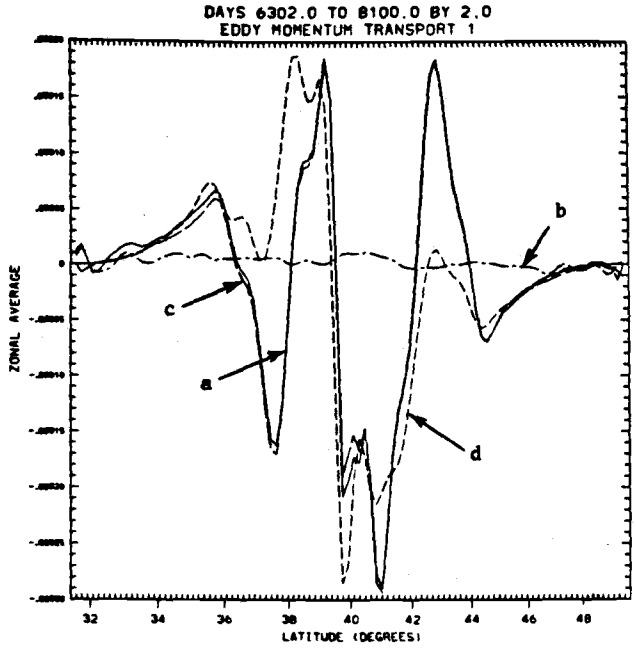

Fig. 6.30 Time-mean of the zonally-averaged eddy momentum transports in the upper layer: a) u_1v_1, b) $\chi_{1x}\chi_{1y}$, c) $-\psi_{1y}\psi_{1x}$ (PE), d) $-\psi_{1y}\psi_{1x}$ (QG).

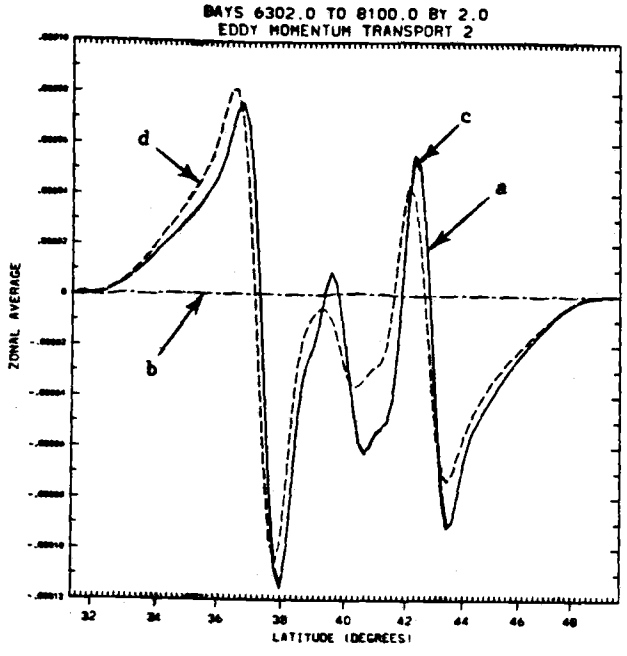

Fig. 6.31 Time-mean of the zonally-averaged eddy momentum transports in the lower layer: a) u_2v_2, b) $\chi_{2x}\chi_{2y}$, c) $-\psi_{2y}\psi_{2x}$ (PE), d) $-\psi_{2y}\psi_{2x}$ (QG).

Again, as in the single-gyre experiment, the $\overline{u'v'}$ correlations, although retarding the mean flow in some areas and driving it in others, are probably unimportant as momentum transports. Instead they are just signatures of the instability processes.

6.7 PE heat transports

6.7.1 Meridional heat transports

The spatial distribution of the time-mean and eddy, meridional heat transports in each layer and for both layers is shown in Figs. 6.32-6.37. As in the single-gyre case, the eddies generally act against the mean transport of heat. Eddy heat transport occurs in the recirculation regions, in the area of the free jet, and along the western and eastern boundaries. For each layer, both divergent and rotational eddy heat transports are significant. The main contribution for eddy heat transport by the rotational component occurs in the recirculation region and in the vicinity of the free jet. Fig. 6.38 emphasizes the mean-poleward and eddy-equatorward transports of heat in these regions. The slight imbalances seen are due to the transport of heat by biharmonic heat diffusion processes. Again the main contribution for eddy meridional heat transport by the divergent component occurs along the western and eastern boundaries. Presumably the main contribution for eddy zonal

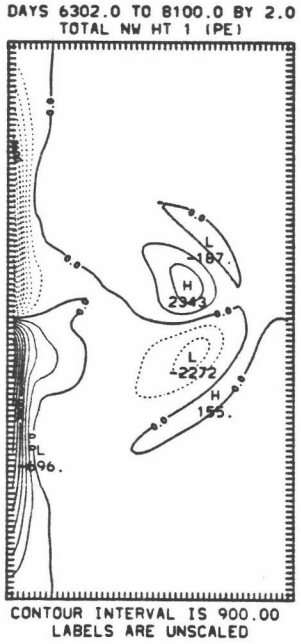

a

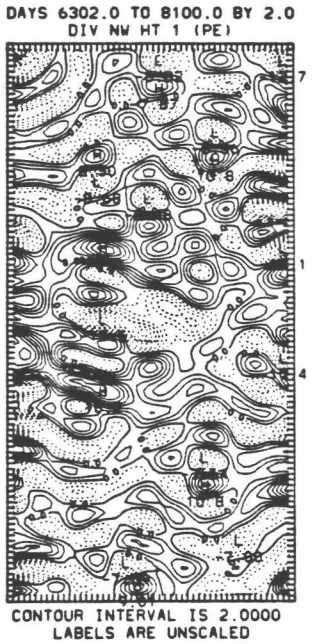

b

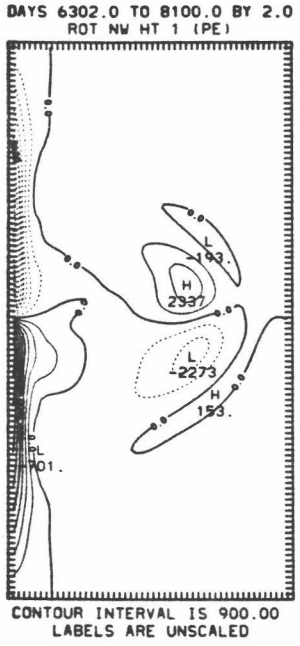

c

Fig. 6.32 Spatial distribution of the time-averaged, meridional heat transport in the upper layer: a) $h_1 v_1 T_1$, b) $h_1 \chi_{1y} T_1$, c) $h_1 \psi_{1x} T_1$.

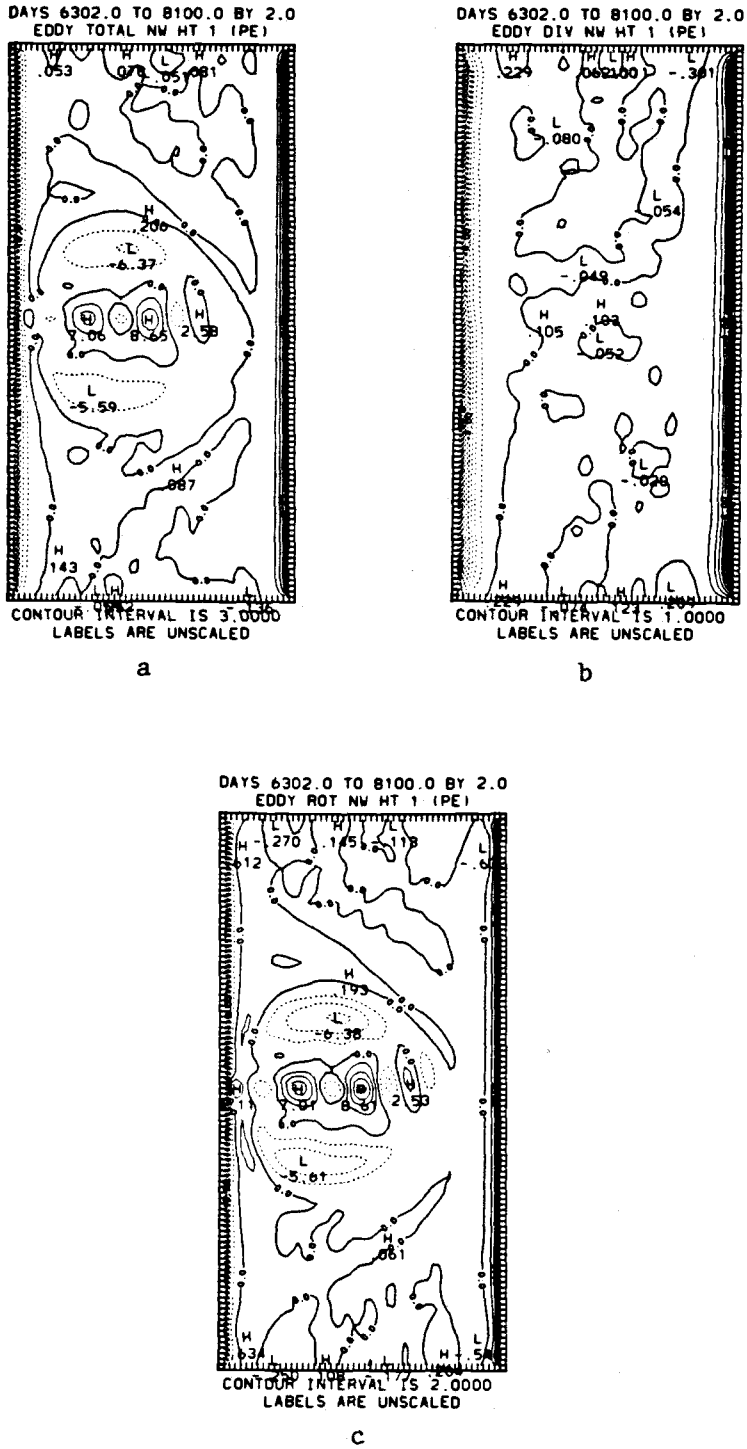

Fig. 6.33 Spatial distribution of the eddy meridional heat transport in the upper layer: a) $h_1 v_1 T_1$, b) $h_1 \chi_{1y} T_1$, c) $h_1 \psi_{1x} T_1$.

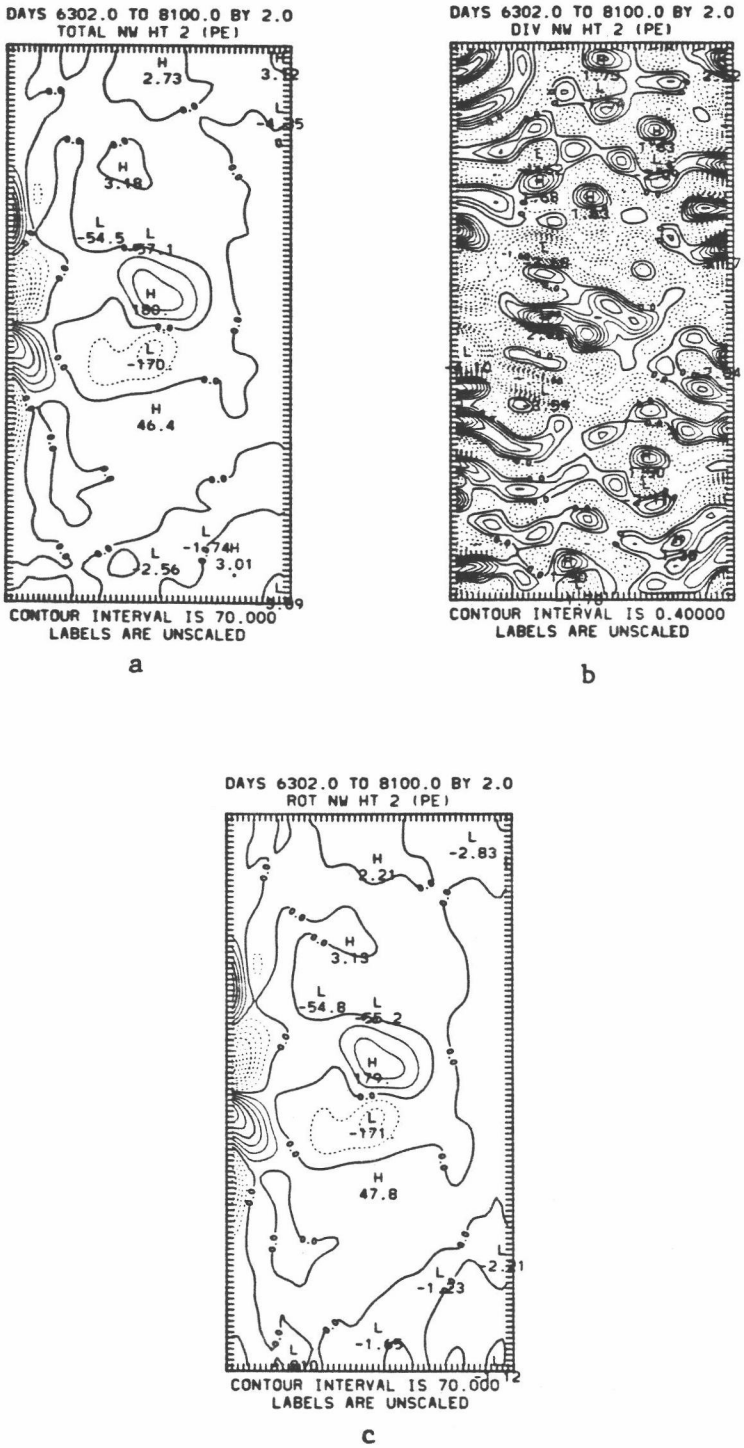

Fig. 6.34 Spatial distribution of the time-averaged meridional heat transport in the lower layer: a) $h_2 v_2 T_2$, b) $h_2 \chi_{2y} T_2$, c) $h_2 \psi_{2x} T_2$.

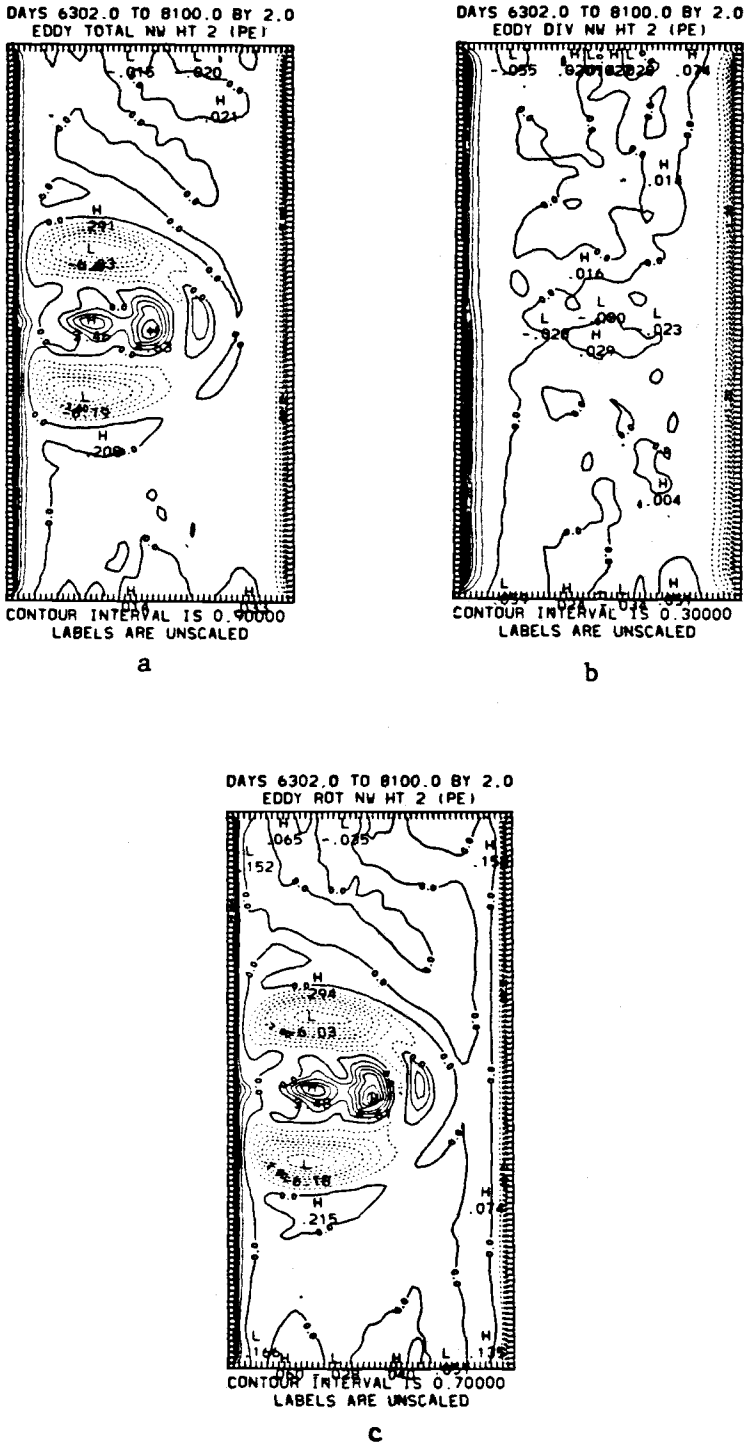

Fig. 6.35 Spatial distribution of the eddy meridional heat transport in the lower layer: a) $h_2 v_2 T_2$, b) $h_2 \chi_{2y} T_2$, c) $h_2 \psi_{2x} T_2$.

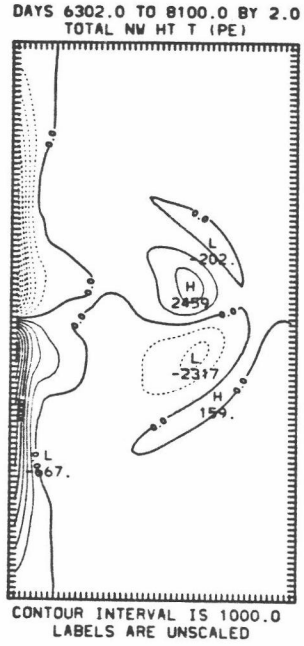

a

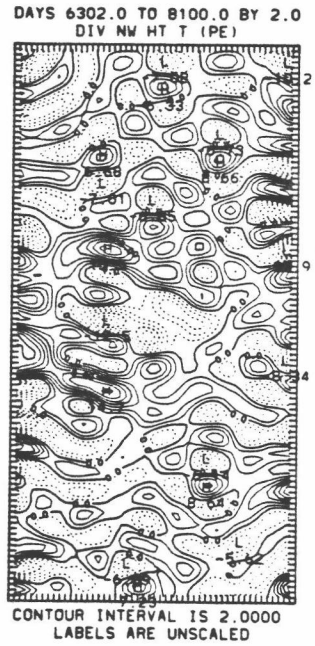

b

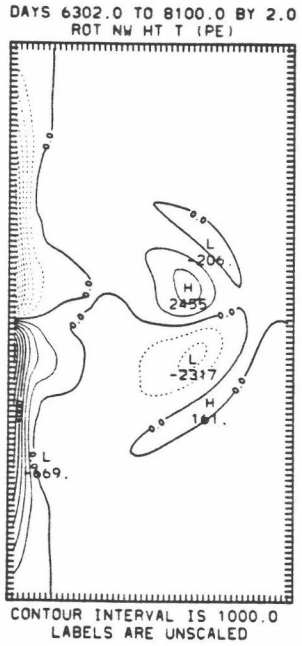

c

Fig. 6.36 Spatial distribution of the time-averaged, meridional heat transport summed for both layers: a) $h_1 v_1 T_1 + h_2 v_2 T_2$, b) $h_1 \chi_{1y} T_1 + h_2 \chi_{2y} T_2$, c) $h_1 \psi_{1x} T_1 + h_2 \psi_{2x} T_2$.

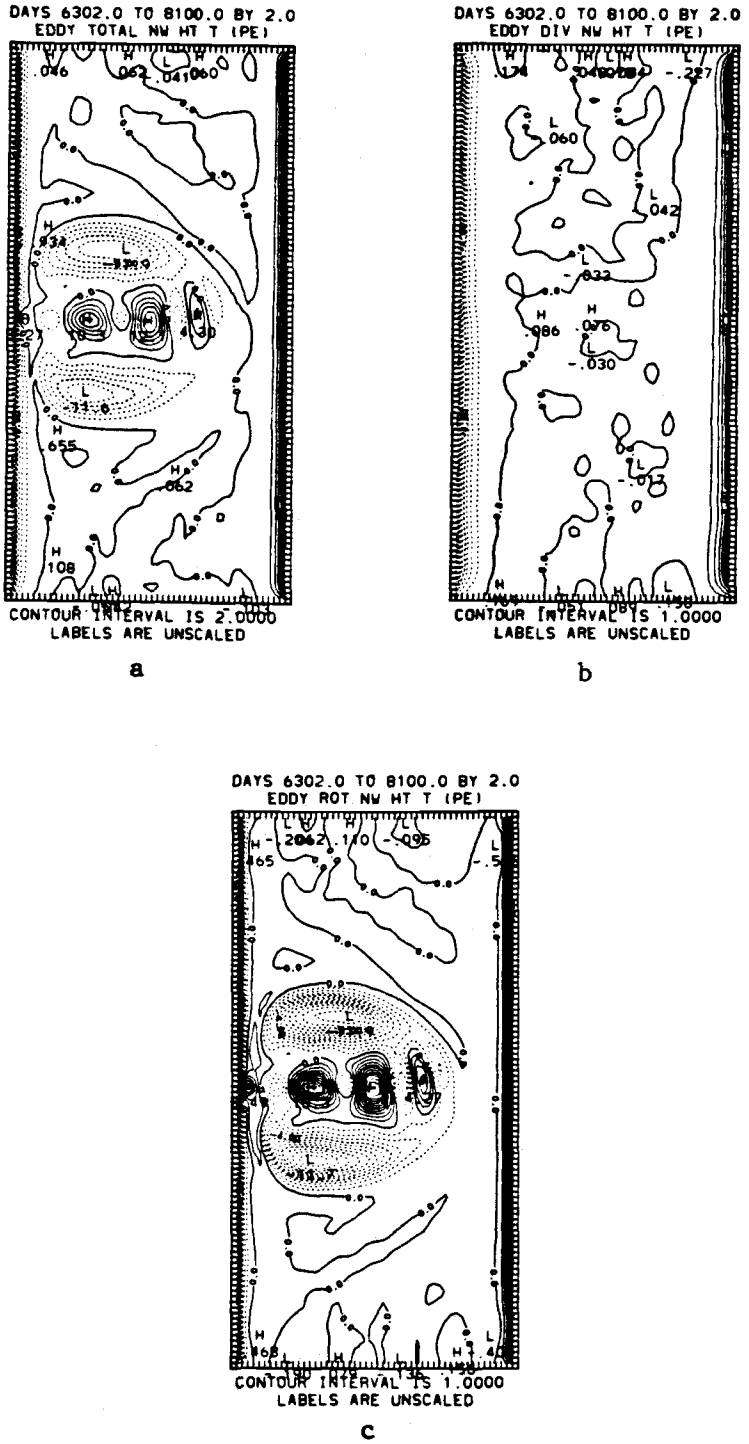

Fig. 6.37 Spatial distribution of the eddy meridional heat transport summed for both layers:
a) $h_1 v_1 T_1 + h_2 v_2 T_2$, b) $h_1 \chi_{1y} T_1 + h_2 \chi_{2y} T_2$,
c) $h_1 \psi_{1x} T_1 + h_2 \psi_{2x} T_2$.

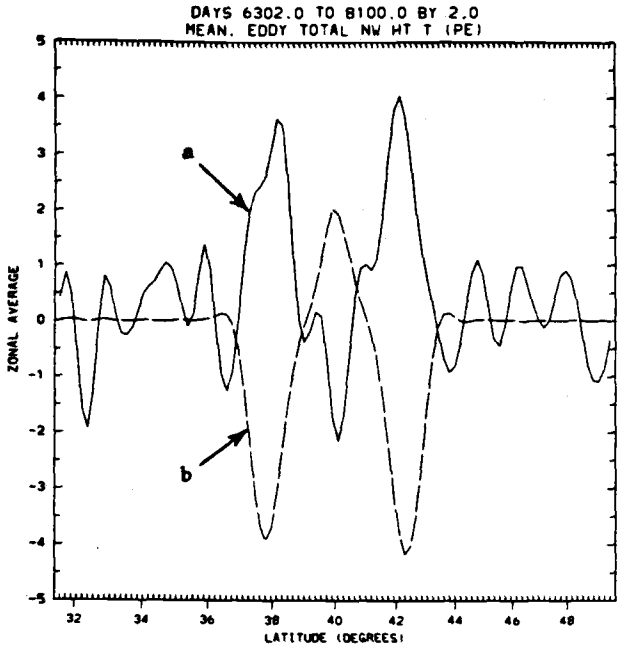

Fig. 6.38 Zonal average of the a) time-mean and b) eddy, vertically-integrated, meridional heat transport.

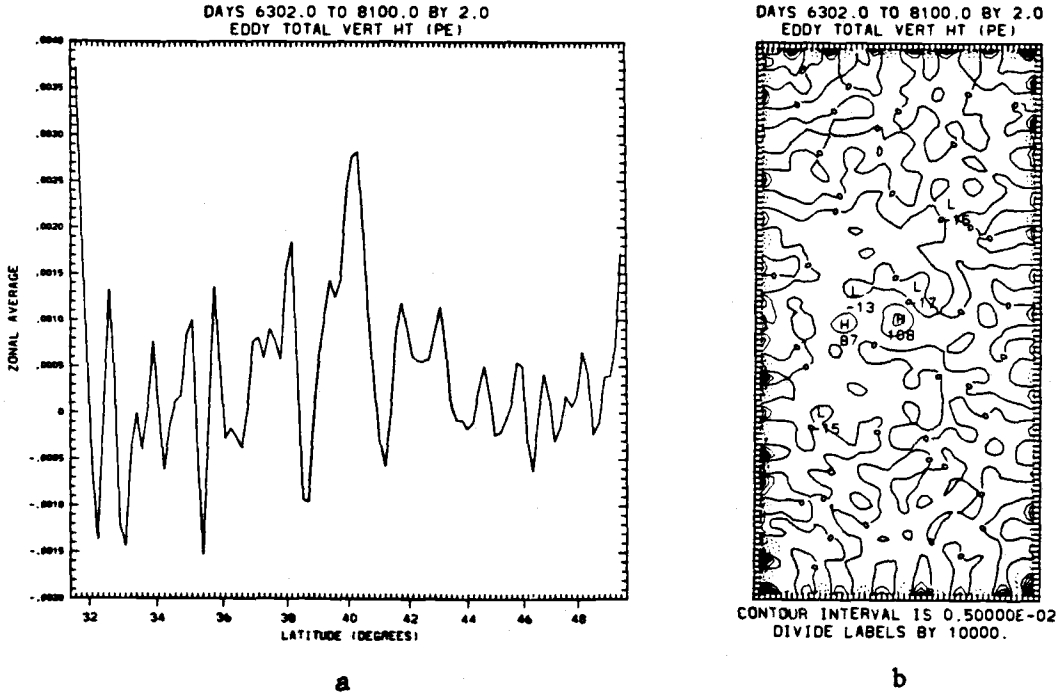

Fig. 6.39 Zonal average (a) and spatial distribution (b) of the time-mean, vertically-integrated, vertical heat transport.

heat transport by the divergent component occurs along the northern and southern boundaries, so that overall the divergent component may not play much of a role in actual eddy heat transports. These divergent transports are due to Kelvin waves, whose properties will be discussed further in the following chapter.

6.7.2 Vertical heat transports

The vertically-integrated, time-mean vertical heat transport is shown in Fig. 6.39. The presence of alternate regions of positive and negative heat transport throughout most of the basin looks very much like the signature of gravity waves. This suggests that a longer time averaging is needed in the double-gyre experiment to average out these waves.

CHAPTER 7. DISCUSSION OF RESULTS

Based on the results of the two QG and PE numerical experiments, it is obvious that the two models can be configured to give nearly similar results. Extensive analyses have shown that similar results for both models can be obtained for 1) basic quantities, such as horizontal velocities and streamfunctions, 2) energetics, 3) relative and potential vorticity, and 4) momentum transports.

Although overall the results are fairly similar between the two models, a closer examination does reveal some significant differences. In both experiments, consistently higher PE energies and energy transfer rates are obtained. An examination of the geographical distributions of these energy quantities shows that most of the differences between the models occur along the lateral boundaries of the basin. This appears to be the result of Kelvin waves traveling along these boundaries in the PE model. Instead of being dissipated, these waves travel counterclockwise around the basin and perhaps even interact with the eddies and mean general circulation. Although these experiments were not designed with the Kelvin waves in mind, the results can be used to deduce some of the basic properties of these waves.

From the instantaneous plots of p_1 in Figs. 5.18a and 6.13a, we determine that the basic wavelength is ~666 km for

both experiments. For two layers, the propagation speed of Kelvin waves is given by $c = (g' h_1 h_2 / H)^{1/2} = 4$ m s^{-1} (same for both experiments). Using the wavelength and propagation speed, we calculate a period of 1.9 days. Fig. 7.1 is a time series of the vertical velocity at a single grid-point near the southern boundary of the basin for the last 1000 days of the single-gyre experiment. (The point plotted here has coordinates (26,1), where point (1,1) is the center of the southwest-corner grid box and point (50,50) is the center of the northeast-corner grid box). The sampling frequency for this time series is 0.5 days. The dominant feature of this time series is a very regular wave with a period of 1.9 days, which exactly matches the period calculated for the Kelvin waves.

Kelvin waves also have the "pecularity" that they can travel along lateral boundaries in one direction only, i.e., counterclockwise in the Northern Hemisphere. A time sequence of the vertical velocity field at four-hour intervals (not shown) establishes that this is the direction of propagation of the observed waves near the boundaries.

Finally, Kelvin waves have the characteristic that the amplitudes decay rapidly with distance from the boundary, and become insignificant beyond a distance on the order of the Rossby radius of deformation. Fig. 7.2 shows ten-day time series of p_1 and p_2 at half-day intervals for five separate grid points in the single-gyre basin. The five points form a line

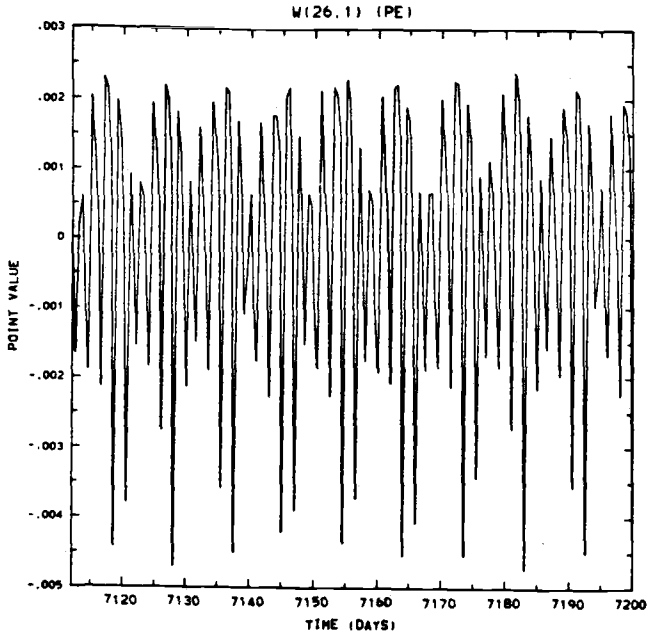

Fig. 7.1 Time series of the vertical velocity at a single grid-point near the southern boundary of the basin for the last 1000 days of the single-gyre experiment.

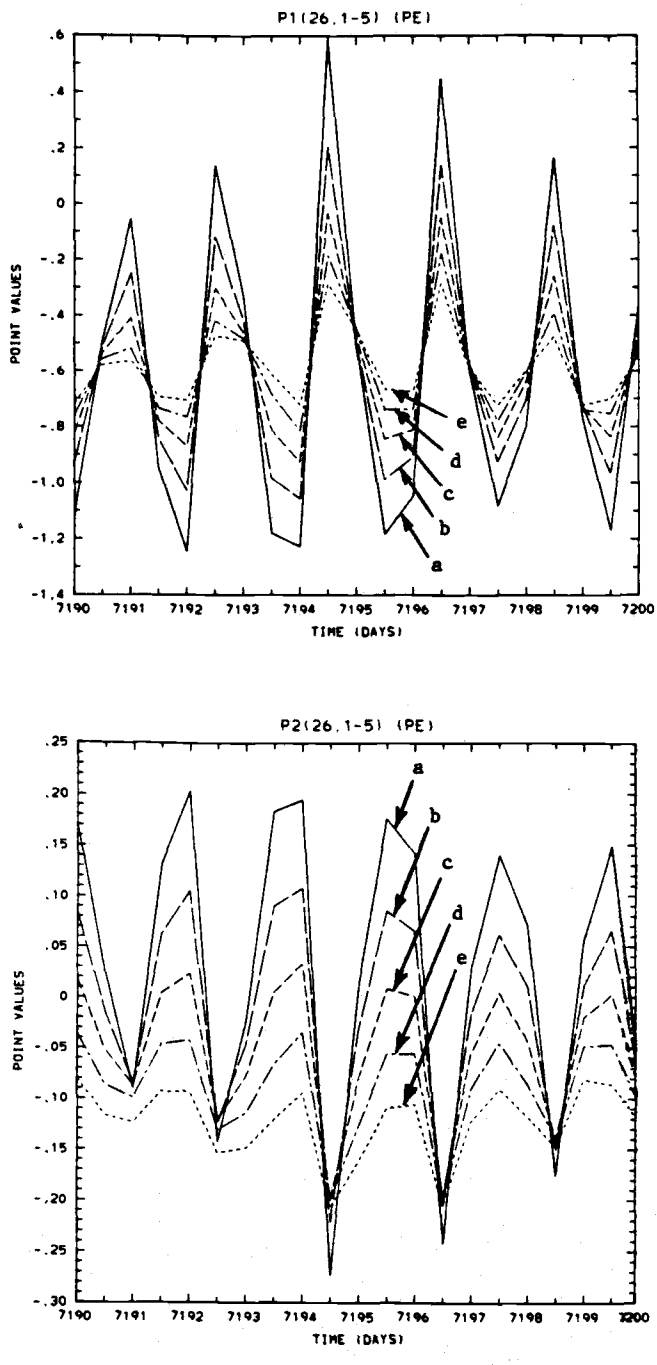

Fig. 7.2 Time series of p_1 (top) and p_2 (bottom) at half-day intervals for five grid points near the southern boundary of the single-gyre basin. The grid points plotted are: a) (26,1), b) (26,2), c) (26,3), d) (26,4), e) (26,5).

moving northward from the center of the southern boundary. These time series clearly show the decay in amplitudes away from the boundaries. The 1.9 day period of the waves is also evident. Note that Fig. 7.2 also shows that p_1 and p_2 are 180° out of phase.

We next show that the Kelvin waves are the likely mechanism for the meridional eddy heat transport by the divergent component shown in Figs. 5.42b, 5.44b, 6.33b, and 6.35b. Fig. 7.3 shows ten-day time series plots of the total meridional eddy heat transport (i.e., $h_1v_1'T_1' + h_2v_2'T_2'$) at the midpoint of each lateral boundary. Along the northern (Fig. 7.3c) and southern (Fig. 7.3a) boundaries, there is no net meridional transport. Along the western boundary (Fig. 7.3b) there is net equatorward transport, while along the eastern boundary (Fig. 7.3d) there is net poleward transport. Figs. 7.4 and 7.5 shows how these transports are accomplished in layers 1 and 2, respectively. Along the northern (Figs. 7.4c and 7.5c) and southern (Figs. 7.4a and 7.5a) boundaries, the kinematic boundary condition ($v = 0$) results in insignificant meridional eddy heat transports. Along the western boundary in the upper layer (Fig. 7.4b) and along the eastern boundary in the lower layer (Fig. 7.4d), the v' and T' waves are 180° out of phase, with the result that the meridional eddy heat transports are equatorward in these regions. Along the eastern boundary in the upper layer (Fig. 7.4d), and along the western boundary in the lower layer

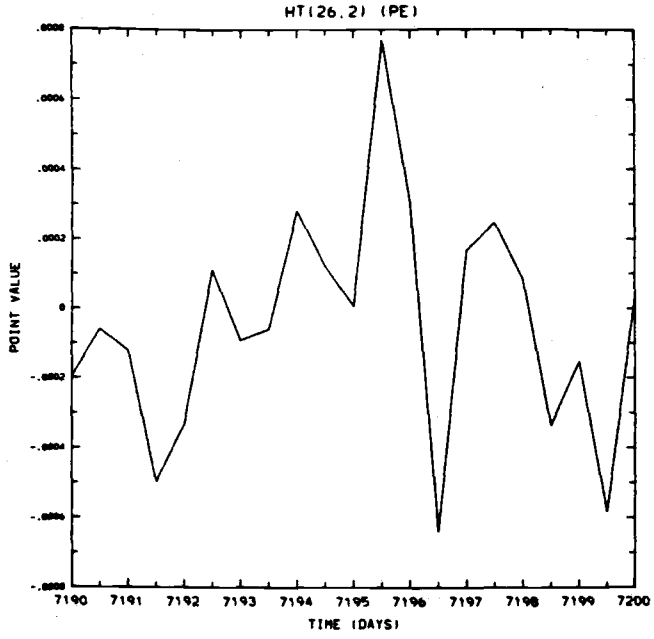

a

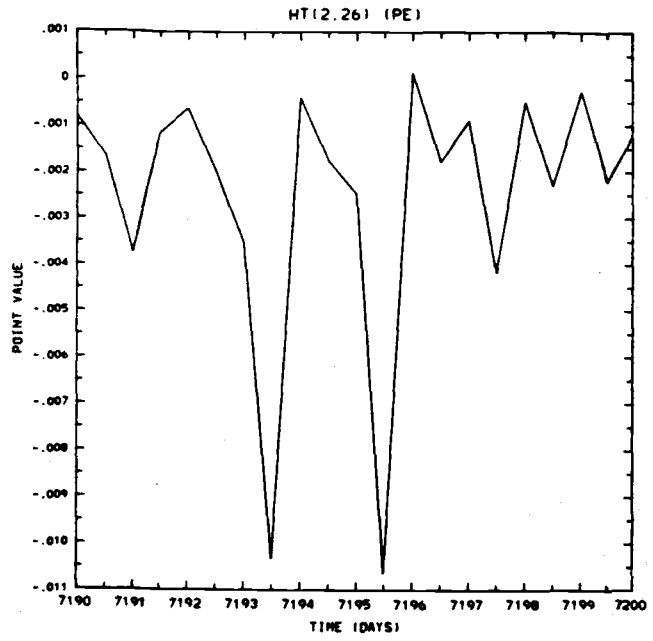

b

Fig. 7.3 Time series of the total meridional, eddy heat transport $(h_1 v_1'T_1' + h_2 v_2'T_2')/H$ for points near the middle of the a) southern, b) western, c) northern, d) eastern boundaries.

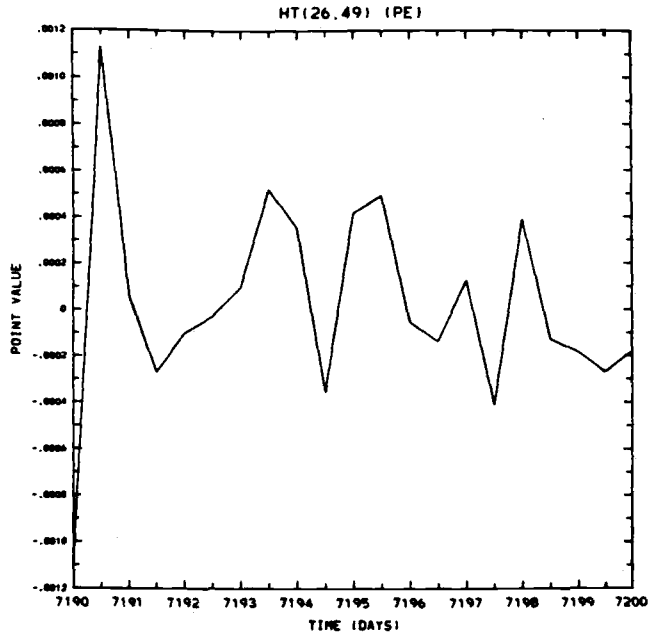

c

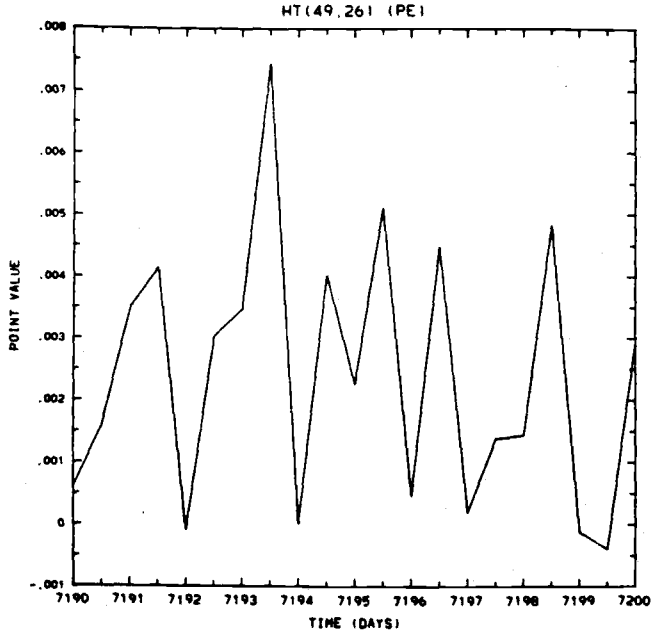

d

Fig. 7.3 (cont.)

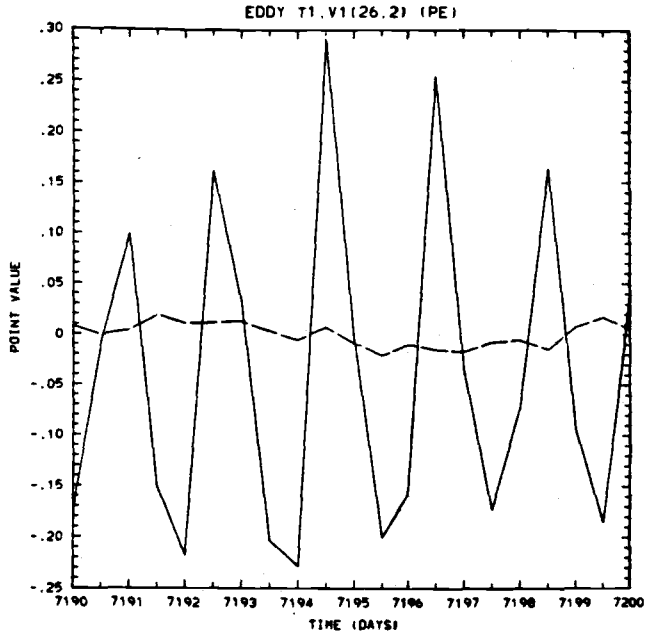

a

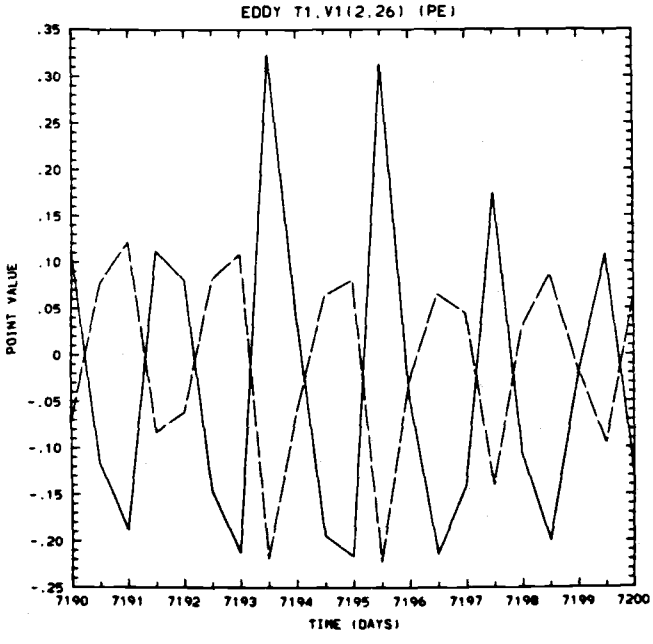

b

Fig. 7.4 Time series of T_1' (solid line) and v_1' (dashed line) for points near the middle of the a) southern, b) western, c) northern, d) eastern boundaries.

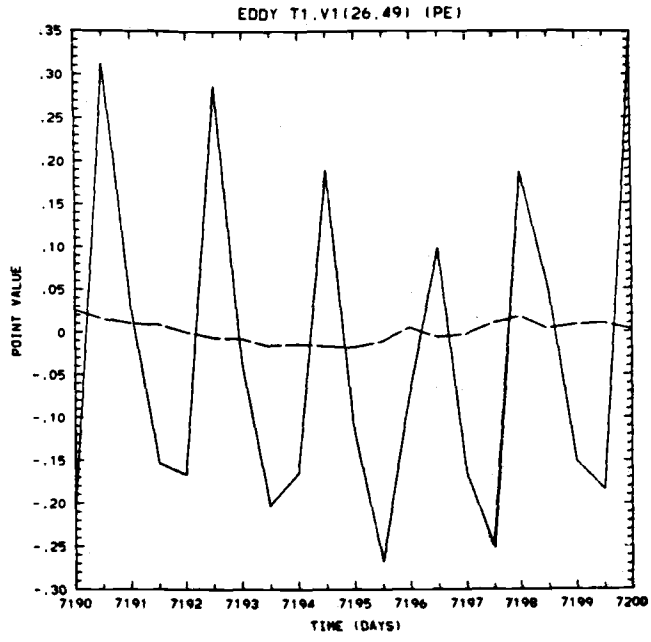

c

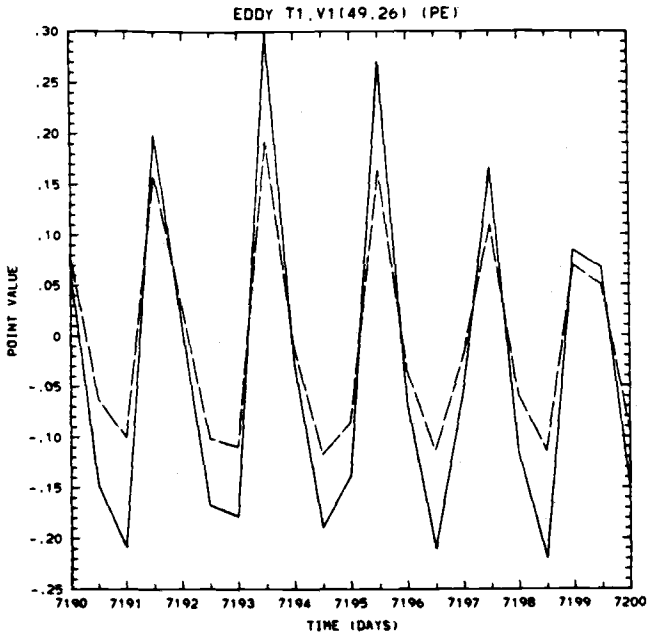

d

Fig. 7.4 (cont.)

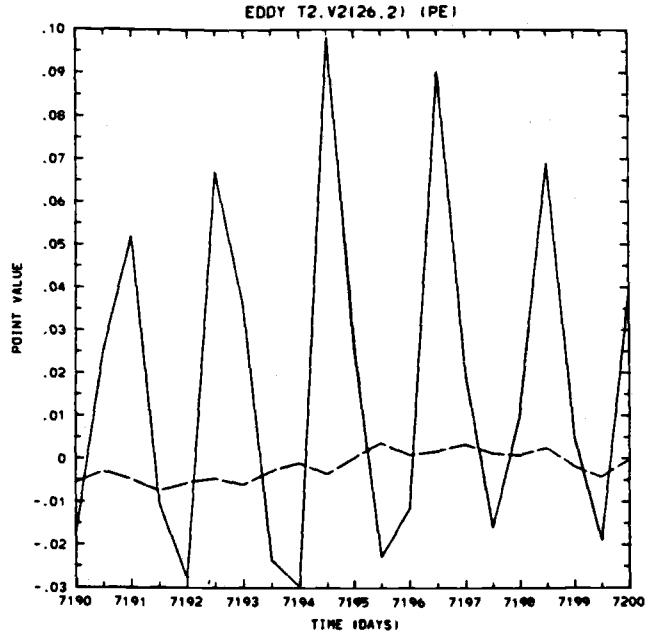

a

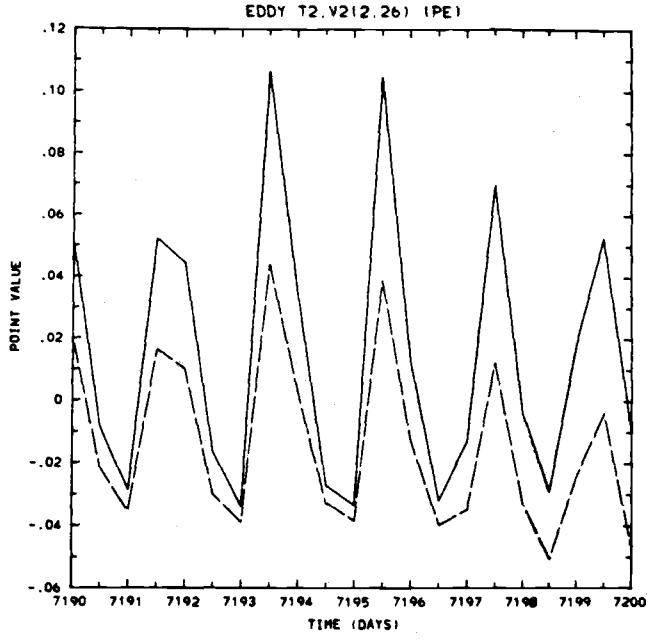

b

Fig. 7.5 Time series of T_2' (solid line) and v_2' (dashed line) for points near the middle of the a) southern, b) western c) northern, d) eastern boundaries.

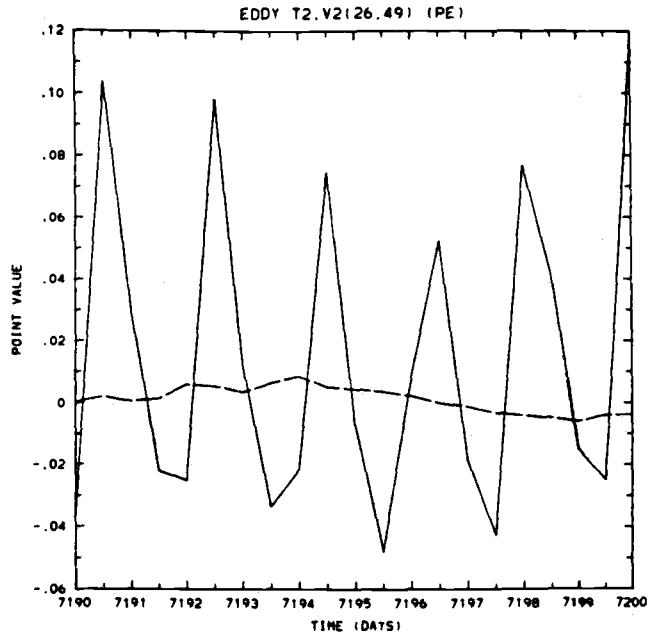

c

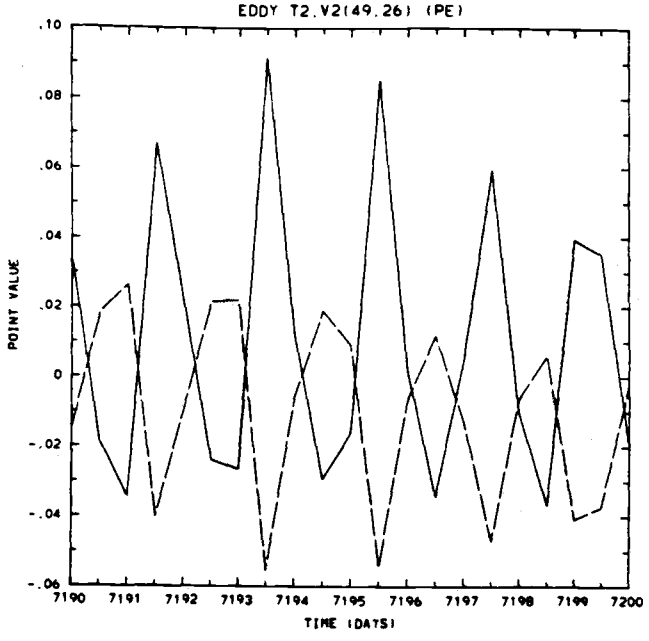

d

Fig. 7.5 (cont.)

(Fig. 7.5b), the v' and T' waves are in phase, with the result that the meridional eddy heat transports are poleward in these regions. Because the upper layer transports are so much larger than the lower layer, the total meridional eddy heat transports shown in Fig. 7.4 reflect the upper layer values. In all of these figures, the 1.9 day period signature of the Kelvin waves is clearly seen. As stated previously, there would also be divergent components of zonal eddy heat transports along the northern and southern boundaries to close the circuit. Thus the Kelvin waves just rotate heat around the basin. As a result, the divergent heat flux probably plays no important role but is just the "signature" of the Kelvin waves.

Finally, Fig. 7.6 shows strong evidence that the Kelvin waves are also the likely cause of the maximum in the divergent component of the eddy kinetic energy near the lateral boundaries. Both the 1.9 day period and the decrease in amplitude away from the lateral boundaries are clear signatures of these waves. Lastly, Fig. 7.7 suggests the interesting possibility that these waves can also contribute to the rotational component of the eddy kinetic energy near the lateral boundaries.

In all of the figures presented so far in this chapter, we have used half-day time intervals. In the five-year analyses presented in Chapters 5 and 6, two-day time intervals were used. Because the Kelvin waves have a period of 1.9 days, it is likely that the two-day sampling interval introduced aliasing into the five-year statistics. Fig. 7.8 is a comparison of the

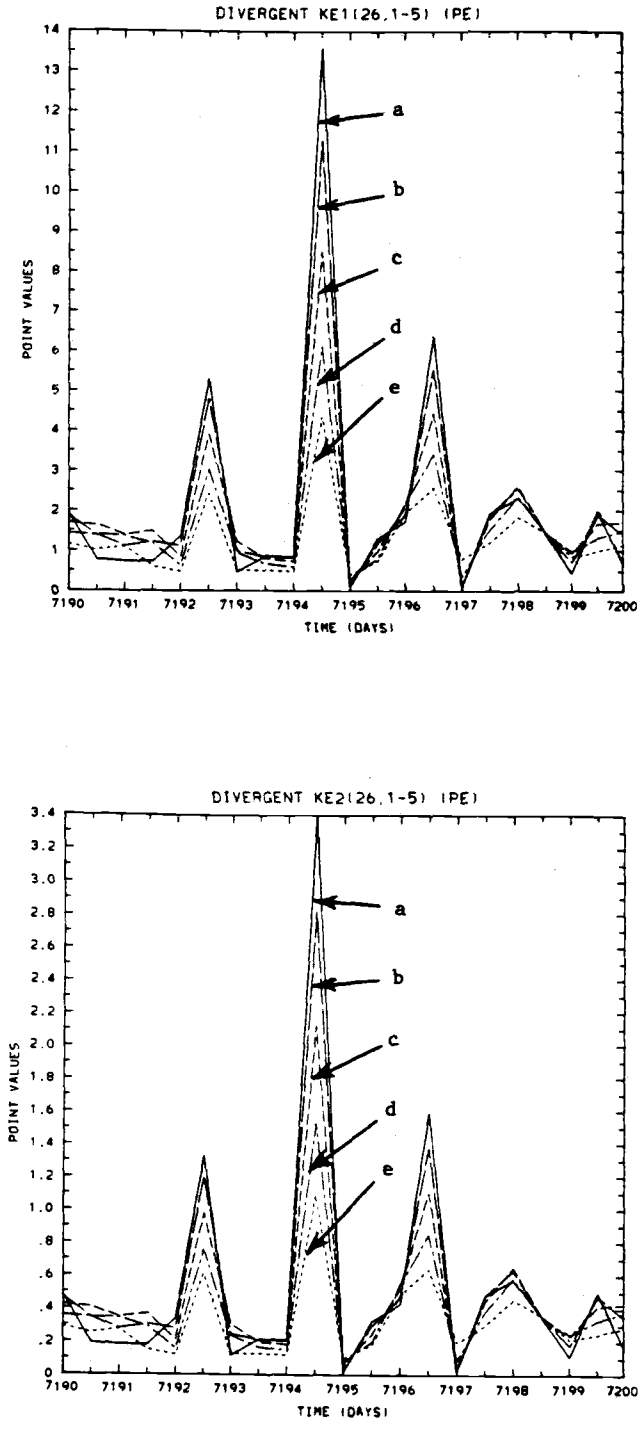

Fig. 7.6 Time series of K'_{1D} (top) and K'_{2D} (bottom) at half-day intervals for five grid points near the southern boundary of the single-gyre basin. The grid points plotted are: a) (26,1), b (26,2), c) (26,3), d) (26,4), e) (26,5).

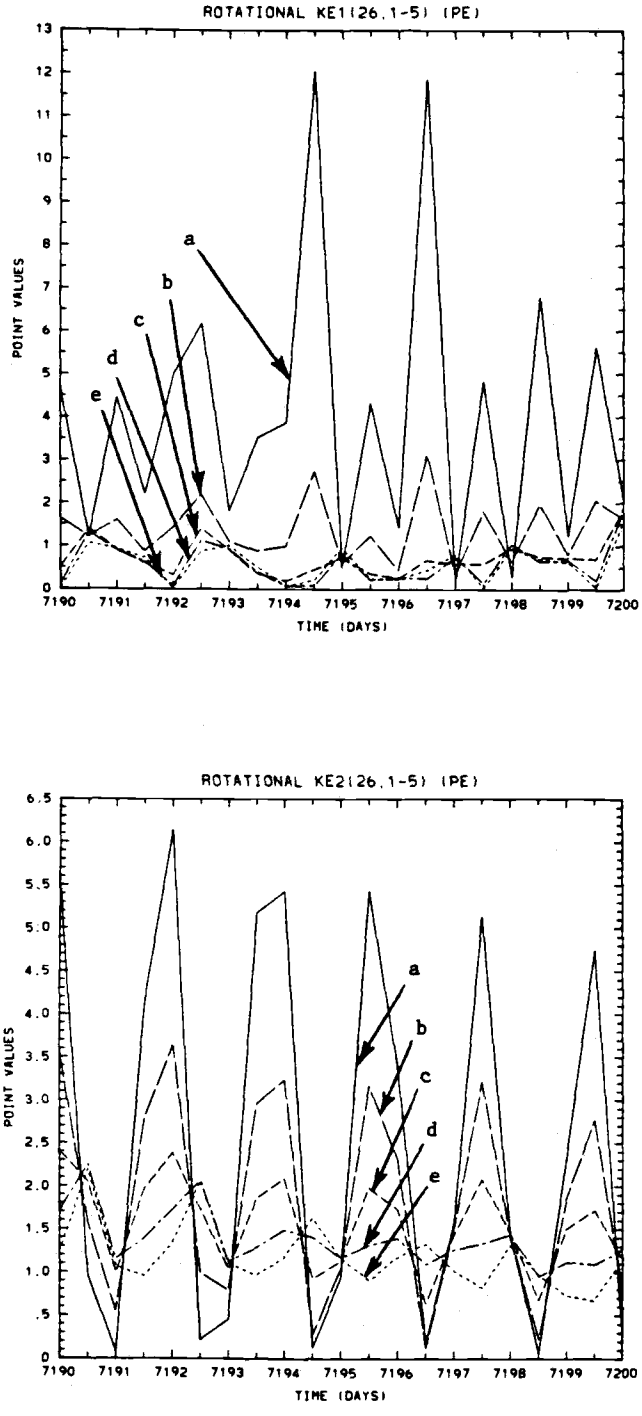

Fig. 7.7 Time series of K'_{1R} (top) and K'_{2R} (bottom) at half-day intervals for five grid points near the southern boundary of the single-gyre basin. The grid points plotted are: a) (26,1), b) (26,2), c) (26,3), d) (26,4), e) (26,5).

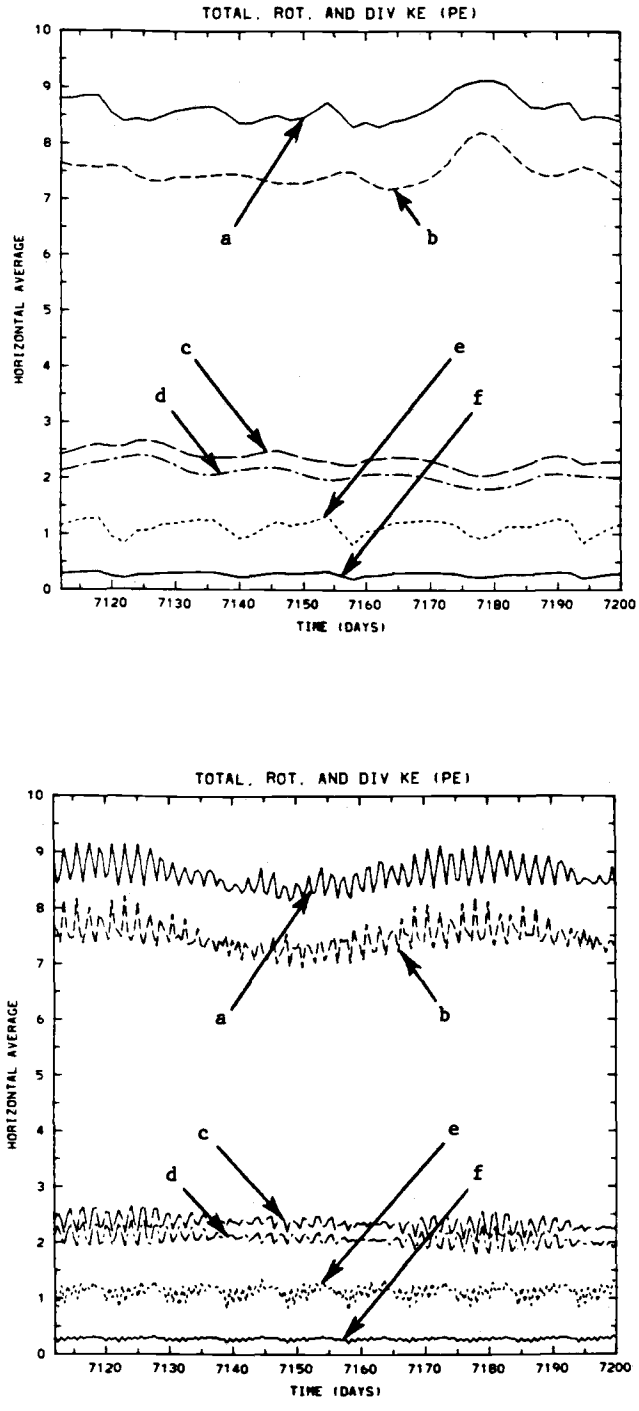

Fig. 7.8 Time series of the horizontally-averaged kinetic energies at two-day (top) and half-day (bottom) intervals: a) K_1, b) K_{1R}, c) K_2, d) K_{2R}, e) K_{1D}, f) K_{2D}.

time series of the horizontally-averaged kinetic energy components for each layer at two-day and half-day intervals. Although the time averages for these energy statistics are probably not affected by the aliasing, it certainly seems possible that other, higher-order statistics could be.

Whether the presence of these Kelvin waves is due to numerics or to physics remains uncertain. The questions of how Kelvin waves are generated, maintained and dissipated, and how they interact with eddies and the ocean general circulation need to be better understood not just in this type of PE model, but in real oceans as well. Kelvin waves are known to be sensitive to wind forcing, but a steady wind forcing, as used here, cannot give rise to transient waves. It is worth noting, however, that during the model spin-up, when wind forcing is first introduced, it is not steady. It is possible that, in the absence of a suitable dissipative mechanism, the waves introduced during spin-up could remain, even after 20 years. A comparison of Kelvin wave amplitudes at 15 and 20 years into the single-gyre integration showed no change in amplitude. This implies either 1) dissipation is very small for these waves, or 2) the waves are being continuously forced. Another possibility is that they are generated by nonlinear interactions of the mesoscale eddy field or by physical or numerical instability processes.

Recent theoretical studies by Davey et al. (1983) have shown that the use of lateral and vertical viscosity can influence free Kelvin waves. Lateral viscosity can signifi-

cantly affect baroclinic Kelvin waves, whereas vertical viscous effects can affect barotropic Kelvin waves. Hsieh et al. (1983) have shown that in addition to viscosity, horizontal grid resolution, the type of grid, and the choice of boundary conditions can significantly influence the behavior of free Kelvin waves. Based on their results, each of our PE model choices, i.e., the use of a fine-grid horizontal resolution with a C-grid scheme and free-slip boundary conditions, should have the least effect on the behavior of these waves. As a result, our model seems to be ideal for their study.

More extensive analysis of the PE model results is clearly needed in order to gain a deeper understanding of the underlying physics. This comparison study highlights similarities in the PE and QG models, but further investigations of the results should highlight differences. The possible interaction of Kelvin waves with mesoscale eddies and the ocean general circulation is a new and important problem which deserves further investigation.

CHAPTER 8. SUMMARY

The present study provides a foundation for the first quantitative intercomparison of QG and PE models, which have both been modified in order to make the numerics as similar as possible so that the differences in PE and QG physics can be understood. In order to give nearly similar results, we had to overcome differences 1) in model equations and prognostic variables, and 2) in the basic model configurations. We started with the PE system of equations and derived a set of equations which had the same form and prognostic variables as the QG system. We then made the QG approximation to this set. As a result we obtained a consistent set of PE and QG comparison equations and prognostic variables, which could be used to make systematic comparisons between the PE and QG systems. We obtained a consistent model configuration by choosing the same parameters for both models, and by using the same vertical and horizontal distribution of variables.

Using this set of analysis equations, we developed analysis procedures in the following areas: 1) energy, 2) relative and potential vorticity, and 3) eddy momentum and heat transports. The results of two QG and PE numerical experiments were then analyzed in each of these areas.

In the first experiment, two-layer versions of the QG and PE models were spun up with fine-grid horizontal resolution (20

km) using a single-gyre wind forcing in a 1000 x 1000 km rectangular basin centered at midlatitudes. It is important to note that the small basin size tended to diminish one of the important differences between PE and QG models, the variation in the Coriolis parameter in some terms. Both models used lateral Laplacian friction and no bottom friction. Biharmonic heat diffusion was used in the PE model. The choice of parameters was made on the basis of making the models as similar as possible.

The second experiment was similar to the first, but differed in the following respects: 1) a double-gyre wind forcing was used, with the result that the northern boundary of the single-gyre experiment was replaced by a free jet at midlatitudes, 2) the north-south extent of the basin was increased from 1000 to 2000 kilometers, and 3) bottom friction was incorporated. The model parameters used in this experiment were chosen in order to explore the roles of a free jet and bottom friction in the ocean general circulation for both models, while still allowing some comparisons to be made between the single-gyre and double-gyre results. Another difference between the two experiments is the value of the constant Coriolis parameter f_o; this alone would cause such processes as baroclinic instability to change.

The results of the single-gyre and double-gyre experiments were quite similar. The reason for this is most likely due to

the use of a rather large Laplacian friction coefficient. In both experiments, 65 to 75% of the upper layer mean kinetic energy input by the wind was dissipated by Laplacian friction, leaving only 25 to 35% of the energy to participate in the eddy generation process. This suggests that in both experiments Laplacian friction dominated over eddy processes, with the result that rather weak instabilities and nonlinearities were observed. If the friction were reduced, the eddy processes could play a greater role, and stronger instabilities might be observed (see Holland, 1978). In particular, barotropic instabilities would be more likely to occur in the free jet of the double-gyre case, resulting in a different stability problem than the single-gyre.

In both experiments and models, the spin-up process was characterized by an increase in both upper layer kinetic energy and available potential energy, with the lower layer remaining nearly motionless until some critical shears were reached. Between ~2 and 4 years, the available potential energy and the upper layer circulation had built up sufficiently for the flow to become baroclinically unstable. The release of available potential energy then gave rise to eddy motions, which generated deep mean flows in the lower layer via energy transfers from the upper layer. Between ~1500 and 5000 days, the system came into a statistical equilibrium in which eddies and the mean flow were in mutual balance.

A comparison of the PE and QG time-dependent energetics showed similar energetics and energy transfer rates for both experiments. The main differences were: 1) the upper and lower layer kinetic energies were higher by about 35% for the PE model, and 2) the PE model had high frequency oscillations, which corresponded to the frequency of Kelvin waves.

The basic time-averaged PE and QG quantities were compared with each other in both experiments in order to assess similarities and differences. Most quantities were quite similar. The main difference in the models was due to the presence of Kelvin waves along the lateral boundaries of the PE model. These waves propagated counterclockwise along the boundaries with the phase speed of inertia-gravity waves, i.e., ~4 m s^{-1}.

An examination of instantaneous, time mean and eddy fields for both models showed that in the upper layer, the eddies and mean flow had about the same amplitude, while in the lower layer, the eddies were dominant and were the main driving mechanism for the lower layer mean circulation. The eddies propagated westward at ~5.5 km per day. In the single-gyre experiment, the eddies were baroclinic in the northern half of the basin, and barotropic in the southern half. In the double-gyre experiment, the eddies tended to be quite barotropic in the interior. The main difference between the PE and QG eddy fields in both experiments was the additional eddy field

propagating counterclockwise around the basin in the PE model. This field was due to the Kelvin waves and was entirely baroclinic.

An examination of the horizontally-averaged, time-mean energetics showed consistently higher PE total and rotational kinetic energy components than QG, and small but significant divergent components of PE kinetic energy. Geographical distributions of PE eddy kinetic energy suggested the following regions of active transience: 1) the boundary, where Kelvin waves are present, 2) the recirculation region, where the mesoscale eddies are driven by baroclinic instability processes, and 3) in the double-gyre experiment, the area of the free jet, where the mesoscale eddies are driven by barotropic instability processes. In the QG model only the latter two regions were present.

The results of the relative vorticity analysis showed similar QG and PE vorticity patterns, but generally larger QG values of both clockwise and counterclockwise vorticity. The change of vorticity due to the eddies was concentrated in the recirculation region for the single-gyre experiment, and in the vicinity of the free jet region for the double-gyre experiment. Analysis of relative vorticity terms showed similar PE and QG "mean vorticity tendencies", except for Kelvin wave effects in the boundary regions of the PE model. Except in the recirculation region, the LB terms were smaller than any other vorticity terms. The small basin sizes used in these experiments

tended to diminish the importance of these LB terms. The FB and PE terms were calculated as a residual, and shown to be significant. Further analysis would be necessary to determine what terms in particular, were important.

An examination of the geographical distributions of the time-averaged quasigeostrophic potential vorticity showed that the PE and QG potential vorticity patterns were very similar in both layers. The reason for this similarity was that only the lowest order (i.e., the quasigeostrophic) component had been calculated for the PE model. Again further analysis of the higher order PE components would be necessary to address differences.

The zonally-averaged off-diagonal component of the eddy momentum transports showed that the PE rotational component was dominant over the divergent, and was generally larger than the QG. In some areas the $\overline{u'v'}$ correlations tended to retard the mean flow, whereas in others they tended to drive it.

Both eddy and mean meridional heat transports were calculated for the PE model. In general the eddies acted against the mean transport of heat. Both divergent and rotational components were significant in transporting eddy meridional heat transports. The main contributions for eddy heat transport by the rotational component was in the recirculation area, an area shown by Holland and Lin (1975a) and Holland (1978) to be of possible importance for eddy transports of heat equatorward.

The main contribution for eddy meridional heat transport by the divergent component was along the western and eastern boundaries, and was shown to be due to the Kelvin waves. Presumably the main contribution for eddy zonal heat transport by the divergent component would be along the northern and southern boundaries to close the circuit. As a result, the divergent heat flux probably plays no role but is just the "signature" of the Kelvin waves.

Thus most of the differences in the PE and QG models were due to the presence of Kelvin waves along the lateral boundaries of the PE model. Whether the presence of these waves is due to numerics or to physics remains uncertain and awaits further investigation.

CHAPTER 9. BIBLIOGRAPHY

Arakawa, A., 1966. Computational design for long term numerical integration of the equations of fluid motion: Two-dimensional incompressible flow. Part I. J. Comput. Phys., 1, 119-143.

Arakawa, A., 1972. Design of the UCLA general circulation model. Tech. Rep. No. 7, Dept. Meteor., Univ. of Calif., Los Angeles, 116 pp.

Arakawa, A. and V. R. Lamb, 1977. Computational design of the basic dynamical processes of the UCLA general circulation model. In Methods of Computational Physics, 17, Academic Press, New York, 173-265.

Baker, D. J., Jr., W. D. Nowlin, Jr., R D. Pillsbury and H. Bryden, 1977. Antarctic circumpolar current: Space and time fluctuations in the Drake Passage. Nature, 268, 696-699.

Batteen, M. L. and Y.-J. Han, 1981. On the computational noise of finite-difference schemes used in ocean models, Tellus, 33, 387-396.

Bennett, A. J., 1983. The South Pacific including the East Australian Current. In: Eddies in Marine Science, (A. R. Robinson, Ed.), Springer-Verlag, New York, 219-244.

Bernstein, R. L., 1983. Eddy structure of the North Pacific Ocean. In: Eddies in Marine Science (A. R. Robinson, Ed.), Springer-Verlag, New York, 158-166.

Bernstein, R. L., and W. B. White, 1974. Time and length scales of baroclinic eddies in the central North Pacific Ocean. J. Phys. Oceanogr., 4, 613-624.

Blandford, R. R., 1971. Boundary conditions in homogeneous models. Deep-Sea Res., 18, 739-751.

Bourne, D. E. and P. C. Kendall, 1968. Vector analysis. Allyn and Bacon, Boston, Masachusetts.

Bretherton, F. P., 1975. Recent developments in dynamical oceanography. Quart. J. Roy. Meteor. Soc., 101, 705-721.

Bretherton, F. P. and D. B. Haidvogel, 1976. Two-dimensional turbulence above topography. J. Fluid Mech., 78, 129-154.

Bretherton, F. P., and M. Karweit, 1975. Mid-ocean mesoscale modeling. In: Numerical Models of Ocean Circulation, U.S. NAS, Washington, D.C., 237-249.

Bryan, K., 1969. A numerical method for the study of the circulation of the world ocean. J. Comp. Physics, 4, 347-376.

Bryan, K. and L. J. Lewis, 1979. A water mass model of the world ocean. J. Geophys. Res., 84, 2503-2517.

Bryden, H. L., 1983. The Southern Ocean. In: Eddies in Marine Science, (A. R. Robinson, Ed.), Springer-Verlag, New York, 265-277.

Charney, J., 1947. The dynamics of long waves in a baroclinic westerly current. J. Meteor., 4, 135-162.

Crease, J., 1962. Velocity measurement in the deep water of the Western North Atlantic. J. Geophys. Res., 67, 3173-3176.

Cushman-Roisin, B., 1983. Analytical, linear stability criteria for the leap-frog, Dufort-Frankel method. Submitted to J. Comp. Phys.

Dantzler, H. L., 1976. Geographical variations in intensity of the North Atlantic and North Pacific oceanic eddy fields. Deep-Sea Res., 23, 783-794.

Dantzler, H. L., 1977. Potential energy maxima in the tropical and subtropical North Atlantic. J. Phys. Oceanogr., 7, 512-519.

Davey, M. K., W. W. Hsieh, and R. C. Wajsowicz, 1983. The free Kelvin wave with lateral and vertical viscosity. J. Phys. Oceanogr., 13, 2182-2191.

Dickson, R. R., 1983. Global summaries and intercomparisons--Long-term current meter moorings. In: Eddies in Marine Science, (A. R. Robinson, Ed.), Springer-Verlag, New York, 278-353.

Eady, E. J., 1949. Long waves and cyclone waves. Tellus, 1, 33-52.

Emery, W., 1983. Global summary: Review of eddy phenomena as expressed in temperature measurements. In: Eddies in Marine Science, (A. R. Robinson, Ed.), Springer-Verlag, New York, 354-403.

Frankignoul, C., and P. Müller, 1979. Quasi-geostrophic response of an infinite β-plane ocean to stochastic forcing by the atmosphere. J. Phys. Oceanogr., 9, 104-127.

Gill, A. E., 1983. Eddies in relation to climate. In: Eddies in Marine Science, (A.R. Robinson, Ed.), Springer-Verlag, New York, 441-445.

Gill, A. E., J. S. A. Green, and A. J. Simmons, 1974. Energy partition in the large-scale ocean circulation and the production of mid-ocean eddies. Deep Sea Res., 21, 499-528.

Gould, W. J., 1983. The Northeast Atlantic Ocean. In: Eddies in Marine Science, (A. R. Robinson, Ed.), Springer-Verlag, New York, 145-157.

Gründlingh, M. L., 1983. Eddies in the Southern Indian Ocean and Agulhaus Current. In: Eddies in Marine Science, (A. R. Robinson, Ed.), Springer-Verlag, New York, 245-264.

Haidvogel, D. B., 1979. A discussion of certain modeling factors which influence the results of eddy-resolving ocean circulation studies. Dyn. of Atmos. and Oceans, 3, 181-190.

Haidvogel, D. B., 1983. Periodic and regional models. In: Eddies in Marine Science, (A. R. Robinson, Ed.), Springer-Verlag, New York, 404-437.

Haidvogel, D. B., and W. R. Holland, 1978. The stability of ocean currents in eddy-resolving general circulation models. J. Phys. Oceanogr., 8, 393-413.

Haltiner, G. J., 1971. Numerical weather prediction. John Wiley and Sons, Inc., 317 pp.

Haltiner, G. J. and R. T. Williams, 1980. Numerical prediction and dynamic meteorology. John Wiley and Sons, Inc., 477 pp.

Han, Y.-J., 1975. Numerical simulation of mesoscale ocean eddies, Ph.D. thesis, Univ. of Calif., Los Angeles, 153 pp.

Han, Y.-J., and W. L. Gates, 1982. Preliminary analysis of the performance of the OSU six-level oceanic general circulation model. Part 1. Basic design and barotropic experiment. Rep. No. 30, Climatic Research Institute, Oregon State University, Corvallis, 53 pp.

Haney, R. L., 1974. A numerical study of the response of an idealized ocean to large-scale surface heat and momentum flux. J. Phys. Oceanogr., 4, 145-167.

Harrison, D. E., 1979. Eddies and the general circulation of numerical model gyres: An energetic perspective. Rev. Geophys. Space Phys., 17, 969-979.

Harrison, D. E. and W. R. Holland, 1981. Regional eddy vorticity transport and the equilibrium vorticity budgets of a numerical model ocean circulation. J. Phys. Oceanogr., 11, 190-208.

Harrison, D. E. and A. R. Robinson, 1978. Energy analysis of open regions of turbulent flows--mean eddy energetics of a numerical ocean circulation experiment. Dyn. Atmos and Oceans, 2, 185-211.

Heinmiller, R. H., 1983. Instruments and methods. In: Eddies in Marine Science, (A. R. Robinson, Ed.), Springer-Verlag, Inc., New York, 542-567.

Holland, W. R., 1967. On the wind-driven circulation in an ocean with bottom topography. Tellus, 19, 582-599.

Holland, W. R., 1978. The role of mesoscale eddies in the general circulation of the ocean -- Numerical experiments using a wind-driven quasi-geostrophic model. J. Phys. Oceanogr., 8, 363-392.

Holland, W. R., 1983. Mesoscale eddy activity as part of the large-scale ocean circulation. In: Large-scale oceanographic experiments in the WCRP, Report of the JSC/CCCO Study Conference in Tokyo, 10-22 May 1982, WCPP Publication Series No. 1, 135-146.

Holland, W. R. and D. B. Haidvogel, 1980. A parameter study of the mixed instability of idealized ocean currents. Dyn. Atmos. Oceans, 4, 185-215.

Holland, W. R., D. E. Harrison, and A. J. Semtner, Jr., 1983. Eddy-resolving numerical models of large-scale ocean circulation. In: Eddies in Marine Science (A.R. Robinson, Ed.), Springer-Verlag, N.Y., pp. 379-403.

Holland, W. R. and L. B. Lin, 1975a. On the generation of mesoscale eddies and their contribution to the oceanic general circulation. I. A preliminary numerical experiment. J. Phys. Oceanogr., 5, 642-657.

Holland, W. R. and L. B. Lin, 1975b. On the generation of mesoscale eddies and their contribution to the oceanic general circulation. II. A parameter study. J. Phys. Oceanogr., 5, 658-669.

Holland, W. R. and P. B. Rhines, 1980. An example of eddy-induced ocean circulation. J. Phys. Oceanogr., 10, 1010-1031.

Hsieh, W. W., M. K. Davey, and R. C. Wajsowicz, 1983. The free Kelvin wave in finite-difference numerical models. J. Phys. Oceanogr., 13, 1383-1397.

Kim, J.-W., 1979. Design and preliminary performance of the OSU four-level oceanic general circulation model. Rep. No. 6, Climatic Research Institute, Oregon State University, Corvallis, 49 pp.

Kitano, K., 1974. Note on the Kuroshio anticyclonic eddy. J. Phys. Oceanogr., 4, 670-672.

Kitano, K., 1975. Some properties of the warm eddies generated in the confluence zone of the Kuroshio and Oyashio currents. J. Phys. Oceanogr., 5, 245-252.

Koshlyakov, M. N. and Y. M. Grachev, 1973. Mesoscale currents of a hydrophysical polygon in the tropical Atlantic. Deep-Sea Res., 20, 507-526.

Leetma, A., P. Niiler, and H. Stommel, 1977. Does the Sverdrup relation account for the mid-Atlantic circulation? J. Mar. Res., 35, 1-10.

Lilly, D. K., 1965. On the computational stability of numerical solutions of time-dependent non-linear geophysical fluid dynamics problems. Mon. Wea. Rev. 93, 11-26.

Lorenz, E. N., 1955. Available potential energy and the maintenance of the general circulation. Tellus, 7, 157-167.

Lorenz, E. N., 1960. Energy and numerical weather prediction. Tellus, 12, 364-373.

Lorenz, E. N., 1962. Simplified dynamic equations applied to the rotating-basin experiments. J. Atmos. Sci., 19, 39-51.

MacLeish, W. H., Ed., 1976. Ocean Eddies. Oceanus, 19, The Woods Hole Oceanographic Institution, Woods Hole, MA.

Manabe, S., 1983. Oceanic influence on climate--Studies with mathematical models of the joint ocean-atmosphere system. In: Large-scale oceanographic experiments in the WCRP, Report of the JSC/CCCO Study Conference in Tokyo, 10-22 May 1982, WCPP Publication Series No. 1, 1-27.

Matsuno, T., 1966. Numerical integrations of the primitive equations by a simulated backward difference method. J. Met. Soc. Japan, Ser. 2, 44, 76-84.

McWilliams, J. C., 1979. A review of research on mesoscale ocean currents. Rev. Geophys. and Space Phys., 17, 1548-1558.

McWilliams, J. C., 1983. On the mean dynamical balances of the Gulf Stream recirculation zone. J. Mar. Res., 41, 427-460.

McWilliams, J. C., et al., 1983: The local dynamics of eddies in the Western North Atlantic. In: Eddies in Marine Science, (A. R. Robinson, Ed.), Springer-Verlag, New York, 92-113.

McWilliams, J. C., W. R. Holland, and J. H. S. Chow, 1978. A description of numerical Antarctic Circumpolar Currents. Dyn. Atmos. and Oceans, 2, 213-291.

Mintz, Y., 1979. On the simulation of the oceanic general circulation. Report of the JOC Study Conf. on Climate Models: Performance Intercomparison and Sensitivity Studies (Washington, D.C., April 1978), GARP Publ. Series 22, WMO, Geneva, 607-687 (Vol. 2).

Needler, G. T., 1983. Subpolar gyres and the Arctic Ocean. In: Eddies in Marine Science, (A. R. Robinson, Ed.), Springer-Verlag, New York, 167-180.

Orlanski, I. and M. D. Cox, 1973. Baroclinic instability in ocean currents. Geophys. Fluid Dyn., 4, 297-332.

Owens, W. B., and F. P. Bretherton, 1978. A numerical study of mid-ocean mesoscale eddies. Deep-Sea Res., 25, 1-14.

Phillips, N. A., 1956. The general circulation of the atmosphere: A numerical experiment. Quart. J. Roy. Meteor. Soc., 82, 123-164.

Phillips, N. A., 1966. The equations of motion for a shallow rotating atmosphere and the "traditional approximation". J. Atm. Sci., 23, 626-628.

Phillips, N. A., 1973. Principles of large scale numerical weather prediction. In: Dynamic Meteorology (Morel, Ed.), D. Reidel Publishing Co., Holland, 1-97.

Phillips, O. M., 1969. The dynamics of the upper ocean. Cambridge University Press, 216 pp.

Rhines, P., 1975. Waves and turbulence on a beta-plane. J. Fluid Mech., 69, 417-443.

Rhines, P., 1977. The dynamics of unsteady currents. In The Sea, Vol. 6, J. Wiley and Sons, New York, 189-318.

Rhines, P. B. and W. R. Holland, 1979. A theoretical discussion of eddy-driven mean flows. Dyn. Atmos. Oceans, 3, 289-325.

Richardson, P. L., 1983. Eddy kinetic energy in the North Atlantic from surface drifters. J. Geophys. Res., 88, 4355-4367.

Richman, J. G., C. Wunsch, and N. G. Hogg, 1977. Space and time scales of mesoscale motion in the western North Atlantic. Rev. Geophys, and Space Phys., 15, 385-420.

Richtmeyer, R. D. and K. W. Morton, 1967. Difference methods for initial-value problems. Wiley-Interscience, 399 pp.

Robinson, A. R., 1983. Overview and summary of eddy science, In: Eddies in Marine Science, (A. R. Robinson, Ed.), Springer-Verlag, Inc., New York, 1-15.

Robinson, A. R., D. E. Harrison, and D. B. Haidvogel, 1979. Mesoscale eddies and general ocean circulation models. Dyn. Atmos. and Oceans, 3, 143-180.

Robinson, A. R., D. E. Harrison, Y. Mintz, and A. J. Semtner, 1977. Eddies and the general circulation of an idealized ocean gyre: A wind and thermally driven primitive equation numerical experiment. J. Phys. Oceanogr., 4, 182-207.

Robinson, A. R., and J. C. McWilliams, 1974. The baroclinic instability of the open ocean. J. Phys. Oceanogr., 7, 281-294.

Rossby, H. T., S. C. Riser, and A. J. Mariano, 1983. The Western North Atlantic - A Lagrangian viewpoint. In: Eddies in Marine Science, (A. R. Robinson, Ed.), Springer-Verlag, Inc., New York, 66-91.

Schmitz, W. J., 1977. On the deep general circulation in the western North Atlantic. J. Mar. Res., 35, 21-28.

Schmitz, W. J., 1978. Observations of the vertical distribution of low frequency kinetic energy in the western North Atlantic. J. Mar. Res., 36, 295-310.

Schmitz, W. J. and W. R. Holland, 1982. Numerical eddy resolving general circulation experiments: preliminary comparison with observation. J. Mar. Res., 40, 75-117.

Schmitz, W. J., W. R. Holland and J. F. Price, 1983. Mid-latitude mesoscale variability. Rev. Geophys. and Space Physics, 21, 1109-1119.

Schoenstadt, A. L., 1978. A transfer function analysis of numerical schemes used to simulate geostrophic adjustment. Report NPS-53-79-001. Naval Postgraduate School, Monterey, Calif., 44 pp.

Schulman, E. E., 1967. The baroclinic instability of a mid-ocean circulation. Tellus, 19, 292-305.

Semtner, A. J., 1974. An oceanic general circulation model with bottom topography. Technical Report. No. 9, Numerical Simulation of Weather and Climate. Dept. of Meteorology, Univ. of Calif., Los Angeles, 37 pp.

Semtner, A. J. and W. R. Holland, 1978. Intercomparison of quasigeostrophic simulations of the western North Atlantic circulation with primitive equation results. J. Phys. Oceanogr., 8, 735-754.

Semtner, A. J. and Y. Mintz, 1977. Numerical simulation of the Gulf Stream and mid-ocean eddies. J. Phys. Oceanogr., 7, 208-230.

Siedler, G., 1983. Tropical equatorial regions. In: Eddies in Marine Science (A. R. Robinson, Ed.), Springer-Verlag, Inc., New York, 181-199.

Swallow, J. C., 1983. Eddies in the Indian Ocean. In: Eddies in Marine Science (A. R. Robinson, Ed.), Springer-Verlag, Inc., New York, 200-218.

Swallow, J. C., and B. V. Hamon, 1960. Some measurements of deep currents in the eastern North Atlantic. Deep-Sea Res., 6, 155-168.

Takano, K., 1974. A general circulation model for the world ocean. Tech. Rep. No. 8, Dept. of Meteorology, Univ. of California, Los Angeles, 46 pp.

Tang, C. M., 1975. Baroclinic instability of stratified shear flows in the ocean and atmosphere. J. Geophys. Res., 80, 1168.

Thompson, P. D., 1961. Numerical weather analysis and prediction. The Macmillan Co., 170 pp.

Veronis, G., 1966. Wind-driven ocean circulation. Part 2. Numerical solution of the non-linear problem. Deep-Sea Res., 13, 31-55.

Warren, B. A., 1963. Topographic influences on the path of the Gulf Stream. Tellus, 15, 167-183.

Winninghoff, F., 1968. On the adjustment toward a geostrophic balance in a simple primitive equation model with application to the problem of initialization and objective analysis. Ph.D. dissertation., Univ. of Calif., Los Angeles, 161 pp.

Wunsch, C., 1983. Western North Atlantic Interior. In: Eddies in Marine Science (A. R. Robinson, Ed.), Springer-Verlag, Inc., New York, 46-65.

Wyrtki, K., L. Magaard, and J. Hager, 1976. Eddy energy in the oceans. J. Geophys. Res., 81, 2641-2646.

APPENDICES

Appendix A. Numerical details of the PE model

The PE model used in this study is a new one. It has much of the same basic model structure (e.g., C-grid horizontal distribution of variables) as the adiabatic PE model of Holland and Lin (1975a,b), yet has complete thermodynamics. Essentially the prognostic layer depth equations of the Holland and Lin model (see the Appendix in Holland and Lin, 1975a) are replaced by prognostic thermodynamic energy equations and constant layer depths. In this section, we describe numerical details of the PE model not presented in previous sections of the thesis, namely, vertical differencing (Section A.1), horizontal and time differencing (Section A.2), method of solution (Section A.3), and some integral properties of the PE finite-difference equations (Section A.4).

A.1 Vertical differencing

The vertical structure of the model, shown as a two-layer version in Fig. 3.1, has multi-layers. Here we use the subscripts $k + 1$ and $k - 1$ to denote the layers above and below, respectively, the layer k the vertical differencing is applied to. As in Fig. 3.1, the layers are numbered from top to bottom with the layer thickness given by h_k. The vertical coordinate

is the height z, which is positive upwards with z = 0 at the surface. The horizontal velocities, temperature and pressure are all defined at layer mid-points. The vertical velocity is defined at layer interfaces.

The thermodynamic energy equation (Eq. 3-5) in vertical difference form is

$$T_{kt} + L\,(T_k) + \frac{1}{2h_k}\left[w_k T_k + w_k T_{k-1} - w_{k+1} T_k - w_{k+1} T_{k+1}\right]$$

$$= \frac{2\kappa_H}{h_k(h_{k-1}+h_k)}\,(T_{k-1}-T_k) - \frac{2\kappa_H}{h_k(h_k+h_{k+1})}\,(T_k-T_{k+1})$$

$$\left\{ \begin{array}{c} +A_H\nabla^2 T_k \\ \text{or} \\ -B_H\nabla^4 T_k \end{array} \right. . \qquad \text{(A-1)}$$

In Eq. (A-1), $(T_k+T_{k-1})/2$ and $(T_k+T_{k+1})/2$ have been chosen for the vertical differencing of $(wT)_z$ in order to satisfy the conservation of the first and second moments of temperature, as far as vertical advection is concerned (Lorenz, 1960). A demonstration of this conservation principle for the PE model is given in Section A.4.

The vertical-difference form of the hydrostatic equation Eq. (3-3) is chosen to be

$$\frac{p_k - p_{k-1}}{z_k - z_{k-1}} = -\frac{g}{\rho o}\left(\frac{\rho_k + \rho_{k-1}}{2}\right) \qquad \text{(A-2)}$$

in order to be consistent with the vertical advection differencing of temperature. This form of the hydrostatic equation, under adiabatic,inviscid conditions, guarantees total energy conservation (Bryan, 1969; Semtner, 1974; Han, 1975).

The equation of state (3-6) in vertical difference form is

$$\rho_k = \rho_o(1-\alpha(T_k-T_o)) \qquad \text{(A-3a)}$$

for k layers and

$$\rho_{k+1} = \rho_o(1-\alpha(T_{k+1}-T_o)) \qquad \text{(A-3b)}$$

for k+1 layers. If we differentiate Eqs. (A-2), (A-3a) and (A-3b) with respect to x, and subsequently substitute the differentiated forms of Eqs. (A-3a) and (A-3b) into Eq. (A-2), we obtain

$$p_{kx} = p_{1x} - \frac{g\alpha}{4} \sum_{k=1}^{N} (h_k + h_{k+1}) (T_{kx} + T_{(k+1)x}) , \qquad \text{(A-4a)}$$

where N denotes the bottom layer. Similarly, differentiating Eqs. (A-2), (A-3a), and (A-3b) with respect to y and subsequently substituting the differentiated forms of Eqs. (A-3a) and (A-3b) into Eq. (A-2) results in

$$p_{ky} = p_{1y} - \frac{g\alpha}{4} \sum_{k=1}^{N} (h_k + h_{k+1}) (T_{ky} + T_{(k+1)y}). \qquad \text{(A-4b)}$$

Using Eq. (A-4a), the zonal momentum equation (3-1) in vertical difference form is

$$u_{kt} + L(u_k) + \frac{1}{2h_k}\left[w_k u_k + w_k u_{k-1} - w_{k+1}u_k - w_{k+1}u_{k+1}\right]$$

$$= fv_k + \tau_k^x - p_{1x} - C_B u_k \begin{cases} +A_m\nabla^2 u_k \\ \text{or} \\ -B_m\nabla^4 u_k \end{cases}, \qquad \text{(A-5)}$$

where the following notation has been used:

$$p_{1x} \equiv \frac{p_{1x}}{\rho_o}, \text{ as in Holland and Lin (1975a,b);}$$

$$\tau_1^x = \frac{1}{h_1}\tau(y) \text{ for } k=1; \text{ and}$$

$$\tau_k^x = \frac{g\alpha}{4}\sum_{k=1}^{N}(h_k + h_{k+1})(T_{kx} + T_{(k+1)x}) \text{ for } k > 1.$$

Similarly, using Eq. (A-4), the meridional momentum equation (3-2) in vertical difference form is

$$v_{kt} + L(v_k) + \frac{1}{2h_k}\left[w_k v_k + w_k v_{k-1} - w_{k+1}v_k - w_{k+1}v_{k+1}\right]$$

$$= -fu_k + \tau_x^y - p_{1y} - C_B v_k \begin{cases} +A_m\nabla^2 v_k \\ \text{or} \\ -B_m\nabla^4 v_k \end{cases}, \qquad \text{(A-6)}$$

where the following notation has been used:

$$p_{1y} \equiv \frac{p_{1y}}{\rho_o}, \text{ as in Holland and Lin (1975a,b);}$$

$$\tau_1^y \equiv \frac{1}{h_1}\tau = 0 \quad \text{for } k=1; \text{ and}$$

$$\tau_k^y = \frac{g\alpha}{4}\sum_{k=1}^{N}(h_k + h_{k+1})(T_{ky} + T_{(k+1)y}) \text{ for } k > 1.$$

The continuity equation Eq. (3-4) in vertical difference form, is

$$u_{kx} + v_{ky} + \frac{1}{h_k} w_k - \frac{1}{h_k} w_{k+1} = 0 \ . \qquad \text{(A-7)}$$

A.2 Horizontal and time differencing

To keep the finite-difference analogues of the equations relatively compact, the operators δ_x and $(\bar{\ })^x$ are defined such that

$$\delta_x \eta(x) \equiv \frac{1}{\Delta} \left[\eta(x + \tfrac{\Delta}{2}) - \eta(x - \tfrac{\Delta}{2})\right]$$

and

$$\overline{\eta(x)}^x \equiv \frac{1}{2} \left[\eta(x + \tfrac{\Delta}{2}) + \eta(x - \tfrac{\Delta}{2})\right] \ ,$$

where $\eta(x)$ is any function of x. The finite-difference Laplacian $\nabla^2(\ )$ is defined as

$$\nabla^2(\ ) = \delta_x^2(\ ) + \delta_y^2(\ ).$$

Using this notation, the finite-difference analogue of the governing equations (A-1), (A-5), (A-6) and (A-7) can be written as

$$T_k^{n+1} = T_k^{n-1} - 2\Delta t \left\{\delta_x (\overline{T_k}^x u_k) + \delta_y(\overline{T_k}^y v_k)\right.$$

$$\left. + \frac{1}{2h_k} \left[w_k(T_k + T_{k-1}) - w_{k+1}(T_k + T_{k+1})\right]\right.$$

$$- \frac{2\kappa H}{h_k(h_{k-1}+h_k)}(T_{k-1}^{n-1} - T_k^{n-1}) + \frac{2\kappa H}{h_k(h_k+h_{k+1})}(T_k^{n-1} - T_{k+1}^{n-1})$$

$$\begin{cases} +A_H\nabla^2 T_k \\ \text{or} \\ +B_H\nabla^4 T_k^{n-1}, \end{cases} \qquad \text{(A-8)}$$

$$u_k^{n+1} = u_k^{n-1} - 2\Delta t \left\{\delta_x(\overline{u_k}^x\,\overline{u_k}^x) + \delta_y(\overline{v_k}^x\overline{u_k}^y)\right.$$

$$+ \frac{1}{2h_k}\left[\overline{w_k}^x(u_k + u_{k-1}) - \overline{w_{k+1}}^x(u_k + u_{k+1})\right]$$

$$\left. - \overline{\overline{fv_k}^y}^x - \tau_k^x + C_B u_k^{n-1} \begin{cases} -A_m\nabla^2 u_k^{n-1} \\ \text{or} \\ +B_m\nabla^4 u_k^{n-1} \end{cases}\right\} - 2\Delta t\delta_x p_1, \qquad \text{(A-9)}$$

$$v_k^{n+1} = v_k^{n-1} - 2\Delta t \left\{\delta_x(\overline{u_k}^y\overline{v_k}^x) + \delta_y(\overline{v_k}^y\overline{v_k}^y)\right.$$

$$+ \frac{1}{2h_k}\left[\overline{w_k}^y(v_k + v_{k-1}) - \overline{w_{k+1}}^y(v_k + v_{k+1})\right]$$

$$\left. + \overline{\overline{fu_k}^x}^y - \tau_k^y + C_B v_k^{n-1} \begin{cases} -A_m\nabla^2 v_k^{n-1} \\ \text{or} \\ +B_m\nabla^4 v_k^{n-1} \end{cases}\right\} - 2\Delta t\delta_y p_1, \qquad \text{(A-10)}$$

$$w_{k+1} = h_k\delta_x u_k + h_k\delta_y v_k + w_k \quad . \qquad \text{(A-11)}$$

In Eq. (A-9), for k =1,

$$\tau_1^x = \frac{1}{h_1}\,\tau(y) \quad ;$$

for k > 1,

$$\tau_k^x = \frac{g\alpha}{4}\sum_{k=1}^{N}(h_k + h_{k+1})(T_{kx} + T_{(k+1)x}) \quad .$$

In Eq. (A-10), for k=1,

$$\tau_1^y = 0 \ ;$$

for $k > 1$,

$$\tau_k^y = \frac{g\alpha}{4} \sum_{k=1}^{N} (h_k + h_{k+1}) \ (T_{ky} + T_{(k+1)y}) \quad .$$

In both Eqs. (A-9) and (A-10), p_{1x} and p_{1y} are the x and y derivatives of the upper layer pressure divided by ρ_o, the mean density.

Eq. (A-8) is written with reference to a T point, Eq. (A-9) with reference to a u point, Eq. (A-10) with reference to a v point and Eq. (A-10) with reference to a w point. As in Holland and Lin (1975a), the horizontal differencing scheme is similar to that of Lilly (1965) for homogeneous problems. The scheme conserves both total energy and mass (See Section A.4).

The superscripts n-1 and n+1 in the equations denote the time level. Denoting the present time level as n, n-1 is one time step in the past and n+1 is one time step in the future. All terms which are not superscripted are at time level n. The friction terms are lagged a time step in order to avoid linear numerical instability (Thompson, 1961; Richtmyer and Morton, 1967; Haltiner, 1971; Phillips, 1973; Haltiner and Williams, 1980).

The principal time differencing scheme used in the model is the leap-frog scheme. Periodically, we use Euler's backward scheme (Matsuno, 1966) to suppress "time splitting", which is inherent in the leap-frog scheme. At the beginning of the integration the backward scheme is used for ten consecutive time steps. The leap-frog scheme is then used to continue the integration. Every 47 time steps the backward scheme is used again. According to Haltiner (1971), gravity waves of wavelength comparable to two grid intervals should be damped by periodic use of the backward scheme.

As a reference value for what the time step Δt should be in the model, the classical stability criterion, i.e., the CFL condition, can be used. Since the rigid lid condition excludes external gravity waves, the highest frequency motions are internal, inertial gravity waves. The propagation speed c of these waves is

$$c = \left(\frac{g' h_1 h_2}{H} \right)^{1/2} ,$$

where g' is reduced gravity, h_1 and h_2 are layer thicknesses and H is the total depth. Using the model choices of Holland (1978), i.e., a grid inverval Δ of 20 km, $g' = 0.02\ m^2 s^{-1}$, $h_1 = 1000$ m, and $h_2 = 4000$ m, the CFL condition for the time step Δt is

$$\Delta t < \frac{\Delta}{c} = 5 \times 10^3 s,$$

when one-dimensional criteria are used, and

$$\Delta t < \frac{\Delta}{\sqrt{2}c} = 3.5 \times 10^3 s,$$

when two-dimensional criteria are used (Haltiner and Williams, 1980).

It should be noted, as in Holland and Lin (1975a), that since the CFL condition is deduced from simple linear theory, this criterion should only be used as a reference value for the choice of Δt. Indeed, a trial-and-error process showed that a time step of 1200 s led to an unstable integration.

Another stability criterion for the time step comes from a consideration of the Laplacian lateral momentum diffusion. Using a viscosity coefficient A_m of 330 $m^2 s^{-1}$, we can obtain

$$\Delta t < \frac{1}{4} \frac{\Delta^2}{A} < 3 \times 10^5 \text{ s},$$

which is a less stringent criterion than the CFL condition.

The above criteria are obtained from either diffusive or advective considerations. Cushman-Roisin (1983) has shown that consideration of both advective and diffusive criteria can lead to more restrictive stability conditions. This consideration could lead to a criterion closer to our trial-and-error instability value of ~1200 s.

To be on the safe side, we use a time interval of 600 s for all PE experiments.

A.3 Method of solution

The rigid-lid assumption, $w = 0$ at the surface of the ocean, puts a constraint on solving the system of equations (A-8) - (A-11). Because of this assumption, the vertically-integrated horizontal velocity must satisfy a non-divergent condition, i.e.,

$$\frac{\partial}{\partial x} \int_{-H}^{0} u\,dz + \frac{\partial}{\partial y} \int_{-H}^{0} v\,dz = 0, \qquad \text{(A-12)}$$

obtained by integrating Eq. (3-4) and applying both the rigid-lid and flat-bottom assumptions. This condition then requires that the vertically integrated pressure satisfy a balance equation that can be obtained from Eqs. (3-1) and (3-2) using Eq. (A-12). Because of this condition, the pressure cannot be obtained by integrating the hydrostatic equation from the free surface. Instead, the pressure must be determined such that Eq. (A-12) is satisfied. This leads to a rather special solution procedure, developed by Bryan (1969) and used extensively by ocean modelers (e.g., Semtner, 1974; Haney, 1974; Takano, 1974; Holland and Lin, 1975a; Han, 1975; Kim, 1979; Han and Gates, 1982). The solution procedure described below closely

follows the method discussed in Holland and Lin (1975a).

We first derive the vorticity equation for the vertically integrated flow. This eliminates the upper layer pressure p_1. The resulting vorticity equation is then solved for the transport streamfunction Ψ at time step n+1. The vertical velocities w_k at time step n+1 can be calculated directly from the continuity equation (A-11) using the boundary conditions $w_1 = w_{N+2} = 0$. The temperature T_k^{n+1} can be calculated calculated directly from the thermodynamic energy equation (A-8).

As in Holland and Lin (1975a), we use the continuity equation (A-11) and vertical averaging to obtain

$$\sum (h_k \delta_x u_k) + \sum (h_k \delta_y v_k) = 0 \ ,$$

which, since h_k is constant, can be rewritten as

$$\delta_x \left(\sum h_k u_k\right) + \delta_y \left(\sum h_k v_k\right) = 0 \ .$$

This equation enables us to define a finite-difference transport streamfunction such that

$$-\delta_y \Psi = \sum h_k u_k \qquad \text{(A-13a)}$$

and

$$\delta_y \Psi = \sum h_k v_k \quad . \tag{A-13b}$$

To eliminate the upper-layer pressure, we first write the finite-difference forms of Eqs. (A-9) and (A-10) in shorthanded forms. Thus, multiplying Eqs. (A-9) and (A-10) each by h_k, we can write

$$h_k u_k^{n+1} = h_k u_k^{n-1} - h_k 2\Delta t \; U_k - 2\Delta t \; h_k \delta_k p_1 \tag{A-14}$$

and

$$h_k v_k^{n+1} = h_k v_k^{n-1} - h_k 2\Delta t \; V_k - 2\Delta t \; h_k \delta_y p_1 \; , \tag{A-15}$$

where, U_k, for instance, is the abbreviation for the bracketed terms in Eq. (A-9), which are not shown explicitly in Eq. (A-14), and is a number evaluated at every u point.

Substituting Eqs. (A-13a) and (A-13b) into Eqs. (A-14) and (A-15), respectively, we obtain

$$-\delta_y \Psi^{n+1} = -\delta_y \Psi^{n-1} - 2\Delta t \sum h_k U_k - 2\Delta t H \delta_x p_1 \tag{A-16}$$

and

$$\delta_x \Psi^{n+1} = \delta_x \Psi^{n-1} - 2\Delta t \sum h_k V_k - 2\Delta t H \delta_y p_1 \quad . \tag{A-17}$$

Next, we operate δ_y on Eq. (A-16) and δ_x on Eq. (A-17) and then subtract Eq. (A-16) from Eq. (A-17) to obtain

$$\nabla^2 \Psi^{n+1} = \nabla^2 \Psi^{n-1} + \delta_y (2\Delta t \sum h_k U_k) - \delta_y (2\Delta t \sum h_k V_k) \quad . \tag{A-18}$$

If the values of u_k and v_k are given at every point for time levels n-1 and n and if the values of w_k are given for time level n, the right hand side of Eq. (A-18) is a known function of space and is a finite-difference Poisson equation in ψ^{n+1} with Dirichlet boundary conditions.

Once the solution for the Poisson equation is obtained, Eqs. (A-16) and (A-17) can be used to evaluate $-2\Delta t\delta_x p_1$ and $-2\Delta t\delta_y p_1$:

$$-2\Delta t\delta_x p_1 = \frac{1}{H}\left(-\delta_y \psi^{n+1}+\delta_y \psi^{n-1}+2\Delta t\sum h_k U_k\right) \tag{A-19}$$

and

$$-2\Delta t\delta_y p_1 = \frac{1}{H}\left(\delta_x \psi^{n+1}-\delta_x \psi^{n-1}+2\Delta t\sum h_k V_k\right) \quad . \tag{A-20}$$

Substituting the right hand side of Eq. (A-19) into Eq. (A-9) and Eq. (A-20) into Eq. (A-10), Eqs. (A-9) and (A-10) can be used to solve for u_k^{n+1} and v_k^{n+1}. Explictly, these equations become

$$\begin{aligned} u_k^{n+1} = u_k^{n-1} &-2\Delta t\Big\{\delta_x(\overline{u_k}^x\,\overline{u_k}^x) + \delta_y(\overline{v_k}^x\,\overline{u_k}^y) \\ &+ \frac{1}{2h_k}\left[\overline{w_k}^x(u_k+u_{k-1}) - \overline{w_{k+1}}^x(u_k+u_{k+1})\right] \\ &- \overline{\overline{fv_k}^y}^x - \tau_k^x + C_B u_k^{n-1}\left\{\begin{array}{l} -A_m\nabla^2 u_k^{n-1} \\ \text{or} \\ +B_m\nabla^4 u_k^{n-1}\end{array}\right\}\Big\} \\ &+ \frac{1}{H}\left[\delta_y \psi^{n+1} + \delta_y \psi^{n-1} + 2\Delta t\sum h_k U_k\right] \end{aligned} \tag{A-21}$$

and

$$v_k^{n+1} = v_k^{n-1} - 2\Delta t \left\{ \delta_x(\overline{u_k}^{y}\,\overline{v_k}^{x}) + \delta_y(\overline{v_k}^{y}\overline{v_k}^{y}) \right.$$

$$+ \frac{1}{2h_k}\left[\overline{w_k}^{y}(v_k + v_{k-1}) - \overline{w_{k+1}}^{y}(v_k + v_{k+1})\right]$$

$$\left. + \overline{\overline{fu_k}^{x}}^{y} - \tau_k^{y} + C_B v_k^{n-1}\left\{ \begin{array}{l} -A_m\nabla^2 v_k^{n-1} \\ \text{or} \\ +B_m\nabla^4 v_k^{n-1} \end{array} \right\} \right\}$$

$$+ \frac{1}{H}\left[\delta_y \psi^{n+1} - \delta_y \psi^{n-1} + 2\Delta t \sum h_k V_k\right] \quad . \qquad \text{(A-22)}$$

The equations of motion can be integrated indefinitely. The method used for solving the Poisson equation (A-15) gives the exact solution to the finite-difference Poisson equation in a rectangular domain with zero boundary conditions. An efficient Fast Fourier Transform is used for this purpose.

A.4 Some integral properties of the PE finite-difference equations

1. Conservation of the first and second moments of temperature

We first show that the differential form of the temperature equation conserves the first and second moments of temperature. First, we horizontally average Eq. (3-5) to obtain

$$\iint T_t \, dxdy + \iint (uT)_x \, dxdy + \iint (vT)_y dxdy$$

$$+ \iint (wT)_z dxdy = \iint Q \, dxdy, \tag{A-23}$$

where

$$Q \equiv k_H T_{zz} \begin{cases} +A_H \nabla^2 T \\ \text{or} \\ -B_H \nabla^4 T \end{cases}, \tag{A-24}$$

and $\iint(\,)dxdy$ denotes the horizontal integration. We note that the second and third terms in Eq. (A-23) integrate to zero. Next, we vertically average Eq. (A-23) and apply the boundary conditions of a rigid lid at the surface and a flat bottom. Then

$$\iiint (wT)_z \, dxdydz = 0,$$

so that Eq. (A-23) reduces to

$$\iiint T_t dxdydz = \iiint Q \, dxdydz, \tag{A-25}$$

which, under adiabatic conditons, proves that the first moment of temperature is conserved.

Next, we multiply Eq. (3-5) through by the temperature to obtain

$$1/2(T^2)_t + T(uT)_x + T(vT)_y + T(wT)_z = TQ, \tag{A-26}$$

where Q is given by Eq. (A-24). We note that

$$T(uT)_x = 1/2(uT^2)_x + Tu_x \tag{A-27}$$

and

$$T(vT)_y = 1/2(vT^2)_y + Tv_y \, . \tag{A-28}$$

If we add Eqs. (A-27) and (A-28), use the continuity equation and substitute the resulting equation into Eq. (A-26), we obtain

$$\frac{1}{2}(T^2)_t = \frac{1}{2}(uT^2)_x + \frac{1}{2}(vT^2)_y - Tw_z + T(wT)_z = TQ. \qquad \text{(A-29)}$$

We note that

$$T(wT)_z = \frac{1}{2}(wT^2)_z + Tw_z \ . \qquad \text{(A-30)}$$

If we substitute Eq. (A-30) into (A-29), globally integrate the resulting equation and apply the boundary conditions of a rigid lid at the surface and a flat bottom, then Eq. (A-29) reduces to

$$1/2\iiint(T^2)_t dxdydz = \iiint TQ\ dxdydz, \qquad \text{(A-31)}$$

which, under adiabatic conditions, proves that the second moment of temperature is conserved.

We next show that the finite-difference form of the temperature equation preserves the first and second moments of temperature. First, if we take a summation of Eq. (A-8) for all i,j and apply the kinematic boundary conditions, we find that

$$\sum_{i,j} \delta_x(\bar{T}_k^x u_k) + \sum_{i,j} \delta_y(\bar{T}_k^y v_k) = 0, \qquad \text{(A-32)}$$

where $\sum_{i,j}$ denotes a summation taken over the horizontal ocean domain. Next it we multiply Eq. (A-8), through by h_k, take a summation of Eq. (A-8) for all k and apply the boundary conditions $w_1 = w_{n+1} = 0$, we find that

$$\sum_k((w_k(T_k + T_{k-1}) - W_{k+1}(T_k + T_{k+1})) = 0. \qquad \text{(A-33)}$$

Using (A-32) and (A-33) in the global average of Eq. (A-8), under adiabatic conditions, we obtain

$$\sum_{i,j,k} h_k \left(\frac{T_k^{n+1} - T_k^{n-1}}{2\Delta t}\right) = 0$$

or

$$\frac{\partial}{\partial t} \sum_{i,j,k} h_k T_{i,j,k} = 0, \tag{A-34}$$

which is the finite-difference form of the conservation of the first moment of temperature.

To obtain the second moment of temperature, we multiply Eq. (A-8) through by $h_k T_k$ and note that

$$h_k T_k \delta_y (\bar{T}_k^x u_k) = \frac{1}{2} h_x \delta_x (\bar{T}_k^{x^2} u_k) = \frac{1}{2} h_k (\bar{T}_k^{x^2}) \delta_x u \tag{A-35}$$

and

$$h_k T_k \delta_k (\bar{T}_k^y v_k) = \frac{1}{2} h_k \delta_y ((\bar{T}_k^y)^2 u_k) - \frac{1}{2} h_k (T_k)^2 \delta_y v. \tag{A-36}$$

If we add Eqs. (A-35) and (A-36), use the continuity equation for the last terms in Eqs. (A-35) and (A-36), substitute the equations into Eq. (A-8) and take a summation of Eq. (A-8) for all i,j, we find that the first terms on the right hand sides of Eqs. (A-35) and (A-36) = 0. If we take a summation of Eq. (A-8) for all k and apply the boundary conditions $w_1 = w_{n+1} = 0$, we find that the last terms in Eqs. (A-35) and (A-36) and the

vertical advection of temperature terms in Eq. (A-8) sum to zero. Hence, under adiabatic conditions, we obtain

$$\sum_{i,j,k} h_k \left(\frac{(T_k^{n+1})^2 - (T_k^{n-1})^2}{4\Delta t}\right) = 0$$

or

$$\frac{\partial}{\partial t} \sum_{i,j,k} h_k \frac{(T_{i,j,k})^2}{2} = 0, \qquad \text{(A-37)}$$

which is the finite-difference form of the conservation of the second moment of temperature.

Conservation of mass

We first show that the differential form of the continuity equation conserves mass. First, we horizontally integrate Eq. (3-4):

$$\iint u_x \, dxdy + \iint v_y \, dxdy = -\iint w_z \, dxdy \, . \qquad \text{(A-38)}$$

We note that the left hand side of Eq. (A-38) integrates to zero. Next, we vertically integrate Eq. (A-38). Applying the boundary conditions of a rigid lid at the surface and a flat bottom, we find that the right hand side of Eq. (A-38) integrates to zero. This proves, for the differential form, that mass for the total ocean is conserved.

Next, we show that the finite-difference form preserves mass. First, we take a summation of Eq. (A-11) for all i,j to obtain

$$\sum_{i,j} w_{i,j,k+1} - \sum_{i,j} w_{i,j,k} = (h_k/\Delta)\sum_{i,j} [u_{i+1,j,k} - u_{i,j,k} + v_{i,j+1,k} - v_{i,j,k}] , \qquad \text{(A-39)}$$

We note that all terms on the right hand side of Eq. (A-39) cancel out, except those at lateral boundaries, which are set to zero as kinematic boundary conditions. Consequently, the right hand side of Eq. (A-39) = 0. If we take a summation of Eq. (A-39) for all k and use the boundary conditions $w_1 = w_{n+1} = 0$, we find that the left hand side of equation = 0. This proves, for the finite-difference form, that mass for the total ocean is conserved.

Appendix B. Notes on the processing and plotting of the data

The processing and plotting of the data is complicated by the fact that the PE model has a staggered grid, and some QG variables (such as vertical velocity) are not defined on the same grid points as the PE. The following notes describe how these problems are handled and clarify the relationship between the plots and the model grid.

1) For both models, the physical basin grid size is 51 x 51 for the single gyre, and 51 x 101 for the double gyre (This leaves 50 x 50 or 50 x 100 grid spaces). The stream-function is defined on the basin boundaries.

2) One- or two-dimensional linear interpolation is used to get variables on the same grid for computations.

3) All horizontal averages are area averages over the basin (Data points located on the basin boundaries are half-weighted).

4) The boundary of the physical basin is located one grid point inside of the perimeter of all horizontal slab-plots. The latitude and longitude axes in these plots are linear with respect to the model grid. The interior tick marks along these

axes locate the points at which the streamfunction is defined (both models). When data are defined on grid points other than the streamfunction points, they are plotted midway between the tick marks.

5) The vector plots combine scalar components to form velocity vectors. For clarity, only every other vector is plotted, starting at the lower left. The arrow length is scaled to the velocity magnitude as specified by the key (the longest arrow always spans four-grid spaces).

6) On the zonal average plots, the interior tick marks locate the model streamfunction grid points, in the same manner as the horizontal slab plots. The exterior tick marks locate latitudes in a manner consistent with the β-plane assumption (the latitude scale is therefore nonlinear).